12-2022

Wet chemical synthesis and properties of argyrodite sulfide solid electrolytes for solid state lithium batteries.

William Arnold
University of Louisville

WET CHEMICAL SYNTHESIS AND PROPERTIES OF ARGYRODITE SULFIDE SOLID ELECTROLYTES FOR SOLID STATE LITHIUM BATTERIES

By
William R. Arnold
B.S., University of Kentucky, 2016
M.S., University of Louisville, 2018

A Dissertation
Submitted to the Faculty of the
J.B. Speed School of Engineering of the University of Louisville
in Partial Fulfillment of the Requirements
for the Degree of

Doctor of Philosophy
in Mechanical Engineering

Department of Mechanical Engineering
University of Louisville
Louisville, KY

December 2022

WET CHEMICAL SYNTHESIS AND PROPERTIES OF ARGYRODITE SULFIDE SOLID ELECTROLYTES FOR SOLID STATE LITHIUM BATTERIES

By

William Richard Arnold
B.S., University of Kentucky, 2016
M.S., University of Louisville, 2018

A Dissertation Approved on

November 18, 2022

by the following Dissertation Committee:

_____

Dissertation Director

Dr. Hui Wang

_____

Dr. Jacek Jasinski

_____

Dr. Badri Narayanan

_____

Dr. Gamini Sumanasekera

_____

Dr. Sam Park

DEDICATION

This dissertation is dedicated to my parents Anne and Bobby Arnold

for always supporting me both in school and in life

and to my brothers Robert and Winston

for giving me an example to follow and a goal to strive for.

ACKNOWLEDGEMENTS

I would like to acknowledge first and foremost my PI, Dr. Hui Wang, for her mentorship, guidance, patience, and kindness. I had so much to learn when I began this journey, and she went above and beyond being available for all my questions while also serving as an example of the value of hard work and dedication. More than anything else, she is a genuinely good person and I feel lucky to have been her student. I would like to acknowledge the many professors I have had over the years who have given me opportunities in science and helped foster my interest. I would like to thank my committee members, Dr. Badri Narayanan, Dr. Jacek Jasinski, Dr. Gamini Sumanasekera, and Dr. Sam Park for their assistance and advice on my dissertation and throughout my doctorate. Finally, I would also like to acknowledge my colleagues in the Solid State Energy Lab at 2929 S. Floyd for being good friends and making this journey easier to bear. I couldn't have done it without them.

ABSTRACT

WET CHEMICAL SYNTHESIS AND PROPERTIES OF ARGYRODITE SULFIDE SOLID ELECTROLYTES FOR SOLID STATE BATTERIES

William Arnold

November 18, 2022

The commercialization of the lithium-ion battery (LIB) in 1991 was responsible for the explosion in portable electronic technologies that has been seen over the past 30 years. With the advent of electric vehicles and other high-powered technologies, there is tremendous demand for LIBs with higher energy density and high safety. To achieve this, new electrode materials must be explored. The obvious choice of anode material would be pure metal lithium, which has a theoretical specific capacity of 3860 mAh g^{-1}. Unfortunately, metal lithium anodes have not been widely commercialized due to their tendency to react violently with the flammable liquid electrolytes used in today's batteries.

Battery safety can best be achieved by adopting solid electrolytes in place of liquid electrolytes. Solid electrolytes are nonvolatile and nonflammable, safely allowing for the combination of high-capacity cathode materials with a Li metal anode. Argyrodite sulfide solid electrolytes such as halogen-doped Li_6PS_5X (X = Cl, Br, I) are noted for their high ionic conductivity. But before sulfides can be commercially adopted, they possess several disadvantages which must be addressed, including time- and energy-consuming synthesis processes, poor electrochemical stability, and intrinsically poor air stability. This

dissertation seeks to address each of these challenges through materials design an synthesis strategies. In this work, we pioneer a solvent-based approach for the synthesis of argyrodite solid electrolytes Li_7PS_6 and Li_6PS_5X instead of a stringent solid-state synthesis. Nontoxic ethanol is employed as the solvent, enabling a rapid synthetic approach to produce argyrodite solid electrolytes with high phase purity and compositional flexibility. Compared with Li_7PS_6, halogen doping (i.e. X = F, Cl, Br, I) not only increases the ionic conductivity, but also enhances the electrochemical stability at the interface towards Li metal. Specifically, F-doped argyrodites produce a robust SEI layer containing LiF, contributing to enhanced interfacial stability. Finally, to address the air instability challenge, argyrodite-incorporated composite solid electrolytes (CSEs) are designed and prepared to produce stable and flexible membranes that are demonstrated in solid-state Li metal batteries. These advances push argyrodite sulfide solid electrolyte research further and pave the way for the proliferation of next generation lithium metal batteries.

TABLE OF CONTENTS

LIST OF FIGURES

FIGURE PAGE

CHAPTER 1

INTRODUCTION

1.1 Background and Motivation

The invention of a commercially viable lithium-ion battery (LIB) in 1991 was a significant moment in the history of electricity. For the first time, a relatively safe energy storage system touting high energy density, light weight, and high reversibility with long cycle life was available for mass consumption. The effect this invention has had has been total in its impact, allowing for the proliferation of everything from cell phones to electric vehicles to grid scale energy storage systems.

Traditional LIBs consist of four constituent parts: the positive cathode, negative anode, and a dual-function barrier between them composed of a separator material and an organic electrolyte (**Figure 1.1**). The first commercially successful LIB was produced by the Sony Corporation of Japan and utilized an oxide-based $Li_{1-x}CoO_2$ cathode, a carbon-based Li_xC anode, and a carbonate-based liquid electrolyte. While slight improvements would be made to the cobalt-oxide-based cathode and carbon-based anode, this basic blueprint would remain standard for the following 10 to 15 years.

During the charge process, lithium cations are shuttled away from the cathode and stored via redox reactions in the layers between the Li_xC_6 graphite in a process known as intercalation. During discharge, the same process happens in reverse as Li^+ ions

deintercalate from the anode and are transferred into a similarly layered cathode. The key function of the electrolyte and separator is that it *only* allows for Li^+ transport to occur, blocking electrons which must travel through an external circuit to link back up with their preferred cations. These electrons can then be directed into devices such as an electric motor or a heat pump and used to perform useful work for us. The significance of the LIB is its reversibility, allowing for charge and discharge cycles to take place many hundreds of times in the lifespan of a typical battery.

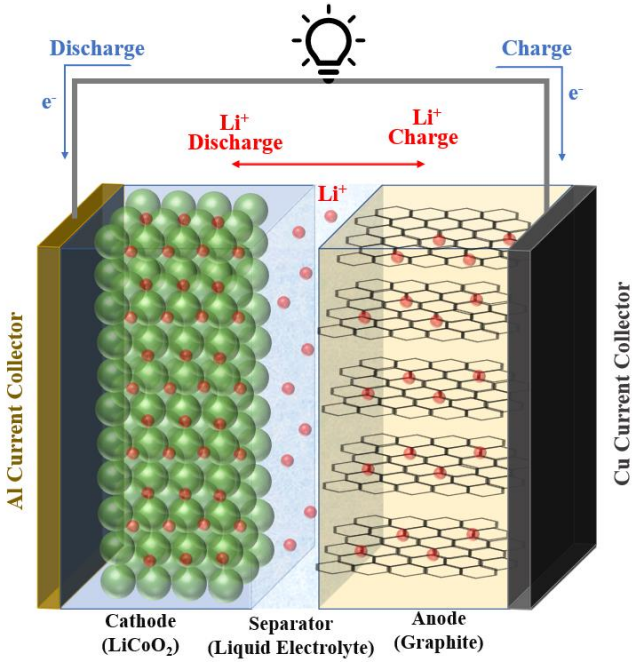

Figure 1.1. A traditional Li-ion battery composed of an oxide-based cathode, a graphite-based anode, and organic liquid electrolyte.

1.1.1 The Lithium Metal Battery

The history of LIBs did not begin in 1991, however. The search for a rechargeable battery goes back to at least 1913, when Lewis and Keyes demonstrated the first cell that resembled a lithium metal battery (LMB) with a lithium electrode.[1] Decades later, a

forerunner of the modern nonaqueous secondary battery utilizing a lithium metal anode was pioneered by Hill et al. (1965).[2] They described the plating phenomenon of lithium ions at the metal surface, a process that is distinct from the intercalation of modern batteries. Indeed, the LMB was amongst the first commercially available rechargeable batteries when, in 1976, Whittingham et al. demonstrated the intercalation process using a TiS_2 cathode.[3] This first age of the LMB was to be short lived, however, as several issues became immediately apparent.

On the one hand, the use of lithium metal in batteries seems obvious, and, in many respects, lithium is the ideal anode material for use in rechargeable LIBs. Lithium metal has the highest theoretical capacity of any potential anode material (3,860 mAh g^{-1}) in conjunction with the most negative electrochemical potential (-3.04 V *vs* standard hydrogen electrode).[4,5] In contrast with graphite- or silicon-based anodes, lithium metal anodes do not intercalate Li ions into a layered structure, but rather directly converts Li ions into Li metal, becoming oxidized during discharge cycles and reduced during charge cycles. This provides tremendous benefits regarding energy density, with several prominent LMB prospects such as Li-air batteries (5,210 Wh kg^{-1}) or Li-S batteries (2,600 Wh kg^{-1}) dwarfing the performance of current commercial LIBs (~250 Wh kg^{-1}). As such, the lithium metal anode is often touted as the "Holy Grail" of rechargeable lithium batteries, and much research has been dedicated to its implementation.

1.1.2 Challenges for Lithium Metal Batteries: Lithium Dendrites

Unfortunately, after the initial commercialization of LMBs in the 1970's, several problems became immediately apparent. The primary problem was safety, which was demonstrated when a string of cell phone fires in the late 1980's prompted Moli Energy

Ltd to issue a total recall of their Li/MoS_2 batteries.[6] Safety issues in LMBs stem from an unstable Li metal/liquid electrolyte interface, resulting in a short circuit event caused by the propagation of lithium dendrites through the electrolyte.

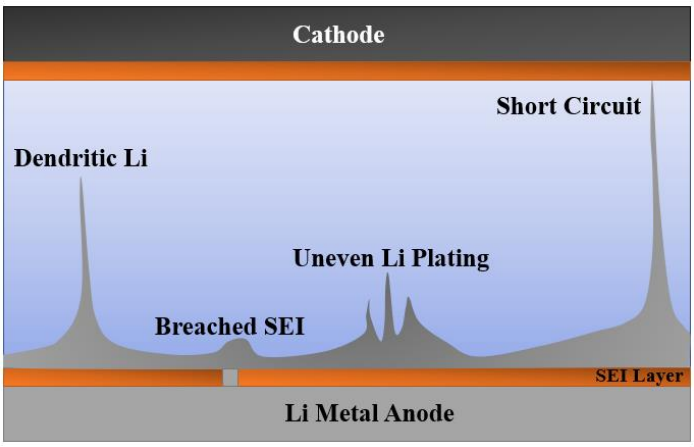

Figure 1.2. Schematic diagram of Li dendrite formation in a Li metal battery.

Dendrites are one of the primary problems for all rechargeable LIBs (**Figure 1.2**). Dendrites form from uneven plating of Li ions, either on the surface of the lithium metal or the surface of the solid electrolyte interphase (SEI), which may cause this critical component to break.[7] Once the SEI layer is breached, lithium is plated over the damage before more SEI can reform, which then attracts more lithium in a positive feedback loop from which dendrites will sprout. These finger-like tendrils continue to grow over subsequent cycles, making their way through the electrolyte and towards the opposite electrode. Connection of the anode and cathode via lithium dendrites means instant battery failure through short circuit, as electrons can now easily pass through the electrolyte and battery voltage goes to 0. Dendrite formation is more likely to occur at higher charge and discharge rates, making this an especially important problem to solve for the future of high-powered energy applications.

Battery failure is not the only problem to contend with following a short circuit, however. Short circuits often lead to a more serious process known as thermal runaway, whereby higher temperatures from rapid electronic conduction results in the breakdown of cathode and electrolyte materials, resulting in free oxygen and organic particles to be present in a now highly pressurized and combustible liquid electrolyte. As oxygen and other compounds seep from the cathode into the electrolyte solution, pressure is further increased, which further increases temperature in a positive feedback loop.[8] This is the perfect environment for fire and cell explosion events. As such, preventing dendrites while simultaneously lowering the likelihood of catastrophic thermal runaway are both key goals in the development of a viable LMB.

The root cause of dendrite formation in LMBs lies in uneven plating of lithium ions onto the lithium metal anode. This leads to certain hot spot areas receiving progressively more lithium than other areas due to preferential nucleation, eventually leading to mechanical pressure and the breakdown of the SEI layer. The SEI layer is critical both to dendrite prevention and to the general performance of a well-functioning battery.

First identified by Peled in 1979, the SEI layer is a decomposition layer which results from the reaction of electrolyte with electrode, and serves a dual function of a) preventing direct contact and further reactions between electrode and electrolyte, and b) facilitating Li plating.[9] SEI layers can inhibit the growth of lithium dendrites, but they do not prevent the dendrite formation completely, and can be mechanically compromised if not properly formed. This cracking in turn exposes new lithium metal which attracts more localized Li ion flow and more rapid dendrite formation.[4]

While Li dendrites have been shown to occur in all LIBs, they are exceptionally likely to form in LMBs using a metal Li anode. As such, safety concerns have been far too high for LMBs to reemerge onto the market after their failure in the late 1980's, despite the obvious advantages they offer with regards to energy density. For LMBs to return as a viable alternative to current graphite-based LIBs, several conditions must be met. First, a robust and stable SEI layer must be formed which can effectively prevent short circuit events caused by the propagation of Li dendrites. Second, this SEI layer must not come with the cost of excessive Li use or decreased ionic conductivity. And third, in the event of a possible short circuit, the battery itself should be free of the combustible material that is likely to result in an explosion.

1.1.3 Addressing the Solid Electrolyte Interface Layer

The SEI layer problem has seen much work in recent years, although there is still a good amount of mystery surrounding both its formation and its mechanisms. Understanding the SEI layer is critical to the designing of a functional battery, and it is useful now to dive deeper into its properties. There are several features which any SEI must possess in a safe and efficient batteries:[5]

1. Material thickness which can prevent electron flow while still allowing ion transport
2. High enough ionic conductivity to easily facilitate Li ion flow from the electrode to electrolyte
3. Excellent mechanical properties which allow for volume changes seen during charge and discharge cycles

4. High chemical stability which prevents further reactions and completely separates the electrode and electrolyte

SEI formation occurs due to chemical reactions which take place between the electrodes and electrolyte, creating an interlayer which more fully separates the different parts of the battery. This process has been described by Goodenough and Kim.[7] In short, the formation of the SEI depends on four variables: the lowest unoccupied molecular orbital (LUMO), the highest occupied molecular orbital (HOMO) of the electrolyte, and the electrochemical potentials μA and μC of the anode and cathode, respectively. If μA is greater than the LUMO of the electrolyte, then the electrolyte will be reduced by the anode until a passivation layer (the SEI) blocks further electron migration. Likewise, if μC is less than the HOMO of the electrolyte, then the electrolyte will be oxidized by the cathode until an SEI layer is formed to provide an electron barrier.

The SEI layer is especially important to understand in a LMB, as the extremely negative electrochemical potential of lithium metal makes redox reactions impossible to avoid.[5] Reactions take place in two stages. First, passive contact between electrode and electrolyte results in electron exchange which occurs in milliseconds. Second, battery cells are often "aged" during the first several cycles, where change in potential values result in additional reactions taking place. In traditional liquid electrolytes, electron exchange is facilitated even more when anion species within the solvent coordinate with Li^+ to thermodynamically lower the reduction enthalpy.

Eventually, the reaction must stop due to a lack of free electrons. If the right conditions were met, the result is a thin film (the SEI layer) which plays three crucial roles to battery function: it ensures contact between the electrode and electrolyte while

simultaneously blocking electron flow and preventing further side reactions; it facilitates the flow of ions across the electrode/electrolyte interface; and it prevents the spread of lithium dendrites into the electrolyte. As such, SEI development and formation is vital to future battery success in solid state lithium metal batteries.

The exact mechanism by which a robust SEI layer accomplishes these goals is not fully understood, although much work has been done to better understand the role that different compounds play in the process. Most commonly, the SEI layer is described using a dual-layer structure, with different products forming on the electrolyte and electrode sides. Standard organic liquid electrolytes have been well studied, with compounds such as Li_2O, LiOH, LiF, LiCl, and Li_2CO_3 being widely cited as key components in an SEI layer.[5,10,11] Li ions migrate through the SEI via grain boundaries or interstitials/vacancies, although there is disagreement in the literature on the precise mechanism.[12,13]

The mechanical nature of the SEI layer is also critical to battery functioning and dendrite formation. Li metal volume expansion can be significant during charge cycles, which is commonly cited as a reason for SEI breakage and dendrite nucleation. Li metal is also particularly prone to nucleation sites due to its low surface energy and high migration energy.[5,14] It has been found that lithium halides (LiF, LiCl) exhibit low surface diffusion barriers, meaning that Li^+ ions are less likely to nucleate on the Li metal surface, and will instead migrate to form even layers.[15] This revelation provides a possible path forward for intelligent SEI design with dendrite suppression in mind.

1.1.4 The Solid-State Battery

Even with a stable and robust SEI layer in place, LMBs still present a serious safety issue due to the presence of a combustible liquid electrolyte. The answer to this problem is

the solid-state battery (SSB) (**Figure 1.3**), which is characterized by the replacement of the flammable organic liquid electrolyte with an ion-conducting solid electrolyte. Solid electrolytes are inherently nonflammable, making them safer for use in technologies such as electric vehicles whose batteries may be subjected to severe mechanical stress and high charge and discharge rates. Like their liquid counterparts, solid electrolyte chemistries will react with both the cathode and anode to form an SEI layer which can be tuned to form an effective electrode/electrolyte barrier which allows for Li ion transport while blocking dendrite formation and maintaining mechanical integrity.

These traits make solid electrolytes the ideal separator for the realization of a safe and functional Li metal anode, meaning SSBs have an extraordinary potential for a greatly increased energy density in batteries. As increasingly small portable electronic devices require constantly increasing power, as electric vehicles grow ever more common, and as demands for grid scale battery technologies become more necessary, the SSB stands poised to answer these calls by providing a battery which is both high in energy density and safe for a multitude of scenarios.

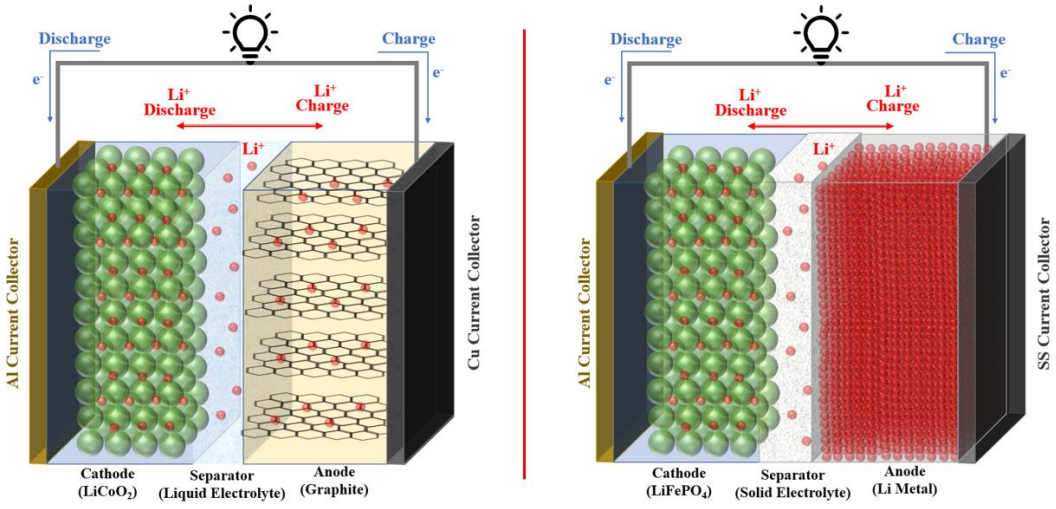

Figure 1.3. Comparison of conventional Li-ion battery and a solid-state Li metal battery.

Before these challenges can be met, there are several key concerns which SSBs must overcome. The first challenge is ionic conductivity. Organic liquid electrolytes typically possess ion conduction values on the order of 10^{-3}–10^{-2} S cm^{-1}, which allows for high charge and discharge rates of $\geq$ 1C to be achieved. For SSBs to be viable, Li ion migration must be able to approach these values, at least achieving a value of 10^{-4} S cm^{-1}, and higher if possible. The second challenge is interfacial stability and low reactivity with both the cathode and the anode. Chemical reactions between the electrolyte and electrode are inevitable in battery cycling, and as such the challenge becomes more about controlling these reactions to produce favorable products. The third challenge is the prevention of Li dendrites which, contrary to early hopes, are not mechanically inhibited by the solid electrolyte as they are able to propagate along grain boundaries and into defects in the solid crystal lattice. These latter two challenges can both be addressed through the formation of a stable and robust SEI layer.

In general, there are several key requirements which solid electrolytes must possess before they can be viable for implementation in commercial SSBs:

1. They need a high ionic conductivity, at least on the order of 10^{-4} S cm^{-1}
2. They require a wide electrochemical window, preferably from 0-5 V to maximize energy density
3. They require good chemical and electrochemical stability with different electrode materials, in particular towards lithium metal
4. They need a cheap, scalable, and easy synthesis process which is suitable for manufacturing

The vast body of work on SEI layers is focused on traditional batteries using a graphite anode and an organic liquid electrolyte. There are additional problems which must be considered when an SEI layer is brought into the sphere of the solid electrolyte. The primary issue here is the physical contact between electrode and electrolyte, which can wax and wane during charge and discharge cycles.[16] The secondary issue is the difference in chemical composition between liquid and solid electrolytes, which can result in different compounds in the SEI layer which have not yet been well-studied. For example, ceramic solid electrolytes do not contain carbon-based molecules, meaning Li_2CO_3 will not be present. Likewise, sulfide solid electrolytes will be more likely to form Li_2S than Li_2O, and the exact effect this may have in unknown.

One possible solution put forth is the insertion of an artificial SEI layer made of either a polymer or a Li-metal alloy.[4,17,18] This layer would block ions and provide mechanical integrity just as a naturally formed SEI layer would, but adds complication to battery assembly, and still presents issues with interfacial reactions now occurring at multiple junctions. This dissertation will instead focus on the formation of an *in situ* formed SEI layer created in multiple steps: first by passive electrode/electrolyte contact, and second by charge and discharge events during the first several cycles. Battery cycling takes place through an elegant balance between the cathode, anode, and electrolyte, and as such this process will be dependent on the exact composition of the materials being analyzed.

1.2 Solid Electrolyte Materials: Oxides, Halides, and Sulfides

There are several potential candidates for solid electrolyte materials, which broadly fall into one of two categories: polymers or ceramics. Both have advantages and disadvantages when it comes to battery performance. Polymers are thin, flexible materials

with good manufacturability and desirable mechanical properties, but they suffer from typically low ionic conductivity.[19] Ceramics are comprised of either oxides, halides, and sulfides, and are known for their high ion conductivity, but they suffer from mechanical issues and high interfacial resistance with electrode materials.

1.2.1 Oxides

Oxides are a widely studied solid electrolyte candidate for use in SSBs. Some of the most common compositions seen are $Li_7La_3Zr_2O_{12}$ (LLZO)[20–22], $Li_{3x}La_{2/3-x}TiO_3$ (LLTO)[23–25], and $Li_{1+x}Al_xTi_{2-x}(PO_4)_3$ (LATP)[26–28]. Some oxides, such as LATP, are noted for their high oxidation potential (up to ~4.2 V) which grants them the potential for great stability against high voltage cathode materials. In addition, oxides produce electronically insulating oxidation products which are favorable in the formation of a stable SEI layer. LATP and LLTO unfortunately have poor reduction potential against Li metal. In these materials, Ti^{4+} is reduced to Ti^{3+} when contact is made with lithium, increasing electronic conduction across the interface.[20,29]

Garnet-type oxide materials such as LLZO are also noted for their high bulk ionic conductivity (~10^{-3} S cm^{-1}), making it a particularly promising SE candidate.[21] The highest reported ionic conductivity value for an LLZO material was reported to be 2.06×10^{-3} S cm^{-1}, which was achieved via Ga-doping to synthesize $Li_{6.55}Ga_{0.15}La_3Zr_2O_{12}$.[30] In addition, the exceptionally low reduction potential (0.05 V *vs* Li^+/Li) means it is likely to form a very stable interface with lithium metal. Unlike LATP and LLTO, LLZO theoretically begins to oxidize at potentials above ~3 V, meaning it will react with many of the more common cathode materials used in secondary batteries. Specific strategies such as Al-

doping can be implemented to overcome this shortcoming, with experimental observations showing an electrochemical window from 0-6 V.[22,31]

The mechanical properties of oxide materials are one of the primary concerns when implementing them in SSBs. Oxides, especially garnet-type materials like LLZO, are known for their rigidity. On the one hand, this mechanical trait might be beneficial to the suppression of dendrite formation in addition to providing resistance to mechanical degradation due to volume expansion of charge and discharge cycles.[22] On the other hand, the high resistance to elastic deformation might prevent good interfacial contact between the electrode and electrolyte, greatly increasing interfacial resistance.[20] $Li_{6.4}Al_{0.24}La_3Zr_2O_{11.98}$ was reported to have a Young's modulus of ~150 GPa, which is an order of magnitude higher than that of Li metal (4.9-13.0 GPa), and thus should be more than sufficient in preventing dendrites.[32,33]

Garnet-type oxides require stringent synthesis conditions to achieve the ion-conducting properties necessary for SSBs. This includes high sintering temperatures (900–1200+ °C) and long sintering times. This process, in addition to being expensive and difficult to conduct at large scale, results in other problems as well, including Li loss, low density due to high volume of defects, and two-phase structure (tetragonal and cubic) which are unstable at room temperature.[21] While certain strategies such as the utilization of dopants and a carefully controlled sintering process can alleviate some of these concerns, the fact remains that oxide SEs will always be both energy and time intensive to produce.

1.2.2 Halides

One interesting and newer type of ceramic SE are the class of halide solid electrolytes. Lithium halide salts such as LiF, LiCl, LiBr, and LiI have long been known to

possess some ion conducting properties, with LiI possessing the highest value of 10^{-7} S cm^{-1}.[34] The exceptional performance of $LiAlCl_4$ (3.5×10^{-1} S cm^{-1} at 174 ℃, when dissolved in nonaqueous solvent) has allowed for its use in thermal batteries since the 1940's.[35]

Recent years has seen the development of halide SEs with trivalent metal cations which utilize elements either from group 3 (Sc, Y, La) or group 13 (Ga, In). While these group of SEs have been on the radar for decades, they were, until recently, largely unexplored due to repeatedly being shown to possess low ionic conductivity. They reemerged onto the scene in 2018 when Li_3YCl_6 and Li_3YBr_6 were synthesized via high energy ball milling and high temperature sintering to achieve ionic conductivity values of $0.03–1.7\times10^{-3}$ S cm^{-1}.[36] Interestingly, it was found that 50 h of ball milling followed by annealing led to a decrease in value for the Cl-containing halide and an increase for the Br-containing halide. This was possibly explained by disordered Y^{3+} and Li^+ creating channel-blocking defects in Li_3YCl_4.[36] Regardless, this result brought interest back to halide SEs by overcoming the challenge of low ionic conductivity.

Halide SEs containing group 13 metals, especially Li_3InBr_6, have also been extensively studied in recent years. Possessing low conductivity at RT (10^{-7} S cm^{-1}) this material undergoes a phase transition at 41 ℃ which renders it an super ionic conductor with conductivity values on the order of 10^{-3} S cm^{-1} even after cooled back to RT.[37] These excellent properties are attributed to the presence of a large number of structural vacancies caused by the large cations, as well the presence of highly polarizable halogen anions.[35]

Synthesis of halide SEs had long been done only via solid state methods which, like oxides, require high sintering temperatures and high sintering time in addition to high energy ball milling applications. However, in recent years, the solvent based synthesis

process has gotten more attention, and is especially attractive due to the possibility of using a water solvent without the need for inert atmosphere preparation.[38] The liquid synthesis is appealing as it provides the possibility for easy scalability and better homogeneity with a more controlled morphology.

The halide's main drawback is electrochemical stability with electrodes, especially the anode, which is due to a high valence state associated with halide SEs. Reduction reactions occur spontaneously with all SEs when paired with a Li anode, but it appears that in halides these reactions do not lead to the development of a stable SEI layer, which in turn leads to increased interfacial resistance and a large overpotential.[35] One strategy to address this concern is to use Li-metal alloys such as Li-In, which can prevent side reactions but lowers the cells overall voltage. Another strategy is the use of sulfide solid electrolytes as an interlayer between the anode and halide SE.

1.2.3 Sulfides

No SE material comes without its drawbacks. Oxides have a high rigidity which increases interfacial resistance and induces large grain boundary resistance. Halides are especially prone to reacting with lithium metal. When designing a LMB using a Li anode, it seems likely that the best possible candidate is the class of SEs known as the sulfides.

Sulfide SEs are made of a combination of Li_2S and P_2S_5, and they possess many inherent advantages. For starters, the large size and polarizability of sulfide ions contributes to some of the highest ionic conductivities ever reported for SE materials. Additionally, sulfides are known for low grain boundary resistance. They show excellent chemical stability with both high voltage cathode and low voltage Li metal with a wide electrochemical window (at least 0–5 V). Possessing much softer mechanical properties

than oxides, sulfides can be easily densified at room temperature using cold pressing techniques. This mechanical softness also results in much better electrode/electrolyte solid-to-solid contact than is seen in oxides. The following section will delve deeper into the different categories of sulfide SE materials and will draw comparisons between them.

1.3 Categories and Properties of Sulfide Solid Electrolytes

1.3.1 Glassy Sulfides

Sulfide solid electrolytes are a result of the binary system of Li_2S and P_2S_5, which can be combined to form either glass, glass-ceramics, or ceramic SEs.[29] Glassy sulfides ($(100 - x)Li_2S–xP_2S_5$) possess isotropic structure and ion conduction properties. Typically, these materials exhibit ionic conductivities on the order of 10^{-4} S cm^{-1}, but this value can be increased by the incorporation of oxides such as P_2O_5, or by cold pressing to reduce the number of voids and defects present.[39,40]

One common strategy is incorporation of a halide-based lithium salt such as LiI or LiCl to increase Li concentration in glasses, thus increasing ionic conductivity as well.[41] These strategies often have deleterious side effects, however, most prominent of which is a decrease of the stable electrochemical window. Sulfide glasses require low synthesis temperatures due to the low melting point of sulfides, which can be achieved either through melt quenching or ball milling. These methods would be cost-effective and easily scalable, making glassy sulfides one of the more promising candidates for industrial-level synthesis.

1.2.2 Glass-Ceramic Sulfides

Another interesting possibility are the sulfide glass-ceramics, which are the result of a partial crystallization of the $Li_2S–P_2S_5$ binary system. This results in a dual phase

material consisting of both crystalline and amorphous regions. Most often, these materials are made simply through single-step ball milling, although solution-based methods have been investigated in recent years.[42,43] Metastable phases are obtained through glass crystallization, with the exact composition of the metastable phase being subject to heat treatment conditions.[44] The incorporation of crystallinity in the glass-ceramics also introduces grain boundaries regions, which means that grain boundary resistances now play a role in ion transport. As a general rule, grain boundary resistances are higher than bulk resistances in sulfides, and thus should be minimized in order to maximize ion transport properties.

These materials can be divided into two groups of mostly glassy or mostly ceramic, with the material properties dependent on the amount of crystallization. With low molar concentrations of Li_2S, compositions such as $Li_4P_2S_6$ or Li_3PS_4 are formed, which often display ionic conductivities on the order of 10^{-5} S cm^{-1}. Increasing the Li_2S molar concentration to >70 mol% results in the formation of $Li_7P_3S_{11}$ with significantly higher ionic conductivity values on the order of 10^{-3} S cm^{-1}.[45]

The molar amount of Li_2S also plays a significant role in the types and amounts of anionic species which form in the Li_2S–P_2S_5 binary system. PS_4^{3+} tetrahedra (ortho-thiophosphate moieties) are the most common crystal formed when Li_2S concentration is high (>75 mol%). When Li_2S is <75 mol%, $P_2S_7^{4-}$ pyro-thiophosphate moieties are formed, which result from two PS_4 tetrahedra sharing two corner atoms. The third most common crystal is $P_2S_6^{4-}$ (hypo-thiodiphosphate moieties), which form when Li_2S concentration is about 60 mol%. These are the result of two edge sharing PS_4 tetrahedra units.[46]

Glass-ceramic materials can and often do contain all these different units in relative concentrations. $Li_4P_2S_6$, for example, is obtained from a Li_2S concentration of 67 mol%, which results in a mixture of $Li_4P_2S_6$ (composed of mostly $P_2S_6^{4-}$) and $Li_4P_2S_7$ (composed of mostly $P_2S_7^{4-}$). Meanwhile, $Li_7P_3S_{11}$ (composed of mostly PS_4^{3-}) is also known to degrade at higher temperatures, leading to the formation of $Li_4P_2S_6$.[46] As such, obtaining high conductivity $Li_7P_3S_{11}$ can be difficult due to the narrow annealing temperature range and its tendency to break down to lower order species. Crystalline phases containing $P_2S_6^{4-}$ and $P_2S_7^{4-}$ typically are reported to possess low ion conducting abilities (10^{-11} S cm^{-1}), and should be avoided if possible.[47]

Special attention will now be given to the glass-ceramic material Li_3PS_4, which possesses several unique attributes pertinent to this work. A member of the thiophosphate sulfide family, this material initially received little attention due to its low reported ionic conductivity of 3×10^{-7} S cm^{-1}.[48] Later works pioneered the synthesis of nanosized SE particles, which greatly increased Li_3PS_4's ion conducting properties.[49] Notably, this process could be achieved either through ball milling to form glassy Li_3PS_4 (2×10^{-4} S cm^{-1})[50] or through solvent-based synthesis methods to form β-Li_3PS_4 (1.6×10^{-4} S cm^{-1}).[51]

1.3.3 Ceramic Sulfides

Ceramic sulfide SEs are those which have been fully crystallized through heat treatment. In addition to being a glass-ceramic material, Li_3PS_4 has also been reported as four different crystalline polymorphs: α-Li_3PS_4, δ-Li_3PS_4, γ-Li_3PS_4, and β-Li_3PS_4. Of these, crystalline β-Li_3PS_4 has received by far the most attention owing to its high conductivity and relatively easy synthesis methods. In particular, the development of the liquid synthesis method was important to the realization of Li_3PS_4 as a viable SE material

as this process stabilizes the material at room temperature in addition to creating nano-porous particle size. The nano-porosity is thought to contribute to the high ionic conductivity through the mechanism of increases surface area.[51] This greatly increases the surface energy of the Li_3PS_4, and facilitates ion transport via large concentrations of interstitials. The synthesis process involves the dissolution of Li_2S and P_2S_5 in tetrahydrofuran (THF) solvent, which is then filtered and heated to the crystallization temperature of 140 °C to achieve the proper balance of crystal formation and high surface area. Further heating this material to 200 °C decreases available surface area and thus has a negative impact on ion transport. In addition to this, nanoporous β-Li_3PS_4 retains chemical and electrochemical stability with Li metal, as evidenced both by CV tests with a potential scan of -0.2–5 V *vs* Li^+/Li, and by excellent cycling in Li symmetric cells.[51]

The exact ion conduction mechanism of β-Li_3PS_4 is still not fully understood. There are three possible options which may be responsible for ion transport through the glass-crystalline matrix: 1) ions move through the interconnected nano-crystallites via ion hopping between tetrahedral and octahedral Wyckoff positions;[52] 2) ions move through the interfacial area between amorphous and crystalline regions;[53] 3) ions move directly through the amorphous region. It may be that some combination of all three is responsible for the high conductivity observed for β-Li_3PS_4, but more work is needed to confirm the mechanism in greater detail.[46]

Argyrodites are the most prominent family of crystalline sulfide SE, which follow the general formula of $Li_{7+x-y}M^{IV}_xM^{V}_{1-x}Ch_{6-y}X_y$ (M^{IV} = Si, Ge, Sn; M^V = P, Sb; Ch = O, S, Se; X = F, Cl, Br, I; $0 \leq x \leq 1$; $0 \leq y \leq 2$).[54] This class of materials have seen a great deal of research attention owing largely to their high intrinsic ionic conductivities, including the

highest value reported for any sulfide SE of 24 mS cm^{-1} for $Li_{6.6}Si_{0.6}Sb_{0.4}S_5I$.[55] This is well within the range of values reported even for liquid electrolytes.

The first representative of mineral argyrodites was Ag_8GeS_6, which showed high mobility of Ag^+ ions.[56] It was found through study of this composition that the structure is versatile in its ability for elemental substitution while still maintaining the basic argyrodite topology. The first report of Li containing argyrodites was published in 1976, when Brice et al. successfully synthesized Li_7PS_6,[57] but very little work was done on single crystalline phase sulfide SEs for the next 30 years. Deiseroth et al. made a significant contribution to SE research in 2008 when they first reported the synthesis of Li_6PS_5X (X = Cl, Br, I) by substituting one chalcogen atom with one halogen atom, thereby lowering the required number of Li atoms from seven to six.[56] This pioneering work detailed the structure, properties, and ion transport mechanisms of argyrodites, setting off a decades-long delve into argyrodite research.

1.3.4 Argyrodite Crystal Structure

Figure 1.4 shows the Li_6PS_5X (X = F, Cl, Br, I) crystal structure. The basic crystal unit of this material is the PS_4^{3-} tetrahedra which, unlike the glass-ceramic materials, do not share S1 atoms. Instead, they are kept well separated by S2 and X atoms occupying the 4a and 4d Wyckoff sites. This results in a material with the ionic formula of $(Li^+)_6(PS_4^{3-})S^{2-}X^-$. Upon cubic high temperature modification, the argyrodite crystallizes in space group *F-43m*, with a unit cell size of ~10 Å. This yields a disordered arrangement of Li ions which cluster together in octahedrally arranged cages in the empty spaces between the PS_4^{3-} tetrahedra. Li2 atoms occupy the 24g site, which is closely neighboured by a pair of

Li1 atoms occupying the 48h site. Inside of these cages lies the 4d site, which can be occupied by either S or X atoms.

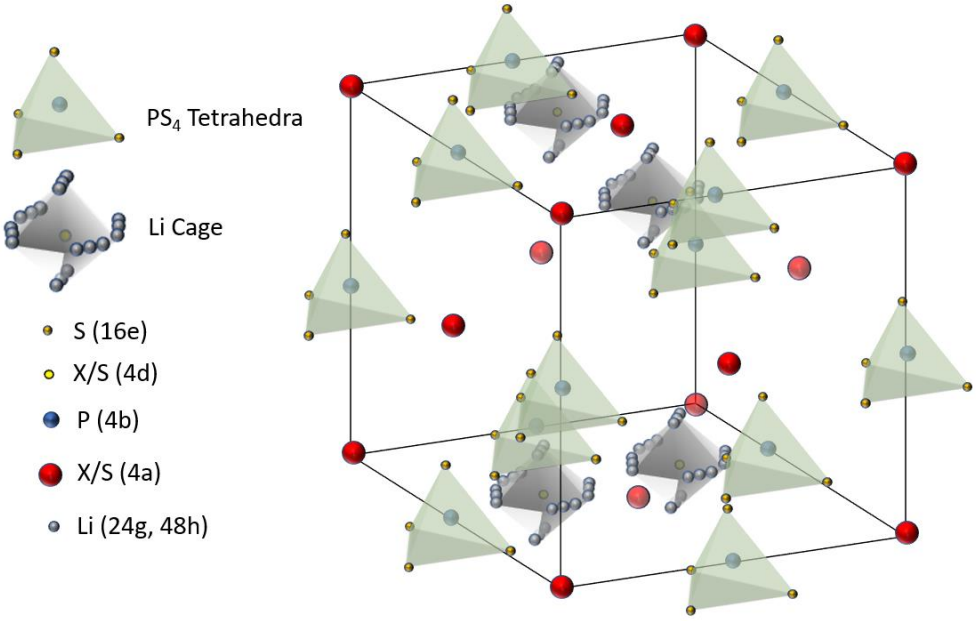

Figure 1.4. Representation of the Li_6PS_5X (X = F, Cl, Br, I) crystal structure.

Li ion transport through the argyrodite crystal structure takes place via these octahedral Li cages. There are three basic movements which Li ions make. Type (i) jumps indicate a localized jump between a pair of 48h site Li ions, which occurs over a distance of 1.9 Å.[58] Type (ii) jumps occur within the greater cage structure, as different 48h pairs of Li ions are able to exchange positions around the centralized 4d atom. This second intracage jump occurs over a distance of 2.25 Å. Finally, type (iii) jumps are intercage jumps which are able to connect the four octahedral cages in the unit cell.[58] This last jump is the most crucial for the achievement of a true ion-conducting solid, although all three must be present. As such, diffusion rates are limited by the least common jump rate of the three, which will most often be type (iii) jumps.

Ionic conductivity in argyrodites is highly dependent on the ability of the ions to engage in intercage jumps within the bulk crystal. Of all argyrodite possibilities, the material that has by far received the most attention has been Li_7PS_6 and its halide-doped counterpart, Li_6PS_5X (X = Cl, Br, I). MD simulations comparing the four compositions reveal that only type (i) and (ii) jumps are expected to occur in Li_7PS_6 and Li_6PS_5I, greatly limiting their macroscopic conductivity properties.[58] Conversely, Li_6PS_5Cl and Li_6PS_5Br both show a high tendency for type (iii) intercage jumps, meaning their ionic conductivity is expected to be much higher. The predicted order according to MD simulations of the best to the worst conductive material is Li_6PS_5Cl > Li_6PS_5Br > Li_7PS_6 > Li_6PS_5I.[58]

1.3.5 Argyrodite Ionic Conductivity

The origin of the improved ionic conductivity observed for Li_6PS_5Cl is explained by the effect of halogen-doping on the atomic structure of argyrodites. Li_7PS_6 possess a face-centered cubic symmetry with S atoms occupying the corners and face centers (Wycoff 4a sites). PS_4^{3-} tetrahedra act as building blocks with P atoms on the edge centers surrounded by additional S atoms occupying the Wyckoff 16e positions. Finally, and most crucially, S atoms also occupy positions inside of the ion cages (Wyckoff 4d), surrounded by Li atoms partially occupying 48h and 24g sites.

In halide doped Li_6PS_5X, the X halogen anion replaces S anions at either the 4a or 4d sites. Anion site disorder is induced by an uneven sharing of S/X at the 4a and 4d positions, with higher halogen atom occupancy at the 4d Wyckoff site being associated with less homogenous charge disorder and a higher degree of delocalized lithium density.[54] The delocalized lithium atoms create better connectivity between the cages, thus creating a small jump distance for individual ions and allowing for a higher degree of type (iii)

intercage jumps to occur. As such, higher ionic conductivity is directly correlated with the amount anion site disorder in the crystal.

Different halogen anions show a preferential tendency to replace S anions at either the 4a or 4d positions. When Li_7PS_6 is doped with iodine to create Li_6PS_5I, the large I^- ions tend to reside more in the 4a position, replacing the S at the cubic corners/faces, which creates a large degree of Li ion density surrounding the 48h pairs. This dense region promotes the occurrence of type (i) and (ii) intracage jumps to occur, but severely limits the diffusion paths between the Li cages. As a result, crystalline Li_6PS_5I is well reported to possess a low ionic conductivity on the order of 10^{-7}–10^{-6} S cm^{-1}.

Br- and Cl-doping has a wholly different effect. These two ions both show a preference for replacing S at the 4d site inside of the Li cages themselves, with Cl^- occupancy being slightly greater than Br^- occupancy. This results in the Li ion density being spread out and disperse, greatly increasing the tendency for thermodynamically favorable type (iii) intercage jumps to occur. As such, Br- and Cl-doped argyrodites both unambiguously possess much higher ionic conductivities than Li_7PS_6 or Li_6PS_5I, from 10^{-4}–10^{-3} S cm^{-1}. The discrepancy in Li ion density in Br- and Cl-doped materials can be explained by the lower ionic charge of Cl^- and Br^- compared to S^{2-}, meaning the halogens can be compensated by fewer pairs of close-by 48h Li ions.

1.4 Synthesis Techniques for Sulfide Argyrodite Solid Electrolytes

Optimizing the synthesis of argyrodite sulfide solid electrolyte materials is a key step in the development of solid-state batteries. The synthesis process seeks to control several key attributes associated with Li_7PS_6 and Li_6PS_5X. These include a high degree of

crystallinity for excellent bulk ion conductivity as well as an adequate number of defects for easier ion transport. In addition, it is desirable that the synthesis approach be easy to perform for large scale operations, and that the process should use cheap and non-toxic materials and techniques. Currently, there are two primary methods by which argyrodites are made: solid state synthesis and liquid state synthesis (**Figure 1.5**). Both techniques have their benefits and drawbacks, which will now be discussed in further detail.

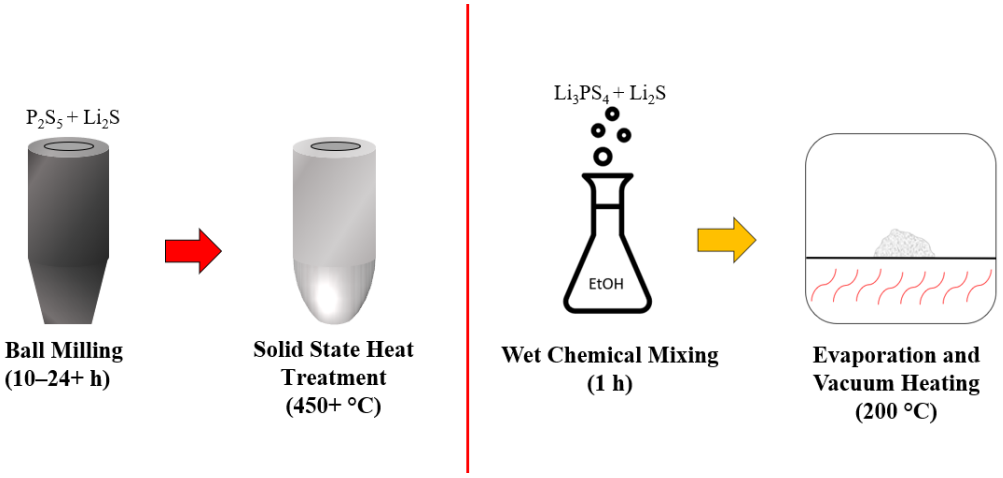

Figure 1.5. Comparison of solid state and wet chemical synthesis techniques for sulfide solid electrolytes.

1.4.1 Solid State Synthesis Methods

By far the most common technique used for argyrodite synthesis has been a solid-state approach. This involves utilizing either ball milling, high temperature reactions, or a combination of both to yield the desired material. Ball milling is a process where the total result of high-speed impacts occurring over a long period of time contributes to the mixing and amorphization of different compounds.[42] The kinetics of the reaction are mediated by point and lattice defects owing to plastic deformation of the materials.

Glassy sulfide materials in the $Li_2S–P_2S_5$ binary system are synthesized through long periods of ball milling without subsequent heat treatment. This results in completely amorphous solid electrolyte materials which nonetheless can achieve excellent ion conducting capabilities.[59] Both mixing speed and time are important factors to consider when ball milling, as it has been shown that Li_6PS_5Cl made with prerequisites Li_2S, P_2S_5, and LiCl requires at least 550 rpm and 8 h of milling to properly synthesize.[60] Longer mixing times result in smaller particle size, which has a sizable impact on the ion conducting properties of the final material.

In addition to ball milling, a high temperature heat treatment is used to crystallize the glassy phase $Li_2S–P_2S_5$ into crystalline Li_7PS_6 and Li_6PS_5X. Here, both temperature and time affect the crystallinity of the final material. Different researchers have used different temperatures, but the most used heat treatment temperature is 550 °C. This temperature provides the proper environment to achieve a balance between crystallinity, particle size, and number of defects which maximizes the type (iii) intercage jumps responsible for high ionic conductivity.[61] While solid state synthesis techniques produce argyrodite materials with a high degree of crystallinity and excellent ionic conductivity, they do so using a very time and energy extensive process. This fact makes the prospect of large-scale operations appear difficult and expensive, and it is therefore desirable to find a different synthesis approach.

1.4.2 Solvent Based Synthesis Methods

In the past decade, sulfide SEs synthesized from solvent-based methods have gained much attention owing to the ease of the procedure, the high degree of compositional control, and the low heat treatment temperatures required. This began in 2013 when Liu et

al. synthesized β-Li_3PS_4 from mixing Li_2S and P_2S_5 in tetrahydrofuran (THF), achieving an ionic conductivity of 1.6×10^{-4} S cm^{-1}.[51]

After obtaining β-Li_3PS_4, which contains fully formed and isolated PS_4^{3-} tetrahedra, one can then use a dissolution—precipitation process in a protic solvent such as ethanol to obtain new materials. Using this knowledge, in 2019 our lab made the first report of solvent synthesized Li_7PS_6 which was made through the dissolution of solvent-synthesized β-Li_3PS_4 and Li_2S in nontoxic ethanol.[43] Using this procedure, we were able to obtain an argyrodite solid electrolyte material with an ionic conductivity of 1.4×10^{-4} S cm^{-1}. This process will be further discussed in Chapter 3.

In the years following that publication, much work has been done by our lab and by others to further explore the solvent synthesis of Li_6PS_5X (X = F, Cl, Br, I). Some have been able to use very high heat treatment to obtain SE materials with ionic conductivities rivaling those from solid state synthesis (>10^{-3} S cm^{-1})[62,63], although this does somewhat take away the appeal of liquid synthesis as being a fast and economical process. **Table 1** shows a summary of argyrodite SEs synthesized from different techniques, either solid state, liquid, or a hybrid of the two.

Table 1. Comparison of synthesis approaches and conductive properties for argyrodites

Formula	Start Materials	Synthesis Method	Heating Temperature/ Time	σ at RT* (mS cm^{-1})	E_a** (eV)	Ref
Li_6PS_5Cl	Li_2S, P_2S_5, LiCl	Solid-state	550 °C /6 h	2.4	0.33	64
Li_6PS_5Cl	Li_2S, P_2S_5, LiCl	Solid-state	550 °C/ 4 h	6.11	0.3	65
Li_6PS_5Cl	Li_2S, P_2S_5, LiCl	Solid-state	N/A	1.3	0.17	66
Li_6PS_5Cl	Li_2S, P_2S_5, LiCl	Solid-state	550 °C /7 days	3.8	0.39	67

Li_6PS_5Cl	Li_3PS_4, P_2S_5, LiCl	Hybrid (THF + ethanol)	550 °C/ 6 h	2.4	N/A	[68]
Li_6PS_5Cl	Li_2S, P_2S_5, LiCl	Hybrid (ethyl acetate)	550 °C/ 5 h	1.1	0.26	[69]
Li_6PS_5Cl	Li_2S, P_2S_5, LiCl	Hybrid (ethanol)	450 °C	0.21	0.5	[70]
Li_6PS_5Cl	Li_2S, P_2S_5, LiCl	Solvent (ACN + ethanol)	180 °C	0.6	N/A	[71]
Li_6PS_5Br	Li_2S, P_2S_5, LiBr	Solid-state	300 °C /12 h, 550 °C /12 h	5.5	0.22	[72]
Li_6PS_5Br	Li_3PS_4, Li_2S, LiBr	Hybrid (THF + ethanol)	550 °C	1.9	0.36	[68]
Li_6PS_5Br	Li_2S, P_2S_5, LiBr	Solvent (EP, ethanol)	180 °C/ 3 h	0.034	N/A	[73]
Li_6PS_5Br	Li_3PS_4, P_2S_5, LiBr	Hybrid (THF + ethanol)	550 °C /6 h	1.9	N/A	[74]
Li_6PS_5Br	Li_2S, P_2S_5, LiBr	Solvent (ethanol)	200 °C / 3 h	0.25	0.39	[75]
$Li_{5.5}PS_5Cl_{1.5}$	Li_2S, P_2S_5, LiCl	Solid-state	550 °C /7 h	9.4	0.29	[76]
$Li_{5.5}PS_5Cl_{1.5}$	Li_2S, P_2S_5, LiCl	Hybrid (EN)	550 °C/ 10 h	2.87	0.26	[62]
$Li_{5.5}PS_{4.5}Br_{1.5}$	Li_2S, P_2S_5, LiBr	Solid-state	400 °C/ 10 h	4.17	0.25	[77]
$Li_6PS_5Cl_{0.5}Br_{0.5}$	Li_2S, P_2S_5, LiCl, LiBr	Hybrid (ethanol)	400 °C/ 6 h	2.0	0.33	[78]
$Li_6PS_5Cl_{0.5}Br_{0.5}$	Li_2S, P_2S_5, LiCl, LiBr	Solid-state	550 °C	3.6	0.31	[79]
Li_7PS_6	Li_3PS_4, Li_2S	Solvent (ethanol)	200 °C /1 h	0.11	0.43	[43]
$Li_6PS_5Cl_{0.3}F_{0.7}$	Li_2S, P_2S_5, LiCl, LiF	Solid-state	550 °C/ 5h	0.71	N/A	[80]
Li_6PS_5F	Li_3PS_4, Li_2S, LiF	Solvent (ethanol)	200 °C/ 1 h	0.24	0.45	[81]
$Li_6PS_5F_{0.5}Cl_{0.5}$	Li_3PS_4, Li_2S, LiF	Solvent (ethanol)	200 °C /1 h	0.35	0.32	[81]

*σ at RT: ionic conductivity at room temperature. **E_a: Activation Energy. EN: Ethylenediamine; EP: ethyl propionate.

1.5 Polymer Solid Electrolytes

Owing to their high ionic conductivity and favorable electrochemical stability, ceramic sulfide solid electrolytes have received much attention. Despite this, sulfides suffer from multiple drawbacks, including a lack of air stability, a brittle mechanical structure prone to fracturing, and large interfacial resistance owing to the solid-to-solid contact between the electrodes and electrolytes. As such, it is useful to explore other potential SE materials which do not possess these limitations.

One such group of materials are the polymer solid electrolytes (PSEs) which use a solid polymer matrix as the separator in the battery. Polymers possess several important advantages over the ceramic SEs, including good processibility, ambient air stability, and flexible mechanical properties which has the dual advantages of easy battery assembly and enhanced interfacial contact.[82–84] In addition, polymer materials are better suited to compensating electrode volume changes during charge and discharge cycles.

Since they were first reported in the 1970's, PSEs have attracted much investigation, with numerous materials having been explored. Some of the most common polymer materials used as SEs are poly(ethylene oxide) (PEO),[85–87] polyacrylonitrile (PAN),[88,89] polymethyl methacrylate (PMMA),[90,91] poly(vinylidene fluoride) (PVDF),[92,93] and poly(vinylidene fluoride)-hexafluropropylene (PVDF-HFP).[94–96]

Most of these matrices possess inadequate ionic conductive properties in their unaltered state, and thus require additives such as alkali metal salts or liquid plasticizers to improve their ion transport abilities. In addition, newer approaches to PSEs involve the incorporation of inorganic fillers, either inert ceramics or ion-conducting active materials. These approaches can improve the performance of PSEs, but they often come with their

own drawbacks such as weakened mechanical properties. This presents PSE research with a particular challenge of choosing the right polymer matrix, salt, liquid additives, and filler material to provide the proper balance between the desired SE properties.

1.5.1 General Strategies used in Solid Polymer Electrolytes

Perhaps the most explored PSE material is PEO, owing largely to its favorable mechanical properties and its good stability with electrodes. It shares many traits with other polymers which are worth exploring in more detail. The polymer backbone in PEO consists of repeating units of $–CH_2–CH_2–O–$, which allows for Li ion migration along the moving chain.[97] The reducing agent ether oxygen groups form bonds with Li ions which can be broken, shuttling the Li ions down the PEO chain.

That said, due to the high degree of crystallinity in PEO, the ions are not able to efficiently transfer, resulting in typically low ionic conductivity. This is because ion migration can only occur in the amorphous regions where PEO molecular chains are able to engage in segmental motion.[85] As a result of this, the temperature is an important factor when considering SPE ionic conductivity. Higher temperatures result in a greater degree of amorphous region, maximizing at the melting point T_m of the polymer.

Reduction of polymer crystallinity is a common strategy used to increase the PSE's ion conducting properties. Very often, this is achieved through the incorporation of an inorganic alkali salt, such as bis(trifluoromethane) sulfonamide lithium (LiTFSI), lithium bis(fluorosulfonyl)imide (LiFSI), or $LiClO_4$.[86,98] The former two salts are notable for several reasons: 1) their excellent solubility; 2) a delocalized charge distribution promotes the lithium salt's dissociation, providing additional free Li ions; 3) the flexible anion $TFSI^-$ (or FSI^-) is adept at reducing the crystallinity of PEO or other polymer materials.[86] Using

this strategy, LiTFSI/PEO and LiFSI/PEO have been reported to possess ionic conductivities of 4.7×10^{-4} S cm^{-1} and 3.3×10^{-4} S cm^{-1} at 60 °C, respectively. This is a vast improvement over typically reported PEO values of 10^{-7} S cm^{-1}.

Liquid plasticizers are very commonly used in the synthesis of gel-type polymer electrolytes. This liquid component plays several important roles in the performance of PSEs. First, the liquid adds a wet layer which is vital for reducing the interfacial resistance at the electrode/electrolyte interface. The liquid itself is often an ion conductor, such as ethylene carbonate (EC), poly (propylene carbonate) (PPC), or propylene carbonate (PC), thereby directly improving the ionic conductivity by providing additional pathways for the Li ions to travel through.[99,100] Moreover, the alkali Li salts are usually soluble in these wetting agents, thereby providing a source of additional Li ions.

Another approach used for improving SPE performance is the introduction of inorganic ceramic fillers into the polymer matrix. Uniformly dispersed fillers can bolster the mechanical properties of the polymer while also improving the interfacial stability between electrode and electrolyte. These fillers can be further broken down into either active or passive, depending on whether they possess free Li ions.

Passive fillers are ceramic additives that do not contain free Li^+, and thus do not directly play a role in ion transport. These are often oxide materials such as Al_2O_2 or TiO_2[101,102]. While not directly implicated in Li ion movement, they do still play a role via the addition of PEO/filler interfaces which are known to greatly improve the SPEs ionic conductivity by reducing the polymer crystallinity. Assuming uniform particle dispersion, this would create a direct path by which Li ions can travel. In addition, the added filler material breaks the regularity of the PEO matrix, thereby increasing the total proportion of

amorphous regions.[85] This has the added benefit of preventing recrystallization of the polymer at lower temperatures after heating past the melting point.

On the other hand, active fillers are those ceramic materials which do possess free Li^+, represented by ceramic solid electrolytes such as LLZO, LATP, LLTO or, most importantly, sulfides and argyrodites such as Li_6PS_5Cl.[103–108] The combination of organic polymer electrolytes with inorganic ceramic electrolytes are known as composite solid electrolytes (CSE), and have been an area of great interest over the past decade. As opposed to passive fillers, active fillers do play a direct role in ionic conductivity through their bulk ion transport properties. In addition, active fillers provide the same effects that passive fillers do through their increase of grain boundary and amorphous regions into the polymer matrix. As such, the Li ion's transport through materials with active fillers is not always easy to model as it involves multiple possible pathways: 1) through the bulk crystal of the active filler; 2) through the defects present in the matrix; 3) along the grain boundaries between polymer and the fillers.

1.5.2 PVDF-Based Polymer Electrolytes

While PEO-based SPEs have received by far the most attention in the literature, they suffer from poor thermal stability, a narrow voltage potential window, and poor room temperature ion transport properties. Another interesting possibility for SPE is PVDF and its cousin, PVDF-HFP. PVDF polymer electrolytes are known to have excellent mechanical properties, a wide potential window, good thermal stability, and excellent electrochemical stability with electrode materials.[92,94,96]

Many of the same principles which applied to PEO-based SPEs also apply to PVDF. However, unlike in PEO, the primary Li ion pathway through the polymer matrix

does not occur along polymer chains. Instead, the addition of lithium salt such as LiTFSI into the PVDF matrix is vital, as the salt will aggregate into clusters which form a percolating network through which the Li ions are able to move. The $TFSI^-$ anions are able to coordinate Li migration through oxygen atoms of their sulfonyl groups.[92]

Using liquid plasticizers to form a gel-type SPE is particularly attractive when using PVDF, owing to the high propensity for the PVDF matrix to absorb the solvent when compared to PEO. PVDF is noted for its excellent wettability to liquid electrolytes like PC or EC while still maintaining its mechanical strength and structure.[92] This approach achieves the notable accomplishment of combining the best elements of both solid and liquid electrolytes. The SPE infused with liquid electrolyte will be generally nonflammable and mechanically robust while also possessing excellent ionic conductivity and much improved interfacial contact with electrode materials.[109,110]

Similarly, ionic liquids may be employed as the plasticizing agent in gel polymer electrolytes. It has been shown that ionic liquid added to PVDF can decrease the degree of crystallization in the polymer matrix.[93] This results in increased segmental motion and, therefore, increased ion conduction. Moreover, alkali salts such as LiTFSI can be introduced to the gel polymer electrolyte through ionic liquids, which acts as a solvent.[111] While the addition of ionic liquid can greatly enhance the ionic conductivity, the Li ion transference number is relatively low, which limits capacity values at high C-rates due to the large relative amounts of ions that are not Li^+.

Another common approach often seen in SPE design is the combination of two separate materials to crosslink the polymer chains and further reduce crystallinity. This decrease in crystallization is responsible for both increasing liquid absorbency and ionic

conductivity, as discussed previously.[92,96] Additionally, the crosslinking results in enhanced mechanical properties. For PVDF specifically, this is very commonly achieved through the copolymerization of vinylidene fluoride (VDF) and hexafluoropropylene (HFP) to yield PVDF-HFP. Materials made with this crosslinking approach are noted for their exceptionally high ionic conductivities, on the order of 10^{-3} S cm^{-1} at room temperature, which is on par with those of liquid electrolytes.[99]

The matter is made more complicated through the addition of fast conducting inorganic active filler materials (**Figure 1.6**). As seen with PEO, the inorganic fillers reduce the crystallinity of the polymer matrix, which increases chain segmental motion thereby increasing ionic conductivity. This occurs with the additional benefit of active fillers being able to act as ion conductors themselves. Moreover, the filler materials bring with them an increase in modulus and hardness, thereby fortifying the CSE's material properties and assisting in the inhibition of dendrites.[112–114]

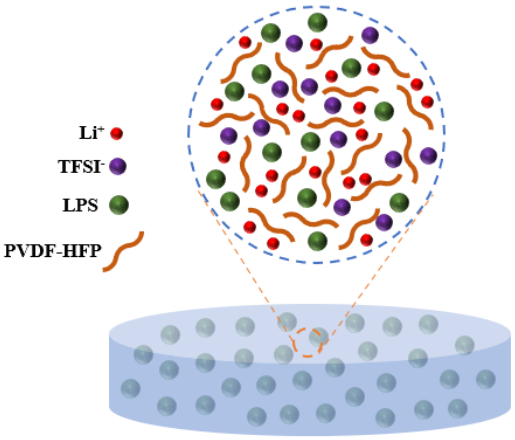

Figure 1.6. Schematic diagram of PVDF-HFP polymer solid electrolyte infused with LiTFSI salt and ceramic LPS material.

To this end, many different oxides and sulfides have been added to different polymer matrices to enhance the desired CSE properties. Zheng et al. was able to show that in PEO/LLZO composite, Li ions prefer to migrate through the ceramic phase as opposed to the interfaces between the PEO and LLZO.[115] Again utilizing garnet LLZO, Lu et al. created a composite using PVDF-HFP polymer and was able to achieve an ionic conductivity of 8.8×10^{-5} S cm^{-1} and an LFP-based battery that reached 500 cycles at a capacity of 110 mAh g^{-1}.[116]

For sulfides, PEO/sulfide composites have been widely studied. For example, Zou et al. achieved an ionic conductivity of 8.84×10^{-4} S cm^{-1} at 80 °C by simply adding 1 wt% of Li_6PS_5Cl to the PEO matrix.[108] Even more impressively, Wang et al. created a PVDF/Li_6PS_5Cl CSE with an ionic conductivity of 1×10^{-3} S cm^{-1} at 25 °C, in addition to showing excellent cycling stability in lithium symmetric cells.[114] While much work has been done on CSEs, the strategy of mixing F-doped argyrodites with polymer materials has thus far been unexplored. This technique could provide the multipronged benefits of increased ionic conductivity, increased mechanical properties, and enhanced interfacial stability with dendrite suppression due to the presence of LiF.

1.6 Summary

The continued development of lithium-ion batteries is one of the most pressing areas of research in our world today. The rapid onset of electric vehicles and demands for grid scale energy solutions requires new chemistries, strategies, and engineering techniques to be developed to create a battery which can meet the myriad of different battery requirements for these applications. These include high energy density, fast charge rate, safety, and a cheap cost.

To that end, this dissertation is focused primarily on the development of the solid-state lithium metal battery, which promises to address all these concerns. The use of a lithium metal anode is key, as it can provide virtually limitless specific capacity, meaning the energy density of the cathode will be the limiting factor for total battery storage capabilities. Lithium metal present serious safety concerns regarding its high propensity to form lithium dendrites, which can lead to a short circuit and, eventually, a flame or explosion event. As such, the key developments of this work revolve around investigations into solid electrolyte materials, whose nonflammable nature make them the perfect fit to pair with lithium metal anodes. Several issues exist which must be overcome before solid electrolytes can be used for LMBs. These include expensive and time-consuming synthesis techniques, low ionic conductivity, poor electrochemical stability with electrodes.

Solid electrolytes can broadly be grouped into two main types: inorganic ceramic and polymer. Within the ceramic group, oxides, halides, and sulfides are all viable options. Oxides can achieve high ionic conductivity and good stability with electrodes, but they suffer from a high degree of hardness and particularly high sintering temperatures (>800 °C). Halides can also possess good ion conducting properties but are known to have poor stability at low voltage, making them difficult to use with most anode materials, especially Li metal. The primary solid electrolyte material explored in this work are sulfide solid electrolytes, more specifically the argyrodite sulfide solid electrolytes Li_7PS_6 and Li_6PS_5X (X = F, Cl, Br, I). These materials are noted for their excellent ionic conductivity, cold-press-induced densification properties, improved interface stability towards electrode materials, and abundant elemental availability.

In addition, this work will seek to address some of the primary drawbacks of sulfides by combining argyrodite materials with polymers to create a composite polymer electrolyte. Polymers have the advantage of excellent and flexible mechanical properties, great stability in ambient air, and easy processibility. By creating a composite material, the resultant CSE should possess the advantages of both ceramic and polymer materials, yielding a material which is better suited for future high energy battery applications.

In summary, the goal of this dissertation is to advance the prospects of LMBs by using safe, nonflammable sulfide argyrodite SEs to make novel SSBs. To achieve this goal, there are several primary objectives which this work aims to achieve:

(1) Demonstrate the wet-chemical synthesis of Li_7PS_6 and halide doped Li_6PS_5X (X = Cl, Br, I) argyrodites;
(2) Investigate the effects of excess Cl doping on the structure, conductivity and stability of $Li_6PS_5Cl{\cdot}LiCl$ argyrodites;
(3) Understand F-doping and hybrid doping (F/Cl) effects on conductivity and interface stability of argyrodites;
(4) Examine the effects of iodine and F/I doping on the structure and conductivity of argyrodites;
(5) Synthesize sulfide-incorporated composite solid electrolyte and test their battery cycling performance.

In all, the techniques and approaches in this work will pave the way for Li metal SSBs to be used in high energy applications.

CHAPTER 2

METHODS

2.1 Synthesis and Preparation of Argyrodite Solid Electrolyte Materials

Argyrodite solid electrolyte materials Li_7PS_6 and Li_6PS_5X (X = F, Cl, Br, I) were synthesized using a novel solvent-based process. Unlike the more commonly used solid state synthesis techniques, the solvent-based process is noted for its simplicity, its rapidity, its low energy consumption, and its relatively inexpensive cost. The solvent of choice is nontoxic ethanol, which contributes to the feasibility of this process being utilized for large scale applications. Before argyrodites can be synthesized in ethanol, the PS_4^{3-} tetrahedra must be present in the precursor materials. As such, a two-step process is required. First, β-Li_3PS_4 must be synthesized, which can then be used to make Li_7PS_6 and Li_6PS_5X.

2.1.1 Synthesis of β-Li_3PS_4 Precursor

The synthesis of β-Li_3PS_4 is carried out through a reaction of reagent-grade lithium sulfide (Li_2S, Alfa Aesar) with phosphorus pentasulfide (P_2S_5, Alfa Aesar) crystalline powders in tetrahydrofuran (THF) solvent at room temperature following **Equation 2.1**. Because of the tendency of sulfide materials to form H_2S in ambient air, all experimental work was carried out in a glovebox filled with inert argon gas (< 1 ppm O_2, < 1 ppm H_2O). In an alternative procedure, acetonitrile (ACN) solvent was used in place of THF.

$$Li_2S + 3P_2S_5 \xrightarrow{THF} Li_3PS_4 \cdot 3THF \quad \textbf{Eq. 2.1}$$

After stirring, the solution was filtered to isolate the powder, followed by a heat treatment at 140 °C to crystallize the powder into nanoporous β-Li_3PS_4. In the alternative procedure using ACN, the material was heated to 200 °C.

2.1.2 Synthesis of Li_7PS_6 and Li_6PS_5X

The synthesis of argyrodite materials Li_7PS_6 and Li_6PS_5X (X = F, Cl, Br, I) was carried out via a dissolution—precipitation process in nontoxic ethanol solvent (**Figure 2.1**). Stoichiometric amounts of Li_3PS_4, Li_2S, and LiX (in the case of Li_6PS_5X) were stirred anhydrous ethanol (**Equations 2.2 and 2.3**). The mixtures were heated at 90 °C under vacuum for 1 h to remove residual ethanol solvent. The temperature was then increased to 200 °C for an additional hour to crystallize the material into Li_6PS_5X. The powder was retrieved from the vacuum tube and ground by hand in a mortar and pestle to make the particles uniform, with a yield weight of ~95%.

The material synthesis yields a dry white powder which will be used as the solid electrolyte material in SSBs. To test the electrochemical properties of this material, it must first be densified via cold pressing. 150 mg of argyrodite powder is loaded into a custom die which is pressed under 480 MPa of pressure to yield a small dense pellet (1/2" diameter, ~0.6 mm thick) (**Figure 2.2**).

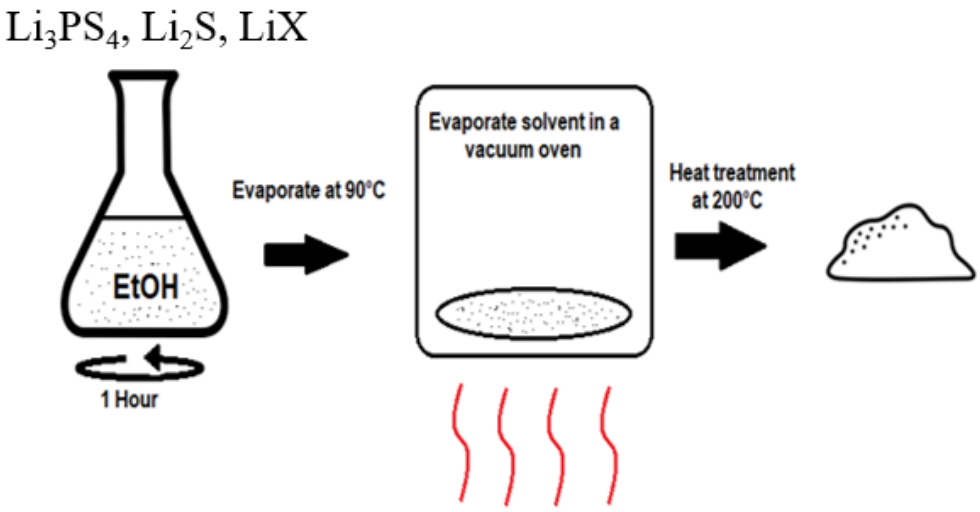

Figure 2.1. Scheme of the Li_7PS_6 synthesis procedure from the chemical reaction of Li_2S and Li_3PS_4 in EtOH medium (evaporation at 90 °C and heat treatment at 200 °C).

Figure 2.2. A densified pellet made from the cold pressing of argyrodite powders under 480 MPa. Approximately 1/2" diameter and 0.6 mm thick.

$$Li_3PS_4 + 2Li_2S \xrightarrow{EtOH} Li_7PS_6 \quad \textbf{Eq. 2.2}$$

$$Li_3PS_4 + Li_2S + LiX \xrightarrow{EtOH} Li_6PS_5X\ (X = F, Cl, Br, I) \quad \textbf{Eq. 2.3}$$

2.1.3 Synthesis of Polymer-Ceramic Composite

The polymer-ceramic composite solid electrolyte membranes were made through the combination of PVDF-HFP crosslinked polymer with LiTFSI salt and argyrodite ceramic sulfide solid electrolyte. THF was utilized as the solvent medium to mix these three ingredients. Separate PVDF-HFP and LiTFSI solutions were made by dissolving the material in THF solvent at a ratio of 100 mg to 1 mL. These two solutions were combined prior to mixing with ceramic. Separately, an appropriate amount of sulfide solid electrolyte ($Li_6PS_5F_{0.5}Cl_{0.5}$) was dissolved in 0.75 mL of THF (0, 2, 5, or 10 wt%), and mixed for 0.5 h. This solution was added to 1.5 mL of the PVDF-HFP/LiTFSI mixture and stirred for an additional 45 minutes. Following this, the solution was taken out of inert atmosphere and transferred to a PTFE dish to evaporate the THF solvent overnight (~16 h). Finally, the polymer composite is placed in a vacuum atmosphere for 0.5 h at room temperature to ensure solvent and moisture evaporation. The resulting polymer composite film is thin and flexible (**Figure 2.3**) and can be hole punched to ½" diameter for electrochemical testing.

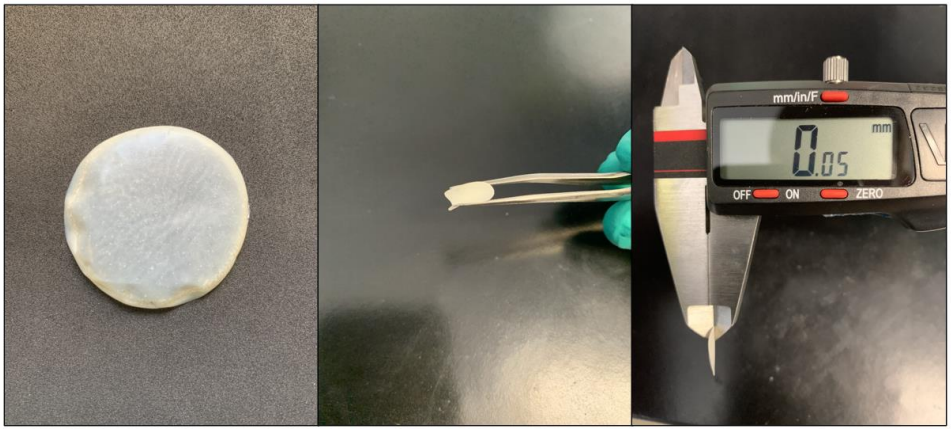

Figure 2.3. Images of the as-prepared polymer-ceramic composite membrane.

2.2 X-Ray Diffraction and Reitveld Refinement

The crystal structure of the synthesized materials was determined using X-ray diffraction (XRD). This technique works on the principle that X-rays are predictably scattered when they interact with crystalline materials. In XRD, X-rays on the order of 1 Å are directed towards crystalline materials through a range of different diffraction angles. The periodic atomic lattice of the crystal structures serves as a diffraction grating which X-rays will interact with differently depending on the specific angle. At certain angles, the X-rays will scatter with sufficient coherency such as to generate constructive interference which can be plotted on a 2-dimensional graph according to Bragg's law (**Equation 2.4**).

$$2d \sin\theta = n\lambda \qquad \textbf{Eq. 2.4}$$

In Bragg's law, λ is the wavelength of the generated X-rays, n (represented by an integer) is the order of reflection, d is the interplanar spacing of the crystal, and θ is the scattering angle (**Figure 2.4**). Because the atomic dimension is the same magnitude as the generated X-rays, the diffraction interference of the reflected X-rays can be used to measure the distance between the atoms in the crystal. When X-rays interact with the sample's electrons, the energy is not sufficient enough to release the electrons from the atom, resulting in X-rays being re-emitted from the sample in a process known as elastic scattering. At particular angles, the emitted X-ray's diffraction patterns will be in alignment, resulting in a signal amplification due to constructive interference. In this dissertation, XRD was performed using a Bruker D8 Discover with nickel-filtered Cu-Kα radiation and λ = 1.5418 Å.

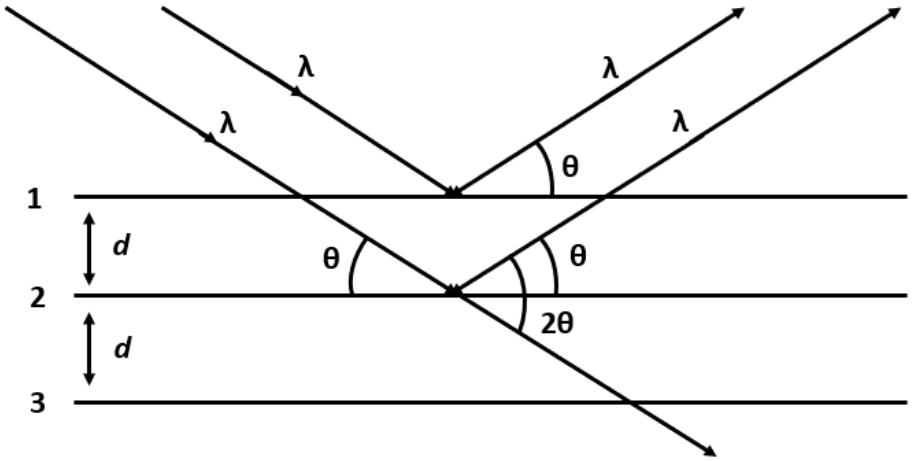

Figure 2.4. Schematic of Bragg's Law for X-Ray Diffraction

Analysis of XRD diffraction patterns is carried out via Reitveld refinement. This method uses a least squares approach to fit a profile to experimentally gathered data, using both structural and instrument parameters to create the best fit (**Figure 2.5**). Using this technique, parameters such as unit cell dimensions and relative amounts of different crystalline materials can be determined. To perform Reitveld refinement, one must estimate and refine three parameters: instrumental parameters which contribute to the peak intensity, unit cell dimensions which control the peak position, and atomic content and coordination data which contributes to the peak shape. After a background is fit to the experimental data, the least squares method is used to determine these three parameters using a combination of Gaussian and LaGrangian models. This dissertation uses the GSAS-II crystallography data analysis software to perform Reitveld refinement.

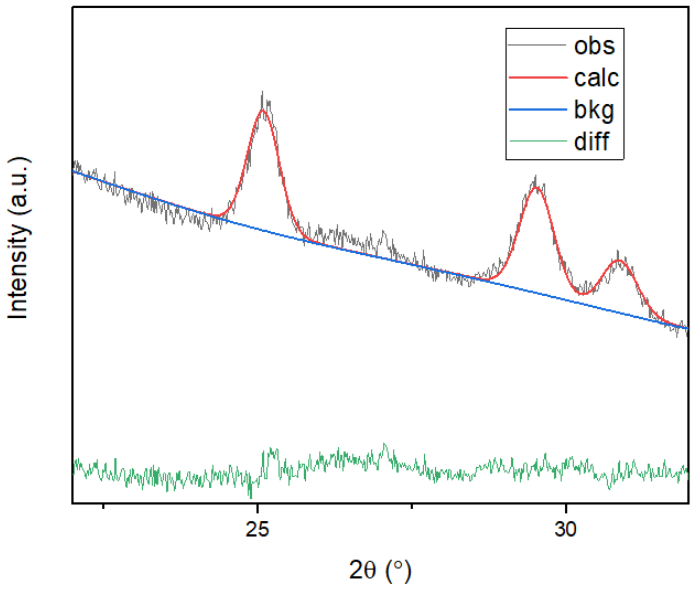

Figure 2.5. Example of Reitveld refinement profile fit to powder diffraction pattern.

2.3 Raman Spectroscopy

Materials characterization was also carried out using Raman spectroscopy, which provides information on the molecular vibrations between bonded atoms. This vibrational signature can be used to identify which bonds are present in a molecule, which gives characteristic identification information about a specific substance. Raman spectroscopy works on the principle of the Raman effect, which is a quantum mechanical phenomenon wherein photons interacting with a molecule cause the molecule to jump to a higher energy state via a polarization of the molecular electron cloud. Upon relaxing in this higher vibrational energy level, the molecule will produce a scattered photon with a different energy than the incident photon. The energy difference of the scattered and incident photon

is known as the Raman shift, and it can be calculated and plotted on a 2-dimensional graph (**Figure 2.6**).

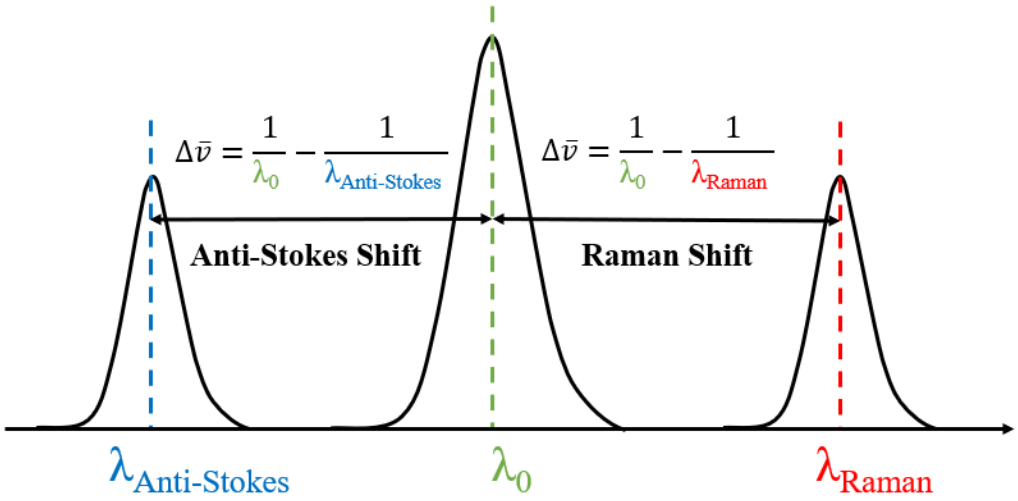

Figure 2.6. Diagram showing the shifted energy spectrum of photons due to Raman scattering.

The photons in Raman spectroscopy are generated using a solid-state laser which, in this dissertation, is transmitted to the sample via fiber optic cables. To eliminate effects from Rayleigh scattering (when scattering photons have the same energy as incident photons) or anti-Stokes scattering (when scattering photons have lower energy than incident photons), both notch filters and holographic gratings must be used. Finally, the light is captured using a CCD detector which is translated into the Raman spectrum. The Raman shift provides information about the phonon vibrational mode, from which a particular bond between two or more atoms can be determined. In this dissertation, Raman spectroscopy was carried out using a Renishaw inVia Raman/PL Microscope and a 632.8 nm emission line of a HeNe laser.

2.4 X-Ray Photoelectron Spectroscopy

Surface level materials characterization was carried out using X-ray photoelectron spectroscopy (XPS). It works through bombarding a substance with AlKα X-rays to ionize electrons from the material surface. These soft X-rays can only penetrate about 5 nm into a sample's depths, and photoelectrons can only escape from ~2 nm below the sample surface, which makes this characterization technique particularly useful for analyzing a material surface. As such, this dissertation uses XPS to analyze the formation of an SEI layer on the surface of a cycled electrolyte or electrode material.

When AlKα X-ray photons (photon energy, hv = 1.5 keV) are fired at an atom, the electrons in specific bound states are excited to a point where some are emitted entirely from the atom. These electrons are collected in an electron analyzer and their kinetic energy (KE) and their intensity (number of photo-ejected electrons vs. time) is measured. Therefore, the atom has undergone a change in energy from its initial state, Ei, to its final state, Ef. The work function, φ, is the minimum energy required to remove an electron from its orbital.

Using the Einstein equation describing the photoelectric effect (**Equation 2.5**), the binding energy (BE) of the of the emitted electron's orbital can be determined and plotted on a 2-dimensional graph. Every element except H and He is associated with its own unique binding energy peak, and the relative intensity of the peaks give information about how much of each element is present in the sample. Molecular bonding where two or more atoms are bonded to each other will affect the electron orbitals of a particular atom. This will be represented as a shift in binding energy, making XPS a powerful tool which is able to distinguish between different molecular configurations of a given atom.

$$KE = hv - BE - \varphi$$ **Eq. 2.5**

Another consideration is spin orbital splitting. (**Figure 2.7**). When the emitted electron comes from an orbital level greater than s, there exists two possible states with different binding energies which results in doublet peaks. This is represented using the nomenclature nl_j, where n is the orbital or principle quantum number, l is the orbital angular momentum number (s = 0, p = 1, d = 2, f = 3), and j is the total angular momentum number, equal to $l \pm ½$. The ratios of the areas of the two doublet peaks will be fixed, with p ratios being 2:1, d being 3:2, and f being 4:3, owing to the degeneracy ratios of the two spin-orbital split energy levels. This information is used when fitting spectra in order to determine relative amounts of the atoms and molecules present in a given sample.

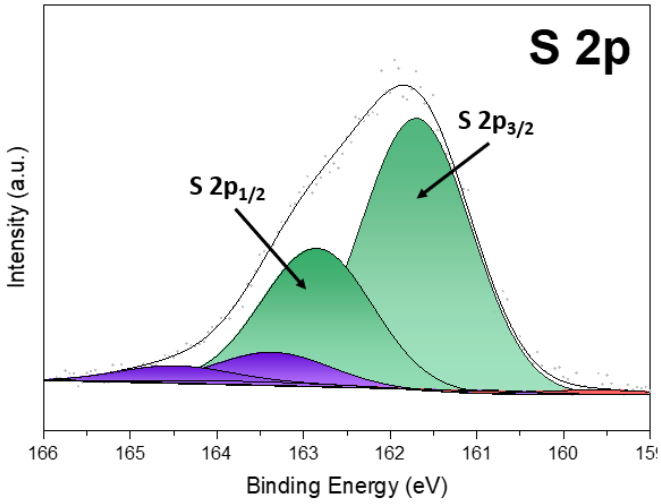

Figure 2.7. An example of spin orbital splitting in the S 2p spectrum.

2.5 Scanning Electron Microscopy and Energy Dispersive X-Ray Spectroscopy

Morphological evaluation of synthesized materials was performed using scanning electron microscopy (SEM). SEM images can be taken on the micron to nanometer scale and are used to determine morphology and topology of a sample. An electron beam with a voltage of 1–40 kV passes through an anode, and then through a series of focusing lenses and apertures which fires it towards the sample where its kinetic energy will interact with the material's electrons (**Figure 2.8**). This interaction causes the sample's electrons to reflect and scatter, producing several different types of signals which can be used to create the image. Detectors which can differentiate between secondary electrons, backscattered electrons, and X-rays then collect the resultant particles emitted from the sample.

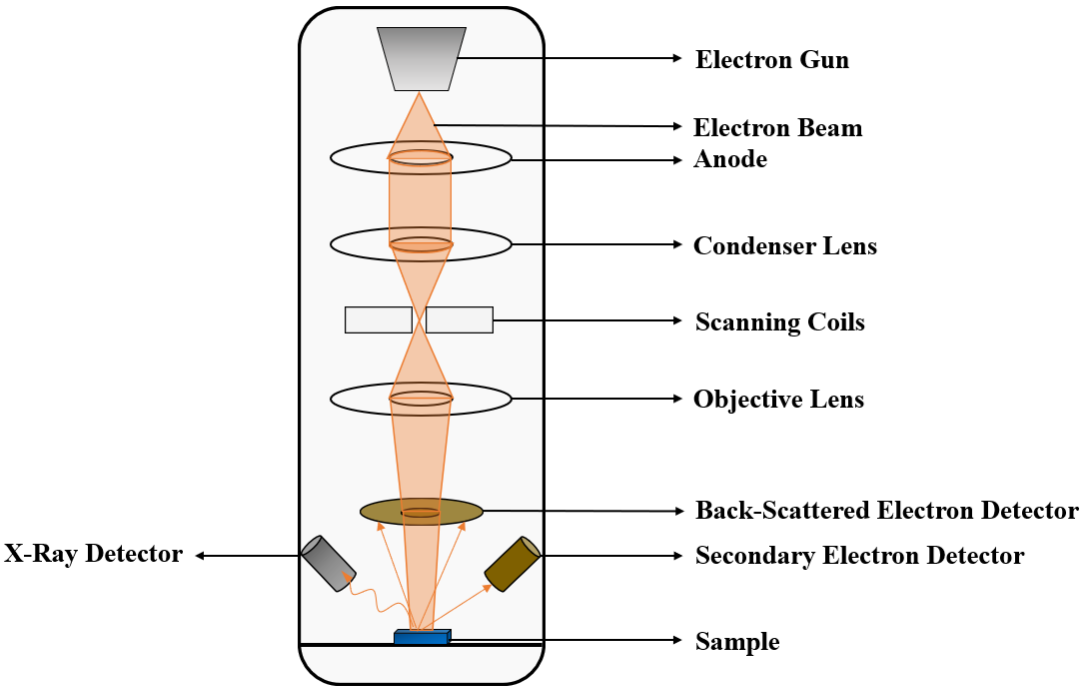

Figure 2.8. Schematic representation of a scanning electron microscope.

Secondary electrons are emitted near the surface of the sample and are responsible for representing the topology and morphology of the material as an image. They are the result of interaction of the electron beam with the sample, and as such only represent the electrons near the surface regions. The difference in number of emitted secondary electrons between different hills and valleys of the sample is the core concept used to develop an image of the sample, where higher regions will reflect more electrons back while lower regions will reflect less. This information can be translated to provide a detailed morphological image of the sample's surface. Backscattered electrons, which result from the interaction of scattered electrons with atoms, have more energy than secondary electrons. These electrons provide useful information detailing the sample's composition, crystallography, and topography.

Energy dispersive X-ray spectroscopy (EDS) can be used to determine the elemental composition of the analyzed sample. EDS works on the principle of Moseley's Law, which states that when X-rays bombard an atom, there is a correlation between the frequency of the ejected electron and the atomic number of the atom. After a core electron is ejected, higher energy electrons will relax into the lower position, which releases a signature amount of energy for each element.

Using this technique, EDS can provide useful information concerning which elements are present in the sample and the relative proportions of said elements. The beam is applied using a raster scan over the entirety of the sample, which can produce of elemental distribution maps which can differentiate the relative position of each element in the sample. This allows for analysis of the homogeneity of synthesized materials, a key consideration for the synthesis of solvent-based solid electrolytes.

2.6 Electronic Impedance Spectroscopy

Ionic conductivities of the synthesized solid electrolyte powders were calculated using electronic impedance spectroscopy (EIS), also known as alternating current impedance spectroscopy. Using this technique, the contributions of both grain boundary and bulk resistances can be separated and used to find the ionic conductivity of the solid electrolyte sample. To execute the test, a solid ion conductor is sandwiched between two conductive electrodes of carbon-coated aluminum and is subjected to an oscillating voltage, as seen in **Equation 2.6**,

$$E(t) = |E| \sin(\omega t) \qquad \textbf{Eq. 2.6}$$

where $\boldsymbol{|E|}$ is the voltage signal amplitude, and $\boldsymbol{\omega = 2\pi f}$. The measured response is an oscillating current, as seen in **Equation 2.7**,

$$I(t) = |I| \sin(\omega t + \theta) \qquad \textbf{Eq. 2.7}$$

where $\boldsymbol{\theta}$ accounts for a phase shift due to capacitance and inductance. The impedance is then calculated using Ohm's law, **Equation 2.8**.

$$Z = \frac{E(t)}{I(t)} = \frac{|E| \sin(\omega t)}{|I| \sin(\omega t + \theta)} \qquad \textbf{Eq. 2.8}$$

Using Euler's formula, **Equation 2.8** can be rewritten using complex numbers (**Equation 2.9**).

$$E = IZ = I|Z|e^{j\theta} \qquad \textbf{Eq. 2.9}$$

where $\boldsymbol{j = \sqrt{-1}}$. It can then be seen from **Equation 2.9** that the impedance can be expressed as a ratio of an oscillating voltage to an oscillating current. This impedance can be graphically represented by on a Cartesian complex plane by breaking **Z** into both real and imaginary parts (**Equation 2.10**).

$$Z = Z' + jZ''$$ **Eq. 2.10**

A Nyquist plot is a graph of the real and imaginary parts of the impedance occurring as an oscillating voltage is applied across the cell over a range of different frequency values. For EIS tests run in this dissertation, an excitation voltage of 100 mV is applied over a frequency range from 100 mHz to 5 MHz, with the high frequency values being represented in the lower left-hand portion of the plot and the low frequency values being represented in the upper right-hand portion (**Figure 2.9**).

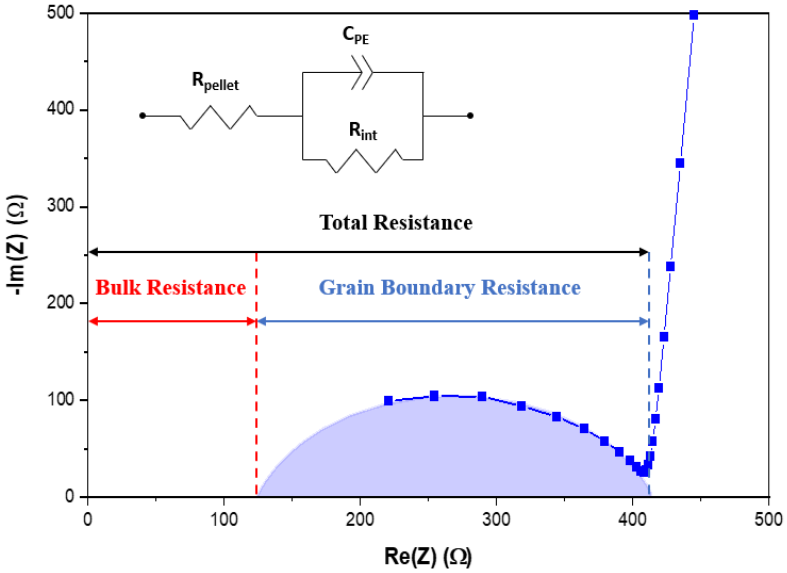

Figure 2.9. A representation of a Nyquist plot, which shows the real and imaginary impedance values over a range of different frequency values.

As can be seen from the graph, the typical shape produced from EIS when testing an ion conductor is a semicircle. This plot provides useful information about the resistance of the solid electrolyte pellet, as well as information about the interfacial resistance between the electrolyte and any electrodes of interest. The bulk resistance of the material occurs in the high frequency region of the graph, the grain boundary regions are represented

in the medium frequency region, and the low frequency region tail represents the pellet/electrode interface region.

In the above graph, there was not sufficient resolution to accurately plot the bulk resistance semicircle with the provided instruments (BioLogic SP300 potentiostat). Bulk resistance can instead be estimated by simulating an equivalent circuit model to the grain boundary resistance semicircle, which in this case is a resistor in series with a parallel resistor and a constant phase element capacitor ($Z_Q Q_0 (j\omega)^n = 1$, where Q is the real-world representation of the capacitor and n is the constant phase, $(-90 \times n)°$).

An accurate equivalent circuit model fitting allows for the separation of bulk and grain boundary contributions to the resistance, and the total resistance can be calculated by summing these two values. Once found, the total ionic conductivity of the solid electrolyte pellet can be calculated using **Equation 2.11**,

$$\sigma = \frac{L}{R \cdot A} \qquad \textbf{Eq. 2.11}$$

where σ is the ionic conductivity in S cm^{-1}, L is the thickness of the pellet, A is the cross-sectional area, and R is the total resistance of the ion conductor.

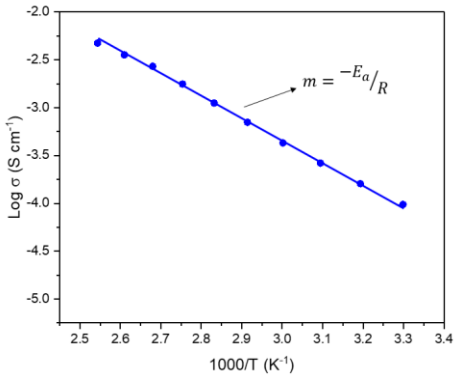

Figure 2.10. An Arrhenius plot showing a slope equal to the activation energy, $-E_a$, over the gas constant, R.

In addition to ionic conductivity measurements, temperature-dependent EIS tests can be used to determine the activation energy associated with ion transport through the solid electrolyte. This is achieved through the application of the Arrhenius Law, which states that the natural log of the rate constant of a reaction is a function of the inverse of the temperature. The Arrhenius law is shown in **Equation 2.12**,

$$k = Ae^{-E_a/RT} \qquad \textbf{Eq. 2.12}$$

where k is the rate constant, A is the pre-exponential factor, R is the gas constant, T is the temperature, and E_a is the activation energy. In a given reaction, a higher temperature means that more molecules have sufficient energy to cross over the activation energy barrier, which results in a higher rate constant. If a reaction obeys the Arrhenius law, a plot of the natural log of the rate constant versus the inverse of temperature will result in a straight line with a slope of $-E_a/R$ and a y-intercept of $\ln A$ (**Figure 2.10**). Using this information, a value for the activation energy can be determined.

2.7 Cyclic Voltammetry

Short-term thermodynamic and chemical stability of redox reactions during cell cycling were determined using cyclic voltammetry (CV). A cell used for CV testing consists of a working electrode, a reference/counter electrode, and an ion conductor between them. In this dissertation, these parts are stainless steel (SS), lithium metal, and argyrodite solid electrolyte, respectively. Using this technique, the redox reactivity of Li metal with sulfide solid electrolytes can be determined over a range of different voltage values. CV tests use a potentiostat to linearly sweep a potential between the reference and working electrodes. Upon reaching the upper limit of a preset voltage range, the sweep will

reverse until the lower limit is reached, after which the cycle is repeated. During this process, the current is recorded as a function of the voltage, which is plotted to create a voltammogram (**Figure 2.11**).

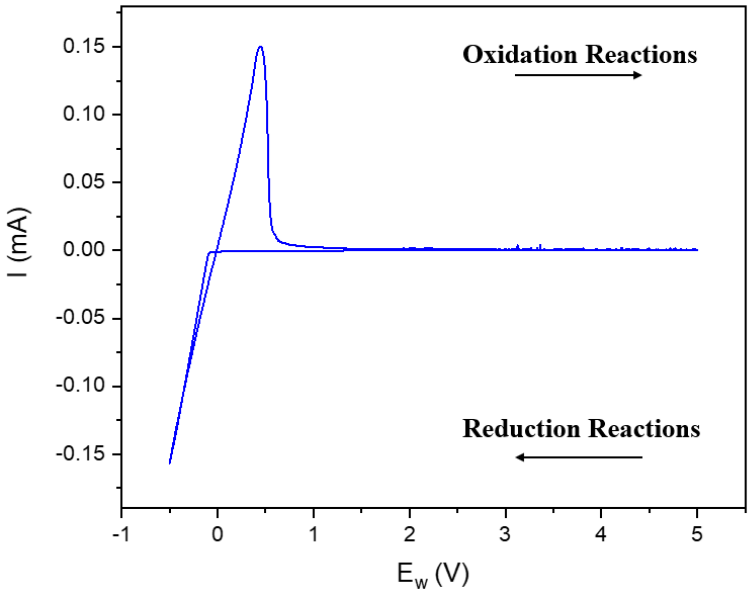

Figure 2.11. An example of a typical voltammogram collected from a Li|SE|SS cell.

CV scans in this work are scanned in a potential window from -0.5 to 5.0 V (vs Li^+/Li) at a scan rate of 50 mV s^{-1}. Because of the low potential of Li, redox peaks are centered around V = 0, with oxidation peaks ($Li \rightarrow Li^+ + e^-$) occurring when $V > 0$ and reduction peaks ($Li^+ + e^- \rightarrow Li$) occurring when $V < 0$. During reduction, Li metal is plated onto the working electrode, whereas reversible lithium dissolution occurs during oxidation. Because battery cells are often cycled up to 4 to 5 V, it is desirable to determine whether Li metal shows adverse reactions at these high potentials. In

Figure 2.11, the lack of prominent peaks from 0.5 to 5.0 V indicates good electrochemical stability between the lithium anode and the solid electrolyte.

2.8 Symmetric Cell Cycling

Electrochemical stability between lithium metal and the sulfide solid electrolyte was also determined through symmetric cell cycling. Symmetric cells use the same material (Li metal) as both the positive and negative electrode, resulting in an average voltage of zero volts. These cells cannot work as practical batteries, but they can provide useful information regarding the electrochemical reactions taking place at the electrode/electrolyte interface over many cycles.

Symmetric cells are cycled using the application of a constant current density, forcing lithium stripping from one of the electrodes and lithium plating on the others. By specifying a time period for cycling, the areal specific capacity can be determined. The graph generated from symmetric cell data displays a plot of voltage vs time. From this graph, much useful information can be determined. In accordance with Ohm's law, voltage is directly proportional to resistance, and so a sudden increase or spike in potential translates to an increase in interfacial resistance between the electrode and electrolyte. This phenomenon is most likely attributable to redox reactions which occur during cycling. Likewise, a sudden drop in potential to near zero indicates a similar drop in resistance across the cell. This data can be interpreted as the propagation of lithium dendrites having caused a short circuit event (**Figure 2.12**).

Symmetric cell data is especially useful if paired with either EIS or XPS testing to confirm resistance changes, or to determine the exact decomposition products from the cycling reactions. Ideal Li symmetric cell data should have a consistent voltage with a flat

profile over a long period of time, which indicates the successful stripping and plating of lithium metal with no side reactions and no dendrite propagation.

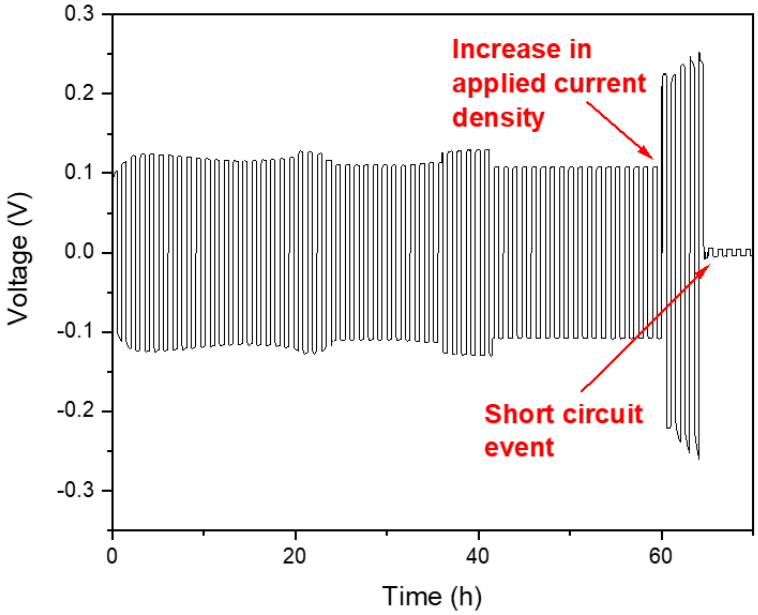

Figure 2.12. Li symmetric cell showing a short circuit event indicated by a sudden drop in potential.

2.9 Full Cell Battery Testing

Battery cycling tests were conducted by applying galvanostatic cycling techniques to a full cell battery consisting of a cathode, a lithium metal anode, and a solid electrolyte separator. Many cathode materials exist which are commonly used in today's commercial batteries, including $LiCoO_2$, $LiMn_2O_4$, and $LiFePO_4$ (LFP).[117] Nickel-based chemistries such as $LiNi_{0.8}Co_{0.15}Al_{0.05}O_2$ (NCA) or $LiNi_{1-x-y}Mn_xCo_yO_2$ (NMC) have been especially popular options in electric vehicles due to their high energy density.[118] The presence of cobalt in nickel-based cells raises concerns over the price of the element and due to the

human rights issues associated with its mining. As such, it is desirable to explore different cathode options for SSBs.

LFP chemistries are the second most popular cathode in today's EVs. Iron is both cheap and abundant, and LFP possesses an energy density comparable to NMC. In addition, LFP has been shown to be stable with sulfide materials up to 4 V. These traits make it the perfect candidate for use in a solid-state battery. Another intriguing cathode option is $Li_4Ti_5O_{12}$ (LTO), which is ordinarily employed as an anode material due to its relatively low voltage (~2.5 V vs Li^+/Li). However, the extremely low voltage of a lithium metal anode makes LTO a viable cathode option as well, though its energy density will be inherently lower than that of LFP. LTO chemistries are noted for their exceptional chemical stability and high degree of safety. As such, the two cathode chemistries used in this dissertation are commercially purchased LFP (Alfa Aesar) and LTO (Alfa Aesar).

Cathode preparation begins with the mechanical mixing of 160 mg of cathode active material and 20 mg of electronically conductive Super P carbon. These materials are mixed by hand in a mortar and pestle for 30 minutes. Following this, a solution of 50 mg/ml PVDF binder in N-methylpyrrolidone (NMP) solvent is added to the mixture to create a smooth slurry. This slurry is transferred to a sheet of aluminum foil and coated on the surface with a thickness of 15 mm. The thin film is then dried at 80 °C overnight before being hole punched into a circle with a diameter of 0.45 cm and an area of 0.64 cm^2.

Battery assembly takes place inside the glovebox to avoid H_2S formation and Li metal oxidation. The assembled coin cell consists of an anode side, a spring, a stainless-steel plate, the Li metal anode, the cold-pressed solid electrolyte pellet, the cathode, and the cathode side (**Figure 2.13**). To overcome the solid-to-solid contact at the

electrode/electrolyte layer, one approach used for interface modification is the application of trace amounts (< 15 μL) of either liquid electrolyte (propylene carbonate, PC) or ionic liquid (N-methyl-N-alkylpyrrolidinium, PYR) with LiTFSI salt added as an interlayer. Similarly, polymer solid electrolytes were soaked in different ratios of PYR to DOL (1,3-dioxolane) to reduce the liquid viscosity and ensure absorption by the PVDF-HFP polymer matrix. Once assembled, the coin cells are crimped using an MSK-110 Hydraulic Crimping Machine and pressed to a pressure of 50 kg/cm^2.

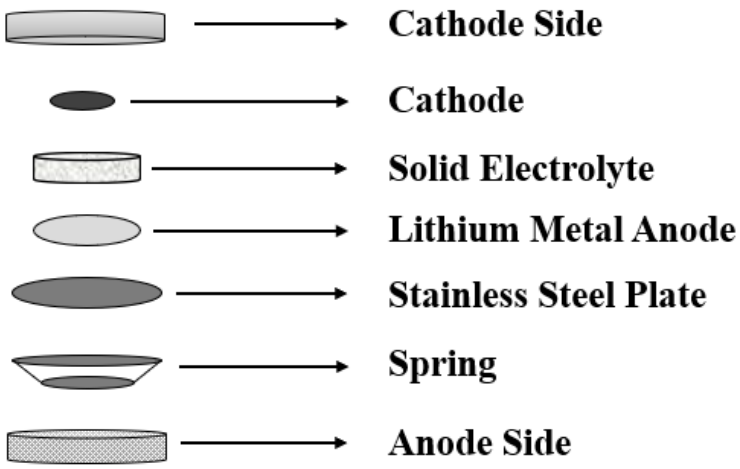

Figure 2.13. Schematic representation of an assembled full battery coin cell.

Galvanostatic cycling was conducted using a Neware Battery Testing System. Before cycling, the battery cells were rested for 8 hours to let any passive interfacial reactions develop. The C-rate (also known as the charge rate) determines how quickly a battery will be fully charged, with 1C meaning the cell will reach full charge in 1 h, 2C will reach full charge in 0.5 h, and C/2 will reach full charge in 2 h. The applied current is calculated based on the amount of cathode active material in the cell and the theoretical specific capacity of the cathode chemistry. The theoretical capacity value of LFP is 170

mAh g^{-1}, and the theoretical capacity value of LTO 175 mAh g^{-1}. Assuming that 80% of the cathode mass is active material, and accounting for the mass of the aluminum foil the coating is on, the applied current can be calculated using **Equation 2.13**.

$$1C = \left(m_{cathode} - m_{foil}\right)(0.8)(theoretical\ capacity) \qquad \textbf{Eq. 2.13}$$

CHAPTER 3

PROPERTIES AND PERFORMANCE OF SOLVENT-SYNTHESIZED ARGYRODITES Li_7PS_6 AND Li_6PS_5X (X = Cl, Bl, I) SOLID ELECTROLYTE[43,119]

3.1 Introduction

When compared with traditional liquid-based batteries, all-solid-state batteries (ASSBs), using solid-state superionic conductors to replace the liquid electrolytes, are expected to show improved safety, increased energy density, and a wide operating temperature range.[120–123] These advantages enable ASSBs to be considered one of the most promising candidates for middle- or large-scale energy storage systems that requires high energy density and safety. In the ASSB structure, the solid electrolyte is an indispensable component and plays a crucial role in the solid-state battery performance. An ideal solid electrolyte should exhibit an ionic conductivity above 10^{-4} S cm^{-1} at room temperature, a large electrochemical stability window, and good stability against electrodes, especially a metallic Li anode. In addition, the production cost is an important factor which must be considered.

Lithium argyrodites, including pure lithium argyrodites (Li_7PS_6), halogen-anion-doped lithium argyrodites (Li_6PS_5X, X= Cl, Br, or I),[124–126] and cation-substituted lithium argyrodites,[127–129] are noted amongst solid electrolyte candidates for their unusually high ionic conductivity, up to 10^{-3} S cm^{-1}. Pure lithium argyrodite (Li_7PS_6) can exist in one of two phases, either a high temperature (HT) phase or a low temperature orthorhombic phase

(LT). It is desirable to synthesize a stable HT phase due to its higher ionic conductivity values (0.7–1.0 × 10–3 S cm–1).[130]

For lithium argyrodite materials, solid-state reactions are the dominant synthesis method used to produce pure phase and crystalline solid electrolytes,[60,124,131–134] which show impressive ionic conductivities (0.1-10 mS cm^{-1}). However, such a synthetic approach strictly requires extensive ball-milling time and high temperature (>500 ºC) heat treatment, thereby increasing the difficulty of their practical applications in ASSBs.

On the other hand, a solvent-based synthesis method, utilizing a solvent as the reaction medium, has been reported to synthesize some sulfide solid electrolytes such as Li_3PS_4 and $Li_7P_3S_{11}$, etc.[51,135–141] Liang et al. used THF and ACN solvents to obtain β-Li_3PS_4 crystallites with an ionic conductivity of 1.6 × 10^{-4} S cm^{-1} at RT.[135,136] Similar results have been achieved using ethyl propionate[142] or ethyl acetate.[138] Likewise, $Li_7P_3S_{11}$ has been synthesized from solvent processes using both ACN[140] and 1,2-dimethoxyethane (DME).[141] In comparison, the synthesis of Li_7PS_6 soldi electrolyte from a liquid synthesis is undeveloped. Moreover, the liquid approaches detailed above all require toxic and expensive solvents such as ACN or THF. For large-scale synthesis, inexpensive and less toxic solvents would be more ideal.

Solvent-synthesis methods have also been reported for halogen-anion-doped lithium argyrodites. Nazar et al. prepared Li_6PS_5X compounds (i.e. $Li_6PS_5Cl_{0.5}Br_{0.5}$) from Li_3PS_4·3THF, Li_2S, and LiX (X = Cl, Br) in mixed solvents (THF and ethanol) [68]. Tatsumisago et al. produced Li_6PS_5Br through THF suspension containing an Li_3PS_4 precursor mixed with Li_2S and LiBr.[63] These findings suggest that solvent-based

synthesis methods provide a feasible approach to achieve compositional flexibility for lithium argyrodites.

In comparison with pure Li_7PS_6, Li_6PS_5X argyrodites with halogen anions (X=Cl, Br, I) replacing S^{2-} possess different crystal structures and properties. First, as opposed to the tetragonal phase displayed by Li_7PS_6, Li_6PS_5X argyrodites are characterized by a cubic phase at room temperature.[130] In addition, halogen anions lead to structural disorder and lattice polarization, thereby influencing ion diffusion mechanisms and Li-ion conductivity.[58,143] Recently, Adeli et al. [76] employed a solid-state synthesis method to produce $Li_{5.5}PS_{4.5}Cl_{1.5}$ and found that increasing halide content increased the Li-ion mobility in argyrodite structure. On this basis, halide doped lithium argyrodites such as Li_6PS_5Cl and Li_6PS_5Br have been tested for their applications in ASSBs using different electrode materials.[60,144–149] Despite these important and interesting findings, Li_6PS_5X argyrodites are mostly synthesized from high temperature solid-state reactions. Additionally, the effect of halide doping on solvent synthesized Li_6PS_5X argyrodites has not yet been explored.

In this chapter, for the first time, both pure phase Li_7PS_6 and halide doped Li_6PS_5X (X= Cl, Br, I) solid electrolytes were synthesized via an ethanol-based method, and the effects of halogen anion doping on the crystal structure, ionic conductivity, and electrochemical stability of the argyrodite electrolytes were investigated. Following a low temperature (200 ºC) heat treatment, Li_6PS_5Cl exhibited the highest ionic conductivity of 0.34 mS cm^{-1} at room temperature, followed by Li_6PS_5Br (0.31 mS cm^{-1}), while Li_6PS_5I showed the worst conductivity. In addition, liquid synthesized Li_6PS_5X (X= Cl, Br, I) solid electrolytes presented good electrochemical stability with Li metal. The solvent-based

synthesis method is a feasible method to precisely control the composition of lithium argyrodites and provides the possibility to obtain better Li-ion conducting argyrodites for future applications in ASSBs.

3.2 Methods

3.2.1 Materials Synthesis

The precursor Li_3PS_4 was prepared using similar methods as described by Liang and Wang et al.[51,135] In brief, the Li_2S and P_2S_5 precursors were dissolved in a solvent (acetonitrile, ACN or tetrahydrofuran, THF), stirred for 8 hours at RT and then filtrated. The obtained white powder was then dried at 80 °C, followed by low temperature heat treatment (200 °C when ACN was the solvent, or 140 °C when THF was the solvent) under vacuum. The obtained Li_3PS_4 material was used for further reactions. A stoichiometric mixture of Li_2S, Li_3PS_4 and LiX (X=Cl, Br, I) was fully dissolved in a small quantity of anhydrous ethanol in argon atmosphere. Afterwards, the solvent was evaporated at 90°C under vacuum to obtain a white precipitate before heat treating at 200°C to produce the final product: Li_6PS_5X (X= Cl, Br, I) (**Figure 3.1**). The synthesis reactions are described in **Equations 3.1-3.4**.

$$Li_3PS_4 + 2Li_2S \rightarrow Li_7PS_6 \quad \textbf{Eq. 3.1}$$

$$LiCl + Li_3PS_4 + Li_2S \rightarrow Li_6PS_5Cl \quad \textbf{Eq. 3.2}$$

$$LiBr + Li_3PS_4 + Li_2S \rightarrow Li_6PS_5Br \quad \textbf{Eq. 3.3}$$

$$LiI + Li_3PS_4 + Li_2S \rightarrow Li_6PS_5I \quad \textbf{Eq. 3.4}$$

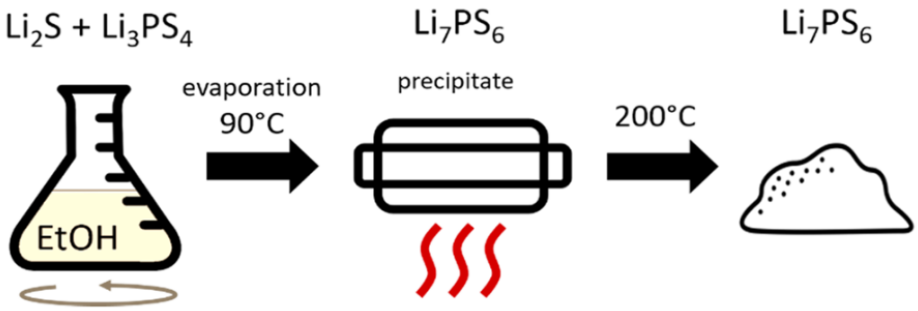

Figure 3.1. Schematic of the synthesis of Li_7PS_6 in ethanol solvent.

3.2.2 Structural and Morphological Investigation

The phase composition and crystal structure were examined using X-ray diffraction (Bruker D8 Discover) with nickel-filtered Cu-Kα radiation (λ = 1.5418 Å). The crystallite size was analysed using the Scherrer equation. The Raman spectra were collected by Renishaw in Via Raman/PL Microscope with a 632.8 nm emission line of a HeNe laser. TESCAN Vega3 scanning electron microscope (SEM) was used to study the morphology of samples.

3.2.3 Electrochemical Characterizations

Electrochemical impedance spectroscopy (EIS) was performed to measure the ionic conductivities of solid electrolyte samples in the frequency range from 1 MHz to 100 mHz with an amplitude of 100 mV using a Bio-Logic SP300. The powder samples were cold-pressed to dense pellets (1/2" diameter and 0.6 mm thickness) with C/Al foil on each side, then the sandwich structure was loaded in Swagelok Cells for EIS measurement. In addition, temperature dependent spectra were recorded from RT to 120 °C to obtain Arrhenius plots. Swagelok cells were also used to complete cyclic voltammetry (CV) and cycling performance measurements. For CV testing, Li/SE/Pt cells were scanned at 50 mV

s^{-1} rate between -0.5 and 5 V *vs* Li/Li^+ at room temperature. For symmetric cell cycling, the Li/SE/Li symmetric cells were assembled and cycled on a battery system (Bio-Logic VSP) under various current densities (0.02, 0.03, 0.05, 0.1 mA cm^{-2}). All the materials handling, and cell preparations took place in a Glovebox under an argon atmosphere.

3.3 Results and Discussion

3.3.1 Structure and Characterization of Li_7PS_6 from Liquid Approach

The most common approach for Li_7PS_6 synthesis is through a solid-state reaction of Li_2S with P_2S_5 at 550 °C for anywhere from several hours to multiple days.[56,124] Liquid synthesis is more appealing, but there are concerns regarding the stability of precursors in a solvent. P_2S_5, for example, can react with ethanol to form dialkyldithiophosphoric acid.[150] Regardless, this section focuses on the synthesis of Li_7PS_6 SE from a simple solvent-based method by reacting Li_3PS_4 and Li_2S in anhydrous ethanol followed by heat treatment at 200 °C.

X-ray diffraction (XRD) was employed for characterization of the synthesized powder (**Figure 3.2**). Diffraction patterns reveal three primary peaks at 2θ = 25.5, 30, and 31.2°, corresponding to (220), (311), and (222) planes in the cubic HT-phase of Li_7PS_6 (space group $F\bar{4}3m$). These characteristic diffraction peaks are in good agreement with XRD patterns from the literature.[131,151] It is also encouraging that the HT cubic phase is present in a stable form from the solvent-based synthesis, as this phase possesses much faster ion-transport abilities than the LT-orthorhombic structure.[56] Indeed, this seems to be a primary benefit of liquid-based synthesis, as previous reports suggest that solvent synthesis of Li_3PS_4 stabilized at β-phase at room temperature as opposed to γ-phase.[51,135]

This high degree of stability is attributed to favorable interactions between ethanol solvent and precursors (Li_2S and Li_3PS_4). During solid-state reactions, a high temperature and longer times are needed for crystal nucleation and Li ion reorganization. In contrast, during solvent-based synthesis, the liquid medium allows for the free movement of solvated ions, thus facilitating Li_7PS_6 formation. The unit cell parameter length of HT cubic Li_7PS_6 was found to be 9.88 Å, which is in good agreement with previous reports.[56,152] Using the Scherrer equation, the crystal size was estimated to be 34 nm.

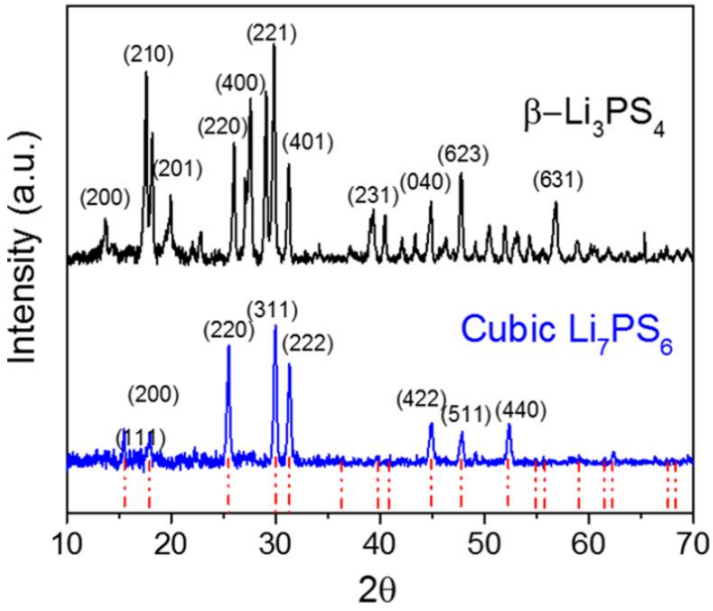

Figure 3.2. Comparison of XRD patterns of Li_7PS_6 crystalline (space group $F\bar{4}3m$, dashed lines is index from ICCD #00-034-0688) and the β-Li3PS4 phase (space group Pnma, a = 12.997 Å, b = 8.081 Å, c = 6.143 Å, ICCD #01-076-0973).

Figure 3.2 shows XRD patterns for the synthesized Li_7PS_6 and β-Li_3PS_4. Li_7PS_6 material displays high phase purity without no observable peaks attributed to either Li_2S or β-Li_3PS. To further test the viability of the solvent-based process, Li_7PS_6 was

synthesized using Li_3PS_4 made from different methods. **Figure 3.3** shows the diffraction peaks from β-Li_3PS_4 made using ACN as the solvent medium. Li_7PS_6 was made using Li_3PS_4 precursor prepared using ball milling. In addition to this, unevaporated $Li_3PS_4 \cdot (ACN)_2$ complex was tested as a precursor material (**Figure 3.3**).

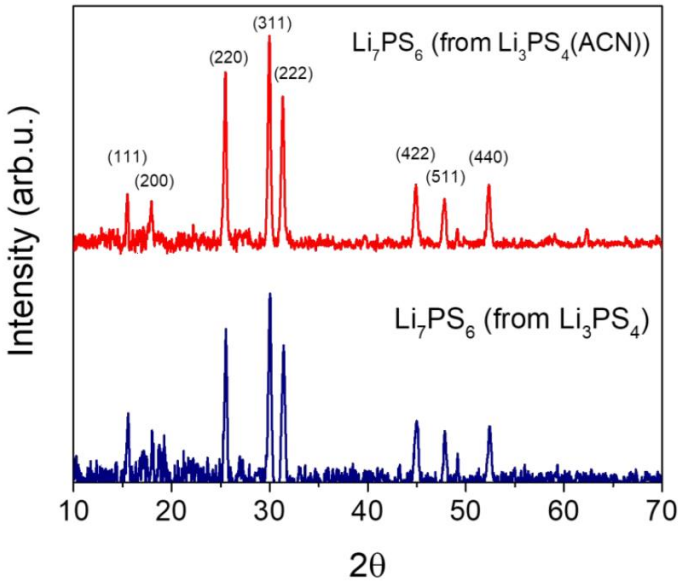

Figure 3.3. XRD patterns of Li_7PS_6 solid electrolyte using different precursors: Li_3PS_4 and $Li_3PS_4 \cdot (ACN)_2$ complex.

The Raman spectra of solvent-synthesized Li_7PS_6 and β-Li_3PS_4 precursor are shown in **Figure 3.4**. A primary peak for Li_7PS_6 can be observed at 421.6 cm^{-1}, which is attributed to the symmetric stretching vibrational mode of $(PS_4)^{3-}$ (ortho-thiophosphate) group.[59] In addition, secondary peak at 497.2 cm^{-1} and 570 cm^{-1} is attributed to the asymmetric vibrational modes of the $(PS_4)^{3-}$ tetrahedra. This is in good agreement with previous reports.[59,153] Raman spectrum of Li_3PS_4 also exhibit a primary peak at 421.1 cm^{-1} which again is attributed to the vibrational mode of $(PS_4)^{3-}$, with two minor peaks at 530.2

and 568.5 cm^{-1} attributed to additional asymmetric $(PS_4)^{3-}$ vibrational modes.[51,59,142,154] No peaks from Li–S interactions are present due to the strong ionic bonds between S^{2-} and Li^+ ions. Notably, the Li_3PS_4 spectrum reveals a minor peak at 387.6 cm^{-1} which corresponds to the $(P_2S_6)^{4-}$ (P–P bond) vibrational mode.[153] This is explained by the presence of a trace amount of $Li_4P_2S_6$. However, after synthesizing Li_7PS_6 this peak disappears, further confirming the high degree purity from the solvent-based synthesis.

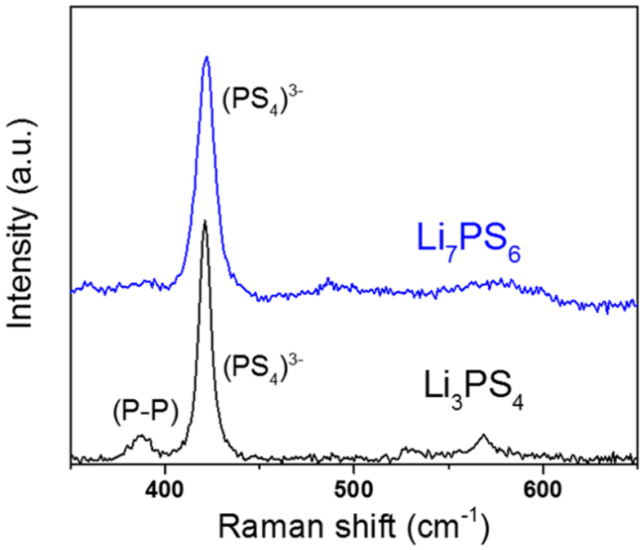

Figure 3.4. Raman spectra of Li_7PS_6 and Li_3PS_4 showing the dominant peak from the vibrational mode of the $(PS_4)^{3-}$ group.

3.3.2 Revealing the Formation Mechanism from Structural Studies

To better understand the reaction mechanism of the solvent-based synthesis, Li_7PS_6 was examined at different stages of the synthesis process. Following ethanol evaporation at 90 °C, the powder was collected and analyzed using XRD. Even prior to the 200 °C heat treatment, the cubic phase of Li_7PS_6 was present, indicating that the reaction happens at room temperature. The XRD patterns (**Figure 3.5**) showed that the Li_7PS_6 pure phase exists

in the intermediate product, indicating that this synthetic reaction in fact happens at room temperature. Unfortunately, the ionic conductivity of this pre-heat-treated material is very low (10^{-7} S cm^{-1}). Unlike the complexes observed in the formation of Li_3PS_4 in ACN or THF,[51,135] the pure phase of Li_7PS_6 indicates that this material does not form a similar complex with ethanol.

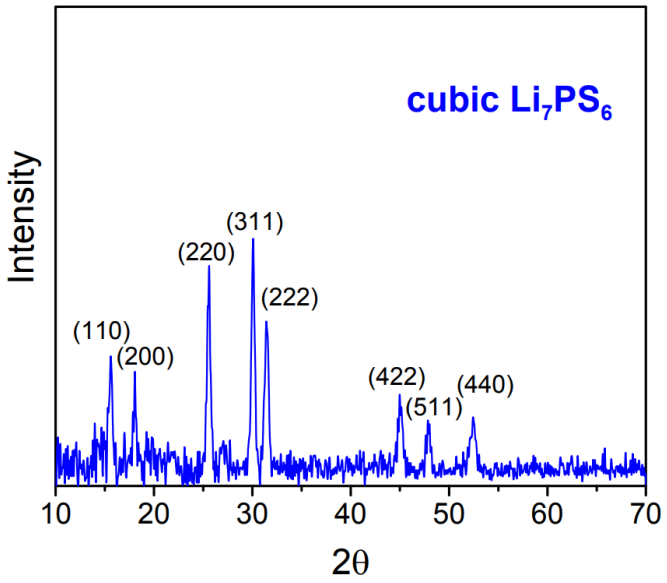

Figure 3.5. XRD patterns of Li_7PS_6 obtained from ethanol evaporation at 90 °C.

In addition, the dissolution and reprecipitation of the Li_3PS_4 precursor in ethanol solvent was investigated using XRD and Raman spectroscopy. After acquiring the solvent-synthesized β-Li_3PS_4, it was re-dissolved in ethanol and subsequently dried at 80 °C to collect the reprecipitated sample. This reprecipitated sample shows no clear signs of crystalline Li_3PS_4 in its XRD patterns, with an unknown phase present instead (**Figure 3.6**). Upon heat treating the reprecipitated sample at 200 °C, an amorphous crystalline phase is observed, suggesting that Li_3PS_4 alone is not sufficient to synthesize Li_7PS_6. Raman spectra of the reprecipitated sample further reveals the structural changes due to

ethanol dissolution, as the characteristic peak for the $(PS_4)^{3-}$ tetrahedra at ~420 cm^{-1} is not present (**Figure 3.7**).

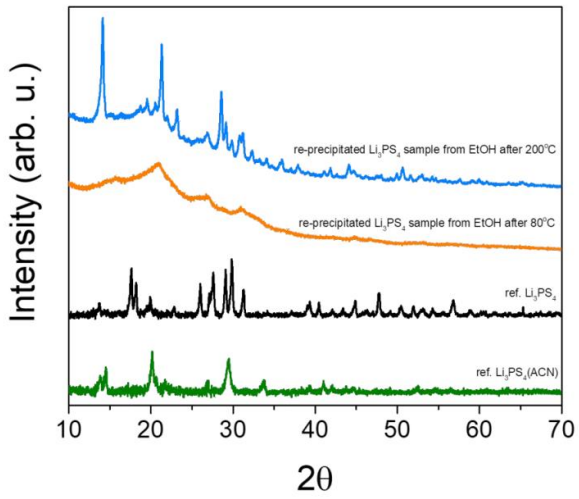

Figure 3.6. XRD patterns of re-precipitated Li_3PS_4 sample from ethanol that dried at 80 °C (unknown crystal structure) and was heated at 200 °C (amorphization). Reference patterns of Li_3PS_4 and $Li_3PS_4 \cdot (ACN)_2$

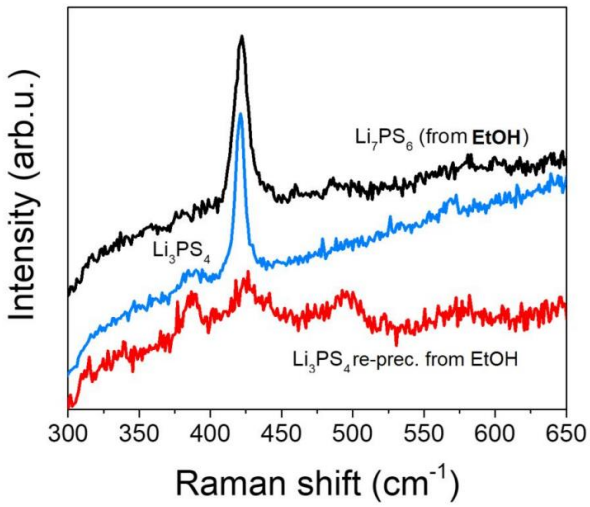

Figure 3.7. Raman spectra of liquid synthesized Li_7PS_6 from EtOH, re-precipitated Li_3PS_4 from EtOH, and Li_3PS_4 precursor.

3.3.3 Characterization of Li_6PS_5X (X = Cl, Br, I) from Liquid Approach

For Li_6PS_5X (where X=Cl, Br or I) synthesis, stoichiometric mixtures of Li_3PS_4, Li_2S and LiX (where X=Cl, Br or I) were dissolved in anhydrous ethanol, stirred, and heat treated at 200°C, yielding white powders for halide doped lithium argyrodites. As shown in XRD patterns (**Figure 3.8**), the as-synthesized final products were identified as Li_6PS_5Cl, Li_6PS_5Br, and Li_6PS_5I, corresponding to LiCl, LiBr and LiI reactants, respectively. Similar to pure Li_7PS_6, all halide-doped samples display sharp peaks at $2\theta \approx 25.5^o$, 30^o, 31.2^o, attributing to (220), (311), and (222) planes in cubic phase (space group *F-43m*), but with a slight peak shift due to the subtle change on unit cell parameters. **Table 3.1** displays the set of unit cell parameters, crystal sizes, and ionic radii of halide and sulfide anions for Li_7PS_6 and Li_6PS_5X materials.

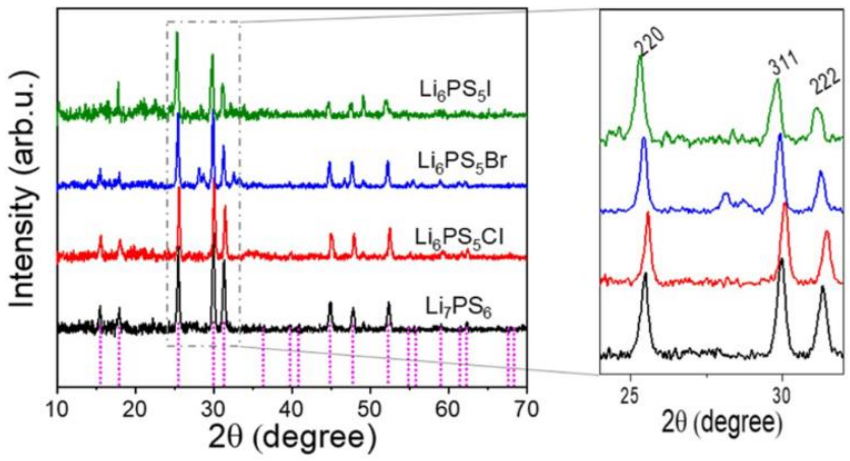

Figure 3.8. XRD patterns of Li_7PS_6 and Li_6PS_5X (X = Cl, Br, I) lithium argyrodites through liquid-based synthesis approach. Pink dash lines refer to standard diffraction peaks for Li_6PS_5X.

The lattice parameter *a* decreases from 9.88 Å for Li_7PS_6 to 9.84 Å for Li_6PS_5Cl and then increases to 9.89 Å for Li_6PS_5Br and 9.95 Å for Li_6PS_5I. This trend is consistent with the ion's radius variations, due to Cl^- (167 pm) < S^{2-}(170 pm) <Br^- (182 pm) <I^- (206 pm). Larger anions (Br^- and I^-) lead to the expansion of the lattice parameter in the cubic structure. This observation fits well with the trend of solid-state synthesized Li_6PS_5X materials.[124,143] In addition, due to the use of ethanol solvent to facilitate the chemical reactions, solvent-based synthesis of Li_6PS_5X samples needs only 2 hours, much shorter than solid-state approaches which not only require ball-milling for several hours,[124,155,153] but must also use longer heating/cooling processes for full crystallization.[124,155,131,133,56]

Table 3.1. The crystal structure parameters, ionic radius, Raman data of Li_7PS_6 and Li_6PS_5X lithium argyrodite samples.

Sample	Crystal size (nm)	Unite Cell Parameter (Å)	Ionic Radius (*p*m)	Raman Shift (cm^{-1})	FWHM (cm^{-1})
Li_7PS_6	34	9.88	(S^{2-}) 170	421.5	10.7
Li_6PS_5Cl	45	9.84	(Cl^-) 167	451.5/ 392.6	10.7/16
Li_6PS_5Br	39	9.89	(Br^-) 182	423.3/ 388.8	9/12
Li_6PS_5I	32	9.95	(I^-) 206	422.7/ 390.1	11.6/17

Raman spectra (**Figure 3.9**) of Li_6PS_5X samples (Li_6PS_5Cl, Li_6PS_5Br, and Li_6PS_5I), were collected and compared with that of pure Li_7PS_6. All three Li_6PS_5X samples show strong lines in the range of 422-425 cm^{-1} attributing to PS_4^{3-} ion vibration [60,137,154,156] and minor lines at about 390 cm^{-1}. These peak positions are consistent with previous Raman

data for Li_6PS_5X materials from solid-state reactions.[63,125,130,144,157] The exact line positions and their full width at half maximum (FWHM) values are given in **Table 3.1**. The Raman shift of PS_4^{3-} ion vibration decreases as the argyrodite unit cell increases. The minor line mode can correspond to a trace of $Li_4P_2S_6$ and its $P_2S_6^{4-}$ vibrational mode.[153,156]

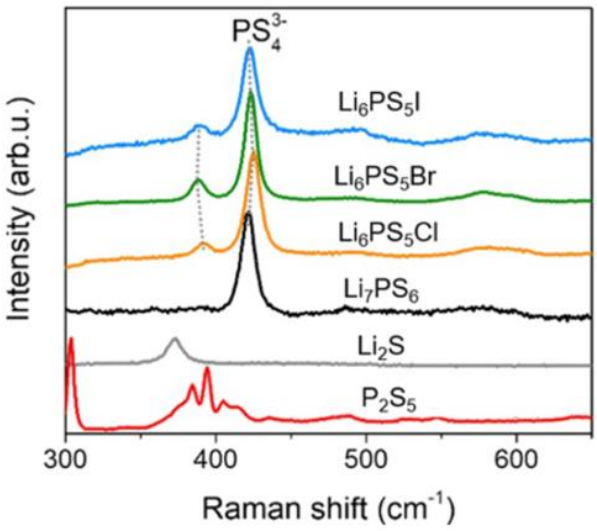

Figure 3.9. Raman patterns of Li_7PS_6 and Li_6PS_5X (X = Cl, Br, I) lithium argyrodites through liquid-based synthesis approach.

3.3.4 Morphological Evaluation of Synthesized Argyrodites

The different morphologies of the Li_3PS_4 precursor and Li_7PS_6 were analyzed using SEM (**Figure 3.10**). For the Li_3PS_4 sample prepared from ACN, an interesting flakelike morphology is observed (**Figure 3.10a**) which is in agreement with a previous report.[158] Solvent-synthesized Li_7PS_6 displays a granular morphology with individual particles of ~100 nm–1 μm in diameter (**Figure 3.10b**). This difference in morphology can be explained due to the unique interactions with the different solvents. For example, when Li_3PS_4 is dissolved in ethanol and reprecipitated, a similar granular morphology is observed (**Figure 3.11**). This changes in Li_3PS_4 morphology based on the solvent used is in line with

previous reports.[51,135,136] The EDX mappings of the Li_3PS_4 precursor and the Li_7PS_6 product are shown in **Figure 3.10c-f**. The homogenous distribution of the P and S atoms reveals the effectiveness of the solvent synthesis technique.

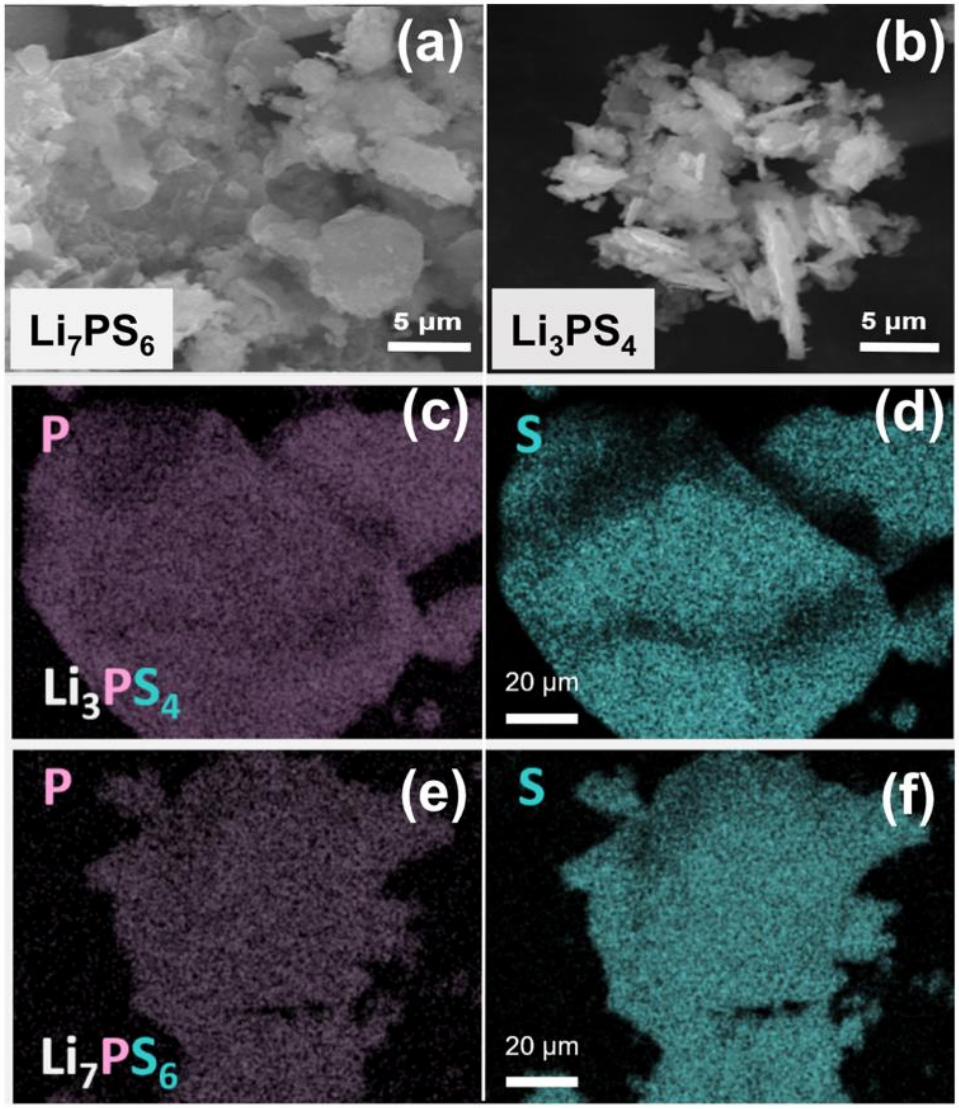

Figure 3.10. SEM images of (a) Li_7PS_6 product and (b) Li_3PS_4 precursor. EDX maps of P and S elements in (c), (d) liquid synthesized Li_7PS_6 product and (e), (f) Li_3PS_4 precursor. Both samples show elemental homogeneity.

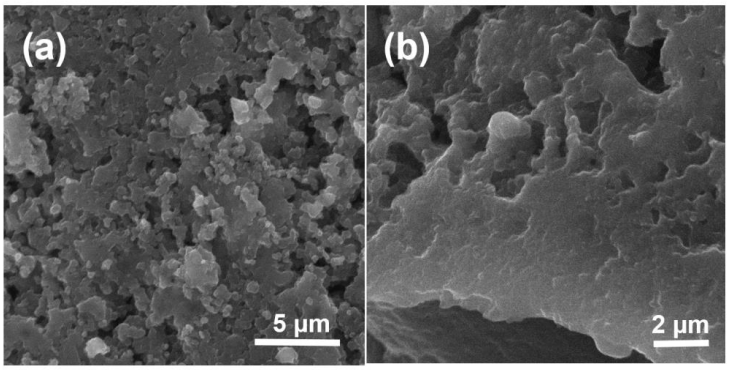

Figure 3.11. SEM images of Li_3PS_4 sample (a) after dissolution and (b) re-precipitation in ethanol. The morphology is different than the original Li_3PS_4 nanoflakes.

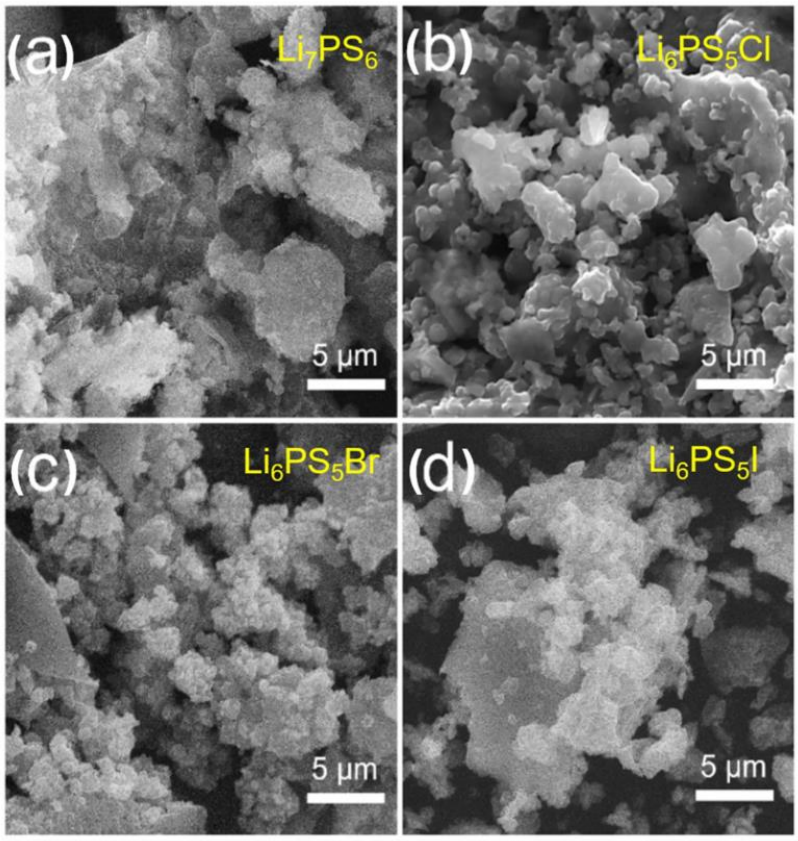

Figure 3.12. SEM images of (a) Li_7PS_6, (b) Li_6PS_5Cl, (c) Li_6PS_5Br, and (d) Li_6PS_5I electrolytes prepared from liquid-based synthesis.

For the halogen doped argyrodite materials, SEM images (**Figure 3.12**) display similar granular nanosized morphologies of Li_6PS_5X materials synthesized from the reactions of Li_3PS_4, Li_2S, and LiX in ethanol solvent (agglomerated particles of about 500 nm in size). In addition, EDX maps (**Figure 3.13**) show uniform distribution of P, S, and X (Cl, Br, and I) atoms, again suggesting the homogeneity of Li_6PS_5X materials from solvent-based synthesis method.

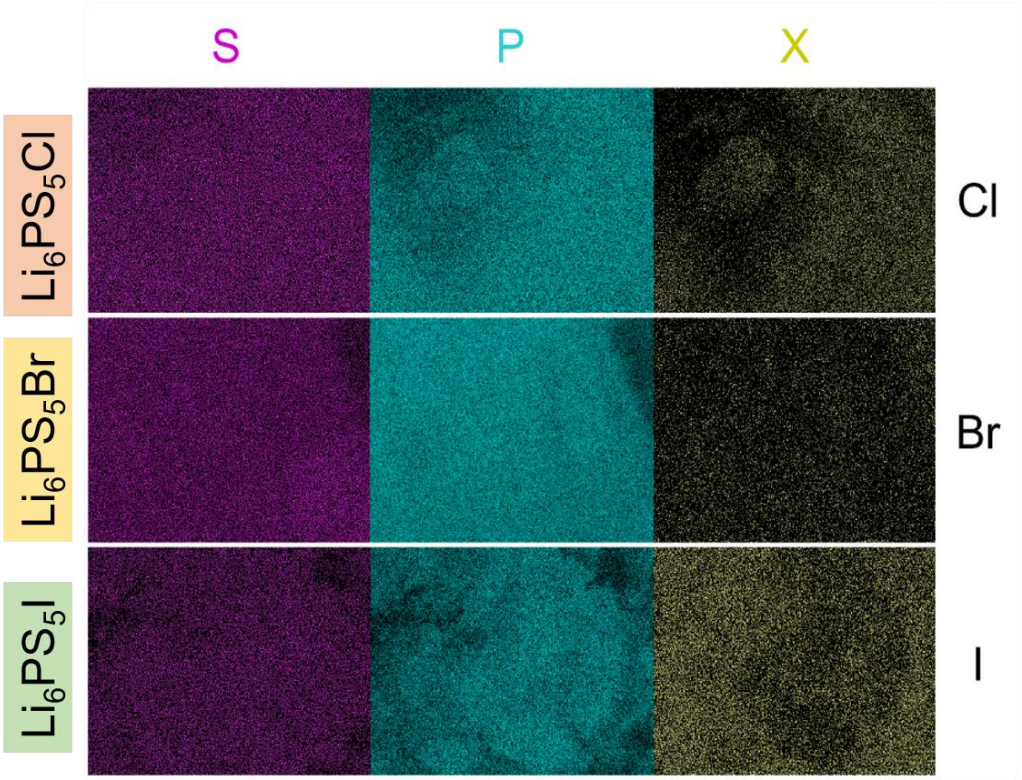

Figure 3.13. EDX maps of Li_6PS_5X (X=Cl, Br and I) electrolytes prepared form liquid-based synthesis indicating the elemental homogeneity of samples.

3.3.5 Ionic Conductivity and Electrochemical Stability Measurements

The ionic conductivity and activation energy of cubic Li_7PS_6 was determined using electronic impedance spectroscopy (EIS). For testing, the synthesized SE powder was cold pressed with Al/C foils on each side to form a dense pellet. It was found that solvent-synthesized Li_7PS_6 has an ionic conductivity of 0.11 mS cm^{-1} at room temperature (**Figure 3.14**). In addition, temperature dependent EIS tests were run to create Arrhenius plots. From these, the activation energy of Li_7PS_6 was determined to be 0.43 eV, close to the value of Li_3PS_4 (0.36 eV). This number is in line with values of Li_7PS_6 and Li_6PS_5Cl materials made using solid-state synthesis methods (0.3–0.48 eV).[146,147] Increasing temperatures also increases ionic conductivity, with this effect being more pronounced with Li_7PS_6 than Li_3PS_4. For example, at 90 °C Li_7PS_6 has an ionic conductivity of 1.5 × 10^{-3} S cm^{-1} compared with 1.0 × 10^{-3} S cm^{-1} for Li_3PS_4. This trend of lower ionic resistance can be observed in the Nyquist plots of Li_7PS_6 and β-Li_3PS_4 (**Figure 3.15**).

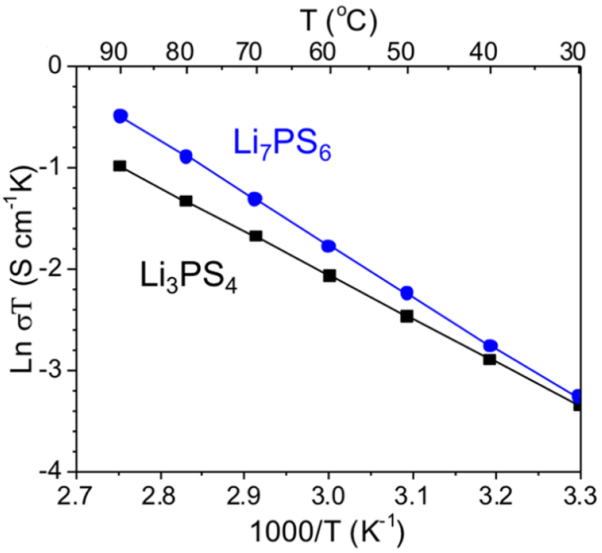

Figure 3.14. Arrhenius plots of Li_7PS_6 from ethanol and β-Li_3PS_4 from ACN (1.5 × 10^{-3} S cm^{-1} for Li_7PS_6 and 1 × 10^{-3} S cm^{-1} for Li_3PS_4 at 90 °C).

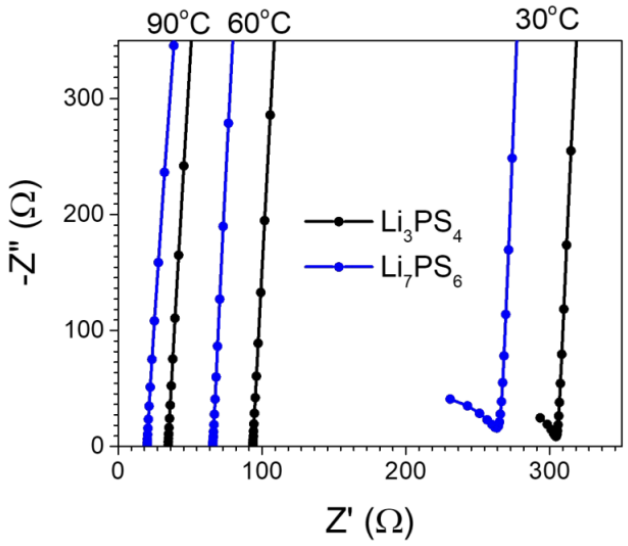

Figure 3.15. Nyquist plots of Li_7PS_6 product and β-Li_3PS_4 precursor under different temperatures (30 °C, 60 °C, and 90 °C).

The Li-ion conductivities of halogen-doped Li_6PS_5X (X= Cl, Br, and I) argyrodites were also evaluated through EIS measurements. The room temperature conductivities of Li_6PS_5Cl and Li_6PS_5Br materials are 0.34 mS cm^{-1} and 0.31 mS cm^{-1}, respectively, both of which are higher than that of pure Li_7PS_6 (0.11 mS cm^{-1}). The faster Li-ion mobility in Li_6PS_5Cl and Li_6PS_5Br is closely related to defects and lattice site disorders that resulted from the ion replacement of S^{2-} with Cl^- (or Br^-) [58,143] This observation is consistent with the trend for Li_6PS_5Cl and Li_6PS_5Br materials synthesised from high temperature (550 ºC) solid-state reactions [134,143,148]. Although the ionic conductivities of liquid-synthesized Li_6PS_5Cl and Li_6PS_5Br are relatively lower than those of solid-synthesized argyrodites, some recent reports (Nazar et al.[68] and Tatsumisago et al.[63]) had demonstrated that subsequent heat treatment at 550 °C after solvent-based synthesis could push the room temperature Li-ion conductivity of Li_6PS_5Cl (or Li_6PS_5Br) above 3 mS cm^{-1}. On the other

hand, solvent-synthesized Li_6PS_5I shows the worst ionic conductivity (0.029 mS cm^{-1}) at room temperature among all other lithium argyrodites (Li_7PS_6, Li_6PS_5Cl and Li_6PS_5Br), which is due to the ordering of the larger I- ion on the crystallographic sites in the argyrodite's structure [56,159].

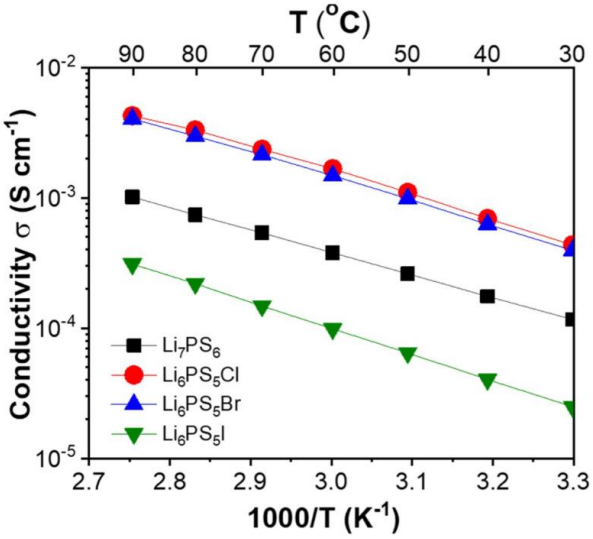

Figure 3.16 Arrhenius plots of solvent-based synthesized lithium argyrodites (Li_7PS_6, Li_6PS_5Cl, Li_6PS_5Br, Li_6PS_5I). Li_6PS_5Cl shows the best conductivity of 0.32 mS cm^{-1} at room temperature.

Figure 3.16 shows Arrhenius plots which reflect the temperature dependence of ionic conductivities for Li_6PS_5X (X=Cl, Br, I) samples and pristine Li_7PS_6. All materials show linear relations of ionic conductivity *vs* temperature, and the slopes are proportional to the activation energy (E_a) for Li-ion conduction according the equation: $\sigma = \sigma_0 e^{\frac{E_a}{RT}}$. The activation energies of Li_6PS_5Cl, Li_6PS_5Br, and Li_6PS_5I are estimated to be 38.57 kJ mol^{-1} (0.399 eV), 40.24 kJ mol^{-1} (0.417 eV), and 40.47 kJ mol^{-1} (0.419 eV), respectively, while the value for Li_7PS_6 is equal to 41.46 kJ mol^{-1} (0.430 eV). This comparison indicates that

introducing halide ions (X=Cl, Br, I) reduces the barrier for Li-ion mobility along the lattice framework and thus decreases the values of activation energy [58,143]. This trend is in good agreement with lithium argyrodites synthesized from solid-state reactions [124,143,144,159]. Among different halogen anions, Li_6PS_5Cl exhibits the lowest activation energy (0.399 eV) and the highest Li-ion conductivity (0.34 m Scm^{-1}).

3.3.6 Electrochemical Stability of Solvent Synthesized Argyrodites

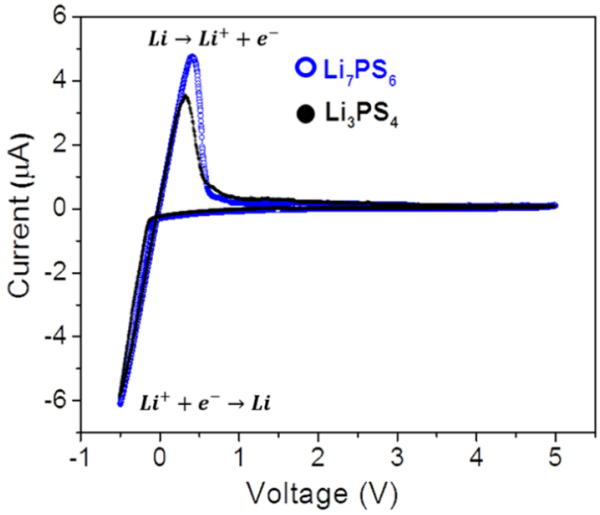

Figure 3.17. CV curves of Li_7PS_6 and β-Li_3PS_4 solid electrolytes with the metallic Li anode with the Li/SE/Pt cell (at a scan rate of 50 mV s^{-1} between −0.5 and 5 V vs Li^+/Li at room temperature).

Cyclic voltammogram (CV) was used to investigate the electrochemical stability between the solvent synthesized Li_7PS_6 and Li metal. A Li/Li_7PS_6/Pt cell was used, with Li serving as the reference electrode and Pt serving as the counter electrode. The potential was scanned from −0.5 to 5.0 V (vs Li^+/Li) at a scan rate of 50 mV s^{-1}. For both Li_7PS_6 and β-Li_3PS_4, a pair of reversible oxidation and reduction peaks is observed at around 0 V (vs Li+/Li) without any other side reactions (**Figure 3.17**). Below 0 V, the cathode current is

attributed to Li deposition on the working electrode ($Li^+ + e^- \rightarrow Li$). Likewise, above 0 V, the anode current is attributed to lithium dissolution.[124] The only observable difference between the two is the slightly higher anode current seen in Li_7PS_6. The lack of side reactions indicates that solvent synthesized Li_7PS_6 possesses a high degree of stability with Li metal over a wide electrochemical window (up to 5 V).

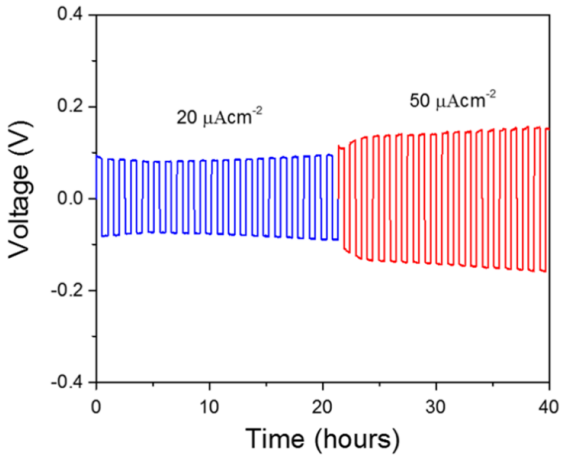

Figure 3.18. Cycling performance of the $Li/Li_7PS_6/Li$ symmetric cell (under current densities of 20 and 50 μA cm^{-2}).

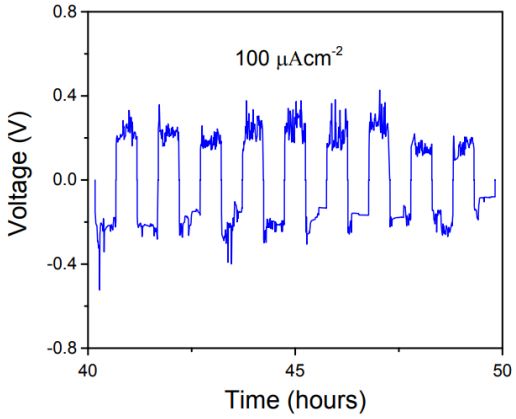

Figure 3.19. Cycling performance of $Li/Li_7PS_6/Li$ symmetric cell under current density of 100 μA cm^{-2}.

The long-term stability of Li_7PS_6 with Li metal was investigated through the testing of a Li/Li_7PS_6/Li symmetric cell under various current densities (20, 50, and 100 μA cm^{-2}) at room temperature. At a low current density of 20 and 50 μA cm^{-2}, the cell displays stable voltage profiles with low overpotential values (**Figure 3.18**). When this current density is increased to 100 μA cm^{-2}, rough curves and spikes begin to appear (**Figure 3.19**). This unstable profile suggests harmful interfacial reaction between the Li anode and the Li_7PS_6 solid electrolyte. To confirm, EIS measurements were taken both before and after cycling. A sharp increase in resistance is observed following symmetric cycling, confirming an unstable interface (**Figure 3.20**). Despite this, a clean Li surface was observed when the cell was disassembled. XRD was run after symmetric cell cycling, revealing that the Li_7PS_6 phase was well-maintained despite the obvious interfacial reactions.

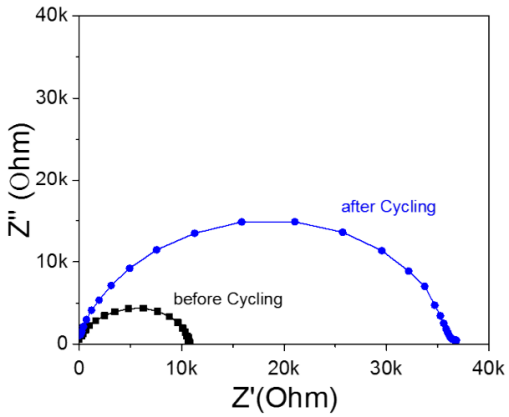

Figure 3.20. EIS comparison of the total impedance for the symmetric cell before and after cycling. After cycling, the impedance is observed to increase due to the interfacial reactions between Li_7PS_6 and Li anode the during the cycling.

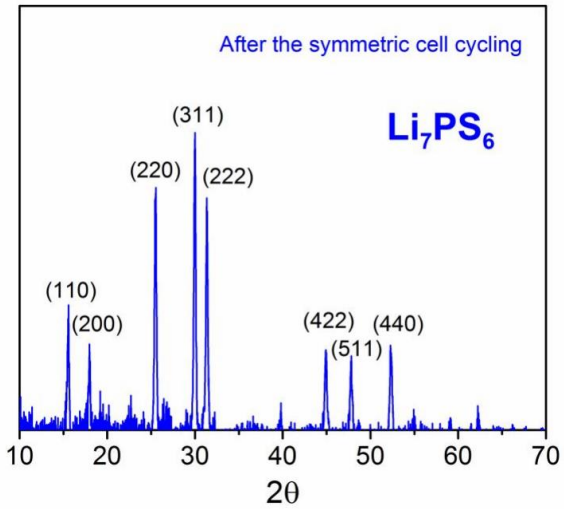

Figure 3.21. XRD patterns of Li_7PS_6 pellet after being cycled in a symmetric cell ($Li/Li_7PS_6/Li$).

Cyclic voltammetry (CV) was also employed to evaluate the electrochemical stability of halogen doped Li_6PS_5X (X=Br, Cl, I) materials against Li metal in a voltage window of 0.5-5.0 *vs* Li/Li^+ (**Figure 3.22**). The assembled cells have a $Li/Li_6PS_5X/SS$ structure, with Li as the reference/counter electrode and stainless steel (SS) as the working electrode. For all Li_6PS_5X (X=Br, Cl, I) materials, only one pair of oxidation and reduction peaks are observed near 0 V *vs* Li/Li^+, attributing to lithium dissolution ($Li \rightarrow Li^+ + e^-$) and lithium deposition ($Li^+ + e^- \rightarrow Li$), respectively. There is no other peak observed up to 5 V , suggesting good electrochemical stability of Li_6PS_5X (X=Br, Cl, I) solid electrolytes against Li metal.

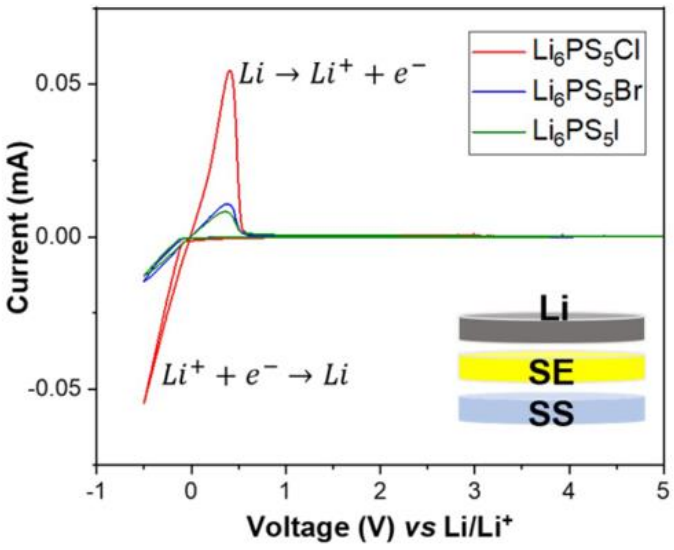

Figure 3.22. CV curves of solvent-synthesized Li_6PS_5X lithium argyrodites in the range of -0.5–5.0 V vs Li^+/Li

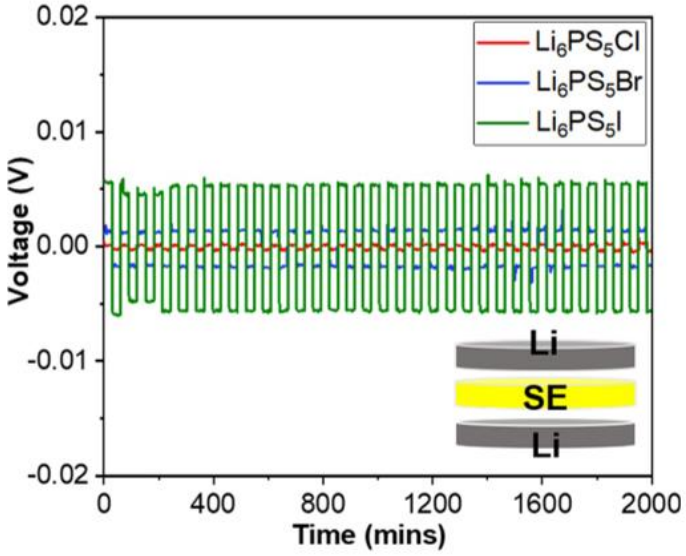

Figure 3.23. Cycling performance of lithium argyrodite symmetric cells under a current density of 0.02 ma cm^{-2}.

Symmetric cells with Li/Li_6PS_5X/Li structure were assembled to evaluate the long-term compatibility of liquid synthesized Li_6PS_5X with Li metal at room temperature. Smooth cycling profiles for these symmetric cells with Li_6PS_5X (X=Br, Cl, I) as solid electrolytes are observed in **Figure 3.23**. In Li/Li_6PS_5X/Li symmetric cells, Li_6PS_5Cl shows the lowest polarization. This is due to the formation of a buffer layer (consisting of Li_2S, Li_3PS_4 and LiCl) [149,160], which passivates the surface from unlimited interfacial reactions. For Li_6PS_5I, its increased polarization is resulted from its high bulk resistance and interface resistance.

3.4 Conclusions

We report a rapid and economic synthesis approach for crystalline Li_7PS_6 solid electrolyte through a stoichiometric reaction of Li_2S and Li_3PS_4 in ethanol medium. Li_7PS_6 has a room-temperature ionic conductivity of 0.11 ms cm^{-1} at room temperature and 1.5 mS cm^{-1} at 90 °C. Furthermore, it also shows good electrochemical compatibility with a metallic Li anode based on symmetric cell cycling performance. This new synthetic approach leads to high phase purity of the Li_7PS_6. Pure phase Li_6PS_5X (X = Cl, Br, I) was obtained through a stoichiometric reaction of LiX, Li_2S and Li_3PS_4 in ethanol solvent. In line with solid-state synthesized Li_6PS_5X materials, Li_6PS_5Cl argyrodite showed the highest room temperature ionic conductivity of 0.34 mS cm^{-1}, followed by Li_6PS_5Br and then Li_6PS_5I. The CV and symmetric cell cycling results indicated that solvent-synthesized, halide-doped lithium argyrodites (Li_6PS_5Cl, Li_6PS_5Br and Li_6PS_5I) had good electrochemical stability with Li metal. This solvent-based synthesis method used to produce Li_7PS_6 and halide doped Li_6PS_5X materials will further push forward Li-ion conducting argyrodites for use in future ASSBs.

CHAPTER 4

INVESTIGATION OF CONDUCTIVE PROPERTIES AND INTERFACE STABILITY OF LiCl-RICH ARGYRODITE Li_6PS_5Cl FOR HIGH-PERFORMANCE BATTERIES[119,161]

4.1 Introduction

Having successfully synthesized Li_7PS_6 and Li_6PS_5X argyrodites through a liquid-based approach, the next step was to test their feasibility as solid electrolytes in batteries. However, several serious issues must first be addressed before this is possible. (1) While sulfides have decent stability towards Li metal and cathodes, reactions will still occur. If these reactions are too serious, it will significantly hamper the practical applications in LMBs. (2) Solid-to-solid contact at the interface is a fundamental challenge in SSBs, and one that has yet to be overcome. Solid electrolytes will never form as complete of an interface as liquid electrolytes will, as they are unable to seep into the small interlayers of the electrodes. Microscopic gaps will exist between the SE and electrodes, greatly increasing interfacial resistance and hampering the performance of the battery.

The solid-to-solid interface problem has been addressed through several different routes in recent years. One possibility is the use of a polymer-ceramic composite material to improve the physical contact between the electrolyte and electrode.[106,162] This strategy will be explored further in a later chapter. A different approach that has been explored is to create an artificial buffer polymer layer that would serve as a bridge between the

electrode and electrolyte.[82,88] This step adds additional complexity to cell construction and creates additional contact interfaces which would be subject to chemical reactions.

Perhaps the most convenient approach would be to create a hybrid electrolyte which consists of both a solid and liquid component.[163,164] By adding trace amounts of liquid at the electrode/electrolyte interface, good interfacial contact can be achieved while the high safety and dendrite suppression abilities of solid electrolytes are maintained (**Figure 4.1**). Unfortunately, liquid electrolytes require expensive additives such as Li salts (e.g., LiTFSI, $LiPF_6$, $LiClO_4$) to create a stable interface, adding to materials cost and processing complexity. The solid electrolyte offers a more economic opportunity to incorporate these salts directly through the synthesis process.

It has been well documented that halogenated Li salts (LiX, X = F, Cl, Br, I) are an important part of a robust and stable SEI layer with a metal Li anode.[165–170] The solvent-based synthesis process detailed in Chapter 3 easily allows for the incorporation of Li salt directly into the solid electrolyte with a high degree of compositional control. The result is a LiX-rich Li_6PS_5X material with both excellent ionic conductivity and stabilization properties. The homogenous distribution of Li halide material can provide a stable and electronically insulative SEI without the need for additional processing or modification of liquid electrolyte.

In this chapter, an efficient and economic strategy for synthesizing LiCl-rich Li_6PS_5Cl (i.e., $Li_6PS_5Cl{\cdot}LiCl$) through a solvent-based process is detailed. Despite the ionically insulative properties of LiCl, it is found that doping with 1 mol of excess LiCl yields a SE material with a higher ionic conductivity (0.53 mS cm^{-1}) than pure phase Li_6PS_5Cl. Moreover, the addition of pure LiCl is utilized at the electrode/electrolyte

interface to create a stable SEI layer with Li metal with dendrite suppressing abilities. Full battery $Li_4Ti_5O_{12}$| Li_6PS_5Cl·LiCl|Li cells with trace amounts of propylene carbonate (PC) liquid electrolyte at the interface displayed a higher specific capacity (135 mAh g^{-}) than the cell made with pure Li_6PS_5Cl (110 mAh g^{-}) at 0.2 C. This cell also showed excellent cycling stability over 1000 h, and an impressive specific capacity (116 mAh g^{-}) at 1C over 200 cycles. These results indicate that LiCl-rich Li_6PS_5Cl is an excellent approach to address interface instability issues in SSBs.

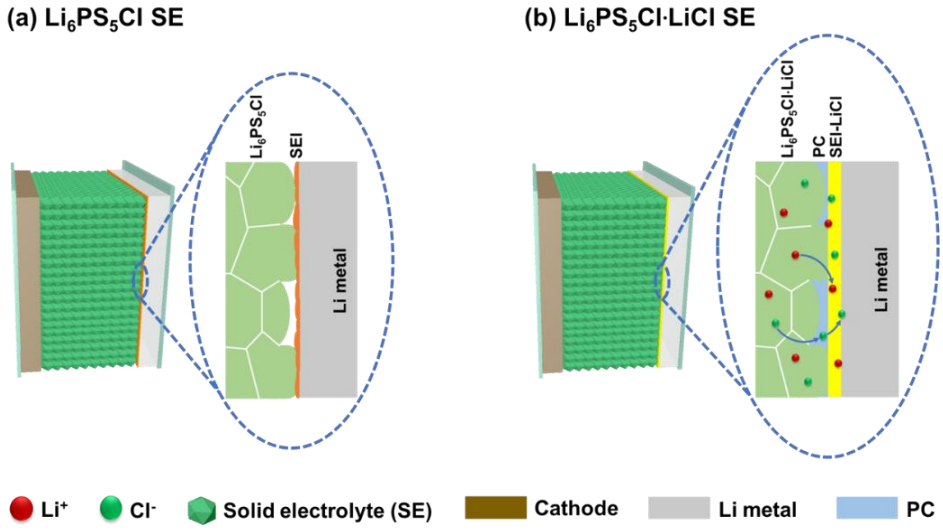

Figure 4.1. Schematic diagram of batteries with (a) Li_6PS_5Cl SE, and (b) Li_6PS_5Cl·LiCl SE with PC at interface.

4.2. Experimental Section

4.2.1 Materials Synthesis

Li_6PS_5Cl·xLiCl materials were synthesized through the same solvent process outlined in Chapter 3. After obtaining Li_3PS_4, a stoichiometric mixture of Li_2S, Li_3PS_4 and LiCl was fully dissolved in a small quantity of anhydrous ethanol in argon atmosphere. Afterwards, the solvent was evaporated at 90°C under vacuum (1 hour) to obtain a white

precipitate before heat treating at 200 °C (1 hour) to produce the final product. Ratios of LiCl:Li_3PS_4 were controlled at 1:1, 1.5:1, 2:1, 2.5:1, and 3:1 to obtain the samples of Li_6PS_5Cl, Li_6PS_5Cl·0.5LiCl, Li_6PS_5Cl·LiCl, Li_6PS_5Cl·1.5LiCl and Li_6PS_5Cl·2LiCl, respectively.

$$(x+1)LiCl + Li_3PS_4 + Li_2S \rightarrow Li_6PS_5Cl \cdot xLiCl \quad \textbf{Eq. 4.1}$$

The phase composition and crystal structure were examined using X-ray diffraction (Bruker D8 Discover) with nickel-filtered Cu-Kα radiation (λ = 1.5418 Å). The crystallite size was analysed using the Scherrer equation. The Raman spectra were collected by Renishaw in Via Raman/PL Microscope with a 632.8 nm emission line of a HeNe laser. TESCAN Vega3 scanning electron microscope (SEM) was used to study the morphology of samples. All electrochemical testing was performed using the same techniques outlined in Chapter 3.

4.2.2 Construction of LTO/Li cells with lithium argyrodite solid electrolyte

The battery performance of the solid electrolyte was tested with $Li_4Ti_5O_{12}$ (LTO)/Li cells. To prepare the electrode, LTO nanopowder, PVDF and Super P (80:10:10 in weight ratio) were mixed in N-methylpyrrolidone (NMP) to form a homogeneous slurry which was subsequently coated on aluminum foil. The prepared electrodes, with an active material loading of around 2.0–3.0 mg cm^{-2}, were dried at 80 °C for 24 h under vacuum prior to use. Thin Li foil (~120 µm) was used as the anode. The solid electrolyte (Li_6PS_5Cl or Li_6PS_5Cl-LiCl) powder was cold-pressed to dense pellets with a thickness of around 600 µm and ½ inch diameter. Prior to electrochemical tests, trace amount of propylene carbonate was added at both sides of the SE pellet. Charge and discharge tests were performed from 1.0–3.0 V with 2032 coin cell after the cells were rested for 8 h.

4.3 Results and Discussion

4.3.1 Excess Cl content effect on LiCl rich lithium argyrodites (Li_6PS_5Cl·xLiCl)

Because Li_6PS_5Cl exhibits the highest ionic conductivity amongst three halogen ions, it was selected to study the effect of excess Cl content on the crystal structure, ionic conductivity, and electrochemical stability of LiCl rich argyrodites Li_6PS_5Cl·xLiCl ($0 \leq x \leq 2$).

4.3.2 XRD and Raman spectra of Li_6PS_5Cl argyrodites with excess Cl content

To synthesize Li_6PS_5Cl lithium argyrodites with excess Cl content, excess amount of LiCl precursor was added during the solvent-based synthesis process. The molar ratio of LiCl: Li_3PS_4 (or Li_2S) was tuned to produce Li_6PS_5Cl·xLiCl ($0 \leq x \leq 2$) materials. **Figure 4.2** displays both the XRD patterns of Li_6PS_5Cl·xLiCl materials containing different amounts of Cl content as well as pure Li_7PS_6 without any Cl doping. Pure Li_7PS_6 exhibits characteristic diffraction peaks at 2θ=25.5, 30, 31.2º, corresponding to (220), (311) and (222) planes, respectively.

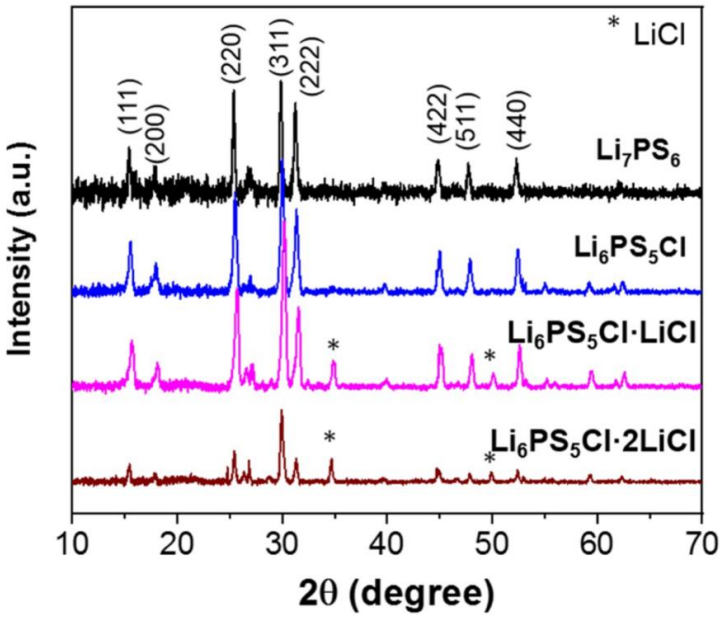

Figure 4.2. XRD patterns of solvent-synthesized lithium argyrodites containing different Cl content (Li_7PS_6, Li_6PS_5Cl, $Li_6PS_5Cl{\cdot}LiCl$, and $Li_6PS_5Cl{\cdot}2LiCl$)

When Cl is initially introduced, Li_6PS_5Cl has almost identical diffraction patterns to those of Li_7PS_6, suggesting the formation of a solid solution where Cl^- replaces S^{2-}. This observation is consistent with previous reports of solid-state synthesized Li_6PS_5Cl materials.[56,144] As Cl content is increased, a secondary phase of LiCl (2θ=34.9°, 49.9°) is observed in addition to the dominant phase of Li_6PS_5Cl, and peak intensity continually increases with increasing LiCl. This observation indicates that the excess Cl cannot properly enter the Li_6PS_5Cl structure at highly doped samples; instead, heterogeneous composite electrolytes of $Li_6PS_5Cl{\cdot}xLiCl$ are formed from the solvent-based synthesis method. Recently, Adeli et al. used solid-state reactions to synthesize argyrodites from the $Li_{6-x}PS_{5-x}Cl_{1+x}$ family and found that $Li_{5.5}PS_{4.5}Cl_{1.5}$ was the limit for Cl doping in the argyrodite structure, with a significant LiCl phase presenting itself when additional chlorine is added into the structure.[76] Yu et al. also reported to have obtained $Li_{5.5}PS_{4.5}Cl_{1.5}$

without the observation of LiCl.[171] The ball milling process may contribute to high Cl doping content in Li_6PS_5Cl structure.

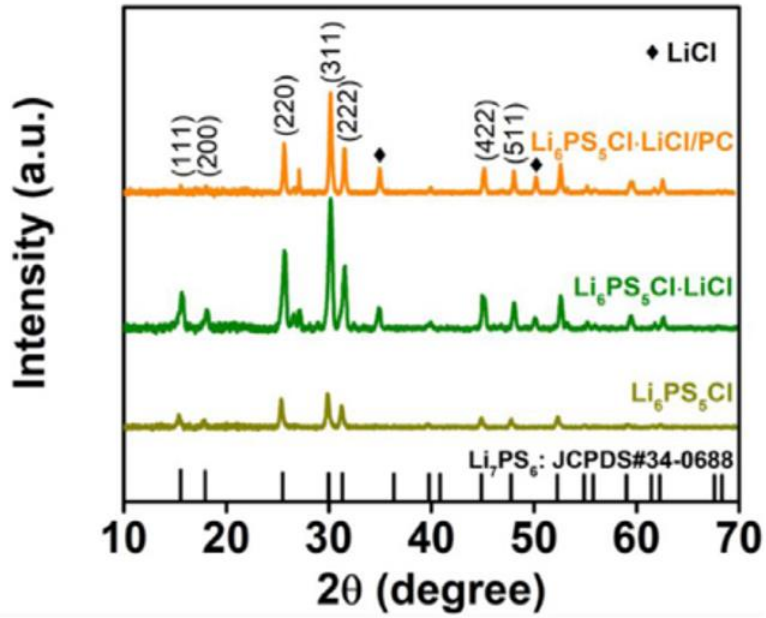

Figure 4.3. XRD patterns of Li_6PS_5Cl, $Li_6PS_5Cl{\cdot}LiCl$ and $Li_6PS_5Cl{\cdot}LiCl$/PC

In this study, the effects of PC liquid electrolyte with $Li_6PS_5Cl{\cdot}LiCl$ were also investigated. **Figure 4.3** shows XRD patterns of Li_6PS_5Cl, $Li_6PS_5Cl{\cdot}LiCl$ and $Li_6PS_5Cl{\cdot}LiCl$/PC. The main diffraction peaks of $Li_6PS_5Cl{\cdot}LiCl$ are maintained and no additional peaks are present. This indicates the structural stability of $Li_6PS_5Cl{\cdot}LiCl$ with PC liquid electrolyte. In addition, $Li_6PS_5Cl{\cdot}LiCl$ pellets were soaked in PC to further

explore the chemical stability between them. After three weeks, the pellets remained dense and there were no observable color changes (**Figure 4.4**).

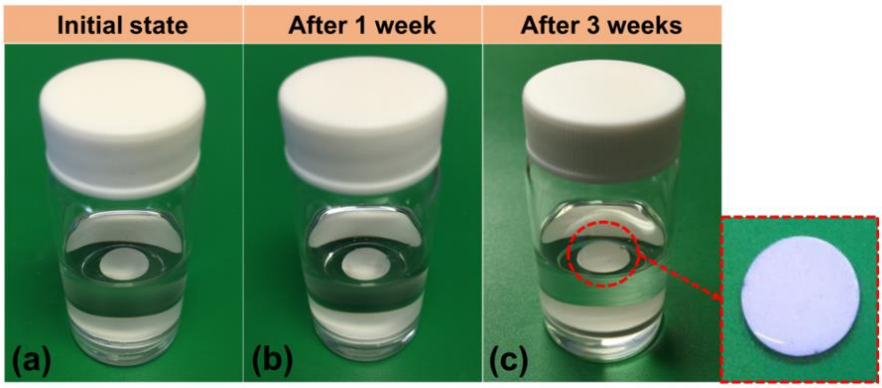

Figure 4.4. Photos of $Li_6PS_5Cl \cdot LiCl$ pellet in PC at the (a) initial state, (b) after 1 week and (c) after 3 weeks.

Raman spectra of Li_7PS_6, Li_6PS_5Cl, $Li_6PS_5Cl \cdot xLiCl$ (x=1, 2) mateirals are shown in **Figure 4.5**. All samples show a strong peak at 421-425 cm^{-1}, corresponding to the symmetric stretching mode of the P-S bond in the $(PS_4)^{3-}$ vibrational mode. This peak is the primary vibrational mode for argyrodite-type solid electrolytes from solid-state synthesis in previous reports [43,130,132]. Additionally, Li_6PS_5Cl and $Li_6PS_5Cl \cdot xLiCl$ (x=1, 2) samples also exhibit a weak and broad bump around 575 cm^{-1}, which is attributed to the asymmetric PS_4^{3-} vibrational mode.

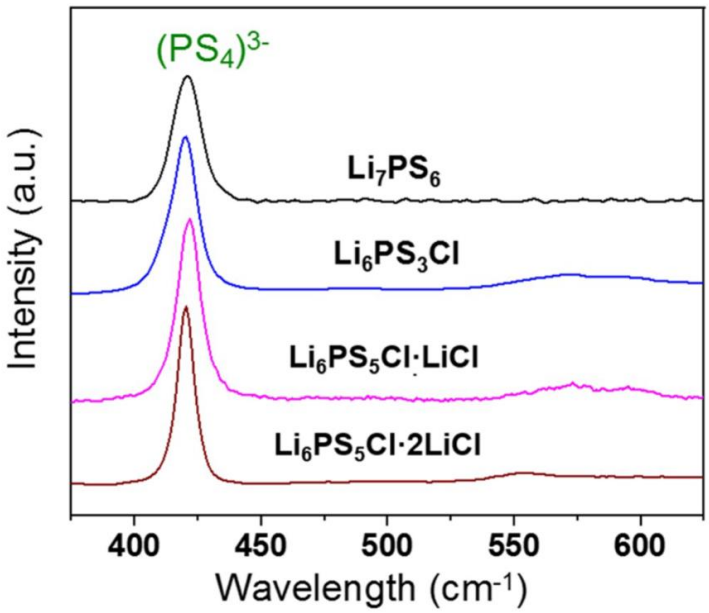

Figure 4.5. Raman spectra of solvent-synthesized lithium argyrodites containing different Cl content (Li_7PS_6, Li_6PS_5Cl, $Li_6PS_5Cl{\cdot}LiCl$, and $Li_6PS_5Cl{\cdot}2LiCl$)

The morphologies of LiCl-rich argyrodites were examined using SEM. SEM images (**Figure 4.6**) of all Li_6PS_5Cl and $Li_6PS_5Cl{\cdot}xLiCl$ (x=1, 2) materials exhibit similar granular morphologies, similar to those seen from undoped Li_7PS_6 (**Figure 4.7**). $Li_6PS_5Cl{\cdot}LiCl$ powder was pressed into a pellet for additional observations. SEM images of the SE pellet confirms a smooth surface with no visable cracks, and a thickness of ~600 μm (**Figure 4.7a and 4.7b**). When PC liquid elecrotlyte is added to the surface of the $Li_6PS_5Cl{\cdot}LiCl$ pellet, small bulges appear as a result of physical reactions between the solid and liquid (**Figure 4.7c and 4.7d**). EDS scans confirm that the $Li_6PS_5Cl{\cdot}LiCl$ phase is not affected by the addition of PC (**Figure 4.7e**).

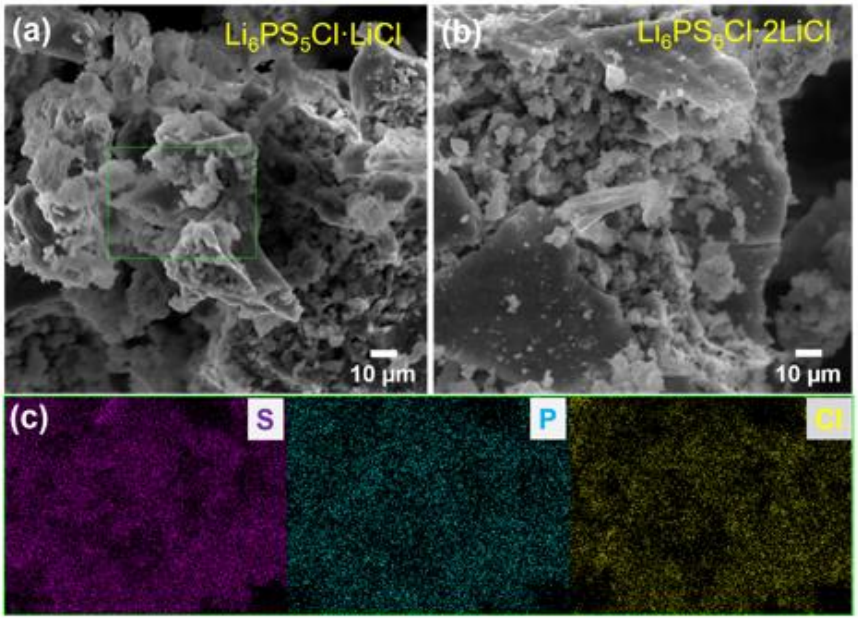

Figure 4.6. SEM images and EDX mapping of lithium argyrodites with excess Cl content: (a) and (c) $Li_6PS_5Cl·LiCl$; (b) $Li_6PS_5Cl·2LiCl$.

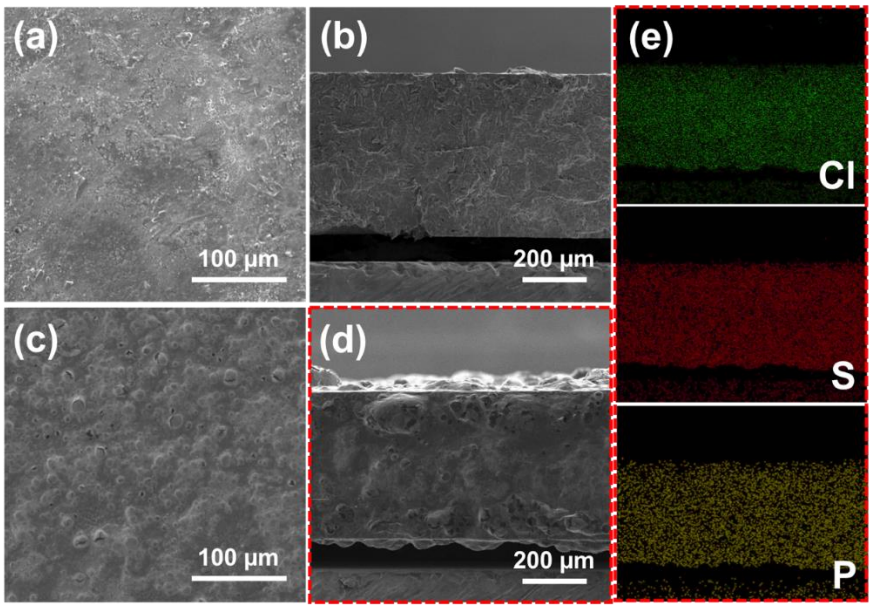

Figure 4.7. SEM images of top surface and cross-section for $Li_6PS_5Cl·LiCl$ SE (a,b) and $Li_6PS_5Cl·LiCl$/PC SE (c,d). (e) EDS mappings of P, S and Cl distributions for the $Li_6PS_5Cl·LiCl$/PC pellet.

4.3.3 Li-ion conductivity of LiCl rich lithium argyrodites

The Li-ion conductivities of lithium argyrodites containing different Cl content were evaluated by EIS measurements. **Figure 4.8** presents the Arrhenius plots of Li_7PS_6 and $Li_6PS_5Cl{\cdot}xLiCl$ (x=0, 0.5, 1, 1.5, and 2). The conductivities of all samples increase linearly with increasing temperatures, and the slopes reflect the activation energy barriers for Li-ion diffusion across the crystalline framework.

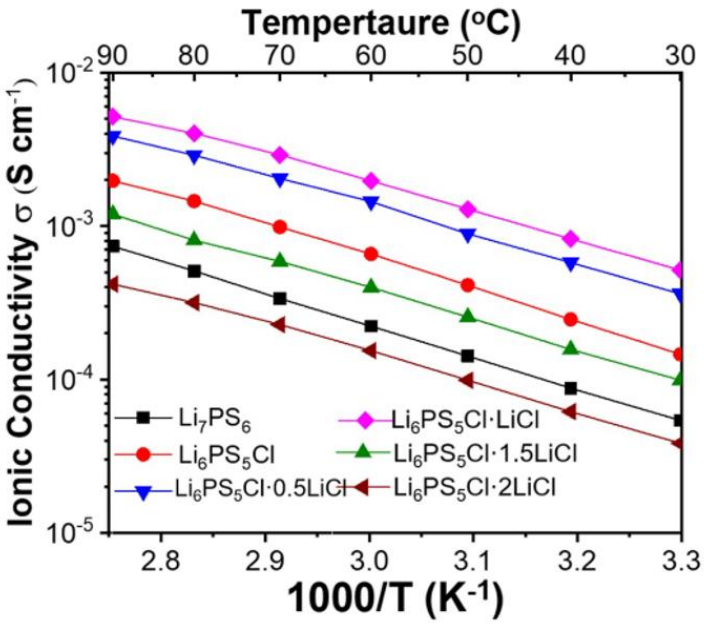

Figure 4.8. Arrhenius plots of solvent-synthesized lithium argyrodites (Li_7PS_6 and $Li_6PS_5Cl{\cdot}xLiCl$ with x = 0, 0.5, 1, 1.5 and 2)

The compositional dependence between conductivities and activation energies for $Li_6PS_5Cl{\cdot}xLiCl$ ($0 \leq x \leq 2$) materials is shown in **Figure 4.9**. As Cl content increases, the room temperature ionic conductivity increases from 0.34 mS cm^{-1} for Li_6PS_5Cl to the highest value of 0.53 mS cm^{-1} for $Li_6PS_5Cl{\cdot}LiCl$ and then decreases beyond it. The increased ionic conductvity in $Li_6PS_5Cl{\cdot}LiCl$ is likely not related to additional defects

created by the replacement of S^{2-} with Cl^- because XRD patterns show that excess Cl didn't enter the argyrodite's structure (**Figure 4.2**). Instead, it is possibly a result of the space-charge effect, which explains the enhanced conductivity of composites due to the formation of charged surface (i.e. Li_3PS_4-LZNO, Li_3PS_4-garnet).[172–175]

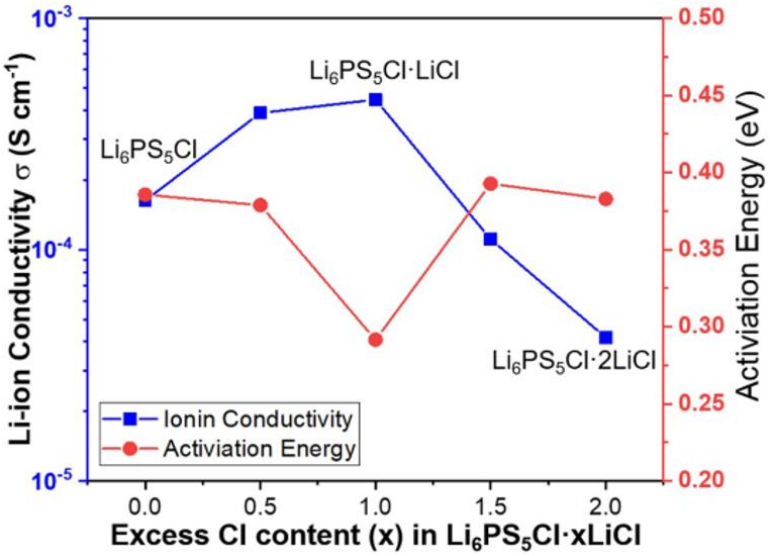

Figure 4.9. Composition dependence of room temperature conductivities and activation energies for lithium argyrodites with excess Cl content.

The little excess amount of LiCl may cause less resistance for the charged particles, which leads to enhanced Li-ion conductivity for the parent electrolyte (Li_6PS_5Cl). However, when the LiCl content is high enough, it will impede the forward motion of Li-ions since LiCl displays a worse room temperature conductivity (10^{-7} S cm^{-1}) than Li_6PS_5Cl. The activation energy data (**Figure 4.9**) collected from Arrhenius plots for Li_6PS_5Cl·xLiCl samples shows a slight fluctuation depending on the composition. Notably, Li_6PS_5Cl·LiCl exhibits the lowest activation energy of 0.29 eV, in comparison with 0.39 eV for Li_6PS_5Cl. The Nyquist plots (**Figure 4.10**) of lithium argyrodites with different Cl content consist of a semicircle

at higher frequency (R_t, total resistance) and a spike at lower frequency (Li-diffusion resistance from blocking electrode). Because the influence of grain boundary resistance for sulfides is significantly lower than it is for oxides, the resistance difference between Li_6PS_5Cl and $Li_6PS_5Cl{\cdot}LiCl$ is considered to originate from the intragranular resistance, that is, from the bulk material.[176]The addition of PC predictably has a positive influence on conductivity as well, and this effect is maintained with increasing temperatures.

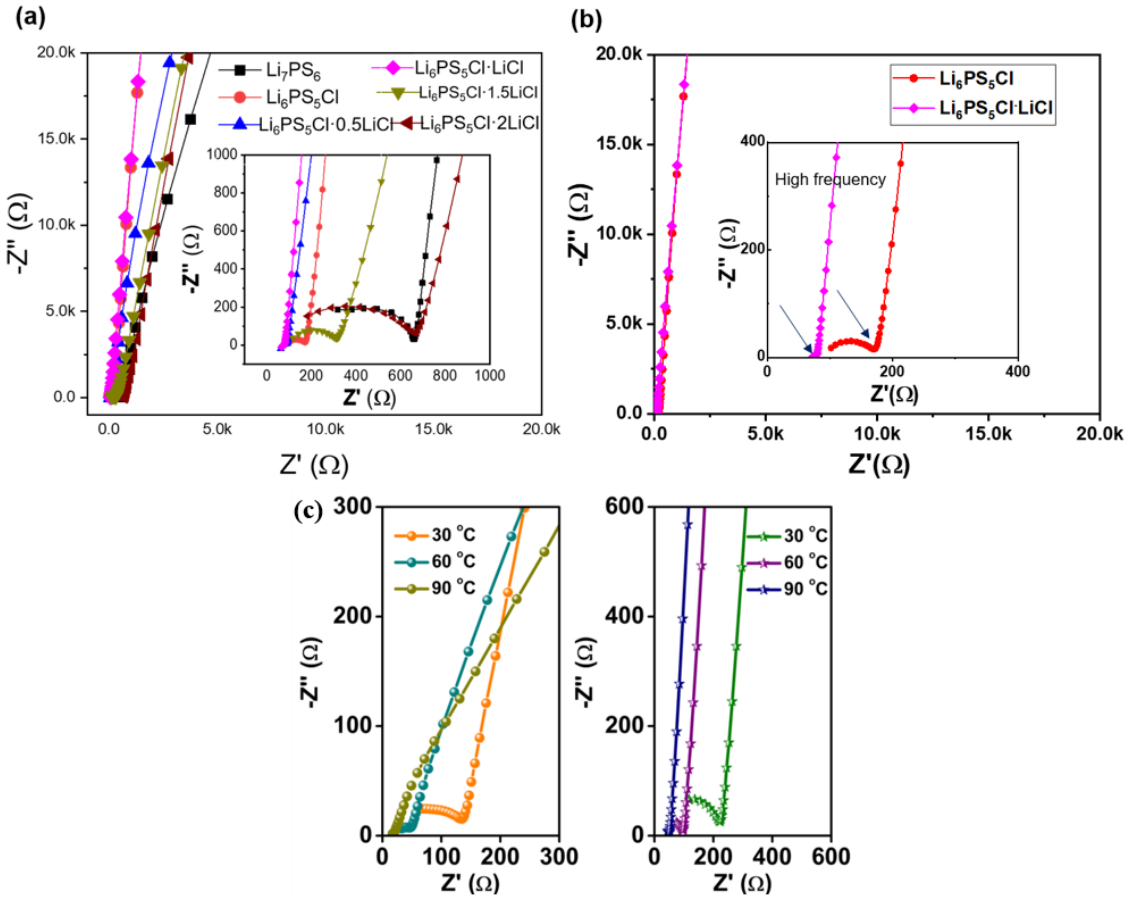

Figure 4.10. Nyquist plots of (a) lithium argyrodites with different Cl content Li_7PS_6 and $Li_6PS_5Cl{\cdot}xLiCl$ (x=0, 0.5, 1, 1.5, 2) at room temperature; and (b) comparison between Nyquist plots of Li_6PS_5Cl and $Li_6PS_5Cl{\cdot}LiCl$. (c) Nyquist plots of $Li_6PS_5Cl{\cdot}LiCl$/PC (left) and Li_6PS_5Cl /PC (right) at temperatures of 30, 60, and 90 °C.

4.3.4 Excess Cl content effect on electrochemical stability of lithium argyrodites

The electrochemical stability of Li_6PS_5Cl and $Li_6PS_5Cl{\cdot}LiCl$ samples against Li metal was evaluated. **Figure 4.11** shows the CV scanning curves collected in $Li/Li_6PS_5Cl{\cdot}xLiCl/SS$ cells up to 5V. There is only a pair of oxidation (Li dissolution, $Li \rightarrow Li^+ + e^-$) and reduction (Li deposition, $Li^+ + e^- \rightarrow Li$) peaks near 0 V *vs* Li/Li^+ without other side reactions, indicating good electrochemical stability with a Li anode. $Li_6PS_5Cl{\cdot}LiCl$ shows the highest values of anodic/cathodic current.

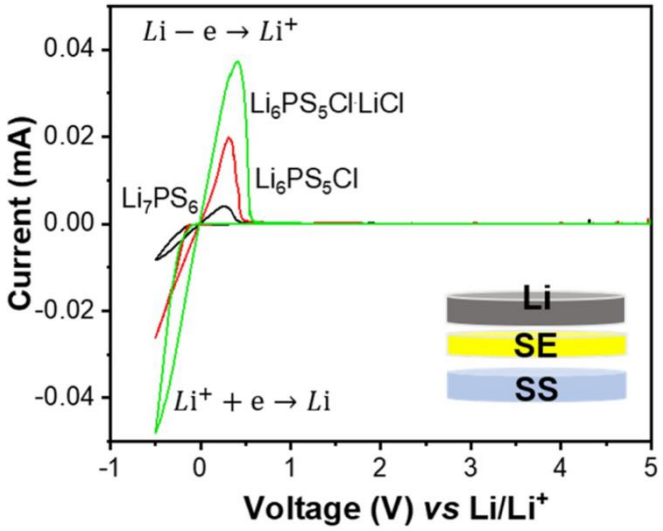

Figure 4.11. Electrochemical stability tests of Li_7PS_6, Li_6PS_5Cl, and $Li_6PS_5Cl{\cdot}LiCl$ SEs.

In addition, symmetric cells of $Li/Li_6PS_5Cl{\cdot}xLiCl/Li$ were assembled to study long-term compatibility against Li metal. **Figure 4.12** displays smooth voltage profiles for three solid electrolytes (Li_7PS_6, Li_6PS_5Cl and $Li_6PS_5Cl{\cdot}LiCl$) under a constant current density of 0.02 mA cm^{-1}, suggesting good cyclability of these solid electrolytes in symmetric cells. Among the three solid electrolytes, $Li_6PS_5Cl{\cdot}LiCl$ exhibits the lowest polarization.

Symmetric cell cycling was also applied to $Li_6PS_5Cl{\cdot}LiCl/PC$ cells under different current densities of 0.1, 0.2, 0.5, 0.8 and 1.0 mA cm^{-2} (**Figure 4.13**). As current density is

increased, the polarization effect causes the voltage values to increase as well. Across all current densities, the voltage profile remained stable with no indication of polarization amplification, even up to 1.0 mA cm^{-2}. This suggests that PC at the interface promotes cycling stability and hinders dendrite formation even at high current densities.

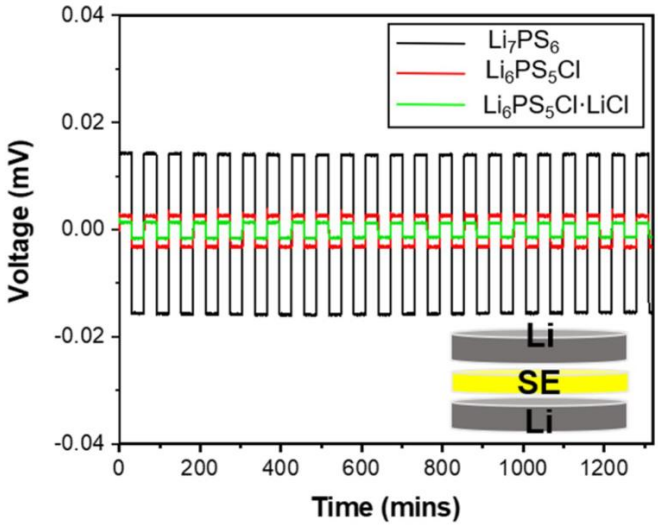

Figure 4.12. Symmetric cells cycling voltage profiles under 0.02 mA cm^{-2}.

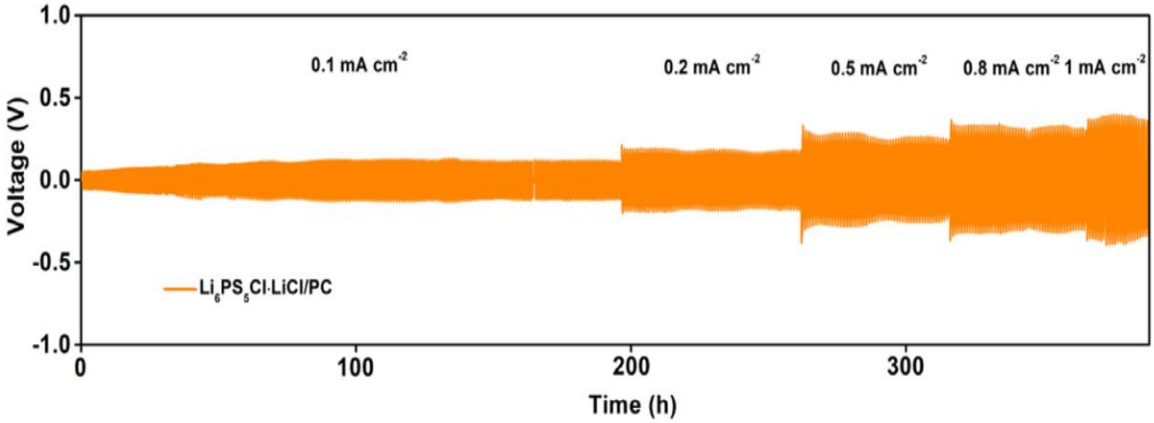

Figure 4.13. Symmetric Li cell with $Li_6PS_5Cl \cdot LiCl$/PC cycled at various current densities of 0.1, 0.2, 0.5, 0.8 and 1.0 mA cm^{-2}.

4.3.5 Excess Cl content effect on battery performance of LTO/Li cells with lithium argyrodites

Solid-state $Li/Li_4Ti_5O_{12}$ (LTO) batteries were assembled with Li_6PS_5Cl and $Li_6PS_5Cl{\cdot}LiCl$ as the solid electrolyte, respectively. Trace amounts (<15 μL) of PC were added at the interface between the electrodes and electrolyte. **Figure 4.14** displays the cycling performance of Li/LTO cells at 0.2C within a voltage range of 1-3V. In comparison, the cell with LiCl rich SE shows a higher specific capacity (135 mAh g^{-1}) than Li_6PS_5Cl-based cell (110 mAh g^{-1}) after 50 cycles of charge/discharge, suggesting the positive role of excess Cl on the enhancement of electrochemical property. The presence of lithium halide (i.e. LiCl) at interface has been reported to stabilize SE/electrode interface and block side reactions.[166,177,178] Thus, the better cycling performance is considered to be related to the formation of a more stable solid electrolyte interphase (SEI) layer due to the excess amount of Cl.

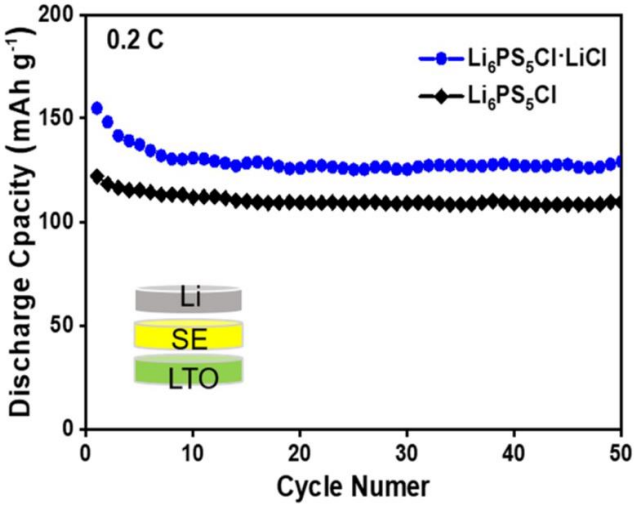

Figure 4.14. Comparison of battery cycling performance of Li/LTO cells with $Li_6PS_5Cl{\cdot}LiCl$ and Li_6PS_5Cl as the solid electrolyte under 0.2 C.

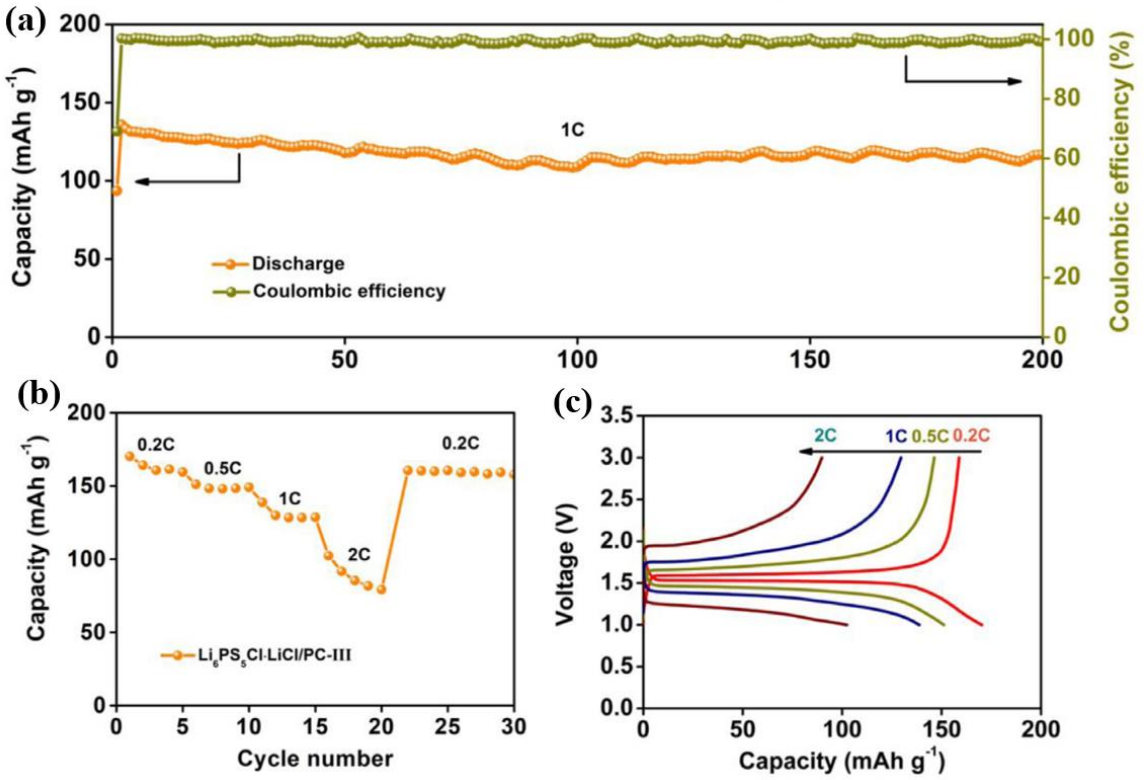

Figure 4.15. (a) Cycling performance and Coulombic efficiency of the LTO/Li cell with Li_6PS_5Cl·LiCl/PC-III SE at 1 C. (b) Rate capabilities at 0.2 C, 0.5 C, 1 C and 2 C. (c) Charge/discharge curves of the LTO/Li cell with the Li_6PS_5Cl·LiCl/PC-III SE at various rates.

The Li_6PS_5Cl·LiCl/PC battery also shows excellent performance at higher C-rates. When the LTO| Li_6PS_5Cl·LiCl/PC|Li cell is cycled at 1C, it displays an impressive specific capacity of 116 mAh g^{-}, with a coulombic efficiency of ~99.9% for over 200 cycles (**Figure 4.15a**). The high stability at high charge rates is shown in C-rate testing where the battery performance was observed at increasing current rates of 0.2C, 0.5C, 1C, and 2C (**Figure 4.15b and 4.15c**). Even at 2C, the cell shows good cycling performance with a capacity of 80 mAh g^{-1}. Moreover, when the current rate is returned to 0.2C, the cell was able to

recover its original capacity and continue cycling, indicating minimal reactions or dendrite formation at high C-rates. Once again, this excellent performance is attributed to the synergistic effect of the LiCl and PC at the interface which forms a stable SEI layer.

After cycling, the LTO|Li_6PS_5Cl·LiCl/PC|Li cell was disassembled, and the surface of the SE was analyzed using SEM and XPS. After 200 cycles at 1C, the cell morphology of the PC-wetted SE indicates that the surface remains smooth, with no obvious cracks appearing (**Figure 4.16**). SEI interfacial reactions were investigated by analyzing the S 2p, C 1s, and O 1s spectra via XPS (**Figure 4.17**). The S 2p spectrum reveals virtually no change before and after cycling, indicating that typically expected decomposition products such as Li_2S were prevented from forming due to the presence of an SEI layer. For the C 1s spectrum, a new peak appears after cycling at 290.2 eV which is attributed to CO_3^{2-} from a reaction of PC with Li metal to form Li_2CO_3. This result is further confirmed through the O 1s spectrum. This indicates that the SEI layer which is formed in the LTO|Li_6PS_5Cl·LiCl/PC|Li cell is a combination of LiCl salt and organic compounds formed from between SE and Li metal.

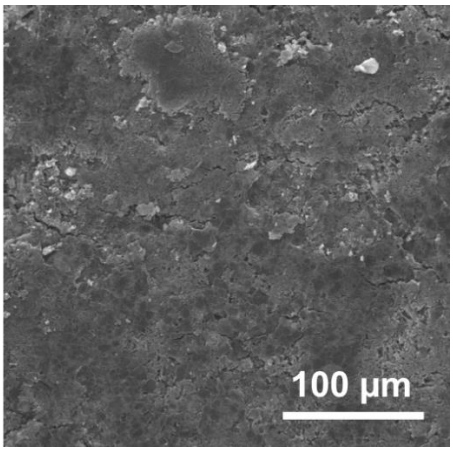

Figure 4.16. SEM image of Li_6PS_5Cl·LiCl/PC pellet surface in LTO/Li cell after cycling.

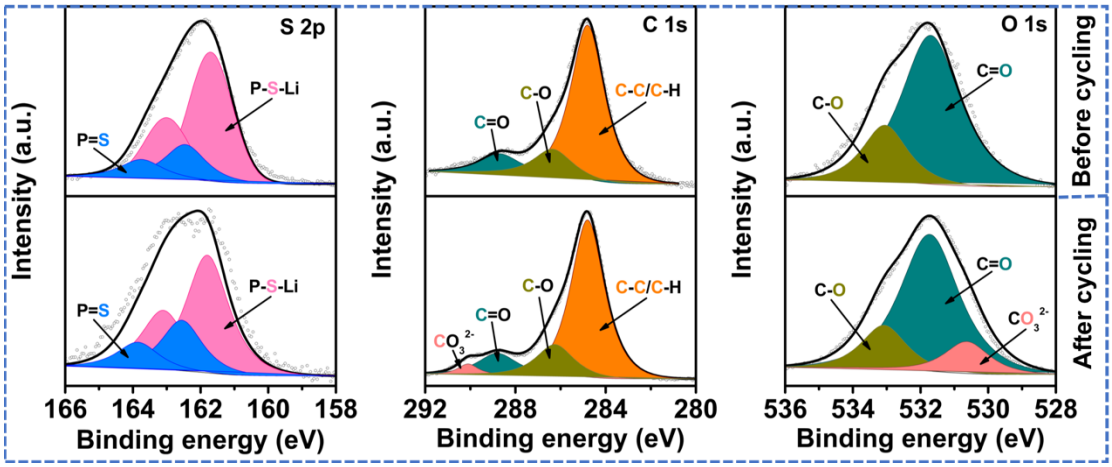

Figure 4.17. Detailed XPS spectra and peak fits of S 2p, C 1s and O 1s obtained from SE of the cell with $Li_6PS_5Cl \cdot LiCl$/PC SE before (top) and after cycling (bottom).

4.4. Conclusions

In summary, following the development of a solvent-based synthesis process for halogen-doped argyrodite SEs, this technique was employed in the synthesis of LiCl-rich $Li_6PS_5Cl \cdot xLiCl$. XRD revealed that excess Cl cannot enter the argyrodite structure, instead creating a composite material. As Cl content is increased, $Li_6PS_5Cl \cdot LiCl$ composite electrolyte exhibited the highest ionic conductivity of 0.53 mS cm^{-1} at room temperature (5×10^{-3} S cm^{-1} at 90 °C), which then decreased as Cl content was further increased. The CV and symmetric cell cycling results indicated that solvent synthesized halide doped lithium argyrodites (Li_6PS_5Cl, Li_6PS_5Br and Li_6PS_5I, $Li_6PS_5Cl \cdot LiCl$) had good electrochemical stability with Li metal. Moreover, the addition of PC at the electrode/electrolyte interface was shown to reduce interfacial resistance, maximize interfacial contact, and prevent excess interfacial redox reactions. LTO-based battery cells with $Li_6PS_5Cl \cdot LiCl$/PC SE showed hgiher capacity and better cycling properties that cells

made with Li_6PS_5Cl/PC. Additionally, $Li_6PS_5Cl \cdot LiCl$/PC-cells could be cycled at very high current rates, achieving a stable capacity of 116 mAh g^{-1} for 200 cycles at 1C. Finally, XPS analysis revealed the formation of a stable SEI layer composed of LiCl and organic compounds. These results indicate that LiCl-rich argyrodites coupled with PC is a good approach for improving the interfacial properties of high performance SSBs.

CHAPTER 5

SYNTHESIS OF FLUORINE-DOPED LITHIUM ARGYRODITE SOLID ELECTROLYTE FOR SOLID-STATE LITHIUM METAL BATTERIES[81]

5.1 Introduction

Rechargeable battery technologies that offer high-energy-density, long cycle-life and safety are urgently needed to meet the growing energy storage demands for the electrification of road transport.[122] State-of-the-art lithium ion batteries (LIBs) for electric vehicles (EVs) employ flammable liquid electrolytes, which pose significant safety concerns.[144,179] This has sparked numerous investigations into alternative solutions that offer high safety without compromising on energy density.[5,180–183] Among these, a particularly lucrative technology is the solid-state Li metal battery (SSLMB), wherein, flammable liquid electrolytes are replaced by solid-state superionic Li-conductors (called solid electrolytes or SEs). Rapid advancements in high-performance ASSLBs requires the development of SEs that exhibit (a) high Li^+ ion conductivity at room temperature ($>10^{-4}$ S cm^{-1}),[159] and (b) good interfacial stability with both Li-metal anodes and cathodes.[180] Additionally, developing simple, economic, and scalable approaches for SE synthesis is vital to bringing ASSLBs to the EV marketplace.[43]

Several sulfides,[134,161] oxides,[176,184] and polymers[78,185] have been proposed as promising SE chemistries for use in ASSLBs. Of these, sulfide SEs exhibit high Li^+ ion conductivity due to the high polarizability of sulfide ions.[147] In particular, much attention has been given to lithium argyrodites such as Li_7PS_6 and halide-doped Li_6PS_5X (X = Cl,

Br, I) whose tetrahedral structure allows for the high mobility of Li ions within the atomic framework.[124,132,186] Alternatively, other anion dopants (i.e. Ge, Sn, Si) have been reported to further increase the ionic conductivity of argyrodite structured solid electrolytes.[55] For Li_6PS_5X SEs, Cl/Br doping not only increases the ionic conductivity, but also improves the argyrodite's electrochemical stability against the Li anode due to the formation of reductive decomposition products (e.g., Li_xP, LiBr/LiCl and Li_2S) at the solid electrolyte interphase (SEI) layer.[166,180,187,188]

The presence of LiF in the SEI layer has been reported to stabilize the SE/Li anode interface[166,167,189–193] and has the potential to provide a wider electrochemical window for sulfide SEs.[166,194] Typically, LiF is incorporated into the SEI layer by introducing additional Li salt additives; this increases the complexity of processing and lacks precise compositional control. From a synthesis standpoint, a more desirable approach would be to directly prepare F-doped argyrodite electrolytes. While such efforts have been devoted to doping Li_7PS_6 with Cl, Br, and I,[180,188] research on the synthesis of fluoride (F)-doped argyrodites (i.e. Li_6PS_5F) remains in its infancy. Zhao et al. have reported the synthesis of $Li_6PS_5Cl_{0.3}F_{0.7}$ via the solid-state method[80] and found that the excellent cycling stability of symmetric cells was attributable to a high concentration of LiF within the argyrodite structure. However, solid-state synthesis methods are both energy- and time-consuming, typically requiring long periods of ball-milling and heat treatments of ≥550 °C. One way to address this issue is to employ a solvent-based synthesis method that requires much lower temperatures (≤200 °C); such liquid-phase methods have been reported to produce high purity argyrodite SEs (Li_7PS_6 and Li_6PS_5X; X = (Cl, Br, I)).[43,119,161]

Herein, for the *first* time, we demonstrate the synthesis of F-doped argyrodites $Li_6PS_5F_y$ and hybrid-doped $Li_6PS_5F_{0.5}Cl_{0.5}$ and $Li_6PS_5F_{0.5}Br_{0.5}$ SEs *via* a simple, fast, and scalable solvent-based approach. Effects of F-doping on the crystal structure, phase purity, and conductivity of doped lithium argyrodites were studied. The results show that $Li_6PS_5F_{0.5}Cl_{0.5}$ holds the highest ionic conductivity of 3.5×10^{-4} S cm^{-1} at room temperature and the lowest activation energy (0.32 eV). Furthermore, $Li_6PS_5F_{0.5}Cl_{0.5}$ also displays the best stability against Li anode due to the synergistic effects of two halogen ions (Cl^- and F^-) at the interface, and the presence of reduced species with good Li^+ ion conductivity (namely Li_3P). This work provides a concrete demonstration of the use of solvent-based synthesis methods to explore new SEs with tunable composition, which will contribute to the development of novel SE materials for the development of ASSLBs.

5.2. Experimental Section

5.2.1 Materials Synthesis

A solvent-based method was employed to synthesize F-doped lithium argyrodites as detailed in previous chapters.[43,119] $Li_{5+y}PS_5F_y$ samples with differing amounts of F doping content were prepared by tuning the molar ratios of LiF to Li_2S (y = 0.1, 0.2, 0.5, 1.0, and 2.0) following the given chemical reaction (**Equation 5.1**). Similarly, dual-doped $Li_6PS_5F_{0.5}X_{0.5}$ (X = Cl and Br) samples were synthesized by mixing the lithium halides using molar ratios for Li_2S:LiF:LiCl (or LiBr) of 1.0:0.5:0.5, as shown in the chemical reaction at **Equation 5.2**.

$$yLiF + Li_2S + Li_3PS_4 \rightarrow Li_{5+y}PS_5F_y \qquad \textbf{Eq. 5.1}$$

$$0.5LiF + 0.5LiX + Li_2S + Li_3PS_4 \rightarrow Li_6PS_5F_{0.5}X_{0.5} \qquad \textbf{Eq. 5.2}$$

5.2.2 Structural Characterizations and Electrochemical Characterizations

For $Li_{5+y}PS_5F_y$ and $Li_6PS_5F_{0.5}X_{0.5}$ powder samples, X-ray diffraction (XRD, Bruker D8 Discover) was carried out using nickel-filtered Cu-Kα radiation (λ = 1.5418 Å) for phase identification. To calculate phase percentages in the electrolytes, XRD refinement was performed using the GSAS-II crystallography data analysis software. Raman spectroscopy (Renishaw in Via Raman/PL Microscope) was performed on synthesized samples using a 632.8 nm emission line of a HeNe laser.

All electrochemical tests were performed using the same techniques detailed in previous chapters. After cycling, the symmetric cells were disassembled for XPS analysis (Thermo VG Scientific) to study the interface. All electrolyte preparation and cell assembly/disassembly took place inside a glovebox filled with Ar (O_2, H_2O<1ppm). The electrochemical performance of F-doped argyrodite electrolytes was tested in full cells of $LiFePO_4$ (LFP)||SE||Li. To prepare the cathode, LFP powder, PVDF and Super P with weight ratio of 80:10:10 were mixed in N-methylpyrrolidone (NMP) to form a homogeneous slurry, which was subsequently coated on an aluminum foil. The prepared cathode with an active material loading of ~2 mg cm^{-2} was dried at 120 ^oC. Prior to battery cycling, trace amounts of nonflammable Pyrrolidinium-based (PYR) ionic liquid with 1M LiTFSI salt was added on both sides of the SE pellet to reduce the resistance from solid/solid contact. Charge and discharge tests were performed over a voltage window of 2.5–4.0 V using 2032-coin cells after the cells were rested for 8 h.

5.3. Results and Discussion

5.3.1 Structural and Ion Transport Behavior of $Li_{5+y}PS_5F_y$ Electrolytes

Using a solvent-based synthesis method, $Li_{5+y}PS_5F_y$ argyrodites with varying F content (y = 0.1, 0.2, 0.5, 1.0, and 2.0) were prepared and subjected to XRD for phase identification (**Figure 5.1**). All samples show strong characteristic diffraction peaks at 2θ = 25.5°, 30°, and 31.2°, attributing to (220), (311), and (222) planes in the argyrodite crystal (cubic *F-43m* symmetry), respectively. At low F content (y = 0.1 and 0.2), the diffraction patterns of $Li_{5+y}PS_5F_y$ samples are almost identical to the characteristic peaks in Li_6PS_5Cl,[119] suggesting that F atoms fully incorporate into argyrodite crystal structure. With increasing F content ($y \geq 0.5$), new diffraction peaks at 2θ = 38.6° and 65.6° (indexed to LiF[189,191]) start to appear and become stronger.

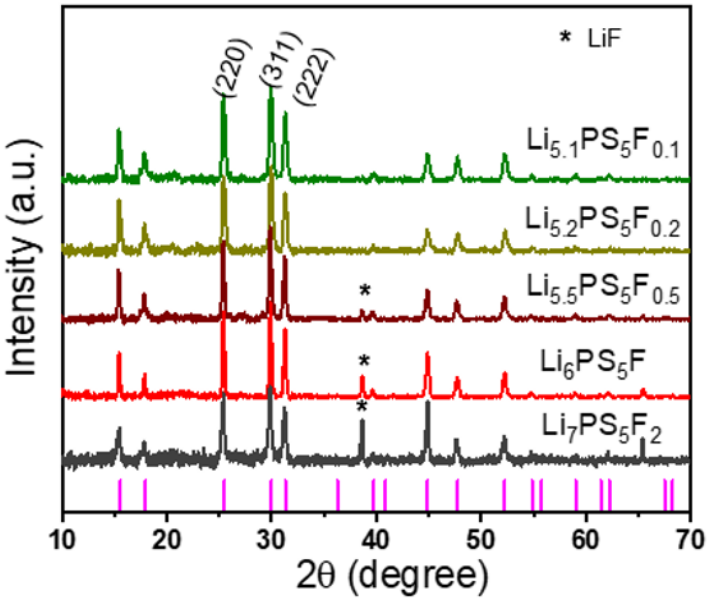

Figure 5.1. XRD patterns of F-incorporated lithium argyrodites $Li_{5+y}PS_5F_y$ (y = 0.1, 0.2, 0.5, 1, 2) that were synthesized from a solvent-based method.

In contrast to the pure argyrodite structure observed for Li_6PS_5Cl,[119] the secondary phase of LiF in $Li_{5+y}PS_5F_y$ ($y \geq 0.5$) indicates low F^- incorporation levels in samples synthesized from a solvent-based approach with low heating temperature (200 °C). Additional LiCl phase was also observed for Li_6PS_5Cl samples when the Cl/P ratio was above 1.5.[76,119] To determine the phase purity and lattice parameters of $Li_{5+y}PS_5F_y$ ($y \geq 0.5$) samples, XRD refinement was undertaken with the results shown in **Figure 5.2** and **Table 5.1**. When $y = 1.0$, Li_6PS_5F is found to have a lattice parameter of $a = 9.889$ Å, accompanied by 9.5 wt% of LiF. In contrast, when the same doping content is used for Li_6PS_5Cl synthesized through solvent-based methods, pure argyrodite structure is observed.[119]

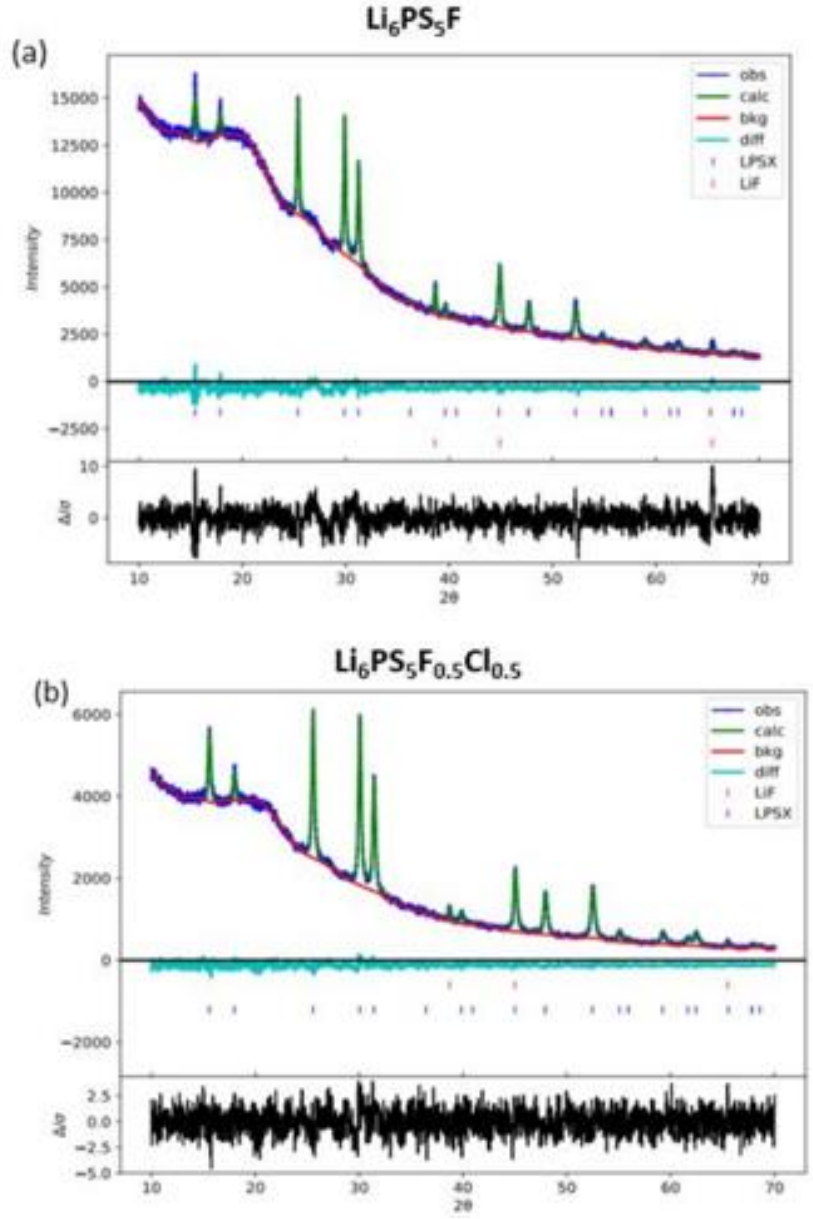

Figure 5.2. XRD Refinements for (a) Li_6PS_5F and (b) $Li_6PS_5F_{0.5}Cl_{0.5}$ argyrodites from solvent-based synthesis. Residual, $R_w \leq 5.000$.

Table 5.1. XRD referments results for Li_6PS_5F and LiF phases in F-doped lithium argyrodites to compare the phase purity and lattice parameters.

Sample Name	Wt % of Li_6PS_5F	Weight % of LiF	Lattice Parameter, *a* (Å)	Conductivity at Room Temp (10^{-4} S/cm)
$Li_{5.1}PS_5F_{0.1}$	N/A	N/A	9.87843	0.134
$Li_{5.2}PS_5F_{0.2}$	N/A	N/A	9.86394	0.142
$Li_{5.5}PS_5F_{0.5}$	91.5	8.5	9.88248	1.14
Li_6PS_5F	90.5	9.5	9.88896	2.24
$Li_7PS_5F_2$	76.8	23.2	9.86306	1.11
$Li_6PS_5F_{0.5}Cl_{0.5}$	92.1	7.9	9.85947	3.51

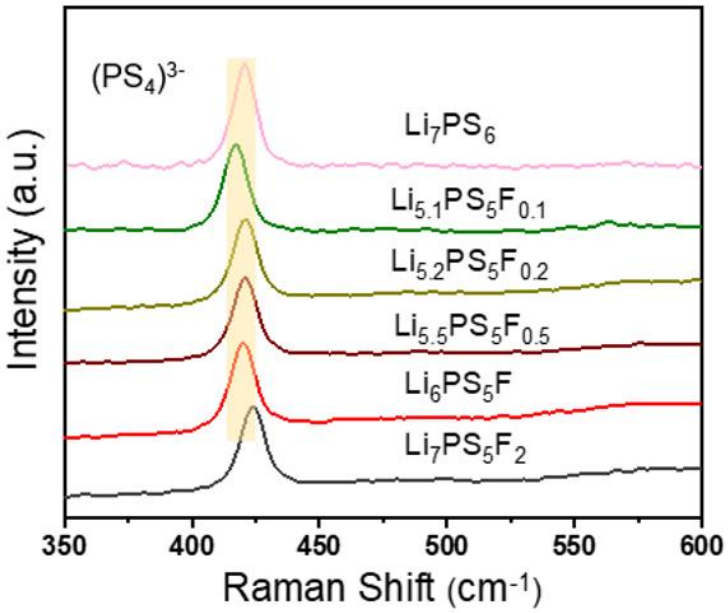

Figure 5.3. Raman spectra of F-incorporated lithium argyrodites $Li_{5+y}PS_5F_y$ (y = 0.1, 0.2, 0.5, 1, 2) that were synthesized from a solvent-based method.

All $Li_{5+y}PS_5F_y$ samples show a strong peak at 421-426 cm^{-1} in their Raman spectra (**Figure 5.3**). This frequency range corresponds to the stretching vibration of the P–S bond in PS_4^{3-} (ortho-thiophosphate), as reported by previous studies on argyrodite electrolytes (Li_7PS_6, Li_6PS_5Br and Li_6PS_5Cl).[187,195] The slight shifts in Raman spectra across the different $Li_{5+y}PS_5F_y$ samples are related to the substitution of S^{2-} anions by F^- anions at the S1 (16*e*) site; PS_4^{3-} tetrahedra arrange into hexagonal cages connected *via* the interstitial anion site in argyrodites.[106]

Figure 5.4a displays the Nyquist plots of $Li_{5+y}PS_5F_y$ samples at room temperature. The resistance R is used to calculate the Li^+ conductivity following the equation of $\sigma = \frac{L}{RA}$, where σ is ionic conductivity, L is the thickness of the cold-pressed pellet, and A is the cross-sectional area of the pellet. $Li_{5+y}PS_5F_y$ (y = 0.1, 0.2) samples show poor ionic conductivity of ~10^{-5} S cm^{-1} despite exhibiting pure argyrodite structure. The highest Li-ion conductivity of 2.3 ×10^{-4} S cm^{-1} is observed for Li_6PS_5F, which contains a small amount of LiF. The enhanced conductivity despite the presence of a secondary phase is similar to previous observations in Cl-rich Li_6PS_5Cl argyrodite.[76,119] Nevertheless, excessive LiF content reduces Li^+ ion conductivity due to the lithium salt's intrinsically poor conductivity (10^{-9} S cm^{-1}).[196] Arrhenius plots in **Figure 5.4b** show the temperature dependence of Li^+ conductivity for $Li_{5+y}PS_5F_y$ samples following a linear relationship. The activation energies are calculated according to the equation $\sigma = \sigma_0 e^{\frac{-E_a}{RT}}$, and results for different compositions are displayed in **Figure 5.5**. Among $Li_{5+y}PS_5F_y$ samples, Li_6PS_5F possesses the lowest activation energy of ~0.45 eV, which is slightly higher than the 0.4 eV displayed by liquid synthesized Li_6PS_5Cl argyrodite.[119]

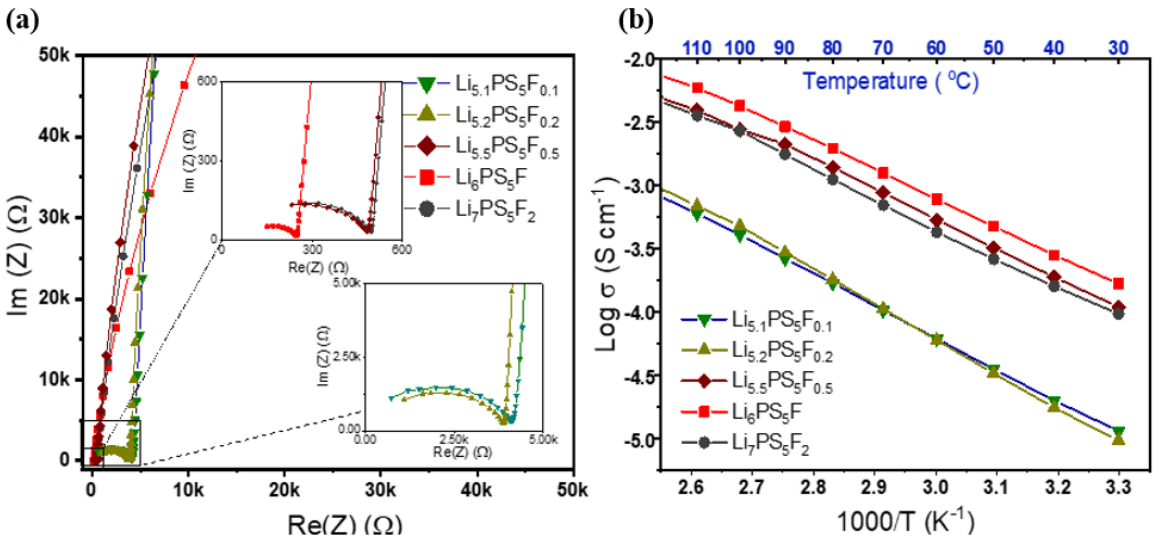

Figure 5.4. (a) Nyquist plots and (b) Arrhenius plots of F-incorporated lithium argyrodites $Li_{5+y}PS_5F_y$ (y = 0.1, 0.2, 0.5, 1, 2) that were synthesized from a solvent-based method.

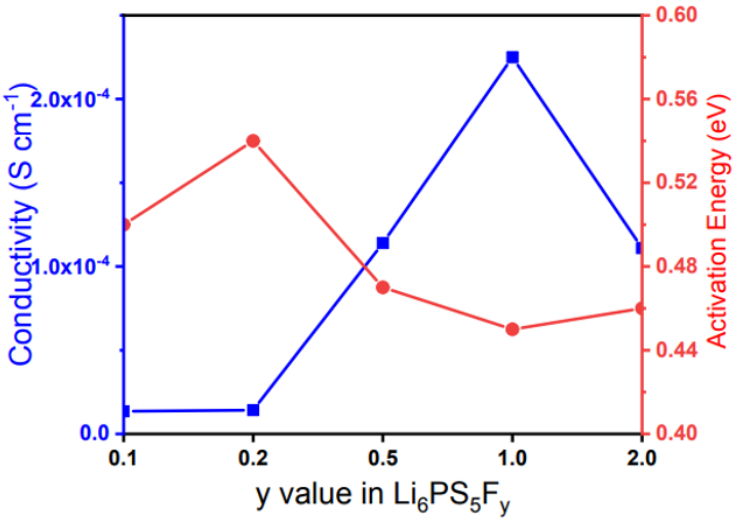

Figure 5.5. Conductivity and activation energy of $Li_{5+y}PS_5F_y$ (y = 0.1, 0.2, 0.5, 1, 2) samples with various amounts of F content.

5.3.2 Synthesis and Characterization of Hybrid Halide Doped $Li_6PS_5F_{0.5}X_{0.5}$ Argyrodites

In addition to single-halogen doping (i.e., F^-), $Li_6PS_5F_{0.5}X_{0.5}$ (X = Cl, Br) samples containing two halogen dopants were also synthesized using a solvent-based method. **Figure 5.6a** presents the XRD pattens for $Li_6PS_5F_{0.5}Cl_{0.5}$ and $Li_6PS_5F_{0.5}Br_{0.5}$ samples, which show characteristic peaks at 2θ = 25.5º, 30º, 31.2º, corresponding to the (220), (311), and (222) planes in the argyrodite structure. These diffraction peaks are in excellent accordance with that for Li_7PS_6 and Li_6PS_5X (X = Cl, Br, I).[119] A small peak at 2θ = 38.6º (indexed to LiF) is still present in $Li_6PS_5F_{0.5}X_{0.5}$ samples. XRD refinement results show that $Li_6PS_5F_{0.5}Cl_{0.5}$ contain 7.9 wt% LiF, slightly lower than that in $Li_6PS_5F_{0.5}$ (8.5 wt%). This comparison suggests that the second halide ion (i.e., Cl^- or Br^-) is beneficial to the incorporation of F^- ions into the argyrodite structure. Raman spectra for $Li_6PS_5F_{0.5}X_{0.5}$ (X = Cl, Br) (**Figure 5.6b**) samples exhibit an obvious peak at 421-423 cm^{-1} attributed to the stretching vibration of P–S bond in PS_4^{3-}, which is the primary vibrational mode for argyrodite SEs.[119]

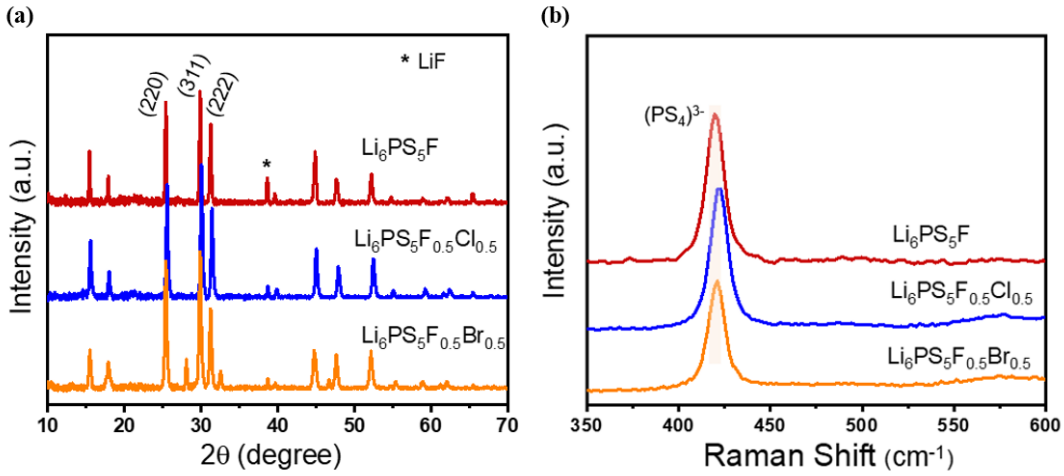

Figure 5.6. (a) XRD patterns, (b) Raman spectra of $Li_6PS_5F_{0.5}X_{0.5}$ samples (X=Cl, Br), in comparison with Li_6PS_5F.

Figure 5.7a shows the Arrhenius plots of $Li_6PS_5F_{0.5}X_{0.5}$ (X = Cl, Br) and Li_6PS_5F from room temperature to 110 °C. $Li_6PS_5F_{0.5}Cl_{0.5}$ sample exhibits the lowest activation energy of 0.32 eV while also possessing the highest ionic conductivity of 3.5×10^{-4} S cm^{-1} at room temperature (**Figure 5.7b**), followed closely by $Li_6PS_5F_{0.5}Br_{0.5}$ at 3.2×10^{-4} S cm^{-1}. Both $Li_6PS_5F_{0.5}Cl_{0.5}$ and $Li_6PS_5F_{0.5}Br_{0.5}$ have faster ion transport properties than those solvent-synthesized argyrodites with single dopants, i.e., Li_6PS_5X (X = Cl, Br),[43,70,119] and Li_6PS_5F (2.3×10^{-4} S cm^{-1}).

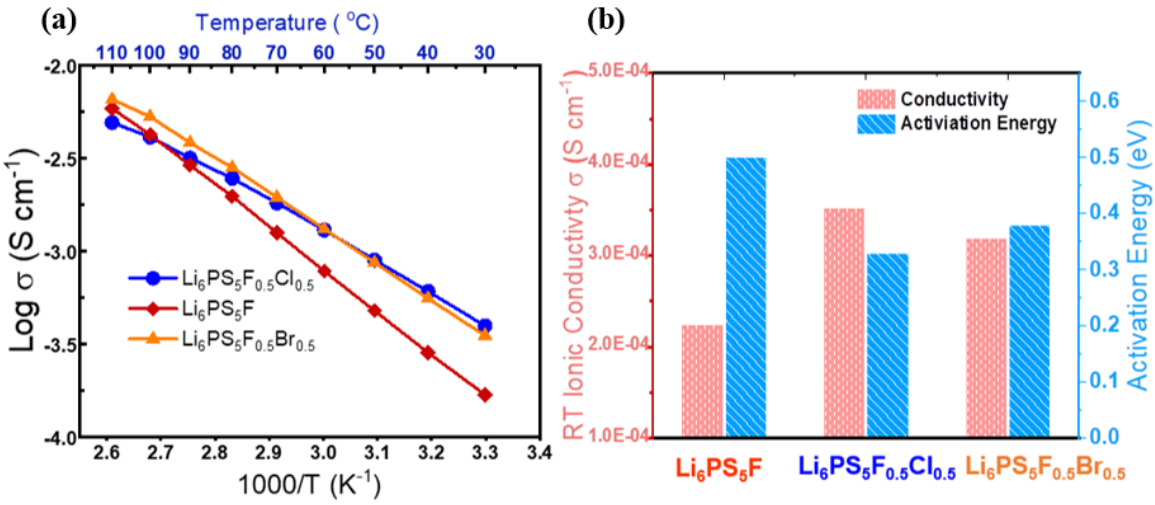

Figure 5.7. (a) Arrhenius plots and (b) RT conductivity/activation energy of $Li_6PS_5F_{0.5}X_{0.5}$ samples (X=Cl, Br), in comparison with Li_6PS_5F.

Table 1.1 displays a large variety of argyrodite SEs synthesized from different methods: solid-state, solvent-based, and hybrid.[64,65,68,69,71,75] In general, the solid-state synthesis approach—which requires extensive ball-milling high temperature heat treatment (~550 °C)—yields argyrodites with the fastest Li-ion transport.[65,72] For the hybrid synthesis method, the starting materials are mixed in solvents and finished by the high temperature heat treatment (400-550 °C).[62,68] Such heat treatment results in higher ionic conductivity

of hybrid-synthesized argyrodites than those from solvent-based synthesis method after heated at low temperature (≤200 °C).[71,75,78] In this work, the ionic conductivity of F-doped and dual doped argyrodites SEs falls well within the expected range (~10^{-4} S cm^{-1}) for low-temperature, solvent-based synthesized Li_6PS_5X (X = Cl, Br) argyrodites. Despite relatively lower ionic conductivity, a solvent-based synthesis method with low heating temperature and a short reaction time (1-3 hours) is attractive for practical applications in large-batch synthesis.

5.3.3 Electrochemical Stability in Li Symmetric Cells

Symmetric cells (Li||SE||Li) were assembled and cycled to evaluate the compatibility of F-doped argyrodite SEs ($Li_6PS_5F_{0.5}Cl_{0.5}$ and Li_6PS_5F) towards metallic Li anode. Before cycling, the impedance of three symmetric cells shows a decreasing trend of 2200 Ω for Li_6PS_5F, 910 Ω for Li_6PS_5Cl, and 370 Ω for $Li_6PS_5F_{0.5}Cl_{0.5}$. Such discrepancies in the total resistance (R_{total}) of the three symmetric cells is ascribed primarily to different interfacial resistances (R_{int}) present in each cell (**Figure 5.8** and **Table 5.2**).

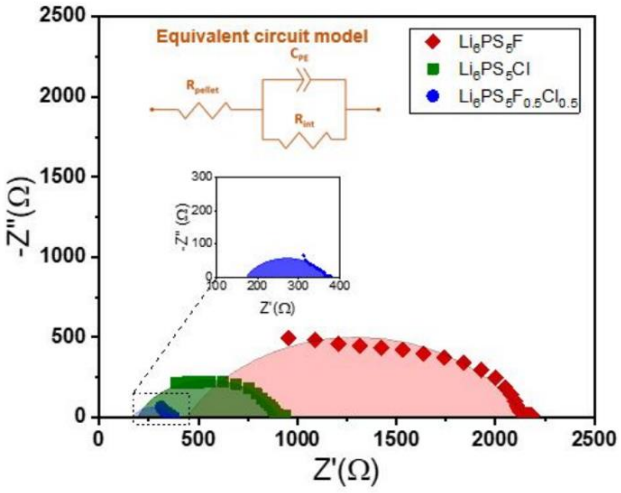

Figure 5.8. Impedance spectra and fitting results of Li symmetric cells before cycling using three SEs ($Li_6PS_5F_{0.5}Cl_{0.5}$, Li_6PS_5F, Li_6PS_5Cl). Insert is the Equivalent circuit.

Table 5.2. Impedance analysis on Li symmetric cells before cycling.

SE material	R_{SE} (Ω)	R_{int} (Ω)	R_{total} (Ω)
$Li_6PS_5F_{0.5}Cl_{0.5}$	175	195	370
Li_6PS_5Cl	200	710	910
Li_6PS_5F	350	1850	2200

Figure 5.9a displays the symmetric cell cycling for three SEs under a low current density of 0.05 mA cm^{-2}, all of which show smooth voltage profiles with polarization voltage values following $Li_6PS_5F_{0.5}Cl_{0.5}$ < Li_6PS_5Cl < Li_6PS_5F. When the current density is increased to 0.1 mA cm^{-2} (**Figure 5.9b**), the Li_6PS_5F-based cell fails first as there is no observable increase in polarization voltage. After cycling for 12 cycles, a sudden voltage drop is observed for the cell with Li_6PS_5Cl SE, which is confirmed to be a short-circuit based on EIS measurement (**Figure 5.10**). In contrast, $Li_6PS_5F_{0.5}Cl_{0.5}$-based symmetric cell exhibits stable cycling performance under the same current density (0.1 mA cm^{-2}). After further increasing the current density to 0.15 mA cm^{-2}, the symmetric cell with $Li_6PS_5F_{0.5}Cl_{0.5}$ SE shows flat and stable voltage profiles for over 300 cycles (**Figure 5.9c**), which indicates stable interface formation between $Li_6PS_5F_{0.5}Cl_{0.5}$ SE and Li anode in the symmetric cells.

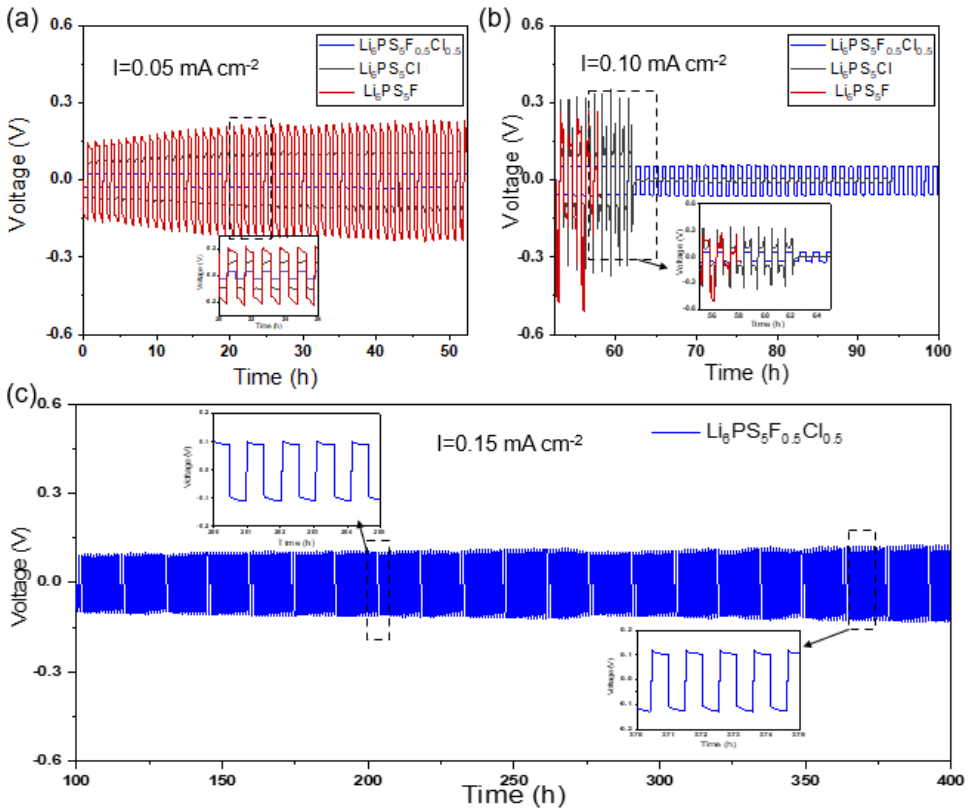

Figure 5.9. Voltage profiles of Li|||SE||Li symmetric cells cycling using three SEs (Li_6PS_5F, Li_6PS_5Cl, $Li_6PS_5F_{0.5}Cl_{0.5}$) under different current densities: (a) 0.05 mA cm^{-2}, (b) 0.10 mA cm^{-2}; (c) 0.15 mA cm^{-2}

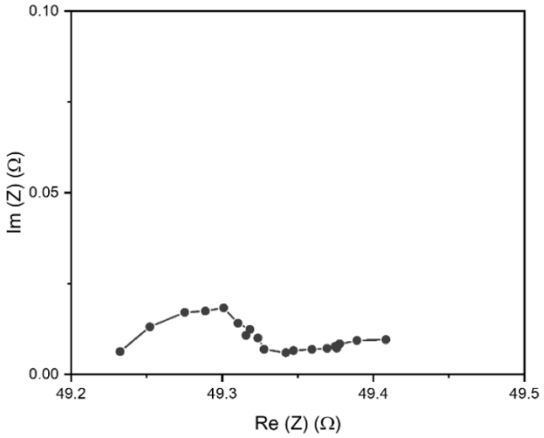

Figure 5.10. Impedance spectrum of Li_6PS_5Cl-based symmetric cell after short circuit happens.

Figure 5.11a shows the XPS spectra of the electrode/electrolyte interface in the $Li_6PS_5F_{0.5}Cl_{0.5}$-based symmetric cell after cycling. Beside strong $(PS_4)^{3-}$ motifs originating from the argyrodite structure, it is observed that the $Li_6PS_5F_{0.5}Cl_{0.5}$ SE undergoes reductive decomposition upon contact with Li metal to form a solid electrolyte interphase (SEI) layer. The best fits for S *2p*, and P *2p* peaks reveal that such an SEI layer in the $Li_6PS_5F_{0.5}Cl_{0.5}$-based cell contains reduced species of P (P_2S_x, Li_3P) and S (Li_2S); the Li *1s* peak fitting suggests the co-presence of LiF and LiCl.[160,180,197] For the two other cycled symmetric cells, reductive species such as P_2S_x, Li_2S, and LiF (or LiCl), are observed at the SE/Li interface, but are notably missing the Li_3P peak at 129.5 eV which is present in the dual-doped SE (**Figures 5.11b and 5.11c**).

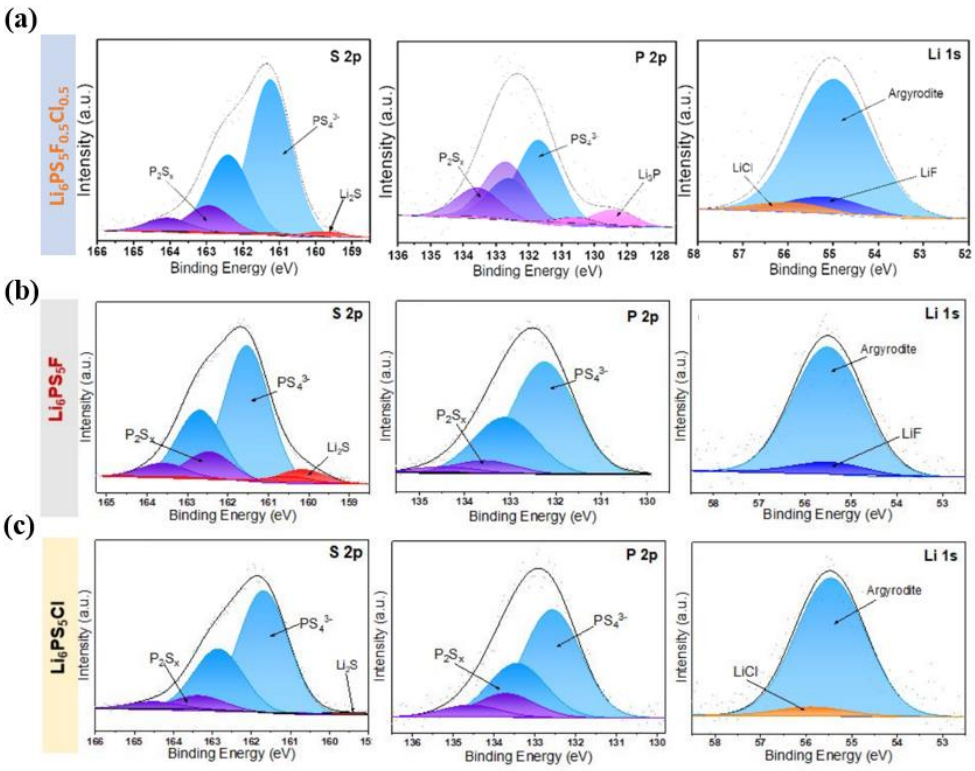

Figure 5.11. XPS spectra of S 2p, P 2p, and Li 1s peaks from the cycled interface of Li symmetric cell using (a) $Li_6PS_5F_{0.5}Cl_{0.5}$, (b) Li_6PS_5F and (c) Li_6PS_5Cl SEs.

5.3.5 Electrochemical Performance in Solid-state Li Batteries Using $Li_6PS_5F_{0.5}Cl_{0.5}$ SE

Solid-state Li batteries were assembled using $Li_6PS_5F_{0.5}Cl_{0.5}$ as SE, Li metal as the anode, and LFP as the active material in composite cathode and were cycled within the electrochemical window of 2.5-4.0 V. **Figure 5.12a** shows the cycling performance of the LFP||$Li_6PS_5F_{0.5}Cl_{0.5}$||Li battery under 0.2 C, which has a specific discharge capacity of 122 mAh g^{-1} for the first cycle. The specific discharge capacity further increases to 130 mAh g^{-1} after a few cycles, which can be attributed to the formation of an LiF and Li_3P-rich SEI layer; by the 50th cycle, a decent value of 105 mAh g^{-1} has been maintained (**Figure 5.13a**).

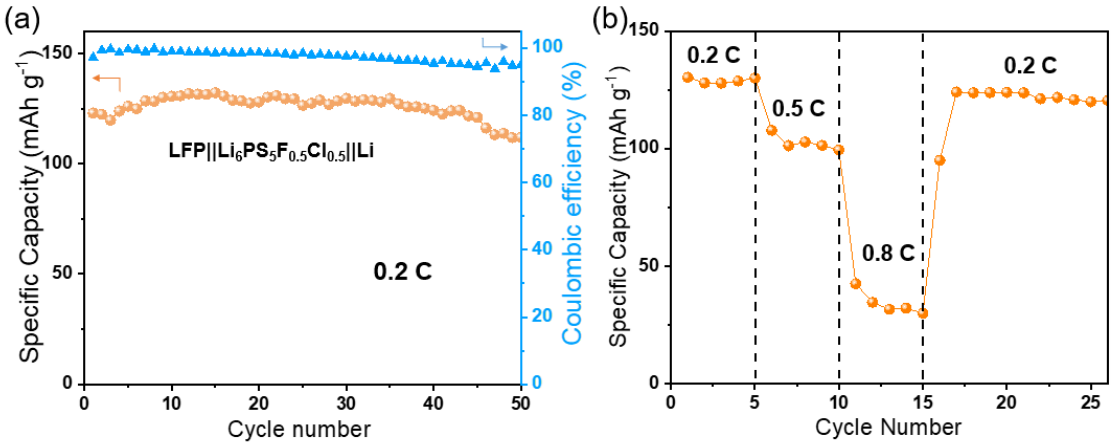

Figure 5.12. (a) Cycling performance of LFP||$Li_6PS_5F_{0.5}Cl_{0.5}$||Li cell under a current density of 0.2 C; (b) Rate performance of the cell under various C-rates (0.2 C, 0.5 C, 0.8 C).

The charge/discharge capacity of LFP||$Li_6PS_5F_{0.5}Cl_{0.5}$||Li battery is clearly better than that of the cell using Li_6PS_5Cl (**Figure 5.13b**), confirming the positive role of F-contained SE. In addition, the C-rate cycling performance of LFP||$Li_6PS_5F_{0.5}Cl_{0.5}$||Li battery under various C-rates (0.2, 0.5, and 0.8 C) is shown in **Figure 5.12b**. As expected, an obvious specific capacity drop is observed when cycling under higher C-rates, but the

battery displays a resumed specific capacity at ~120 mAh g^{-1} after the C-rate is returned to 0.2 C. The great electrochemical performance of $Li_6PS_5F_{0.5}Cl_{0.5}$ SE in LFP||Li cells can be attributed to both the stabilizing effect of F^- and Cl^- from SE, and the adding LiTFSI at the electrode/SE interfaces. Nonetheless, these results demonstrate the excellent potential for F-doped argyrodite SEs to be used in full battery applications.

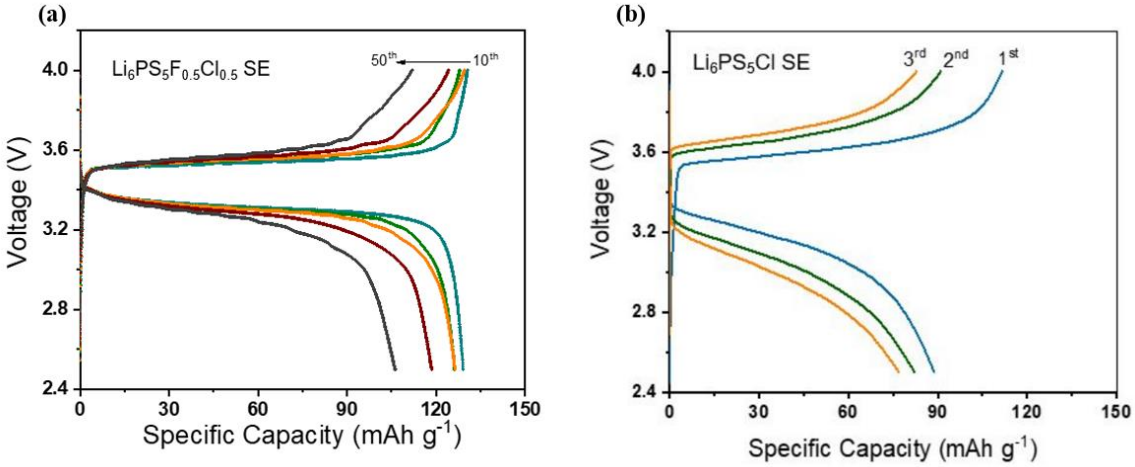

Figure 5.13. Charge-discharge voltage profiles of LFP||Li cell using (a) $Li_6PS_5F_{0.5}Cl_{0.5}$ SE (voltage window 2.5-4.0V) at 10^{th}, 20^{th}, 30^{th}, 40^{th} and 50^{th} cycles, and (b) Charge-discharge voltage profiles of LFP||Li cell using Li_6PS_5Cl SE (voltage window 2.5-4.0V) at 1^{st}, 2^{nd} and 3^{rd} cycles.

5.4. Conclusion

In summary, for the first time, we reported the synthesis of F-doped lithium argyrodites ($Li_{5+y}PS_5F_y$) and hybrid-doped argyrodites ($Li_6PS_5F_{0.5}Cl_{0.5}$ and $Li_6PS_5F_{0.5}Br_{0.5}$) by a solvent-based approach with low temperature heat treatment. The F-content and hybrid-doped content (F/Cl and F/Br) in argyrodites significantly influences the phase purity and ionic conductive properties. Li_6PS_5F exhibits an impressive conductivity of 2.4

$\times 10^{-4}$ S cm^{-1} while $Li_6PS_5F_{0.5}Cl_{0.5}$ exhibits a higher value of 3.5 $\times 10^{-4}$ S cm^{-1} at room temperature. Moreover, $Li_6PS_5F_{0.5}Cl_{0.5}$ SE shows the best stability towards Li metal in symmetric cells among the tested halide-doped argyrodites. XPS analysis and AIMD simulations reveal that such enhanced stability is attributed to the conductive species (Li_3P), and to the co-presence of LiCl and LiF. The assembled LFP||$Li_6PS_5F_{0.5}Cl_{0.5}$||Li cell displays good cycling performance with a specific discharge capacity above 105 mAh g^{-1} after 50 cycles. This work demonstrates the synthesis of F-doped lithium argyrodites and investigates the interfacial stability of F-doped argyrodites against Li metal, contributing to the development of novel solid electrolytes for use in future solid-state Li batteries.

CHAPTER 6

HIGHLY CONDUCTIVE IODINE AND FLUORINE DUAL-DOPED ARGYRODITE SOLID ELECTROLYTE FOR LITHIUM METAL BATTERIES

6.1. Introduction

Current lithium-ion battery (LIB) technologies have seen tremendous success in the past 30 years. However, there are still several challenges concerning safety and energy density which must be overcome to meet the ever-growing energy needs of the future. To achieve high energy density, metallic lithium (Li) is a promising anode candidate due to its highest theoretical capacity (3,860 mAh g^{-1}) and the lowest reduction potential of -3.04 V (*v.s.* standard hydrogen electrode).[64,178] Nevertheless, Li metal batteries that use conventional liquid electrolytes (LEs) suffer from safety issues due to internal short circuits caused by dendrite formation, which leads to thermal runaway.[122] Solid-state Li metal batteries (SSLMBs) with nonflammable solid electrolytes (SEs), offer a great solution for dendrite suppression while simultaneously reducing flammability.[178] The most popular state-of-the-art inorganic SE candidates mainly fall into three categories: oxides,[22,176,184] sulfides,[134,161,198] and halides.[35,36,199] Of these three, sulfides are notable for their impressive Li-ion conductivity at room temperature, lower synthesis temperatures, and cold-press induced densification, making them attractive for use in SSLMBs.[68,119]

The halogen-doped Li_6PS_5X (X = F, Cl, Br, I) argyrodites, as representative sulfides, have received much attention in the past decade.[81,125,132,143,200] In an argyrodite

material, the Li-ion hopping mechanism and ionic conductivity are dependent on the tetrahedral-based structure of the crystal lattice. Compared with Li_7PS_6, halide-doped Li_6PS_5X utilizes the partial replacement of S^{2-} with halogen anions (F^-, Cl^-, Br^-, I^-), thus altering the atomic structure due to differences in ion size and polarization. Moreover, the doping effects are different depending on the specific halogen anion. For instance, both Li_6PS_5Cl and Li_6PS_5Br display obviously enhanced ionic conductivity when compared with Li_7PS_6,[79,119,124] which is attributed to the particularly disordered lattice caused by the unbalanced sharing of the 4*a* and 4*d* anion sites by both S^{2-} and Cl^-/Br^-.[67,201] Therefore, much effort has been devoted to Cl- or Br-doped argyrodites and to the demonstration of their feasibility in solid-state Li batteries.[77,79,80,146,202] In contrast, Li_6PS_5I with iodine doping has continuously been reported to show poor ionic conductivity (10^{-7} S cm^{-1}, 3-4 orders of magnitude lower than its Cl/Br counterparts) due to the lack of disorder in its crystal structure.[58,67,159,203] Recently, it has been reported that Li_6PS_5I with nanocrystalline structure exhibits boosted ionic conductivity (10^{-4} S cm^{-1}) following high-energy planetary ball milling treatment. This is attributed to the mechanically introduced disorder in the nanocrystalline structure.[201]

In addition to Li_6PS_5X argyrodite with single halogen anion doping, hybrid-doped argyrodites (e.g. $Li_6PS_5Cl_{0.5}Br_{0.5}$ and $Li_6PS_5Cl_{0.3}F_{0.7}$)[79,80] have been reported to distribute the occupancy at the 4*a* and 4*d* sites differently, tailoring the disordering in the crystal and leading to increased ionic mobility and thereby improved conductivity. Our recent work also proves the beneficial effect of hybrid-doping-caused disorder through the observation that $Li_6PS_5F_{0.5}Cl_{0.5}$ possesses higher ionic conductivity than either Li_6PS_5F or Li_6PS_5Cl.[81] Additionally, iodine containing hybrid argyrodites such as $Li_6PS_5Cl_{0.7}I_{0.3}$ exhibit much

higher room temperature Li-ion conductivity than pristine Li_6PS_5I.[204] Stemming from this, the introduction of F^- to partially replace I^- in Li_6PS_5I is intriguing, because F^- has the smallest ionic size (133 *pm*) while I^- has the largest ionic size (216 *pm*). It should be possible to generate a more disordered structure by coinhabiting F^- and I^- at anion sites, thus decreasing the energy barriers for Li-ion jumps. Moreover, the presence of fluorine at the electrode/electrolyte interface has been reported to contribute to the formation of a stable solid electrolyte interphase (SEI) layer.[166,189–192,196,205] Nevertheless, to the best of our knowledge, studies on introducing F^- into Li_6PS_5I argyrodites have not been reported.

In this chapter, we report the synthesis of Li_6PS_5I and hybrid-doped $Li_6PS_5F_xI_{1-x}$ (x = 0.25, 0.5, 0.75) argyrodites through a solvent-based approach. After undergoing heat treatment at 200 °C, the produced Li_6PS_5I shows high room temperature ionic conductivity of 2.5×10^{-4} S cm^{-1}. When introducing F^- into the Li_6PS_5I structure, $Li_6PS_5F_{0.25}I_{0.75}$ achieves the highest conductivity of 3.5×10^{-4} S cm^{-1} among hybrid-doped argyrodites with various F/I ratios. With higher F-content, $Li_6PS_5F_{0.75}I_{0.25}$ displays the best electrochemical stability and battery cycling performance. Using $Li_6PS_5F_{0.75}I_{0.25}$ as solid electrolyte, Li symmetric cells display long-term stable cycling up to 1,100 hours under a current density of 0.05 mA cm^{-2}. In addition, solid-state Li metal batteries with LTO as positive electrode show great capacity retention of 105 mAh g^{-1} after 200 cycles at 0.1 C. This research expands new compositions in the argyrodite-class solid electrolytes and promotes the development of solid-state Li metal batteries.

6.2. Experimental Sections

6.2.1 Materials synthesis

Li_6PS_5I and hybrid-doped $Li_6PS_5F_xI_{1-x}$ were synthesized via a solvent-based approach, following our previous chapters.[43,119] For use in the controlled experiment, further heat treatment at 290 °C was performed to produce 290C-Li_6PS_5I sample. For $Li_6PS_5F_xI_{1-x}$ (x = 0.25, 0.5, 0.75) argyrodites, lithium fluoride (LiF, Acer, 99.5%) was introduced as another precursor while the content of LiI was decreased accordingly, followed by the same mixing and heating process at 200 °C.

6.2.2 Structural and morphology characterizations

The produced powder samples (Li_6PS_5I and hybrid-doped $Li_6PS_5F_xI_{1-x}$) were subjected to X-ray diffraction (XRD) measurements using Bruker D8 Discover with nickel-filtered Cu-Kα radiation (λ = 1.5418 Å) for phase identification. XRD refinement was carried out using the GSAS-II crystallography data analysis software. Raman spectroscopy (Renishaw in Via Raman/PL Microscope) was performed on synthesized samples using a 632.8 nm emission line of a HeNe laser. The morphologies of argyrodite samples were analyzed using transmission electron microscopy (TEM, Tecnai F20 FEG-TEM/STEM).

6.2.3 Electrochemical Characterizations

All SE preparation and cell assembly/disassembly took place inside a glovebox filled with Ar. All electrochemical testing was carried out using the methods described in previous chapters. In addition, solid-state Li metal batteries were assembled and cycled. The battery structure used F/I-doped argyrodite as SE, Li metal as the anode, and $Li_4Ti_5O_{12}$ (LTO) as the active cathode. The composite cathode consisted of super P, PVDF binder and LTO with a weight ratio of 1:1:8. In the Li metal batteries, trace amounts (<10 μL) of propylene carbonate were introduced at the interface to reduce the resistance associated with solid-solid contact. The assembled Li metal batteries were cycled under different C-

rates (0.1, 0.2 and 0.6) at room temperature, which were calculated based on the theoretical specific capacity of LTO (0.175 Ah g^{-1}).

6.3 Results and Discussion

6.3.1 Structure analysis and morphology of Li_6PS_5I and F/I co-doped argyrodites

In this work, Li_6PS_5I and hybrid-doped $Li_6PS_5F_xI_{1-x}$ (x = 0.25, 0.5, 0.75) argyrodites were synthesized via a solvent-based approach, and the produced samples were subjected to XRD characterization to identify the crystal structure and phase purity. As shown in **Figure 6.1**, Li_6PS_5I sample shows characteristic diffraction peaks at 2θ = 17.7°, 25.2°, 29.6°, and 31.0°, corresponding to the planes of (200), (220), (311), and (222) in argyrodite structure (space group F-*43m*). The XRD patterns are in good agreement with pure phase Li_6PS_5I as reported from mechanochemical synthesis.[206] In addition, the lattice parameter of as-synthesized Li_6PS_5I is estimated to be 10.1235 Å, which is slightly higher than the

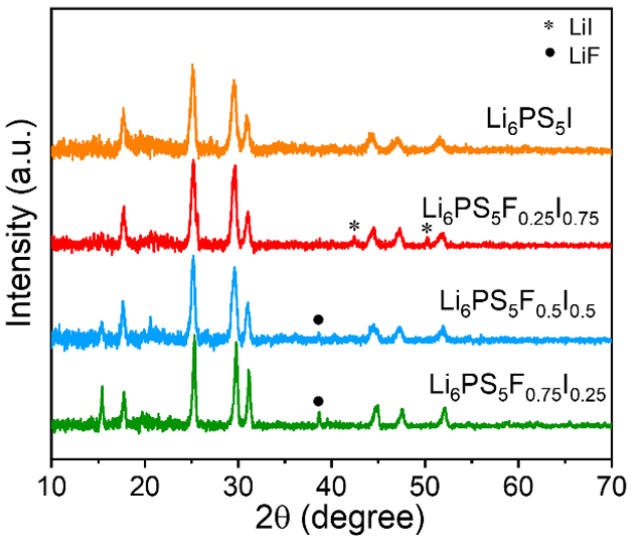

Figure 6.1. XRD pattens of solvent-synthesized Li_6PS_5I, $Li_6PS_5F_xI_{1-x}$ (x = 0.25, 0.5, 0.75) argyrodites

values of Li_6PS_5Cl (9.850 Å) and Li_6PS_5Br (9.980 Å).[119] This is attributed to the larger ionic radius of I^- (206 *pm* for I^- *vs* 182 *pm* for Br^- and 167 *pm* for Cl^-). When both halide ions (I^- and F^-) are introduced, all hybrid-doped samples exhibit strong and dominant argyrodite structure diffraction patterns.[43,119] Notably, while synthesized Li_6PS_5I is a pure phase argyrodite, the addition of 0.25 mols of F^- to synthesize $Li_6PS_5F_{0.25}I_{0.75}$ appears to make it difficult for iodine to fully incorporate, as small secondary peaks corresponding to LiI can be observed at 2θ = 42.4° and 50.2°.[207] As F-content is increased, the LiI peaks disappear. Instead, a minor impurity peak at 2θ = 39.1° starts to appear which is attributed to small amount of secondary LiF phase.[81,191] XRD refinement results (**Figure 6.2**) reveal that the $Li_6PS_5F_{0.5}I_{0.25}$ and $Li_6PS_5F_{0.75}I_{0.25}$ samples contain around 6.7 wt% and 9.0 wt% of LiF, respectively.

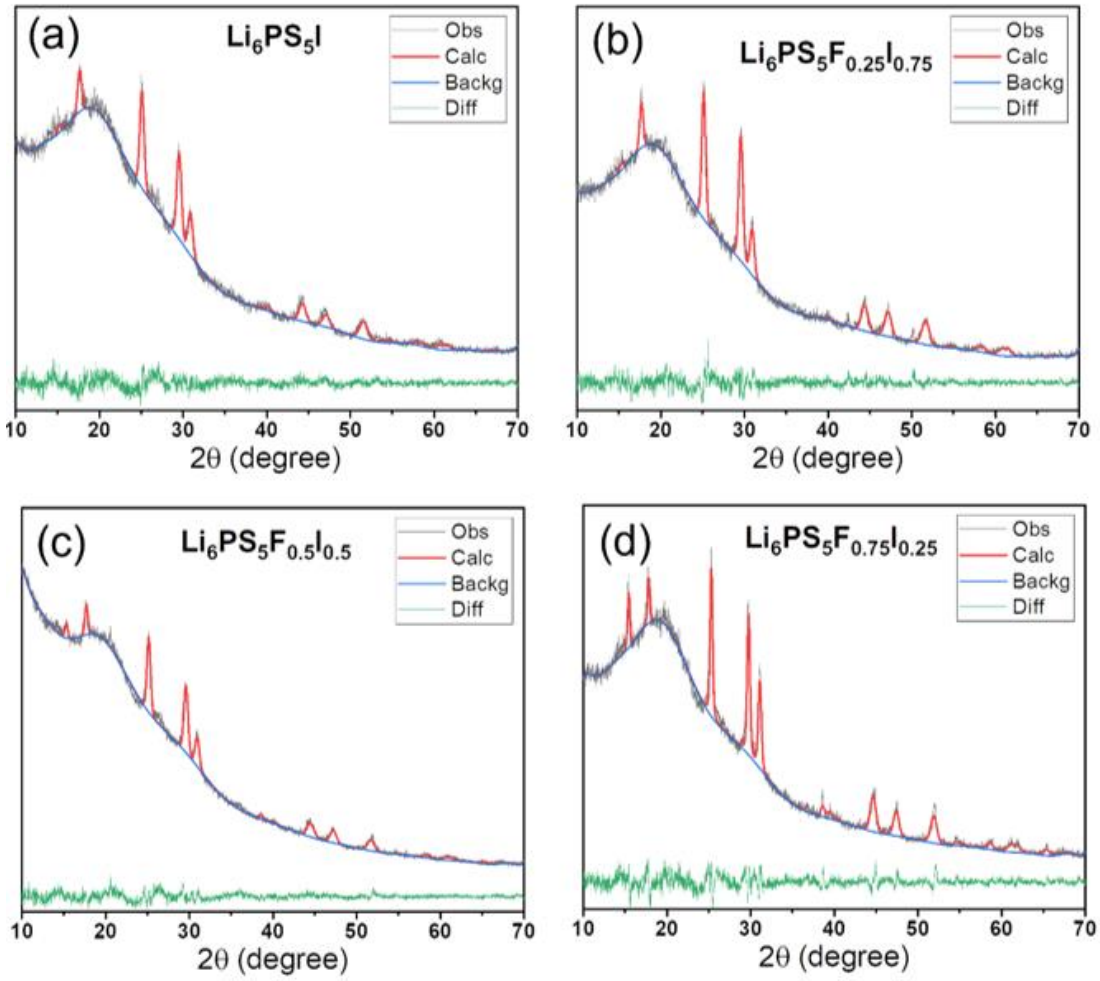

Figure 6.2. XRD refinements of Li_6PS_5I and hybrid-doped $Li_6PS_5F_xI_{1-x}$ argyrodites (x = 0.25, 0.5, 0.75).

Raman spectra (**Figure 6.3**) of the Li_6PS_5I and hybrid-doped argyrodites show strong bands around 420 cm^{-1}, with smaller bands appearing at 575 cm^{-1} and 200 cm^{-1}, all of which have been reported to indicate the presence of the PS_4^{3-} tetrahedra.[63] Very slight shifts in Raman bands between differently doped argyrodite samples have been observed, which is due to the variable substitution of S^{2-} anions with F^- and I^- at the S1 (16*e*) site, as well as the different energy associated with P–S bonds resulting from various proportions

of the dopants.[106] The morphologies of these I-containing argyrodite powders were observed through scanning electron microscopy (SEM) images (**Figure 6.4a** and **6.4b**). These particles are self-adhesive and easily form a solid mass when pressed. Energy-dispersive X-ray spectroscopy (EDS) was employed to examine the elemental distribution of phosphorous (P), sulfur (S), fluorine (F), and iodine (I) in $Li_6PS_5F_{0.75}I_{0.25}$ argyrodite. The aggregation of F is observed in a local area, corresponding to unincorporated LiF phase.

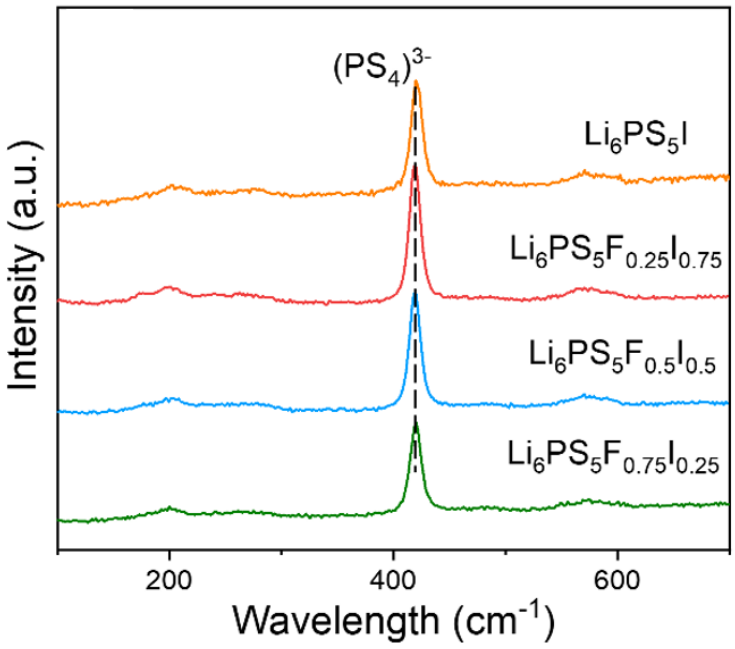

Figure 6.3. Raman spectra of solvent-synthesized Li_6PS_5I, $Li_6PS_5F_xI_{1-x}$ (x = 0.25, 0.5, 0.75) argyrodites

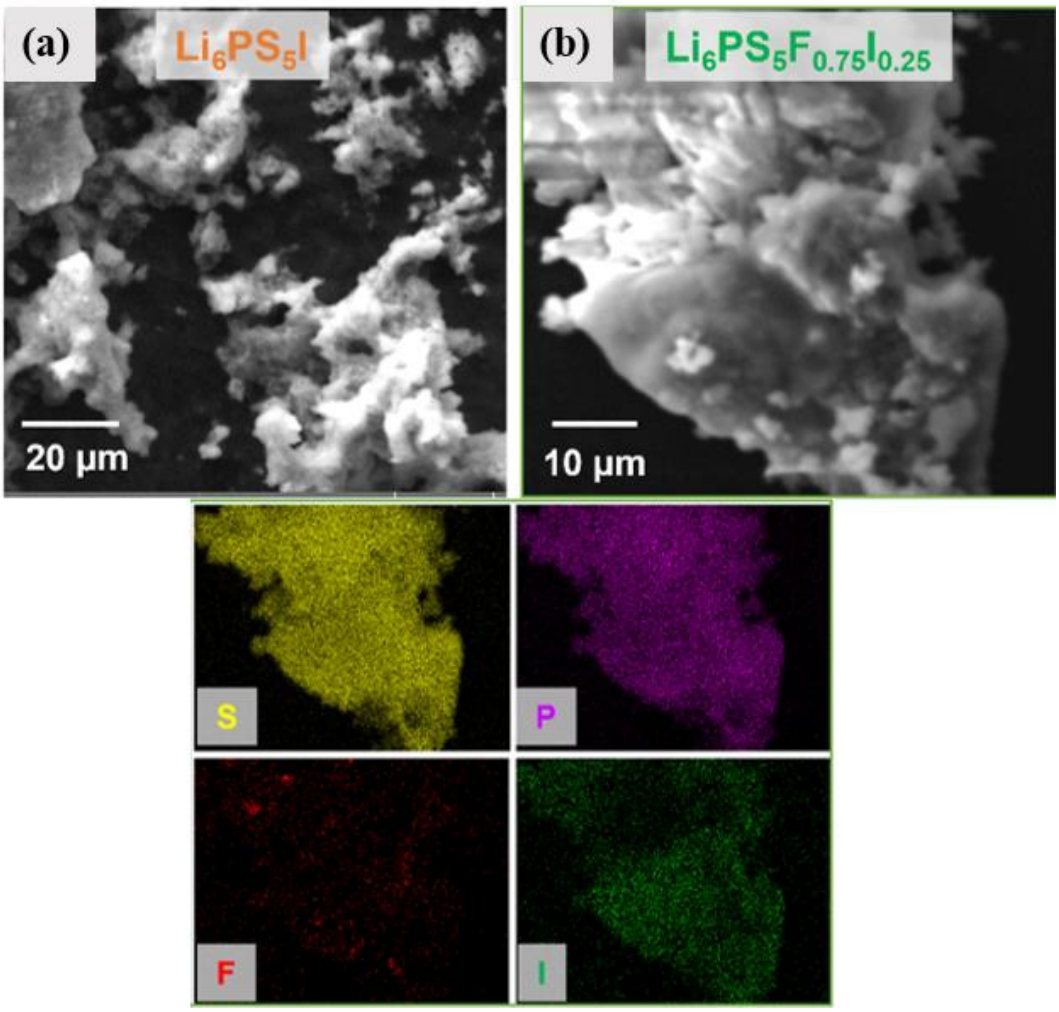

Figure 6.4. SEM images of (a) Li_6PS_5I, and (b) $Li_6PS_5F_{0.75}I_{0.25}$ (x = 0.75) with elemental mapping.

6.3.2 Fast Li-ion transport in solvent synthesized Li_6PS_5I and F/I co-doped argyrodites

The ionically conductive properties of solvent-synthesized Li_6PS_5I and hybrid-doped $Li_6PS_5F_xI_{1-x}$ argyrodites were examined by electrochemical impedance spectroscopy (EIS) measurements. In a halide doped argyrodite structure, octahedrally arranged Li ions form a cubic lattice with PS_4^{3-} tetrahedra and face centered anions (S^{2-} or X^- (X = F, Cl, Br, I)), allowing for three levels of lithium ion jumps to occur: (i) localized jumps, (ii) intra-

cage jumps, and (iii) inter-cage jumps, the latter of which is the primary bottleneck for Li ion mobility.[67,79,201,203,208] Unlike the fast ion transport in Li_6PS_5Cl and Li_6PS_5Br argyrodites, Li_6PS_5I exhibits poor ionic conductivity due to the absence of anion site disorder,[58,159,200] although high-energy ball milling and doping chemistry have been reported to introduce additional disorder and promote ion-transport.[201,209,210]

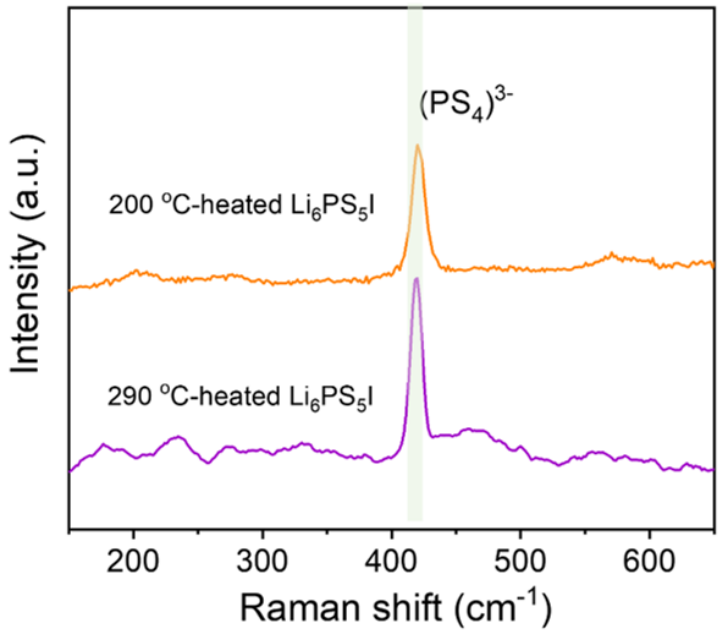

Figure 6.5. Raman spectra of Li_6PS_5I samples that synthesized after 200 and 290 ◦C heating treatment, respectively.

For our Li_6PS_5I argyrodite, two different heat treatment temperatures of 200 °C and 290 °C were employed during the solvent-based synthesis process to form 200C-Li_6PS_5I and 290C-Li_6PS_5I, respectively. Both samples show strong $(PS_4)^{3-}$ bands in Raman spectra (**Figure 6.5**). **Figure 6.6** presents the Arrhenius plots of these two Li_6PS_5I samples. At room temperature (RT), the 290C-Li_6PS_5I sample exhibits an ionic conductivity of 1.8 ×

10^{-6} S cm^{-1}, which is in good agreement with previous reports from solid-state synthesis methods (>400 °C).[132,134]

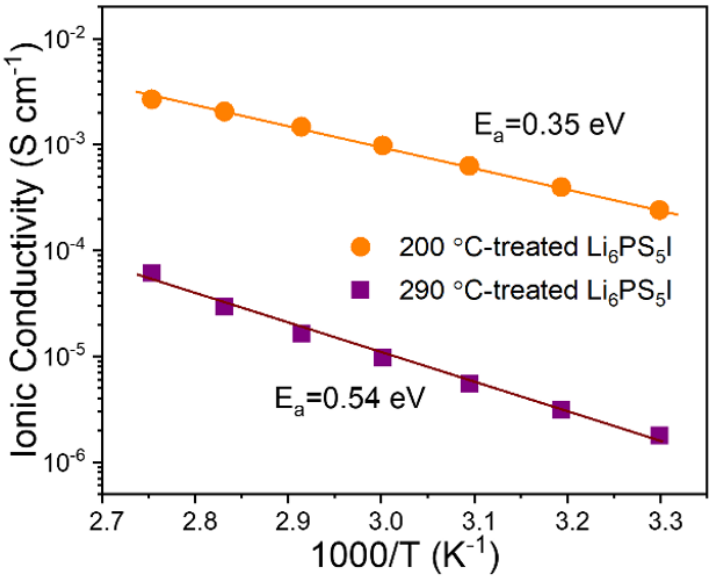

Figure 6.6. Arrhenius plots of solvent synthesized Li_6PS_5I after two different heating treatment temperatures (200, 290 °C).

In contrast, a high ionic conductivity value of 2.5×10^{-4} S cm^{-1} at RT is achieved for the Li_6PS_5I sample after a low heat treatment temperature at 200 °C. This conductivity is not only more than two orders higher than that of 290C-Li_6PS_5I, but also is amongst the highest values for pure Li_6PS_5I argyrodite reported thus far. The Nyquist plots for both samples (**Figure 6.7**) at RT display the typical semicircle in the high frequency range and a spike in lower frequency range, with 200C-Li_6PS_5I sample displaying a much smaller resistance value. Additionally, 200C-Li_6PS_5I argyrodite also achieves a much lower activation energy (0.34 eV) than that of 290C-Li_6PS_5I (0.55 eV).

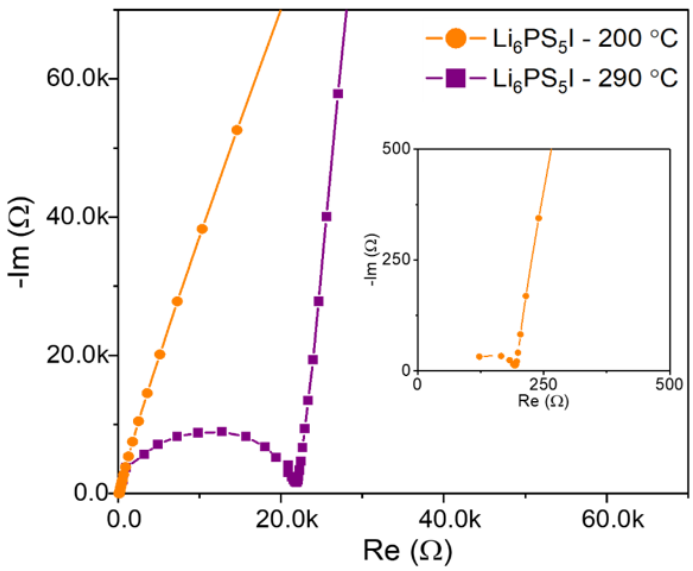

Figure 6.7. Nyquist plots of Li_6PS_5I samples that synthesized after two heating treatments (200 and 290 ◦C).

Figures 6.8a and **6.8b** show transmission electron microscopy (TEM) elemental mapping of the Li_6PS_5I samples after heating treatment under 200 °C and 290 °C, respectively. The 290 °C-heated sample has a homogenous distribution of S and I elements. In contrast, the 200 °C-treated sample displays a mismatched distribution with iodine (I) aggregating at the edges while the sulfur remains in the inner region. Such edge-aggregated iodine may contribute to the decreased grain boundary resistance and promote the fast ion transport, which is similar with observations seen in previous reports.[176,201]

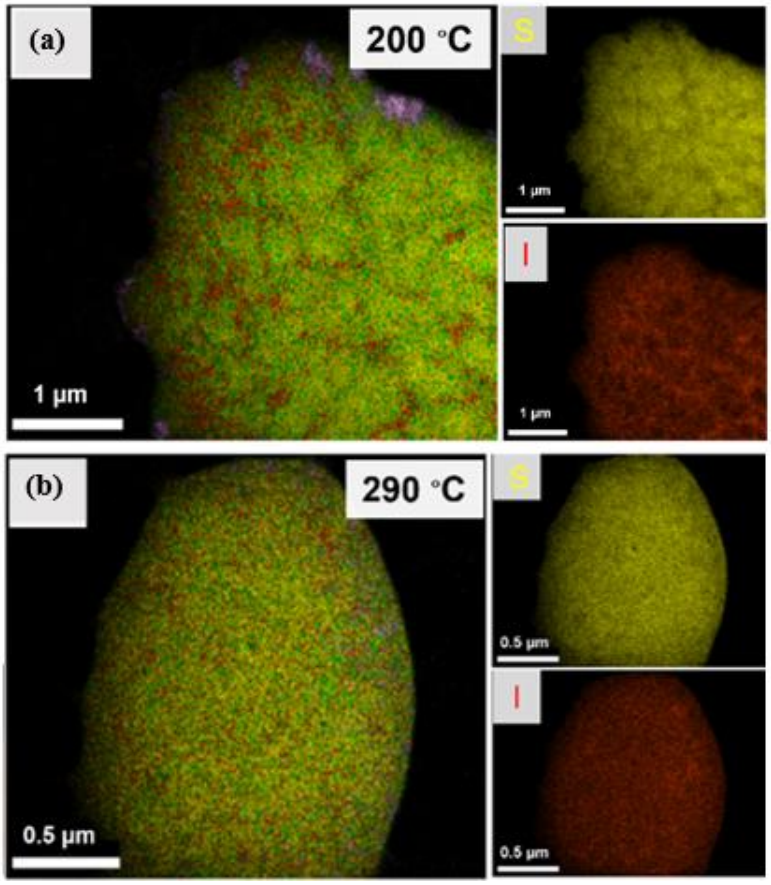

Figure 6.8. TEM elemental mapping of synthesized Li_6PS_5I argyrodite after heating treatment at (a) 200 °C and (b) 290 °C. (S in Yellow, I in Red, O in Pink).

For hybrid-doped $Li_6PS_5F_xI_{1-x}$ (x = 0.25, 0.5, 0.75) argyrodites, **Figures 6.9a** and **6.9b** show their Nyquist plots at RT and Arrhenius plots between temperature range of 30-90 °C. When x = 0.25, $Li_6PS_5F_{0.25}I_{0.75}$ exhibits the smallest resistance and the highest RT ionic conductivity of 3.5×10^{-4} S cm^{-1}, indicating that a minor amount of F mixed with a majority of I provides the best pathway for Li^+ transport across the argyrodite structure. With further increasing F-content, the ionic conductivity continually decreases, with $Li_6PS_5F_{0.75}I_{0.25}$ (x = 0.75) showing the lowest conductivity of 1.5×10^{-4} S cm^{-1}. The slower ion transport is attributed to the increased minor LiF secondary phase in argyrodite

structure (shown in XRD results). Unlike the large fluctuations for ionic conductivity, the activation energy for both hybrid-doped $Li_6PS_5F_xI_{1-x}$ (x = 0.25, 0.5, 0.75) and pristine Li_6PS_5I argyrodites are close to each other (**Figure 6.9a**). For instance, $Li_6PS_5F_{0.25}I_{0.75}$ with low F-content has the lowest activation energy value of 0.34 eV, while $Li_6PS_5F_{0.75}I_{0.25}$ with high F-content exhibits a slightly higher value of 0.37 eV.

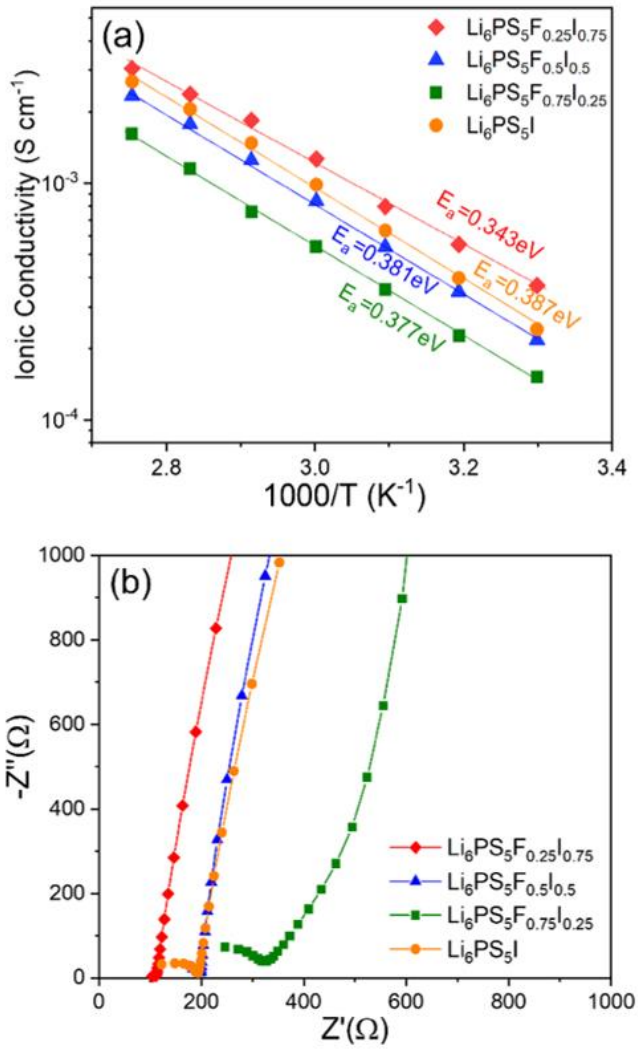

Figure 6.9. (a) Arrhenius plots (30-90 °C) of Li_6PS_5I and hybrid-doped $Li_6PS_5F_xI_{1-x}$ (x = 0.25, 0.5, 0.75) argyrodites and (b) Nyquist plots at room temperature.

6.3.3 Electrochemical stability of F/I hybrid-doped argyrodites in Li symmetric cells

The electrochemical stability of hybrid-doped $Li_6PS_5F_xI_{1-x}$ (x = 0.25, 0.5, and 0.75) and Li_6PS_5I argyrodites towards metallic Li anode was examined in Li symmetric cells. At a current density of 0.05 mA cm^{-2}, stable cycling performance is observed for most argyrodites except $Li_6PS_5F_{0.5}I_{0.5}$.

As shown in **Figure 6.10a**, the polarization voltage of the Li_6PS_5I-cell obviously increases from its initial value of 0.18 V (1st cycle) to 0.37 V (100th cycle), while the other two symmetric cells display more flat voltage profiles. Among them, the $Li_6PS_5F_{0.27}I_{0.25}$-cell shows the lowest polarization voltage at 0.03 V for over 100 cycles, suggesting low interfacial resistance and the formation of a stable interphase layer between the argyrodite and Li metal. **Figure 6.10b** compares the impedance spectra of $Li_6PS_5F_{0.75}I_{0.25}$-based Li symmetric cell before and after 100 cycles, in which the slight change of total resistance (2,950 Ω *vs* 2,780 Ω) further confirms the stable interface in such cell. The long-term cycling stability of $Li_6PS_5F_{0.75}I_{0.25}$-based Li symmetric cell is displayed in **Figure 6.10c**, which runs continuously for 1,100 hours without short circuit. The initial polarization voltage at 0.03 V slightly drops to 0.025V over the first 150 hours due to interfacial reactions to form a stable SEI layer, which further contributes to stable cycling (~0.022 V) for the remaining 950 hours.

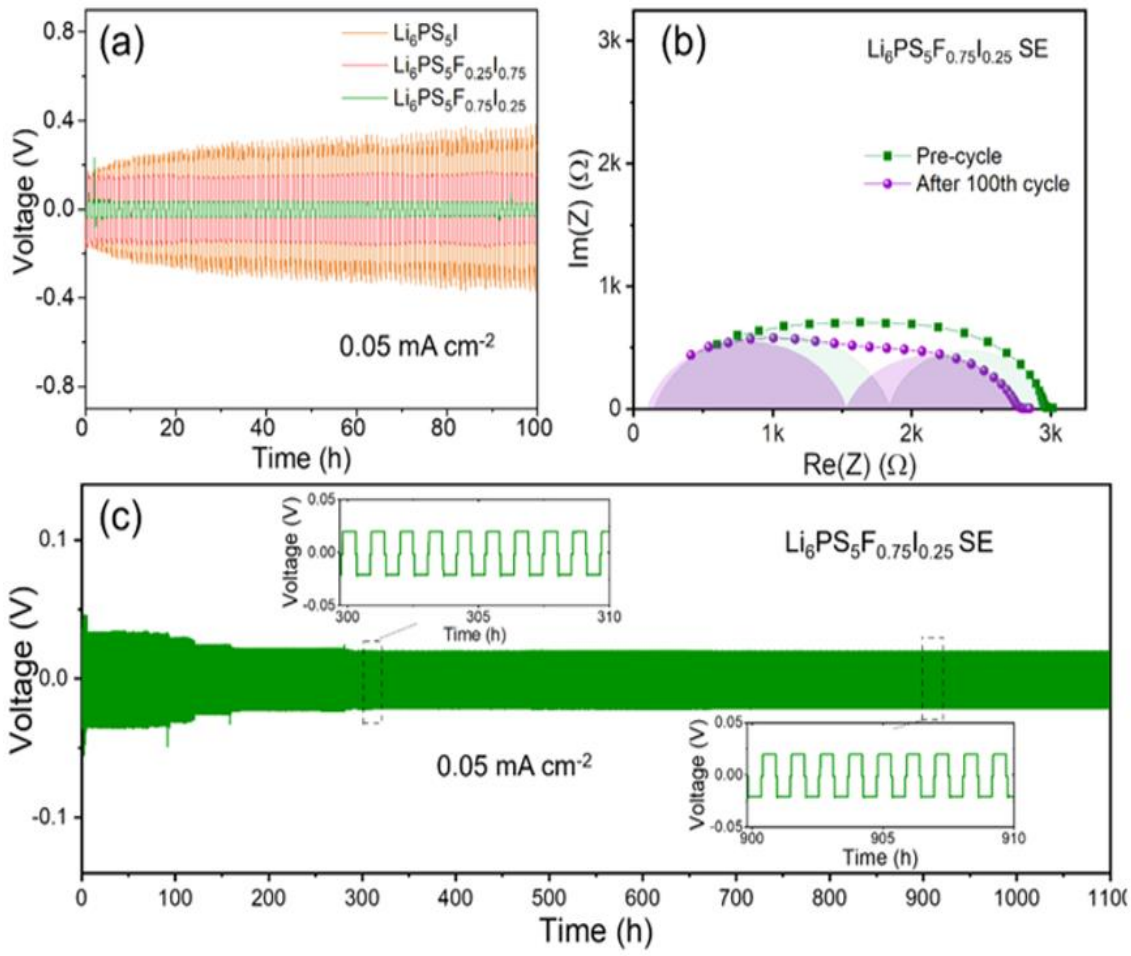

Figure 6.10. (a) Cycling performance of Li symmetric cells with Li_6PS_5I, and hybrid-doped $Li_6PS_5F_xI_{1-x}$ (x = 0.25, 0.75) argyrodites as SEs under current density of 0.05 mA cm^{-2}; (b) Nyquist plots of $Li_6PS_5F_{0.75}I_{0.25}$-based symmetric cell before and after cycling for 100 cycles; (c) voltage profiles of $Li_6PS_5F_{0.75}I_{0.25}$-based symmetric cell cycling up to 1,100 hours (0.05 mA cm^{-2}).

X-ray photoelectron spectroscopy (XPS) was performed on the $Li_6PS_5F_{0.75}I_{0.25}$-symmetric cell after long-term cycling to investigate the chemical composition and to understand the interfacial reactions at the interface layer. In the XPS spectra (**Figure 6.11a-c),** doublet peaks for I 3d at 619.4 eV and 630.5 eV originated from Li-I bonding [206], while

the peak at 56.2 eV for Li 1s is attributed to Li-F bonding.[81] This observation indicates that the interfacial reactions between $Li_6PS_5F_{0.75}I_{0.25}$ and Li metal form an SEI layer that contains both LiF and LiI during the symmetric cell's cycling. In such an SEI layer, the presence of LiF has been found to stabilize interface and prevent Li dendrites in previous reports.[64,166,190–192,196,211] Moreover, LiI may also contribute to the enhancement of interfacial stability, as has been observed for LiBr or LiCl at the interface between Li_6PS_5Br or Li_6PS_5Cl with Li metal.[160,178,212]

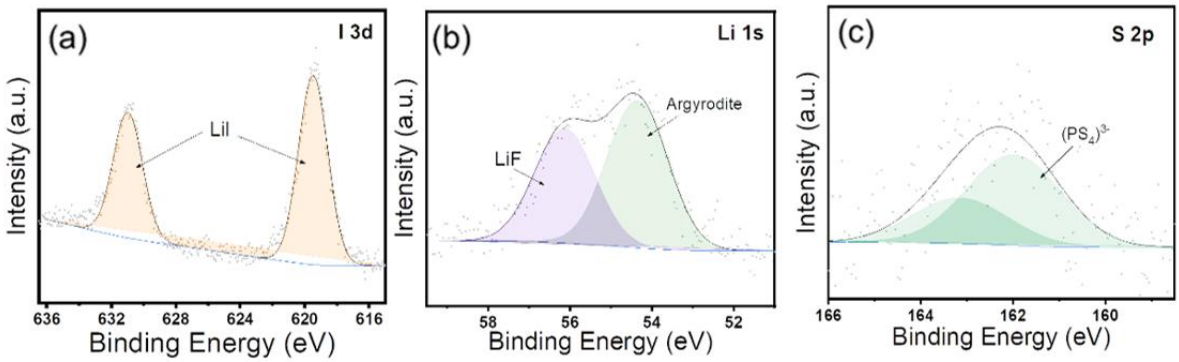

Figure 6.11. XPS spectra of cycled symmetric cell with $Li_6PS_5F_{0.75}I_{0.25}$ SE: (a) I 3d, (b) S 2p, and (c) Li 1s.

6.3.4 Cycling performance of $Li_6PS_5F_{0.75}I_{0.25}$ SE in solid-state Li metal batteries

Using $Li_6PS_5F_{0.75}I_{0.25}$ argyrodite as SE, we assembled solid-state batteries with a structure of Li||SE||LTO, in which LTO is chosen as the positive electrode due to its small volume change and inexpensive elements.[213,214] **Figure 6.12a** presents the charge-discharge voltage profiles within an electrochemical window of 1.0–2.8 V under a C-rate of 0.1 C. The cell delivers an initial specific capacity of about 140 mAh g^{-1}, which slightly decreases to 128 mAh g^{-1} at the 50th cycle. After the 100th and 200th cycles, the cell

maintains decent specific capacity values of 115 and 105 mAh g^{-1}, respectively. In **Figure 6.12b**, a stable cycling performance with high coulombic efficiency close to 99.95% is observed for the $Li_6PS_5F_{0.75}I_{0.25}$-based cell.

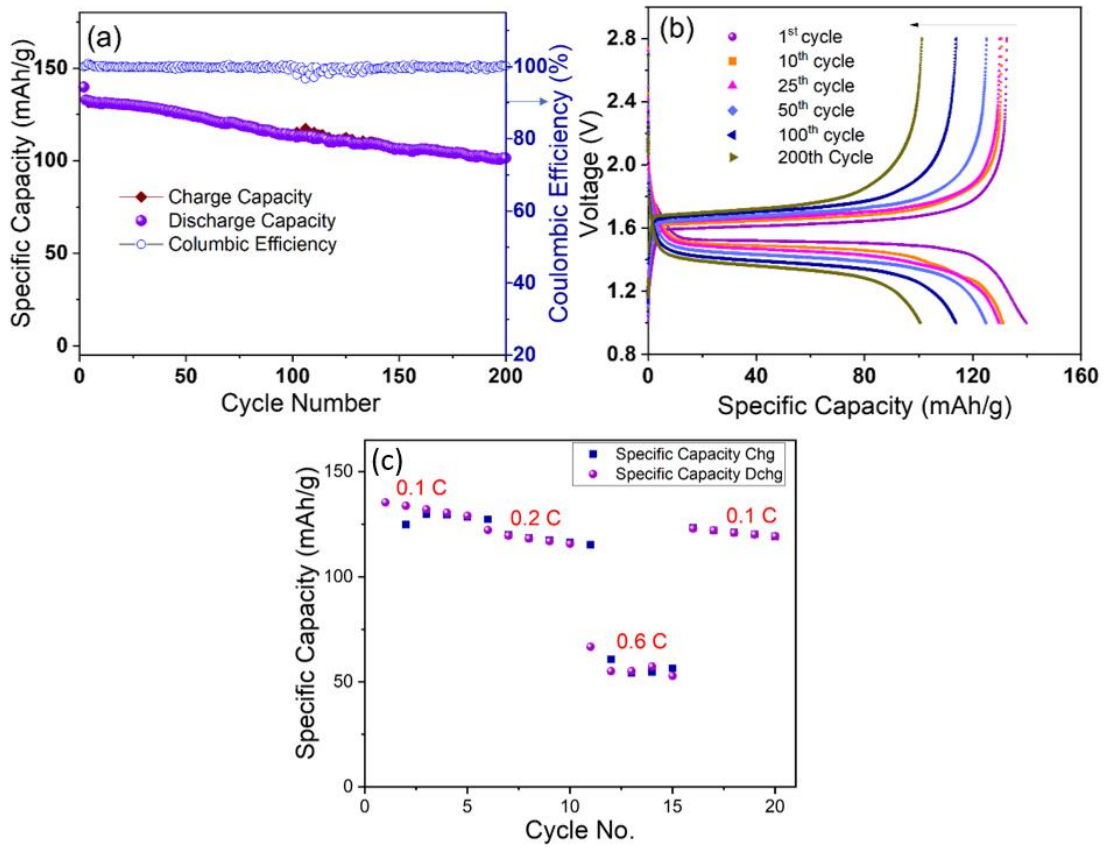

Figure 6.12. (a) Cycling performance and (b) charge-discharge voltage profiles of Li metal batteries with $Li_6PS_5F_{0.75}I_{0.25}$ as SE and LTO as active cathode cycled at 0.1 C rate at room temperature. (c) C-rate performance (0.1, 0.2, and 0.6 C) of solid-state Li metal batteries with $Li_6PS_5F_{0.75}I_{0.25}$ as SE.

When cycled under higher C-rates (**Figure 6.12c**), such a cell retains a high specific capacity of 121 mAh g^{-1} at 0.2 C. While the cell displays a large drop to low capacity at 0.6 C, the specific capacity of the cell returns to values above 120 mAh g^{-1} when the battery

cycling is returned to 0.1 C. The battery cycling performance proves the great electrochemical stability of $Li_6PS_5F_{0.75}I_{0.25}$ argyrodite in solid-state Li metal batteries.

6.4. Conclusion

In summary, we reported the synthesis of highly conductive Li_6PS_5I and hybrid-doped $Li_6PS_5F_xI_{1-x}$ (x = 0.25, 0.5, 0.75) argyrodites through a solvent-based approach. The as-synthesized Li_6PS_5I after 200 °C heat treatment showed an impressive ionic conductivity of 2.5 x 10^{-4} S cm^{-1} at RT. For hybrid-doped $Li_6PS_5F_xI_{1-x}$ argyrodites, $Li_6PS_5F_{0.25}I_{0.75}$ with low F-content displayed the highest ionic conductivity of 3.5 x 10^{-4} S cm^{-1} due to the anion-disordering introduced by F^- and I^- dual dopants. $Li_6PS_5F_{0.75}I_{0.25}$ with high F-content exhibited the best electrochemical stability, which is evidenced by 1,100 hours of stable cycling in Li symmetric cells under 0.05 mA cm^{-2}. Moreover, the assembled solid-state Li metal battery (LTO as cathode) delivered a decent specific capacity of 105 mAh g^{-1} after 200 cycles under 0.1 C. This work expands new compositions in the argyrodite family solid electrolytes and promotes the future development of solid-state Li metal batteries.

CHAPTER 7

POLYMER COMPOSITE WITH LITHIUM FLUORINE-DOPED LITHIUM AGRYRODITE FOR LITHIUM METAL BATTERIES

7.1 Introduction

The continued development of lithium-ion batteries is crucial to meet the ever-growing demands of portable electronics and electric vehicles. Key to this process is the achievement of the Li metal battery, whose unparalleled capacity (3,860 mAh g^{-1}) and high negative reduction potential (-3.04 V *vs* SHE) make it an excellent choice for use as an anode.[215] Several issues continue to plague the use of Li metal in batteries, including instability with electrolyte materials, rapid dendrite formation, and most seriously, high safety issues resulting from flammability and thermal runaway.[182,216] The past decades have seen non-flammable solid electrolytes become a heavily researched topic, with materials such as oxides,[22,29] sulfides[20,54] (including $Li_{10}GeP_2S_{12}$,[217] Li_3PS_4,[218] $Li_7P_3S_{11}$,[140] and Li_6PS_6Cl[64,161]), and polymers (PEO,[85] PVDF,[92] PMMA,[219] and PVDF-HFP[96]) receiving much attention. Each material class has advantages and disadvantages associated with them. For example, sulfides are noted for their high ionic conductivity and thermal stability under high temperatures, but strongly suffer from air instability. Conversely, polymers are highly flexible materials that are relatively easy to process at large scales, but they suffer from low room temperature ionic conductivity.[112]

In recent years, much attention has been devoted to the concept of a ceramic-polymer composite material, which takes advantage of positive aspect of both materials. These efforts have included both oxide-polymer composites,[87,105] and sulfide-polymer composites,[144,216,220] Sulfide-polymer composites are promising due to the possibility of utilizing the high conductivity of sulfide materials alongside the air stable, highly flexible nature of polymer gel membranes. Using this approach, the polymer matrix provides a mechanical scaffolding which can hold the sulfide particles in place, providing an effective web for ion conduction to take place between the inorganic ceramic filler.[114,220,221] The addition of sulfide particles into the matrix also increases ionic conductivity by decreasing crystallinity of the polymer membrane.[108]

Recent research has addressed an important hurdle, as carefully tuned ceramic sulfides have been shown to form a stable SEI layer with electrode materials within a relatively wide voltage window (1.8–4 V), most importantly with metal Li anodes.[222–224] Much of this progress has come with the inclusion of LiF at the electrode/electrolyte interface, a compound which has long been known to be important to the formation of a stable solid electrolyte interface (SEI) layer.[80,167,190,193,225] LiF plays a key role in regulating the transportation of Li^+ ions while simultaneously a) inhibiting the growth of Li dendrites, and b) preventing the decomposition of the electrolyte by blocking electron transfer through the SEI layer.[225] LiF is commonly added through the addition of Li salts in liquid electrolyte solvents, such as LiTFSI, $LiPF_6$, or LiFSI in ethylene carbonate (EC), 1,2-dimethoxyethane (DME), or propylene carbonate (PC).[166,190,226]

An alternative approach for incorporating F into the SEI layer is through doped solid electrolytes. For example, F-doped argyrodites such as $Li_6PS_5F_{0.5}Cl_{0.5}$ or $Li_6PS_5F_{0.7}Cl_{0.3}$

can form a stable and dendrite-preventing SEI layer with lithium metal anodes due to the formation of LiF at the electrode/electrolyte interface layer.[80,81] Utilizing this co-doped halogen material in sulfide-polymer composites creates the possibility for a polymer solid electrolyte that has several desirable attributes, including a) high ionic conductivity, b) high air stability, c) high flexibility, and d) high compatibility with lithium metal anodes. In this work, we report the preparation of a sulfide-polymer composite (PVDF-HFP and fluorine-doped sulfide argyrodite $Li_6PS_5F_{0.5}Cl_{0.5}$) in ambient environment without protective atmosphere. The synthesized composite solid electrolyte (CSE) membranes show that the ionic conductivity is strongly dependent on the weight percentages of sulfide argyrodite in the PVDF-HFP matrix, achieving the highest ionic conductivity of 7.9×10^{-4} S cm^{-1} at room temperature for 5 wt% LPSFCl. Full lithium metal batteries with LFP cathodes are constructed and tested, and a systematic investigation of wetting agent with dissolved LiTFSI is undertaken. PVDF-HFP/5 wt% LPSFCl in conjunction with PYR:DOL (1:1 ratio) and 2M LiTFSI is found to produce an LFP-based battery that maintains a decent capacity of over 125 mAh g^{-1} for 40 cycles, and an LTO-based battery with a capacity of over 120 mAh g^{-1} for 90 cycles. These results indicate the effectiveness of the fluorine-doped sulfide-polymer composite as a possible candidate for use in future solid-state batteries.

7.2 Experimental Sections

7.2.1 Materials synthesis.

Polymer-sulfide composite materials were prepared with commercially purchased PVDF-HFP polymer, LiTFSI salt, and synthesized $Li_6PS_5F_{0.5}Cl_{0.5}$ (LPSFCl) lithium argyrodite solid electrolyte. The ceramic powder was made using the process outlined in

previous chapters.[43] The polymer-sulfide composite was prepared by first creating solutions of PVDF-HFP and LiTFSI in THF at a ratio of 100 mg to 1 mL. These solutions are mixed while a third solution of appropriate amount of ceramic powder is mixed in THF solution for one hour, creating a loose slurry mixture. The PVDF-HFP/LiTFSI solution is combined with the ceramic slurry and stirred via magnetic bar for 45 minutes. The polymer coating is cast on a PTFE plate (Area = 11.34 cm^2) in ambient atmosphere and left to evaporate for ~18 hours. The different amounts of LPSFCl powder added to the polymer matrix were calculated based on weight percentages, either 0% LPSFCl (0-wt%LPSFCl), 2% LPSFCl (2-wt%LPSFCl), 5% LPSFCl (5-wt%LPSFCl), or 10% LPSFCl (10-wt%LPSFCl).

7.2.2 Structural characterizations.

X-ray diffraction (XRD, Bruker D8 Discover) was measured for Li_6PS_5I and co-doped samples using nickel-filtered Cu-Kα radiation (λ = 1.5418 Å) for phase identification. XRD refinement was carried out using the GSAS-II crystallography data analysis software. Raman spectroscopy (Renishaw in Via Raman/PL Microscope) was performed on synthesized samples using a 632.8 nm emission line of a HeNe laser. TESCAN Vega3 scanning electron microscope (SEM) was used to study the morphology of samples.

Differential scanning calorimetry (DSC) was used to determine the crystallinity (x_c) of the polymer electrolyte membrane. The test was run in the temperature range of -60–80 ℃, with a heating rate of 10 ℃ min^{-1}, with a sample mass of 5 mg. The crystallinity was calculated using **Equation 7.1**[108]

$$x_c = \frac{\Delta H_m}{\Delta H_{PVDF-HFP}} \qquad \textbf{Eq. 7.1}$$

where $\Delta H_{PVDF-HFP}$ is the melting enthalpy of pure crystal PVDF-HFP (104.7 J g^{-1})[95] and ΔH_m is the melting enthalpy of the measured composite SE material.

7.2.3 Electrochemical Characterizations.

After being cast for 18 h, the prepared composite membranes were placed in a vacuum chamber for 30 minutes to completely remove residual solvent. Following this, the membranes were cut using a hole puncher into ½" circles for further testing. The polymer membrane samples (with stainless steel on each side) were subjected to electrochemical impedance spectroscopy (EIS) measurements to evaluate the conductive properties using a Bio-Logic SP300 Potentiostat using an excitation voltage of 100 mV within a frequency range of 1 MHz to 1 Hz. The battery structure used composite polymer membranes as SE, Li metal as the anode, and $LiFePO_4$ (LFP) or $Li_4Ti_5O_{12}$ (LTO) as the active cathode. The composite cathode consisted of super P, PVDF binder and LTO with a weight ratio of 1:1:8. Before assembling, the composite membranes were soaked in PYR ionic liquid for 2 minutes, using different ratios of LiTFSI salt and DOL. The assembled Li metal batteries were cycled under different C-rates (0.1, 0.2 and 0.6) at room temperature, which were calculated based on the theoretical specific capacity of LTO (0.175 Ah g^{-1}).

7.3. Results and Discussion

7.3.1 Characterization and Morphology of Sulfide/PVDF-HFP Composites

XRD patterns of the $Li_6PS_5F_{0.5}Cl_{0.5}$/PVDF-HFP composite materials with different weight percentages of LPSFCl are seen in **Figure 7.1**. The dominant phase in this material is the polymer/LiTFSI matrix, with LPSFCl material constituting a small enough percentage as to not show up in XRD scans. PVDF-HFP/LiTFSI is a primarily non-crystalline material, as can be seen in the scan for pure PVDF-HFP/LiTFSI, showing broad

peaks at 2θ = 22° and 40°, in good agreement with previous reports on this material.[113,227–229] The representative diffraction peaks for argyrodite phase at 2θ = 25.5°, 30°, and 31.2°, are not present in the composite XRD.[43,119] When LPS wt% is much higher (75%), these argyrodite peaks are observed, even when the polymer is cast in ambient air. This indicates that the amount of the polymer network encapsulates the small amount LPS particles almost completely when wt% < 10%.

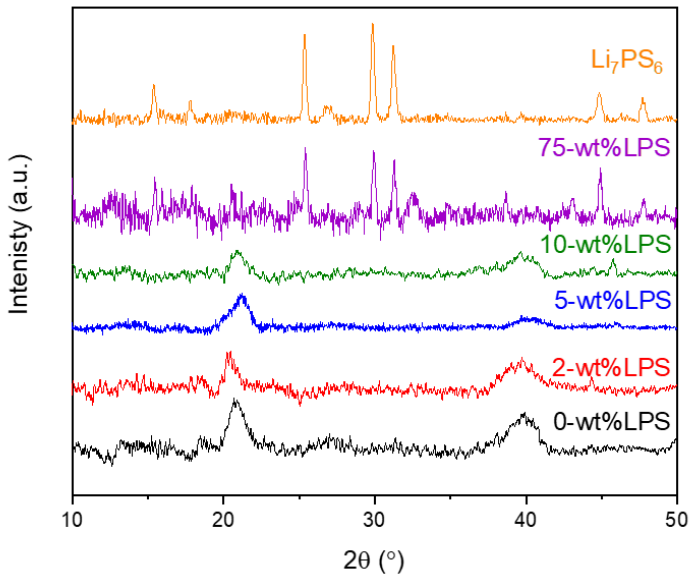

Figure 7.1. XRD patterns of PVDF-HFP/LiTFSI polymer membranes with different amounts of LPS sulfide SE added.

Raman spectra of the composite SEs are shown in **Figure 7.2**. The main peak at 750 cm^{-1} is also attributed to the PVDF-HFP/LiTFSI matrix, with no obvious peaks observed indicating the PS_4^{3-} tetrahedra present in the argyrodite material. This is in accordance with the XRD results.

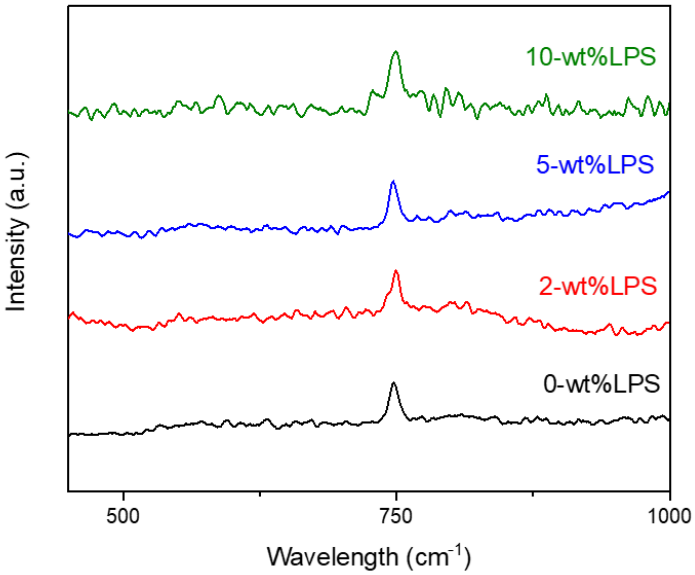

Figure 7.2. Raman spectra of PVDF-HFP/LiTFSI polymer membranes with different amounts of LPS sulfide SE added.

Morphological evaluation was conducted via SEM shown in **Figure 7.3**. Cross sectional imaging of the membrane confirms the width of the membrane as 50 μm (**Figure 7.3a**) Direct imaging of the SE film shows a mostly smooth surface with some amount of small holes as a result of solvent evaporation (**Figure 7.3b**). The pure PVDF-HFP/LiTFSI membrane is clear and transparent, while the addition of LPSFCl materials results in a more opaque film. The composite SEs are confirmed as both thin and flexible, and stable in ambient air. EDS evaluation was conducted to determine the elemental composition of the membrane. The presence of argyrodite $Li_6PS_5F_{0.5}Cl_{0.5}$ SE is evidenced by the even distribution of P, S, and Cl atoms. F atoms can be attributed to both the ceramic solid electrolyte as well as the organic polymer membrane and lithium salt.

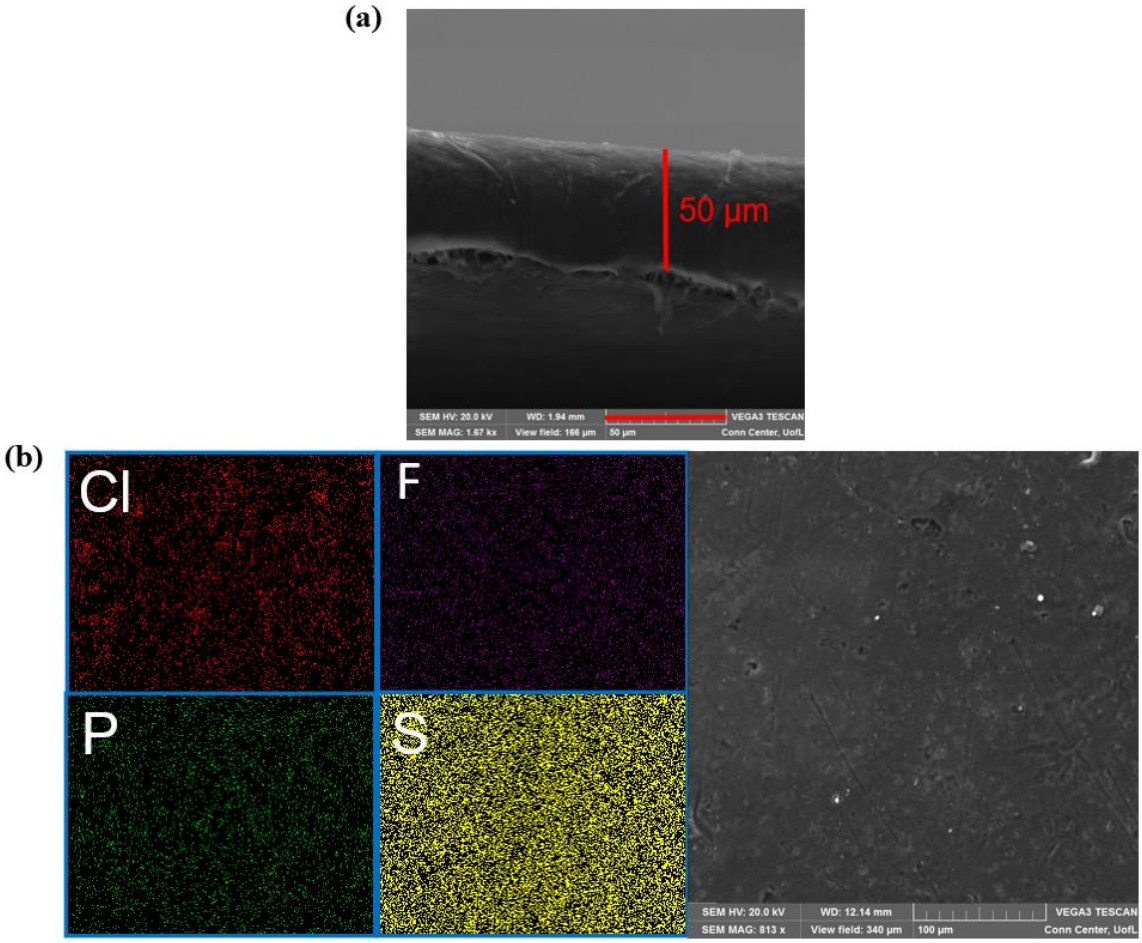

Figure 7.3. (a) Cross sectional SEM image of 5%-LPS PVDF-HFP/LiTFSI polymer membrane. (b) EDS results and SEM image of SEM image of 5%-LPS PVDF-HFP/LiTFSI polymer membrane

7.3.2 Ion Conduction of Composite Polymer Electrolytes.

Figure 7.4 shows the EIS spectra of RT CSEs with differing amounts of ceramic LPSFCl material added. The pure polymer (0 wt%-LPSFCl) sample has a higher resistance value(~180 Ω; 2.2×10^{-5} S cm^{-1}) than the composite samples as a result of its higher degree of crystallinity. The addition of ceramic SE material to the polymer matrix decreases crystallinity and increases the amorphous regions responsible for fast ion conduction, as

evidenced by the drastic drop in resistance observed for the 2 wt%-CSE and 5 wt%-CSE samples, which results in ionic conductivity values of 5.3×10^{-4} S cm^{-1} and 7.9×10^{-4} S cm^{-1}, respectively. These results are an order of magnitude higher than PVDF-HFP composite made with LLZTO and are several times higher than previous PVDF-HFP/Sulfide ceramic composites.[113,116,220,228,229] This is confirmed by DSC results (**Figure 7.5**) which display a drop in crystallinity from 66% in 0 wt%-LPSFCl to 37% and 47% in 2 wt%-LPSFCl and 5 wt%-LPS, respectively. While crystallinity was less in the 2-wt% sample, the increased conductivity observed for the 5-wt% sample can be explained by the beneficial effects of LPSFCl as an ion conductor.

Further increasing the LPSFCl content (10 wt%) results in a decrease of the ionic conductivity, which can likely be attributed to the ambient environment the CSE is cast in. Small amounts of LPSFCl SE can be surrounded and protected by the PVDF-HFP polymer material, but this is not possible with higher amounts of the sulfide material. The overnight exposure to air likely contributes to the formation of H_2S and Li_2S, greatly inhibiting the ion transport properties of the CSE. Regardless, the 10 wt%-LPSFCl sample still achieves a decent ionic conductivity value of 1×10^{-4} S cm^{-1}, which comparable to previous reports where the CSE is cast under protected environment).[113]

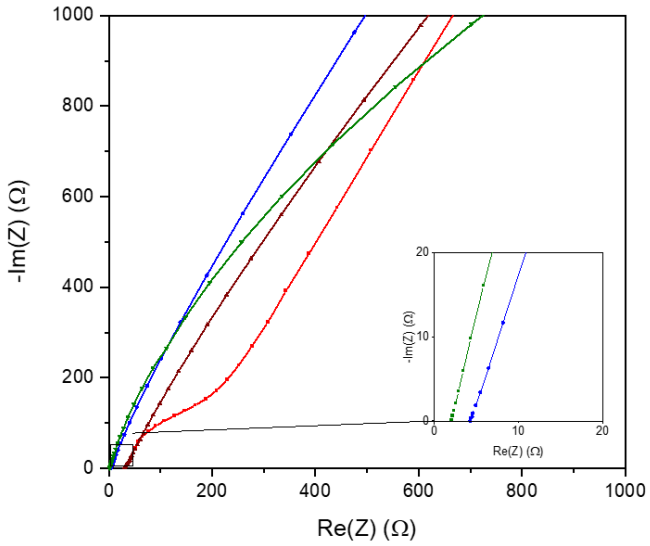

Figure 7.4. EIS results for LPS PVDF-HFP/LiTFSI polymer membrane with 0% (red), 2% (blue), 5% (green), and 10% (brown) weight percent LPS SE.

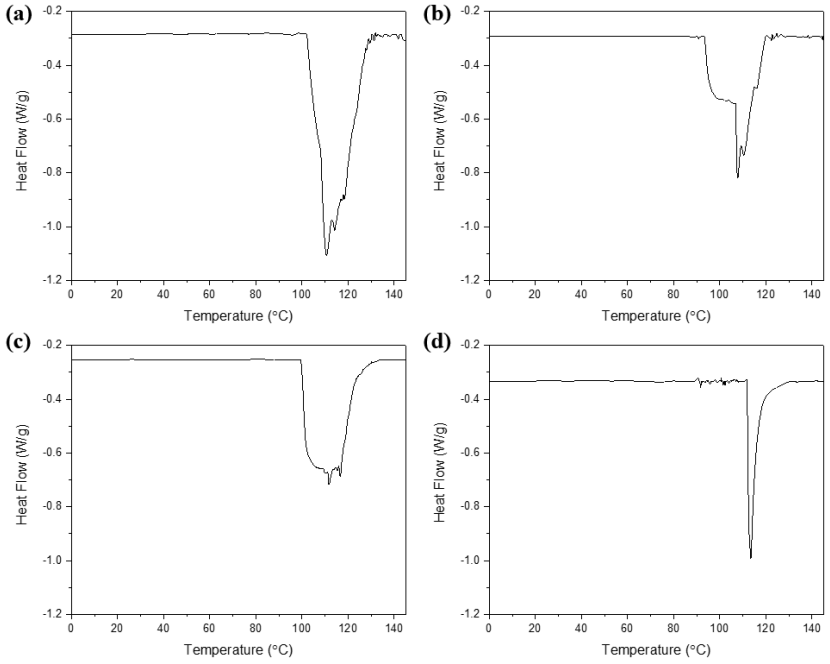

Figure 7.5. DSC results for PVDF-HFP/LiTFSI polymer membranes with different amounts of LPS sulfide SE added. (a) 0 wt%-LPSFCl, (b) 2 wt%-LPSFCl, (c) 5 wt%-LPSFCl, (d) 10 wt%-LPSFCl

7.3.3 Electrochemical Performance of Composite Polymer Electrolytes in Li Metal Batteries

LFP||LPSFCl/PVDF-HFP/LiTFSI||Li full cell batteries were assembled and tested to evaluate the battery cycling performance using different weight percentages of LPSFCl and different PYR ionic liquid-based configurations. Prior to battery assembly, the as-synthesized CSEs were soaked in either PYR or PYR/DOL with variable amounts of dissolved molar LiTFSI salt. **Figure 7.6** shows the cycling performance of a 5-wt%LPS CSE soaked in pure PYR with 1M added LiTFSI (PYR/1M LiTFSI). As can be observed from the capacity values, this battery was unable to cycle at all. This is attributed to the high viscosity value of PYR/1M LiTFSI, which results in prohibitively high interfacial resistance and negligible active material usage.[230]

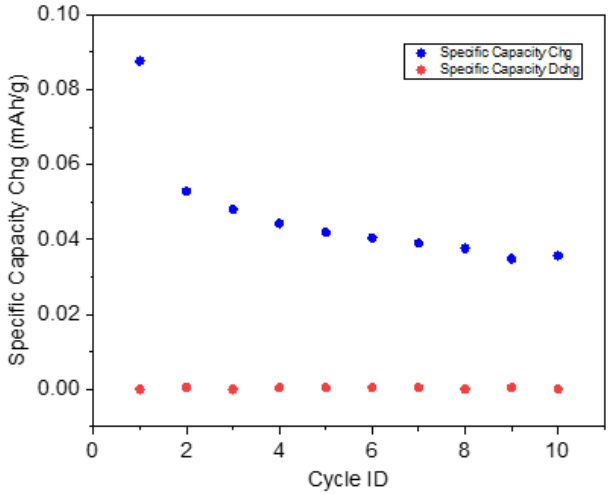

Figure 7.6. Battery data of LFP||5-wt%LPS/PVDF-HFP/LiTFSI||Li cell with 1:1 DOL:PYR/1M LiTFSI ionic liquid.

To reduce the viscosity of PYR ionic liquid, adding a co-solvent such as DOL is one appropriate approach..[230] This strategy was employed and tested on the various LFP||LPSFCl/PVDF-HFP/LiTFSI||Li full cells with differing LPSFCl weight percentages. **Figure 7.7** shows the performance of LFP||Li cell with pure polymer (0-wt%LPSFCl) with 1:1 DOL:PYR/1M LiTFSI at 0.2C. This 1:1 ratio with 1M LiTFSI reduces the viscosity of the ionic liquid to 6.91 cP.[230] The cell with no added ceramic sulfide SE shows a decent first cycle capacity, but displays poor capacity retention over subsequent cycles. By cycle 40, the capacity has dropped to ~65 mAh g^{-1}.

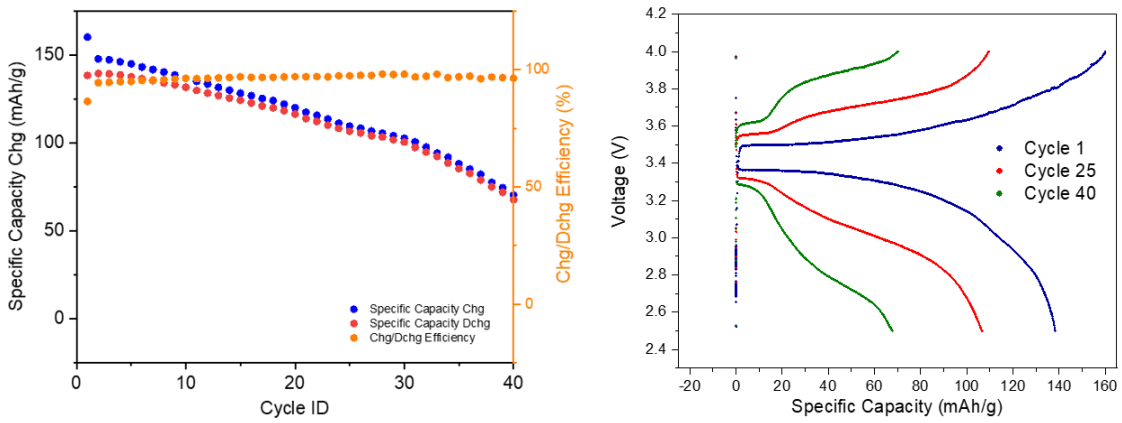

Figure 7.7. Battery data of LFP||0-wt%LPS/PVDF-HFP/LiTFSI||Li cell with 1:1 DOL:PYR/1M LiTFSI ionic liquid.

In comparison, when the cell is assembled using 2-wt%LPSFCl CSE, the charge/discharge curves (**Figure 7.8a)** clearly show a flat plateau at 3.5/3.3 V for the 1st cycle with specific capacity of 140 mAh g^{-1}. As cycling proceeds, the discharge capacity values decrease to 135 mAh g^{-1}at 10th cycle with larger polarization voltages (3.6/3.2 V), and then drops to 83 mAh g^{-1} at the 40th cycle. Although this performance is better than

pure polymer, it seems that the small amount of added sulfide SE was not enough to form the stable SEI layer necessary for long term cycling.

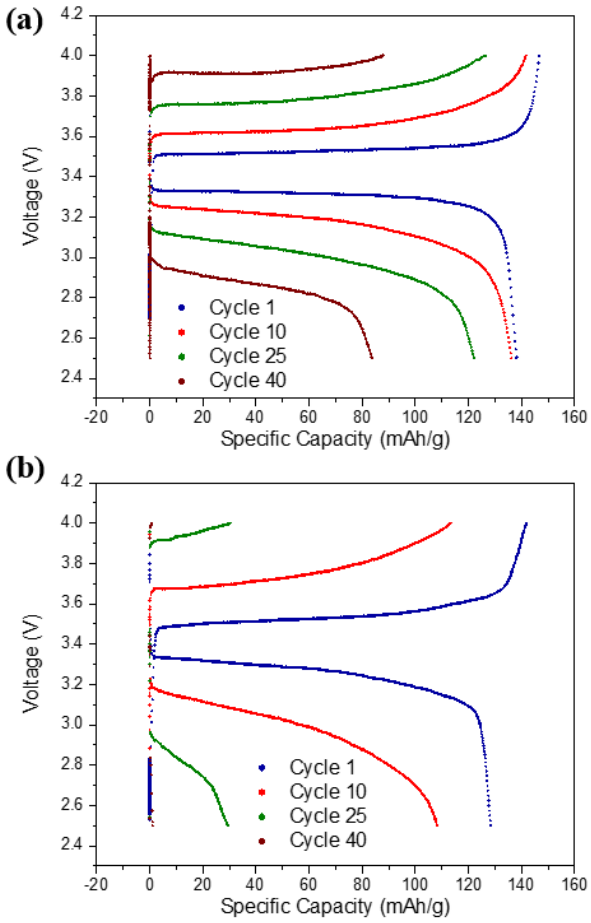

Figure 7.8. (a) Battery data of LFP||2-wt%LPS/PVDF-HFP/LiTFSI||Li cell with 1:1 DOL:PYR/1M LiTFSI ionic liquid. (b) Battery data of LFP||10-wt%LPS/PVDF-HFP/LiTFSI||Li cell with 1:1 DOL:PYR/1M LiTFSI ionic liquid.

Conversely, the LFP||Li cell using 10-wt%LPSFCl CSE with 1:1 DOL:PYR/1M LiTFSI is shown in **Figure 7.8b**. From the beginning, this cell displays both a lower initial capacity (130 mAh g^{-1} for the first cycle) and a pronounced and rapid capacity fade. This resulted in the cell losing nearly all of its capacity by cycle 25. This can likely be attributed

to the poor ion conducting properties of the 10-wt%LPS CSE sample, as well as the possibility of LPS material not being encapsulated by the polymer, meaning the material would have already reacted during the casting process. This could have resulted in H_2S formation and LPS degradation into polysulfides which would have compromised the battery performance.

Finally, the 5-wt%LPSFCl CSE-based LFP||Li cell (**Figure 7.**9) performed the best out of all the tested CSEs, with both high initial capacity (158 mAh g^{-1} for the first cycle) and a steady coulombic efficiency for over 40 cycles. This improved performance is due both the high intrinsic ionic conductivity of the 5-wt% LPS CSE, as well as the small amount of LPS to both be entirely protected by the polymer matrix and still usable at the interface to create good cycling performance. After 40 cycles, this cell still delivers specific discharge capacity pf 125 mAh g^{-1}. The promising performance of 5-wt% LPS CSE led us to choose this composition for further testing.

To further enhance the electrochemical cycling of LFP||Li cell with 5-wt%LPSFCl CSE, the concentration of wetting agent (DOL:PYR/LiTFSI) is investigated. First, we increase the DOL: PYR ratio to 2:1 instead of 1:1 to decrease the viscosity of the ionic liquid. Surprisingly, the cell with the increased ratio of DOL:PYR had a very low initial capacity of ~75 mAh g^{-1}, which then steadily declined over 40 cycles to ~ 10 mAh g^{-1}. (**Figure 7.10**). Such poor cycling performance is possibly due to the fact that high concentration of DOL increases the relative solubility of the ceramic LPS, taking it out of the polymer matrix and to into the solvent.[230]

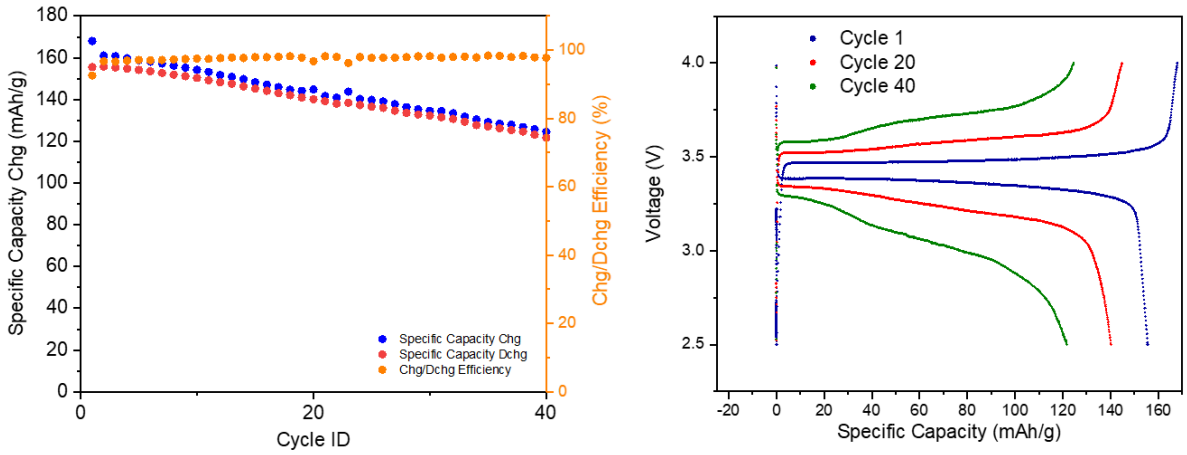

Figure 7.9. Battery data of LFP||5-wt%LPS/PVDF-HFP/LiTFSI||Li cell with 1:1 DOL:PYR/1M LiTFSI ionic liquid.

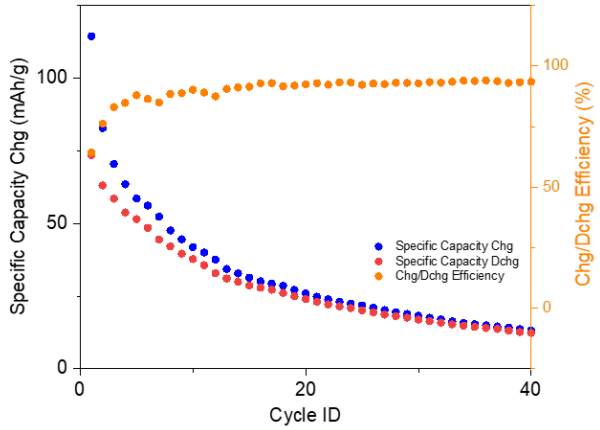

Figure 7.10. Battery data of LFP||5-wt%LPS/PVDF-HFP/LiTFSI||Li cell with 2:1 DOL:PYR/1M LiTFSI ionic liquid.

In response to the previous results, the DOL:PYR ratio was returned to 1:1, and instead the possibility of increasing the concentration of LiTFSI to 2M rather than 1M was explored. **Figure 7.11** shows the cycling performance of an LFP||5-wt%LPS/PVDF-HFP/LiTFSI||Li with the CSE soaked in 1:1 DOL:PYR/2M at 0.2C. Increasing the salt concentration leads to a lower initial capacity of 130 mAh g^{-1}, which is in line with previous

reports on 1:1 DOL:PYR/2M.[230] Additionally, the 2M LiTFSI concentration leads to an increase of coulombic efficiency of >99% (after an initial "aging" process in the first 15 cycles). These phenomena are explained by the increased salt concentration resulting in a reduction of free solvent molecules (i.e. DOL). This shifts the location of the LUMO from the solvent towards the $TFSI^-$ anions, which in turn results in the formation of more inorganic compounds such as LiF and Li_2O.[231] These compounds both limit the Li^+ mobility across the interface (resulting in the lower capacity) and contribute to a stable SEI layer (resulting in the improved coulombic efficiency). This process is observed in real time, where the first several cycles show increased charge capacities, which can be interpreted as excess Li^+ ions being used up in the formation of SEI product molecules. After ~15 cycles, this process has reached equilibrium, and the battery cycling performance resumes with excellent capacity retention and coulombic efficiency.

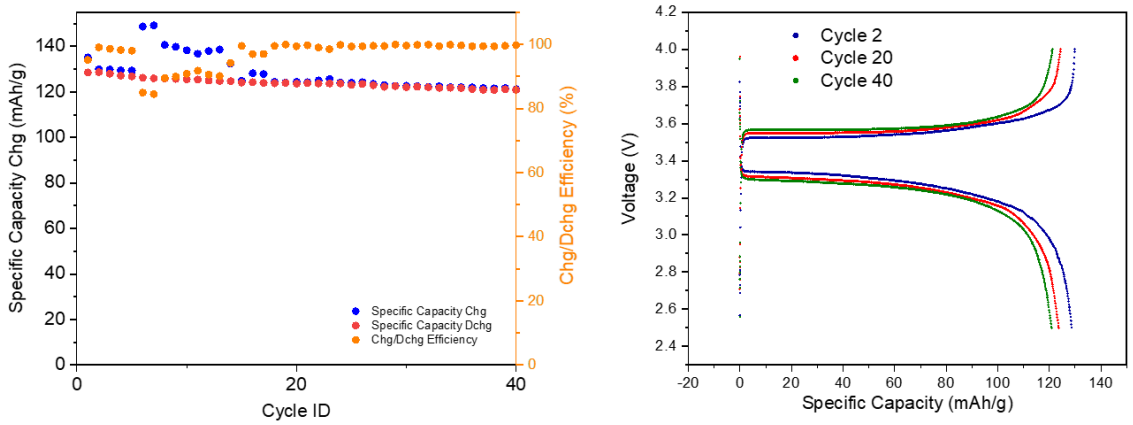

Figure 7.11. Battery data of LFP||5-wt%LPS/PVDF-HFP/LiTFSI||Li cell with 1:1 DOL:PYR/2M LiTFSI ionic liquid.

The previous cells all used an LFP cathode because of its high operating voltage values which leads to batteries with higher energy density. However, the high voltage also

contributes to more rapid molecular decomposition of the various components within the battery, making it difficult to build batteries with high C-rates or very long cycle lives. As such, LTO-based Li metal batteries were also tested, which are noted for their excellent stability and high safety.

Figure 7.12 shows the C-rate performance of an LTO||5-wt%LPS/PVDF-HFP/LiTFSI||Li cell soaked in 1:1 DOL:PYR/2M LiTFSI. At 0.1C, the battery has a good capacity of 125 mAh g^{-1} and maintains good coulombic efficiency. This value is barely changed when the C-rate is increased to 0.2C. The cell maintains a high capacity above 100 mAh g^{-1} even at a very high C-rate of 0.8C, and 85 mAh g^{-1} at 1C. After cycling at 1C for 5 cycles, the cell was returned to 0.1C where it returned to its initial capacity of 125 mAh g^{-1}.

Figure 7.13 shows the cycling performance of a similar cell cycled at 0.2C for an extended period. As with the LFP cell, the first several cycles show variable capacity values as Li^+ is used up in the formation of a stable and robust SEI layer. By the 10^{th} cycle, a stable capacity of 120 mAh g^{-1} has been reached with a coulombic efficiency >99%. This capacity is maintained for over 90 cycles. These results indicate the promising possibility of using 5-wt%LPS CSE with PVDF-HFP/LiTFSI as the electrolyte in both LFP and LTO-based Li metal batteries.

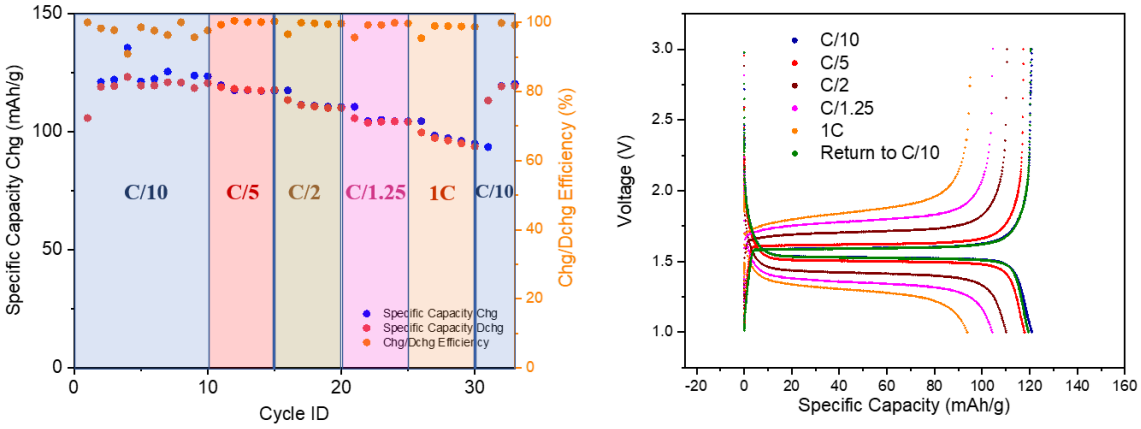

Figure 7.12. C-Rate test of LTO||5-wt%LPS/PVDF-HFP/LiTFSI||Li cell with 1:1 DOL:PYR/2M LiTFSI ionic liquid.

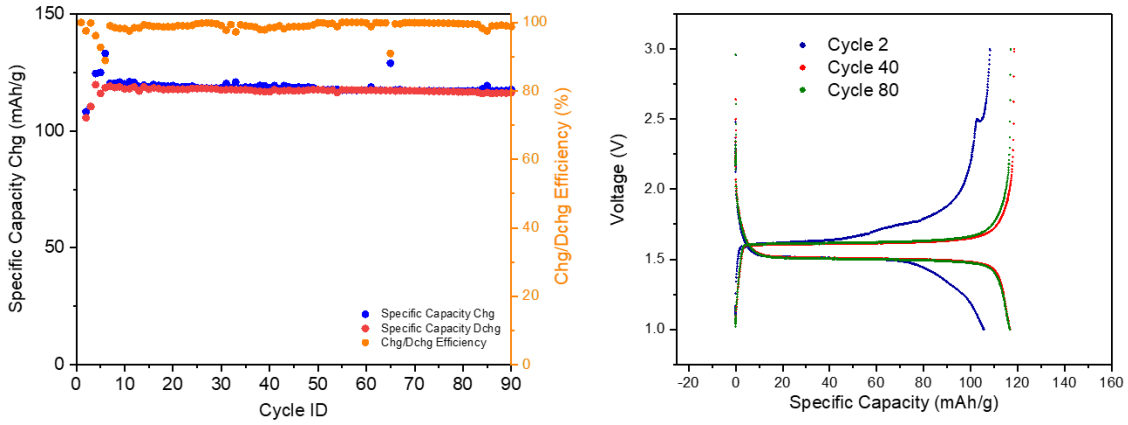

Figure 7.13. Battery data of LTO||5-wt%LPS/PVDF-HFP/LiTFSI||Li cell with 1:1 DOL:PYR/2M LiTFSI ionic liquid.

7.4 Conclusion

In summary, we demonstrated the synthesis of a sulfide-incorporated composite polymer electrolyte in ambient environment by embedding $Li_6PS_5F_{0.5}Cl_{0.5}$ argyrodite into a PVDF-HFP matrix. The preparation process was carried out in an unprotected environment conditions overnight yet showed very little effects of sulfide decomposition,

demonstrating the protective qualities of the PVDF-HFP polymer which. Moreover, the addition of 5-wt% LPSFCl exhibited the highest ionic conductivity of 8×10-4 S cm-1 at room temperature, dramatically higher than that of pure polymer as a result of a decrease in crystallinity. Following this, the effects of different ionic liquid/co-solvent mixtures with varying salt concentrations were explored through the electrochemical cycling of full cells, and an optimized composition of 1:1 ratio of DOL:PYR ionic liquid with a 2M LiTFSI was established. Utilizing 5-wt% LPSFCl CSE, the LFP||Li cell achieved a high initial capacity of 158 mAh g^{-1} for the first cycle and retained a decent value of 120 mAh g^{-1} after 40 cycles. Moreover, the LTO-based cells showed a capacity of 125 mAh g^{-1} with even longer capacity retention of up to 90 cycles. These results demonstrate the feasibility of the preparation of sulfide-CSEs in ambient environment, and show that composite SEs are a promising candidate for use in future solid-state Li metal batteries.

CHAPTER 8

CONCLUSION

This dissertation seeks to address specific issues related to the development of solid electrolytes in solid-state Li metal batteries. These issues include the following: manufacturing concerns of solid electrolyte materials due to harsh synthesis conditions, the low ionic conductivity of solid electrolyte materials, safety concerns associated with Li metal anodes due to the propagation of Li dendrites through the electrolyte, poor interfacial stability between electrodes and solid electrolyte, and the air sensitivity and brittle nature of sulfide solid electrolytes. Each of these issues were addressed in different ways with a common theme of developing sulfide argyrodites as the ideal material for use as solid electrolytes in solid-state batteries. The conclusions are organized in five parts.

8.1 Development of Liquid Synthesis Process for Li_7PS_6 and Li_6PS_5X (X = Cl, Br, I)

Prior to the publication of the manuscripts outlined in Chapter 3, the vast majority of argyrodite solid electrolytes described in the literature were synthesized using harsh solid-state methods. These methods included long periods of ball milling followed by long periods of high temperature heat treatment, typically 550 °C for 10+ hours. In response, this dissertation outlines an alternative, solvent-based process using nontoxic ethanol. This process is both economical and fast, taking less than 3 hours total to complete. As such, solvent-based synthesis is a much more attractive option for large scale manufacturing.

Pure phase argyrodite Li_7PS was synthesized using a stoichiometric mixture of Li_2S and Li_3PS_4 which was dissolved in ethanol and reprecipitated using a 200 °C heat treatment. The resulting powder was collected and further tested to confirm phase purity and electrochemical properties. It was found that Li_7PS_6 displayed pure argyrodite phase, with XRD revealing primary peaks at 2θ = 25.5, 30, and 31.2°, corresponding to (220), (311), and (222) planes in the cubic HT-phase of Li_7PS_6 (space group $F\bar{4}3m$). Additionally, Raman spectroscopy revealed the presence of the $(PS_4)^{3-}$ tetrahedra in liquid synthesized Li_7PS_6. SEM images reveal a granular morphology attributable to use of ethanol solvent, and EDS confirms a homogenous distribution of P and S atoms. The ionic conductivity of solvent-synthesized Li_7PS_6 was found to be 1.1×10^{-4} S cm^{-1} with an activation energy of 0.43 eV. Finally, Li_7PS_6 was shown through CV and symmetric cell testing to have decent stability with Li metal, though higher current densities results in harmful interfacial reactions.

In addition to pure phase Li_7PS_6, the solvent method was utilized to synthesized halogen doped Li_6PS_5X (X = Cl, Br, I). Similar to pure Li_7PS_6, all halide-doped samples display sharp peaks at $2\theta \approx 25.5^o$, 30^o, 31.2^o, and Raman spectroscopy revealed the presence of the $(PS_4)^{3-}$ tetrahedra. Due to the replacement of S^{2-} at the 4d position with either Cl^- or Br^-, Cl and Br-doped samples displayed improved ion conducting properties compared to pure phase Li_7PS_6, with values of 3.4×10^{-4} S cm^{-1} and 3.1×10^{-4} S cm^{-1}, respectively. Additionally, the presence of LiX materials at the interface improved the electrochemical stability of these materials with Li metal.

8.2 Investigation of Conductive Properties and Interface Stability of LiCl-Rich Argyrodite Li_6PS_5Cl for High-Performance Batteries

This chapter focuses on the modification of the electrode/electrolyte interface by two means: excess Cl doping and the addition of trace amounts of PC. LiCl-rich argyrodites $Li_6PS_5Cl \cdot xLiCl$ ($0 \leq x \leq 2$) were made through tuning the ratios of $LiCl:Li_3PS_4$ during solvent synthesis. It was found through XRD that excess LiCl does not enter the argyrodite structure, but instead exists as pure LiCl. Moreover, the addition of PC on the SE surface does not change the crystal structure, even after three weeks of soaking. Despite the presence of pure LiCl, the ionic conductivity of $Li_6PS_5Cl \cdot LiCl$ was not negatively affected, and was actually found to increase to 5.3×10^{-4} S cm^{-1}, which is possibly a result of the space-charge effect. Further LiCl doping does result in a decrease of ionic conductivity, likely due to the insulative properties of LiCl.

The presence of LiCl was found to have an additional advantage, as it could be utilized in the SEI layer at the electrode/electrolyte interface. CV scans show good compatibility with Li metal up to 5 V, with $Li_6PS_5Cl \cdot LiCl$ having higher anodic/cathodic current values than Li_6PS_5Cl. Moreover, during symmetric cell testing, $Li_6PS_5Cl \cdot LiCl$ showed a lower polarization voltage than Li_6PS_5Cl and could withstand higher current densities, up to 0.1 mA cm^{-2}. The interfacial properties of $Li_6PS_5Cl \cdot LiCl$ was further improved through the addition of trace amounts of PC at the interface, where symmetric cells showed stable cycling as high as 1 mA cm^{-2}.

Finally, full cell Li metal batteries were constructed using LTO cathode and $Li_6PS_5Cl \cdot LiCl$ SE with trace amounts of added PC. These cells were able to achieve a high current density of 135 mAh g^{-1} at a C-rate of 0.2C with stable cycling. C-rate tests showed good performance even up to 2C. At 1C, the LTO| $Li_6PS_5Cl \cdot LiCl$/PC|Li cell displayed an impressive capacity of 116 mAh g^{-1} with 99.9% coulombic efficiency for over 200 cycles.

After cycling, the cell was disassembled for XPS testing. Here it was found that the SEI layer formed was a combination of LiCl salt and organic Li_2CO_3. The excellent cycling ability of the full cell battery is attributed to this combination of molecules. These results indicate the promising combination of LiCl-rich argyrodite coupled with PC as a viable route for the development of high performance SSBs.

8.3 Synthesis of Fluorine-Doped Lithium Argyrodite Solid Electrolytes for Solid-State Lithium Metal Batteries

Having investigated the effects of LiCl on the SEI layer in argyrodite-based batteries, it was desirable to explore the effects of LiF, which is a more commonly cited component of robust SEI layers. Moreover, F-doped lithium argyrodites had received very little attention, and had never previously been synthesized using solvent-based methods. A combination of both LiF and LiCl was even more intriguing, as a dual-doped material could possess beneficial properties from both dopants.

F-doped $Li_{5+y}PS_5F_y$ and co-doped $Li_6PS_5F_{0.5}X_{0.5}$ (X = Cl, Br) were synthesized using the solvent method, with properly tuned ratios of LiF to Li_2S. Unlike in Cl and Br-doped argyrodites, very little LiF was able to be successfully incorporated into the crystal structure, with XRD revealing the presence of pure LiF when $y \geq 0.5$. It was found that Li_6PS_5F possessed the highest ionic conductivity and lowest activation energy of all F-doped samples, with values of 2.3×10^{-4} S cm^{-1} and 0.45 eV, respectively. Ion transport properties were improved through co-doping, as $Li_6PS_5F_{0.5}Cl_{0.5}$ displayed an ionic conductivity of 3.5×10^{-4} S cm^{-1} and an activation energy of 0.32 eV.

Compatibility of F-doped and co-doped argyrodites was tested using symmetric cells. Co-doped $Li_6PS_5F_{0.5}Cl_{0.5}$ had the lowest interfacial resistance value of the three, and

was able to withstand a high current density of 0.15 mA cm^{-2} for over 300 cycles. XPS testing on the cycled symmetric cell revealed an SEI layer with a combination of LiCl, LiF, and Li_3P, which was attributed as the cause of the excellent performance by AIMD simulations. Finally, full cell batteries with LFP||$Li_6PS_5F_{0.5}Cl_{0.5}$||Li were cycled at 0.2C and achieved an excellent initial capacity of 130 mAh g^{-1} which remained above 100 mAh g^{-1} after 50 cycles. These results indicate the positive role that F-doping has on the interfacial stability of Li metal batteries with solid electrolytes.

8.4 Highly Conductive Iodine and Fluorine Dual-Doped Argyrodite Solid Electrolyte for Lithium Metal Batteries

Of the three most common halogens used for doping lithium argyrodites (Cl, Br, and I), iodine has traditionally been seen as the worst option as a result of its low intrinsic ionic conductivity. This is due to the tendency for I^- to replace S^{2-} at the 4a site rather than the 4d site, creating a large degree of anion order. However, Li_6PS_5I made using the solvent synthesis process shows a surprisingly high ionic conductivity, and this chapter focuses on exploring the reasons for this phenomenon. In addition, the co-doping technique from the previous chapter was implemented to better improve the interfacial properties of I-doped argyrodites in Li metal batteries. Doping with both F and I provides the benefits of both improved ionic conductivity due to the cohabitation of the 4a and 4d sites, and the interface stabilization properties of LiF.

Following the same liquid-based process as previously described, Li_6PS_5I and $Li_6PS_5F_xI_{1-x}$ (x = 0.25, 0.5, 0.75) solid electrolytes were synthesized. As before, XRD and Raman confirms the presence of argyrodite sulfide solid electrolyte and the $(PS_4)^{3-}$ tetrahedra, with pure LiF appearing when $x \geq 0.5$. The performance of pure phase Li_6PS_5I

was explored after being synthesized at low temperature (200 °C) and high temperature (290 °C). While the 200C-Li_6PS_5I has a high conductivity of 2.5×10^{-4} S cm^{-1}, the 290C-Li_6PS_5I sample has a significantly worse value of 1.8×10^{-6} S cm^{-1}. This discrepancy was investigated through TEM imagery, which revealed that 290C-Li_6PS_5I has a uniform and well-formed crystal with homogenous distribution of S and I elements, whereas the 200C-Li_6PS_5I sample has hotspots of localized concentrations of S and I. This indicates that 200C-Li_6PS_5I is a less crystallized with a higher degree of grain boundary regions, which mitigates the effects of the typically ordered structure of Li_6PS_5I.

For the co-doped samples, $Li_6PS_5F_{0.25}I_{0.75}$ displayed the best ionic conductivity with a value of 3.5×10^{-4} S cm^{-1}. This result was confirmed by AIMD investigation, which showed that this configuration yielded the largest amount of crystal disorder. While $Li_6PS_5F_{0.75}I_{0.25}$ had a worse value of 1.5×10^{-4} S cm^{-1}, it performed the best of the tested samples in symmetric cells and full cell batteries. This is attributable to the large amount of free LiF which could be utilized to form a stable and robust SEI layer. As a result, symmetric cells using $Li_6PS_5F_{0.75}I_{0.25}$ were able to cycle for over 1100 hours at a current density of 0.05 mA cm^{-2}. XPS testing on the deconstructed cell revealed the presence of both LiF and LiI, both of which contribute to a stable SEI layer. Full cell LFP-based Li metal batteries could displayed an excellent initial capacity of 140 mAh g^{-1} which was maintained above 100 mAh g^{-1} by the 200^{th} cycle.

8.5 Polymer Composite with Lithium Fluorine-Doped Lithium Argyrodites for Lithium Metal Batteries

While argyrodite sulfide solid electrolytes excel in their ion conducting properties and have good electrochemical stability with Li metal, their main drawback is their air

sensitivity and brittle mechanical nature. In response, this chapter focuses on using argyrodite SE material which has been incorporated into a polymer matrix which serves as protection against decomposition. Additionally, the polymer membrane is easy to construct, flexible, and provides excellent contact with electrode materials. A crosslinked polymer PVDF-HFP infused with LiTFSI salt was chosen as the polymer matrix due to its high degree of solvent absorption and its relatively high intrinsic ionic conductivity.

Different weight percentages of $Li_6PS_5F_{0.5}Cl_{0.5}$ (0%, 2%, 5%, 10 wt%) were incorporated into the polymer membrane. XRD results indicate that the amount of LPSFCl is too small to be detected, even at 10-wt% LPSFCl, although the argyrodite phase does show up at 75-wt% LPSFCl. SEM imaging confirms a very thin membrane layer of only 50 μm, as well as a smooth surface with homogenous distribution of LPS material.

The pure PVDF-HFP/LiTFSI membrane with no added LPS had a relatively low conductivity of 2.2×10^{-5} S cm^{-1}, which is attributed to its higher degree of crystallinity, confirmed by DSC testing. By adding in small amounts of LPS of 2-wt% and 5-wt%, the ionic conductivity was greatly improved to 5.3×10^{-4} S cm^{-1} and 7.9×10^{-4} S cm^{-1}, respectively. This is explained both by the decrease in crystallinity as well as the positive effects of LPSFCl as an ion conductor. The 10-wt% LPS membrane showed a decrease of conductivity, attributed to the high percentage of LPS not being completely encapsulated by the protective polymer matrix.

Following this, full cell batteries were constructed after soaking the polymer membrane in ionic liquid with dissolved LiTFSI salt, to both improve interfacial contact and lower interfacial resistance. Pure PYR/1M LiTFSI was too viscous for ion migration, so the solution was diluted with DOL. It was found that a 1:1 ratio of DOL:PYR with 2M

LiTFSI was the ideal concentration for the battery cells, as it provided both low enough viscosity for ion transport and high enough concentration of $TFSI^-$ which could be used for the SEI layer. Additionally, the 5-wt%LPSFCl CSE showed the best performance, owing to its very high ionic conductivity and its proper proportion of LPS material which could be used at the interface. The LFP||5-wt%LPS/PVDF-HFP/LiTFSI||Li cell soaked in 1:1 DOL:PYR/2M LiTFSI ionic liquid exhibited a high capacity of 158 mAh g^{-1} for the first cycle and maintained a decent capacity of over 120 mAh g^{-1} for 40 cycles. In addition, the LTO||5-wt%LPS/PVDF-HFP/LiTFSI||Li cell soaked in 1:1 DOL:PYR/2M LiTFSI could also maintain a high capacity of 120 mAh g^{-1} for up to 90 cycles. This indicates the feasibility of using LPS-infused polymer matrix to create Li metal batteries.

8.6 Concluding Remarks

In conclusion, this dissertation furthered the prospects of using sulfide argyrodite solid electrolytes in next-generation Li metal batteries. Each of the aforementioned concerns were thoroughly investigated and addressed in turn.

- A solvent synthesis method was proposed and developed which will alleviate the harsh synthesis conditions of traditionally used solid state methods.
- The low ionic conductivity of the solvent-synthesized argyrodites was improved through halogen doping.
- The prevention of Li dendrites and improvement of interfacial stability was achieved through excess Cl-doping, and by doping with the novel halogen, F. The poor interfacial contact between electrode and electrolyte was improved through the addition of trace amounts of either PC or PYR in full cell batteries.

- And finally, the air sensitivity and brittle mechanical properties of sulfide argyrodites was addressed by incorporating the LPS material into a PVDF-HFP polymer matrix.

8.7 *Future Works*

While this dissertation paves the way forward for sulfide based SSB to be more feasible, there remain several areas of interest which should be explored in future works. For one, while the solvent-based process is ideal for large scale purposes, the SE products showed relatively lower ionic conductivity than those which come from solid state synthesis. The highest value reported in this dissertation was 5.3×10^{-4} S cm^{-1} which was achieved by the Li_6PS_5Cl·LiCl sample. Ideally, this value would be on the order of 10^{-3} S cm^{-1} or higher, meaning there is still room for improvement. This work focused on halogen doping to replace the sulfur atoms, but perhaps other dopants or doping strategies could be implemented to improve the SE's performance.

Another area of research which demands more attention is the characterization of SEI layer. This work showed the positive effects that LiCl and LiF have on battery cycling capabilities, but there is still much mystery surrounding the exact nature and mechanism of the SEI layer. Specifically, the SEI formation could be investigated using *in situ* X-ray microscopy or Raman spectroscopy, both of which would reveal important information regarding compound development during battery cycling. Despite these lingering questions, this dissertation opens the way for a more feasible solid-state Li metal battery using sulfide solid electrolytes.

REFERENCES

(1) Lewis, G. N.; Keyes, F. G. THE POTENTIAL OF THE LITHIUM ELECTRODE. *J. Am. Chem. Soc.* **1913**, *35* (4), 340–344. https://doi.org/10.1021/ja02193a004.

(2) Hill, K. R.; Rao, M. L.; Selim, R. G. *Research and Development of a High Capacity, Nonaqueous Secondary Battery. Final Report, October 1964--December 1965. [Li/CuF/Sub 2/, Li/AgCl]*; N-66-35218; NASA-CR-54969; Mallory (P.R.) and Co., Inc., Burlington, MA (USA), 1965. https://www.osti.gov/biblio/7123176 (accessed 2022-09-08).

(3) Whittingham, M. S. Electrical Energy Storage and Intercalation Chemistry. *Science* **1976**, *192* (4244), 1126–1127. https://doi.org/10.1126/science.192.4244.1126.

(4) Li, J.; Kong, Z.; Liu, X.; Zheng, B.; Fan, Q. H.; Garratt, E.; Schuelke, T.; Wang, K.; Xu, H.; Jin, H. Strategies to Anode Protection in Lithium Metal Battery: A Review. *InfoMat* **2021**, *3* (12), 1333–1363. https://doi.org/10.1002/inf2.12189.

(5) Cheng, X.-B.; Zhang, R.; Zhao, C.-Z.; Zhang, Q. Toward Safe Lithium Metal Anode in Rechargeable Batteries: A Review. *Chem. Rev.* **2017**, *117* (15), 10403–10473. https://doi.org/10.1021/acs.chemrev.7b00115.

(6) Li, M.; Lu, J.; Chen, Z.; Amine, K. 30 Years of Lithium-Ion Batteries. *Advanced Materials* **2018**, *30* (33), 1800561. https://doi.org/10.1002/adma.201800561.

(7) Goodenough, J. B.; Kim, Y. Challenges for Rechargeable Li Batteries. *Chem. Mater.* **2010**, *22* (3), 587–603. https://doi.org/10.1021/cm901452z.

(8) Walker, W.; Yayathi, S.; Shaw, J.; Ardebili, H. Thermo-Electrochemical Evaluation of Lithium-Ion Batteries for Space Applications. *Journal of Power Sources* **2015**, *298*, 217–227. https://doi.org/10.1016/j.jpowsour.2015.08.054.

(9) Peled, E. The Electrochemical Behavior of Alkali and Alkaline Earth Metals in Nonaqueous Battery Systems—The Solid Electrolyte Interphase Model. *J. Electrochem. Soc.* **1979**, *126* (12), 2047. https://doi.org/10.1149/1.2128859.

(10) Kim, S.-P.; Duin, A. C. T. van; Shenoy, V. B. Effect of Electrolytes on the Structure and Evolution of the Solid Electrolyte Interphase (SEI) in Li-Ion Batteries: A Molecular Dynamics Study. *Journal of Power Sources* **2011**, *196* (20), 8590–8597. https://doi.org/10.1016/j.jpowsour.2011.05.061.

(11) Peled, E.; Menkin, S. Review—SEI: Past, Present and Future. *J. Electrochem. Soc.* **2017**, *164* (7), A1703. https://doi.org/10.1149/2.1441707jes.

(12) Single, F.; Horstmann, B.; Latz, A. Revealing SEI Morphology: In-Depth Analysis of a Modeling Approach. *J. Electrochem. Soc.* **2017**, *164* (11), E3132. https://doi.org/10.1149/2.0121711jes.

(13) Peled, E.; Golodnitsky, D.; Ardel, G. Advanced Model for Solid Electrolyte Interphase Electrodes in Liquid and Polymer Electrolytes. *J. Electrochem. Soc.* **1997**, *144* (8), L208. https://doi.org/10.1149/1.1837858.

(14) Jäckle, M.; Groß, A. Microscopic Properties of Lithium, Sodium, and Magnesium Battery Anode Materials Related to Possible Dendrite Growth. *J. Chem. Phys.* **2014**, *141* (17), 174710. https://doi.org/10.1063/1.4901055.
(15) Ozhabes, Y.; Gunceler, D.; Arias, T. A. Stability and Surface Diffusion at Lithium-Electrolyte Interphases with Connections to Dendrite Suppression. arXiv April 22, 2015. https://doi.org/10.48550/arXiv.1504.05799.
(16) Wang, S.; Fang, R.; Li, Y.; Liu, Y.; Xin, C.; Richter, F. H.; Nan, C.-W. Interfacial Challenges for All-Solid-State Batteries Based on Sulfide Solid Electrolytes. *Journal of Materiomics* **2021**, *7* (2), 209–218. https://doi.org/10.1016/j.jmat.2020.09.003.
(17) Liu, Y.; Hu, R.; Zhang, D.; Liu, J.; Liu, F.; Cui, J.; Lin, Z.; Wu, J.; Zhu, M. Constructing Li-Rich Artificial SEI Layer in Alloy–Polymer Composite Electrolyte to Achieve High Ionic Conductivity for All-Solid-State Lithium Metal Batteries. *Advanced Materials* **2021**, *33* (11), 2004711. https://doi.org/10.1002/adma.202004711.
(18) Hou, G.; Ma, X.; Sun, Q.; Ai, Q.; Xu, X.; Chen, L.; Li, D.; Chen, J.; Zhong, H.; Li, Y.; Xu, Z.; Si, P.; Feng, J.; Zhang, L.; Ding, F.; Ci, L. Lithium Dendrite Suppression and Enhanced Interfacial Compatibility Enabled by an Ex Situ SEI on Li Anode for LAGP-Based All-Solid-State Batteries. *ACS Appl. Mater. Interfaces* **2018**, *10* (22), 18610–18618. https://doi.org/10.1021/acsami.8b01003.
(19) Ulvestad, A. A Brief Review of Current Lithium Ion Battery Technology and Potential Solid State Battery Technologies. arXiv March 12, 2018. https://doi.org/10.48550/arXiv.1803.04317.
(20) Shoji, M.; Cheng, E. J.; Kimura, T.; Kanamura, K. Recent Progress for All Solid State Battery Using Sulfide and Oxide Solid Electrolytes. *J. Phys. D: Appl. Phys.* **2019**, *52* (10), 103001. https://doi.org/10.1088/1361-6463/aaf7e2.
(21) Liu, Q.; Geng, Z.; Han, C.; Fu, Y.; Li, S.; He, Y.; Kang, F.; Li, B. Challenges and Perspectives of Garnet Solid Electrolytes for All Solid-State Lithium Batteries. *Journal of Power Sources* **2018**, *389*, 120–134. https://doi.org/10.1016/j.jpowsour.2018.04.019.
(22) Wang, C.; Fu, K.; Kammampata, S. P.; McOwen, D. W.; Samson, A. J.; Zhang, L.; Hitz, G. T.; Nolan, A. M.; Wachsman, E. D.; Mo, Y.; Thangadurai, V.; Hu, L. Garnet-Type Solid-State Electrolytes: Materials, Interfaces, and Batteries. *Chem. Rev.* **2020**, *120* (10), 4257–4300. https://doi.org/10.1021/acs.chemrev.9b00427.
(23) Wolfenstine, J.; Allen, J. L.; Sakamoto, J.; Siegel, D. J.; Choe, H. Mechanical Behavior of Li-Ion-Conducting Crystalline Oxide-Based Solid Electrolytes: A Brief Review. *Ionics* **2018**, *24* (5), 1271–1276. https://doi.org/10.1007/s11581-017-2314-4.
(24) Uhlmann, C.; Braun, P.; Illig, J.; Weber, A.; Ivers-Tiffée, E. Interface and Grain Boundary Resistance of a Lithium Lanthanum Titanate (Li3xLa2/3−xTiO3, LLTO) Solid Electrolyte. *Journal of Power Sources* **2016**, *307*, 578–586. https://doi.org/10.1016/j.jpowsour.2016.01.002.
(25) Lu, J.; Li, Y. Perovskite-type Li-ion Solid Electrolytes: A Review. *J Mater Sci: Mater Electron* **2021**, *32* (8), 9736–9754. https://doi.org/10.1007/s10854-021-05699-8.
(26) DeWees, R.; Wang, H. Synthesis and Properties of NaSICON-Type LATP and LAGP Solid Electrolytes. *ChemSusChem* **2019**, *12* (16), 3713–3725. https://doi.org/10.1002/cssc.201900725.
(27) Pfalzgraf, D.; Mutter, D.; Urban, D. F. Atomistic Analysis of Li Migration in Li1+xAlxTi2−x(PO4)3 (LATP) Solid Electrolytes. *Solid State Ionics* **2021**, *359*, 115521. https://doi.org/10.1016/j.ssi.2020.115521.

(28) Zhao, E.; Ma, F.; Guo, Y.; Jin, Y. Stable LATP/LAGP Double-Layer Solid Electrolyte Prepared via a Simple Dry-Pressing Method for Solid State Lithium Ion Batteries. *RSC Adv.* **2016**, *6* (95), 92579–92585. https://doi.org/10.1039/C6RA19415J.

(29) Kim, K. J.; Balaish, M.; Wadaguchi, M.; Kong, L.; Rupp, J. L. M. Solid-State Li–Metal Batteries: Challenges and Horizons of Oxide and Sulfide Solid Electrolytes and Their Interfaces. *Advanced Energy Materials* **2021**, *11* (1), 2002689. https://doi.org/10.1002/aenm.202002689.

(30) Qin, S.; Zhu, X.; Jiang, Y.; Ling, M.; Hu, Z.; Zhu, J. Growth of Self-Textured Ga3+-Substituted Li7La3Zr2O12 Ceramics by Solid State Reaction and Their Significant Enhancement in Ionic Conductivity. *Appl. Phys. Lett.* **2018**, *112* (11), 113901. https://doi.org/10.1063/1.5019179.

(31) Thompson, T.; Yu, S.; Williams, L.; Schmidt, R. D.; Garcia-Mendez, R.; Wolfenstine, J.; Allen, J. L.; Kioupakis, E.; Siegel, D. J.; Sakamoto, J. Electrochemical Window of the Li-Ion Solid Electrolyte Li7La3Zr2O12. *ACS Energy Lett.* **2017**, *2* (2), 462–468. https://doi.org/10.1021/acsenergylett.6b00593.

(32) Yu, S.; Schmidt, R. D.; Garcia-Mendez, R.; Herbert, E.; Dudney, N. J.; Wolfenstine, J. B.; Sakamoto, J.; Siegel, D. J. Elastic Properties of the Solid Electrolyte Li7La3Zr2O12 (LLZO). *Chem. Mater.* **2016**, *28* (1), 197–206. https://doi.org/10.1021/acs.chemmater.5b03854.

(33) Monroe, C.; Newman, J. The Impact of Elastic Deformation on Deposition Kinetics at Lithium/Polymer Interfaces. *J. Electrochem. Soc.* **2005**, *152* (2), A396. https://doi.org/10.1149/1.1850854.

(34) Ginnings, D. C.; Phipps, T. E. *TEMPERATURE-CONDUCTANCE CURVES OF SOLID SALTS. III. HALIDES OF LITHIUM*. ACS Publications. https://doi.org/10.1021/ja01367a006.

(35) Li, X.; Liang, J.; Yang, X.; Adair, K. R.; Wang, C.; Zhao, F.; Sun, X. Progress and Perspectives on Halide Lithium Conductors for All-Solid-State Lithium Batteries. *Energy Environ. Sci.* **2020**, *13* (5), 1429–1461. https://doi.org/10.1039/C9EE03828K.

(36) Asano, T.; Sakai, A.; Ouchi, S.; Sakaida, M.; Miyazaki, A.; Hasegawa, S. Solid Halide Electrolytes with High Lithium-Ion Conductivity for Application in 4 V Class Bulk-Type All-Solid-State Batteries. *Advanced Materials* **2018**, *30* (44), 1803075. https://doi.org/10.1002/adma.201803075.

(37) Tomita, Y.; Yonekura, H.; Yamauchi, Y.; Yamada, K.; Kobayashi, K. Substitution Effect in the Ion Conductor Li3InBr6, Studied by Nuclear Magnetic Resonance. *Zeitschrift für Naturforschung A* **2002**, *57* (6–7), 447–450. https://doi.org/10.1515/zna-2002-6-728.

(38) Li, X.; Liang, J.; Chen, N.; Luo, J.; Adair, K. R.; Wang, C.; Banis, M. N.; Sham, T.-K.; Zhang, L.; Zhao, S.; Lu, S.; Huang, H.; Li, R.; Sun, X. Water-Mediated Synthesis of a Superionic Halide Solid Electrolyte. *Angewandte Chemie* **2019**, *131* (46), 16579–16584. https://doi.org/10.1002/ange.201909805.

(39) Nagao, M.; Hayashi, A.; Tatsumisago, M. Fabrication of Favorable Interface between Sulfide Solid Electrolyte and Li Metal Electrode for Bulk-Type Solid-State Li/S Battery. *Electrochemistry Communications* **2012**, *22*, 177–180. https://doi.org/10.1016/j.elecom.2012.06.015.

(40) Minami, K.; Hayashi, A.; Ujiie, S.; Tatsumisago, M. Electrical and Electrochemical Properties of Glass–Ceramic Electrolytes in the Systems Li2S–P2S5–P2S3 and Li2S–P2S5–P2O5. *Solid State Ionics* **2011**, *192* (1), 122–125. https://doi.org/10.1016/j.ssi.2010.06.018.

(41) Lau, J.; DeBlock, R. H.; Butts, D. M.; Ashby, D. S.; Choi, C. S.; Dunn, B. S. Sulfide Solid Electrolytes for Lithium Battery Applications. *Advanced Energy Materials* **2018**, *8* (27), 1800933. https://doi.org/10.1002/aenm.201800933.

(42) Trevey, J.; Jang, J. S.; Jung, Y. S.; Stoldt, C. R.; Lee, S.-H. Glass–Ceramic Li2S–P2S5 Electrolytes Prepared by a Single Step Ball Billing Process and Their Application for All-Solid-State Lithium–Ion Batteries. *Electrochemistry Communications* **2009**, *11* (9), 1830–1833. https://doi.org/10.1016/j.elecom.2009.07.028.

(43) Ziolkowska, D. A.; Arnold, W.; Druffel, T.; Sunkara, M.; Wang, H. Rapid and Economic Synthesis of a Li7PS6 Solid Electrolyte from a Liquid Approach. *ACS Appl. Mater. Interfaces* **2019**, *11* (6), 6015–6021. https://doi.org/10.1021/acsami.8b19181.

(44) Mizuno, F.; Hayashi, A.; Tadanaga, K.; Tatsumisago, M. High Lithium Ion Conducting Glass-Ceramics in the System Li2S–P2S5. *Solid State Ionics* **2006**, *177* (26), 2721–2725. https://doi.org/10.1016/j.ssi.2006.04.017.

(45) Minami, K.; Hayashi, A.; Tatsumisago, M. Preparation and Characterization of Superionic Conducting $Li_7P_3S_{11}$ Crystal from Glassy Liquids. *Journal of the Ceramic Society of Japan* **2010**, *118* (1376), 305–308. https://doi.org/10.2109/jcersj2.118.305.

(46) Kudu, Ö. U.; Famprikis, T.; Fleutot, B.; Braida, M.-D.; Le Mercier, T.; Islam, M. S.; Masquelier, C. A Review of Structural Properties and Synthesis Methods of Solid Electrolyte Materials in the Li2S − P2S5 Binary System. *Journal of Power Sources* **2018**, *407*, 31–43. https://doi.org/10.1016/j.jpowsour.2018.10.037.

(47) Dietrich, C.; Sadowski, M.; Sicolo, S.; Weber, D. A.; Sedlmaier, S. J.; Weldert, K. S.; Indris, S.; Albe, K.; Janek, J.; Zeier, W. G. Local Structural Investigations, Defect Formation, and Ionic Conductivity of the Lithium Ionic Conductor Li4P2S6. *Chem. Mater.* **2016**, *28* (23), 8764–8773. https://doi.org/10.1021/acs.chemmater.6b04175.

(48) Tachez, M.; Malugani, J.-P.; Mercier, R.; Robert, G. Ionic Conductivity of and Phase Transition in Lithium Thiophosphate Li3PS4. *Solid State Ionics* **1984**, *14* (3), 181–185. https://doi.org/10.1016/0167-2738(84)90097-3.

(49) Ma, Z.; Xue, H.-G.; Guo, S.-P. Recent Achievements on Sulfide-Type Solid Electrolytes: Crystal Structures and Electrochemical Performance. *J Mater Sci* **2018**, *53* (6), 3927–3938. https://doi.org/10.1007/s10853-017-1827-6.

(50) Hayashi, A.; Hama, S.; Morimoto, H.; Tatsumisago, M.; Minami, T. Preparation of Li2S–P2S5 Amorphous Solid Electrolytes by Mechanical Milling. *Journal of the American Ceramic Society* **2001**, *84* (2), 477–479. https://doi.org/10.1111/j.1151-2916.2001.tb00685.x.

(51) Liu, Z.; Fu, W.; Payzant, E. A.; Yu, X.; Wu, Z.; Dudney, N. J.; Kiggans, J.; Hong, K.; Rondinone, A. J.; Liang, C. Anomalous High Ionic Conductivity of Nanoporous β-Li3PS4. *J. Am. Chem. Soc.* **2013**, *135* (3), 975–978. https://doi.org/10.1021/ja3110895.

(52) Tsukasaki, H.; Mori, S.; Morimoto, H.; Hayashi, A.; Tatsumisago, M. Direct Observation of a Non-Crystalline State of Li2S–P2S5 Solid Electrolytes. *Sci Rep* **2017**, *7* (1), 4142. https://doi.org/10.1038/s41598-017-04030-y.

(53) Tsukasaki, H.; Mori, S.; Shiotani, S.; Yamamura, H. Ionic Conductivity and Crystallization Process in the Li2S–P2S5 Glass Electrolyte. *Solid State Ionics* **2018**, *317*, 122–126. https://doi.org/10.1016/j.ssi.2018.01.010.

(54) Zhou, L.; Minafra, N.; Zeier, W. G.; Nazar, L. F. Innovative Approaches to Li-Argyrodite Solid Electrolytes for All-Solid-State Lithium Batteries. *Acc. Chem. Res.* **2021**, *54* (12), 2717–2728. https://doi.org/10.1021/acs.accounts.0c00874.

(55) Zhou, L.; Assoud, A.; Zhang, Q.; Wu, X.; Nazar, L. F. New Family of Argyrodite Thioantimonate Lithium Superionic Conductors. *J. Am. Chem. Soc.* **2019**, *141* (48), 19002–19013. https://doi.org/10.1021/jacs.9b08357.

(56) Deiseroth, H.-J.; Kong, S.-T.; Eckert, H.; Vannahme, J.; Reiner, C.; Zaiß, T.; Schlosser, M. Li6PS5X: A Class of Crystalline Li-Rich Solids With an Unusually High Li+ Mobility. *Angewandte Chemie International Edition* **2008**, *47* (4), 755–758. https://doi.org/10.1002/anie.200703900.

(57) Brice, J. Preparation and Study of 2 Ternary Lithium-Phosphorus Sulfides - Li8p2s9 and Li7ps6. *Comptes Rendus Hebdomadaires Des Seances De L Academie Des Sciences Serie C* **1976**, *283* (13), 581–584.

(58) de Klerk, N. J. J.; Rosłoń, I.; Wagemaker, M. Diffusion Mechanism of Li Argyrodite Solid Electrolytes for Li-Ion Batteries and Prediction of Optimized Halogen Doping: The Effect of Li Vacancies, Halogens, and Halogen Disorder. *Chem. Mater.* **2016**, *28* (21), 7955–7963. https://doi.org/10.1021/acs.chemmater.6b03630.

(59) Machida, N.; Yamamoto, H.; Asano, S.; Shigematsu, T. Preparation of Amorphous 75L2S·xP2S3·(25−x)P2S5 (Mol%) Solid Electrolytes by a High-Energy Ball-Milling Process and Their Application for an All-Solid-State Lithium Battery. *Solid State Ionics* **2005**, *176* (5), 473–479. https://doi.org/10.1016/j.ssi.2004.08.019.

(60) Yu, C.; van Eijck, L.; Ganapathy, S.; Wagemaker, M. Synthesis, Structure and Electrochemical Performance of the Argyrodite Li6PS5Cl Solid Electrolyte for Li-Ion Solid State Batteries. *Electrochimica Acta* **2016**, *215*, 93–99. https://doi.org/10.1016/j.electacta.2016.08.081.

(61) Yu, C.; Hageman, J.; Ganapathy, S.; Eijck, L. van; Zhang, L.; R. Adair, K.; Sun, X.; Wagemaker, M. Tailoring Li 6 PS 5 Br Ionic Conductivity and Understanding of Its Role in Cathode Mixtures for High Performance All-Solid-State Li–S Batteries. *Journal of Materials Chemistry A* **2019**, *7* (17), 10412–10421. https://doi.org/10.1039/C9TA02126D.

(62) Subramanian, Y.; Rajagopal, R.; Ryu, K.-S. High Ionic-Conducting Li-Argyrodites Synthesized Using a Simple and Economic Liquid-Phase Approach and Their Application in All Solid-State-Lithium Batteries. *Scripta Materialia* **2021**, *204*, 114129. https://doi.org/10.1016/j.scriptamat.2021.114129.

(63) Yubuchi, S.; Uematsu, M.; Hotehama, C.; Sakuda, A.; Hayashi, A.; Tatsumisago, M. An Argyrodite Sulfide-Based Superionic Conductor Synthesized by a Liquid-Phase Technique with Tetrahydrofuran and Ethanol. *J. Mater. Chem. A* **2019**, *7* (2), 558–566. https://doi.org/10.1039/C8TA09477B.

(64) Chen, Y.; Li, W.; Sun, C.; Jin, J.; Wang, Q.; Chen, X.; Zha, W.; Wen, Z. Sustained Release-Driven Formation of Ultrastable SEI between Li6PS5Cl and Lithium Anode for Sulfide-Based Solid-State Batteries. *Advanced Energy Materials* **2021**, *11* (4), 2002545. https://doi.org/10.1002/aenm.202002545.

(65) Liu, G.; Weng, W.; Zhang, Z.; Wu, L.; Yang, J.; Yao, X. Densified Li6PS5Cl Nanorods with High Ionic Conductivity and Improved Critical Current Density for All-Solid-State Lithium Batteries. *Nano Lett.* **2020**, *20* (9), 6660–6665. https://doi.org/10.1021/acs.nanolett.0c02489.

(66) Hikima, K.; Phuc, N. H. H.; Tsukasaki, H.; Mori, S.; Muto, H.; Matsuda, A. High Ionic Conductivity of Multivalent Cation Doped Li 6 PS 5 Cl Solid Electrolytes Synthesized by Mechanical Milling. *RSC Advances* **2020**, *10* (38), 22304–22310. https://doi.org/10.1039/D0RA02545C.

(67) Hanghofer, I.; Brinek, M.; L. Eisbacher, S.; Bitschnau, B.; Volck, M.; Hennige, V.; Hanzu, I.; Rettenwander, D.; R. Wilkening, H. M. Substitutional Disorder: Structure and Ion Dynamics of the Argyrodites Li 6 PS 5 Cl, Li 6 PS 5 Br and Li 6 PS 5 I. *Physical Chemistry Chemical Physics* **2019**, *21* (16), 8489–8507. https://doi.org/10.1039/C9CP00664H.

(68) Zhou, L.; Park, K.-H.; Sun, X.; Lalère, F.; Adermann, T.; Hartmann, P.; Nazar, L. F. Solvent-Engineered Design of Argyrodite Li6PS5X (X = Cl, Br, I) Solid Electrolytes with High Ionic Conductivity. *ACS Energy Lett.* **2019**, *4* (1), 265–270. https://doi.org/10.1021/acsenergylett.8b01997.

(69) Choi, S.; Ann, J.; Do, J.; Lim, S.; Park, C.; Shin, D. Application of Rod-Like Li6PS5Cl Directly Synthesized by a Liquid Phase Process to Sheet-Type Electrodes for All-Solid-State Lithium Batteries. *J. Electrochem. Soc.* **2018**, *166* (3), A5193. https://doi.org/10.1149/2.0301903jes.

(70) Zhang, Z.; Zhang, L.; Liu, Y.; Yan, X.; Xu, B.; Wang, L. One-Step Solution Process toward Formation of Li6PS5Cl Argyrodite Solid Electrolyte for All-Solid-State Lithium-Ion Batteries. *Journal of Alloys and Compounds* **2020**, *812*, 152103. https://doi.org/10.1016/j.jallcom.2019.152103.

(71) Rosero-Navarro, N. C.; Miura, A.; Tadanaga, K. Composite Cathode Prepared by Argyrodite Precursor Solution Assisted by Dispersant Agents for Bulk-Type All-Solid-State Batteries. *Journal of Power Sources* **2018**, *396*, 33–40. https://doi.org/10.1016/j.jpowsour.2018.06.011.

(72) Wang, P.; Liu, H.; Patel, S.; Feng, X.; Chien, P.-H.; Wang, Y.; Hu, Y.-Y. Fast Ion Conduction and Its Origin in Li6–XPS5–XBr1+x. *Chem. Mater.* **2020**, *32* (9), 3833–3840. https://doi.org/10.1021/acs.chemmater.9b05331.

(73) Yubuchi, S.; Uematsu, M.; Hotehama, C.; Sakuda, A.; Hayashi, A.; Tatsumisago, M. An Argyrodite Sulfide-Based Superionic Conductor Synthesized by a Liquid-Phase Technique with Tetrahydrofuran and Ethanol. *J. Mater. Chem. A* **2019**, *7* (2), 558–566. https://doi.org/10.1039/C8TA09477B.

(74) Chida, S.; Miura, A.; Rosero-Navarro, N. C.; Higuchi, M.; Phuc, N. H. H.; Muto, H.; Matsuda, A.; Tadanaga, K. Liquid-Phase Synthesis of Li6PS5Br Using Ultrasonication and Application to Cathode Composite Electrodes in All-Solid-State Batteries. *Ceramics International* **2018**, *44* (1), 742–746. https://doi.org/10.1016/j.ceramint.2017.09.241.

(75) Yubuchi, S.; Uematsu, M.; Deguchi, M.; Hayashi, A.; Tatsumisago, M. Lithium-Ion-Conducting Argyrodite-Type Li 6 PS 5 X (X = Cl, Br, I) Solid Electrolytes Prepared by a Liquid-Phase Technique Using Ethanol as a Solvent. *ACS Appl. Energy Mater.* **2018**, *1* (8), 3622–3629. https://doi.org/10.1021/acsaem.8b00280.

(76) Adeli, P.; Bazak, J. D.; Park, K. H.; Kochetkov, I.; Huq, A.; Goward, G. R.; Nazar, L. F. Boosting Solid-State Diffusivity and Conductivity in Lithium Superionic Argyrodites by Halide Substitution. *Angewandte Chemie International Edition* **2019**, *58* (26), 8681–8686. https://doi.org/10.1002/anie.201814222.

(77) Yu, C.; Li, Y.; Li, W.; Adair, K. R.; Zhao, F.; Willans, M.; Liang, J.; Zhao, Y.; Wang, C.; Deng, S.; Li, R.; Huang, H.; Lu, S.; Sham, T.-K.; Huang, Y.; Sun, X. Enabling Ultrafast Ionic Conductivity in Br-Based Lithium Argyrodite Electrolytes for Solid-State Batteries with Different Anodes. *Energy Storage Materials* **2020**, *30*, 238–249. https://doi.org/10.1016/j.ensm.2020.04.014.

(78) Kim, D. H.; Lee, Y.-H.; Song, Y. B.; Kwak, H.; Lee, S.-Y.; Jung, Y. S. Thin and Flexible Solid Electrolyte Membranes with Ultrahigh Thermal Stability Derived from Solution-

Processable Li Argyrodites for All-Solid-State Li-Ion Batteries. *ACS Energy Lett.* **2020**, *5* (3), 718–727. https://doi.org/10.1021/acsenergylett.0c00251.

(79) Wang, H.; Yu, C.; Ganapathy, S.; van Eck, E. R. H.; van Eijck, L.; Wagemaker, M. A Lithium Argyrodite Li6PS5Cl0.5Br0.5 Electrolyte with Improved Bulk and Interfacial Conductivity. *Journal of Power Sources* **2019**, *412*, 29–36. https://doi.org/10.1016/j.jpowsour.2018.11.029.

(80) Zhao, F.; Sun, Q.; Yu, C.; Zhang, S.; Adair, K.; Wang, S.; Liu, Y.; Zhao, Y.; Liang, J.; Wang, C.; Li, X.; Li, X.; Xia, W.; Li, R.; Huang, H.; Zhang, L.; Zhao, S.; Lu, S.; Sun, X. Ultrastable Anode Interface Achieved by Fluorinating Electrolytes for All-Solid-State Li Metal Batteries. *ACS Energy Lett.* **2020**, *5* (4), 1035–1043. https://doi.org/10.1021/acsenergylett.0c00207.

(81) Arnold, W.; Shreyas, V.; Li, Y.; Koralalage, M. K.; Jasinski, J. B.; Thapa, A.; Sumanasekera, G.; Ngo, A. T.; Narayanan, B.; Wang, H. Synthesis of Fluorine-Doped Lithium Argyrodite Solid Electrolytes for Solid-State Lithium Metal Batteries. *ACS Appl. Mater. Interfaces* **2022**, *14* (9), 11483–11492. https://doi.org/10.1021/acsami.1c24468.

(82) Chi, S.-S.; Liu, Y.; Zhao, N.; Guo, X.; Nan, C.-W.; Fan, L.-Z. Solid Polymer Electrolyte Soft Interface Layer with 3D Lithium Anode for All-Solid-State Lithium Batteries. *Energy Storage Materials* **2019**, *17*, 309–316. https://doi.org/10.1016/j.ensm.2018.07.004.

(83) Li, S.; Zhang, S.-Q.; Shen, L.; Liu, Q.; Ma, J.-B.; Lv, W.; He, Y.-B.; Yang, Q.-H. Progress and Perspective of Ceramic/Polymer Composite Solid Electrolytes for Lithium Batteries. *Advanced Science* **2020**, *7* (5), 1903088. https://doi.org/10.1002/advs.201903088.

(84) Zhou, D.; Shanmukaraj, D.; Tkacheva, A.; Armand, M.; Wang, G. Polymer Electrolytes for Lithium-Based Batteries: Advances and Prospects. *Chem* **2019**, *5* (9), 2326–2352. https://doi.org/10.1016/j.chempr.2019.05.009.

(85) Feng, J.; Wang, L.; Chen, Y.; Wang, P.; Zhang, H.; He, X. PEO Based Polymer-Ceramic Hybrid Solid Electrolytes: A Review. *Nano Convergence* **2021**, *8* (1), 2. https://doi.org/10.1186/s40580-020-00252-5.

(86) Zhang, H.; Liu, C.; Zheng, L.; Xu, F.; Feng, W.; Li, H.; Huang, X.; Armand, M.; Nie, J.; Zhou, Z. Lithium Bis(Fluorosulfonyl)Imide/Poly(Ethylene Oxide) Polymer Electrolyte. *Electrochimica Acta* **2014**, *133*, 529–538. https://doi.org/10.1016/j.electacta.2014.04.099.

(87) Ban, X.; Zhang, W.; Chen, N.; Sun, C. A High-Performance and Durable Poly(Ethylene Oxide)-Based Composite Solid Electrolyte for All Solid-State Lithium Battery. *J. Phys. Chem. C* **2018**, *122* (18), 9852–9858. https://doi.org/10.1021/acs.jpcc.8b02556.

(88) Wang, C.; Adair, K. R.; Liang, J.; Li, X.; Sun, Y.; Li, X.; Wang, J.; Sun, Q.; Zhao, F.; Lin, X.; Li, R.; Huang, H.; Zhang, L.; Yang, R.; Lu, S.; Sun, X. Solid-State Plastic Crystal Electrolytes: Effective Protection Interlayers for Sulfide-Based All-Solid-State Lithium Metal Batteries. *Advanced Functional Materials* **2019**, *29* (26), 1900392. https://doi.org/10.1002/adfm.201900392.

(89) Li, Y.; Yang, L.; Dong, R.; Zhang, T.; Yuan, J.; Liu, Y.; Liu, Y.; Sun, Y.; Zhong, B.; Chen, Y.; Wu, Z.; Guo, X. A High Strength Asymmetric Polymer–Inorganic Composite Solid Electrolyte for Solid-State Li-Ion Batteries. *Electrochimica Acta* **2022**, *404*, 139701. https://doi.org/10.1016/j.electacta.2021.139701.

(90) Such, K.; Stevens, J. R.; Wieczorek, W.; Siekierski, M.; Florjanczyk, Z. Polymer Solid Electrolytes from the PEG-PMMA-LiCF3SO3 System. *Journal of Polymer Science Part B: Polymer Physics* **1994**, *32* (13), 2221–2233. https://doi.org/10.1002/polb.1994.090321309.

(91) Przyłuski, J.; Such, K.; Wyciślik, H.; Wieczorek, W.; Floriańczyk, Z. PEO-Based Polymer Blends as Materials for Solid Electrolytes. *Synthetic Metals* **1990**, *35* (1), 241–247. https://doi.org/10.1016/0379-6779(90)90048-P.

(92) Wu, Y.; Li, Y.; Wang, Y.; Liu, Q.; Chen, Q.; Chen, M. Advances and Prospects of PVDF Based Polymer Electrolytes. *Journal of Energy Chemistry* **2022**, *64*, 62–84. https://doi.org/10.1016/j.jechem.2021.04.007.

(93) Zhang, H.; Shi, W.; Cheng, H.; Chen, S.; Wang, L. Effect of Ionic Liquid on Crystallization Kinetics and Crystal Form Transition of Poly(Vinylidene Fluoride) Blends. *J Therm Anal Calorim* **2018**, *132* (2), 1153–1165. https://doi.org/10.1007/s10973-018-7029-x.

(94) Abbrent, S.; Plestil, J.; Lindgren, J.; Tegenfeldt, J.; Wendsjö, Å. Crystallinity and Morphology of PVdF-HFP-Based Gel Electrolytes. *Polymer* **2001**, *42*, 1407–1416. https://doi.org/10.1016/S0032-3861(00)00517-6.

(95) Cao, J.-H.; Zhu, B.-K.; Xu, Y.-Y. Structure and Ionic Conductivity of Porous Polymer Electrolytes Based on PVDF-HFP Copolymer Membranes. *Journal of Membrane Science* **2006**, *281* (1), 446–453. https://doi.org/10.1016/j.memsci.2006.04.013.

(96) Liu, W.; Zhang, X. K.; Wu, F.; Xiang, Y. A Study on PVDF-HFP Gel Polymer Electrolyte for Lithium-Ion Batteries. *IOP Conf. Ser.: Mater. Sci. Eng.* **2017**, *213*, 012036. https://doi.org/10.1088/1757-899X/213/1/012036.

(97) Xi, G.; Xiao, M.; Wang, S.; Han, D.; Li, Y.; Meng, Y. Polymer-Based Solid Electrolytes: Material Selection, Design, and Application. *Advanced Functional Materials* **2021**, *31* (9), 2007598. https://doi.org/10.1002/adfm.202007598.

(98) Molinari, N.; Mailoa, J. P.; Kozinsky, B. Effect of Salt Concentration on Ion Clustering and Transport in Polymer Solid Electrolytes: A Molecular Dynamics Study of PEO–LiTFSI. *Chem. Mater.* **2018**, *30* (18), 6298–6306. https://doi.org/10.1021/acs.chemmater.8b01955.

(99) Liang, Y. F.; Xia, Y.; Zhang, S. Z.; Wang, X. L.; Xia, X. H.; Gu, C. D.; Wu, J. B.; Tu, J. P. A Preeminent Gel Blending Polymer Electrolyte of Poly(Vinylidene Fluoride-Hexafluoropropylene) -Poly(Propylene Carbonate) for Solid-State Lithium Ion Batteries. *Electrochimica Acta* **2019**, *296*, 1064–1069. https://doi.org/10.1016/j.electacta.2018.11.182.

(100) Bandara, T. M. W. J.; Weerasinghe, A. M. J. S.; Dissanayake, M. A. K. L.; Senadeera, G. K. R.; Furlani, M.; Albinsson, I.; Mellander, B.-E. Characterization of Poly (Vinylidene Fluoride-Co-Hexafluoropropylene) (PVdF-HFP) Nanofiber Membrane Based Quasi Solid Electrolytes and Their Application in a Dye Sensitized Solar Cell. *Electrochimica Acta* **2018**, *266*, 276–283. https://doi.org/10.1016/j.electacta.2018.02.025.

(101) Lim, Y.-J.; An, Y.-H.; Jo, N.-J. Polystyrene-Al2O3 Composite Solid Polymer Electrolyte for Lithium Secondary Battery. *Nanoscale Res Lett* **2012**, *7* (1), 19. https://doi.org/10.1186/1556-276X-7-19.

(102) Croce, F.; Appetecchi, G. B.; Persi, L.; Scrosati, B. Nanocomposite Polymer Electrolytes for Lithium Batteries. *Nature* **1998**, *394* (6692), 456–458. https://doi.org/10.1038/28818.

(103) Liu, L.; Chu, L.; Jiang, B.; Li, M. Li1.4Al0.4Ti1.6(PO4)3 Nanoparticle-Reinforced Solid Polymer Electrolytes for All-Solid-State Lithium Batteries. *Solid State Ionics* **2019**, *331*, 89–95. https://doi.org/10.1016/j.ssi.2019.01.007.

(104) Wang, A.-N.; Nonemacher, J. F.; Yan, G.; Finsterbusch, M.; Malzbender, J.; Krüger, M. Mechanical Properties of the Solid Electrolyte Al-Substituted Li7La3Zr2O12 (LLZO) by Utilizing Micro-Pillar Indentation Splitting Test. *Journal of the European Ceramic Society* **2018**, *38* (9), 3201–3209. https://doi.org/10.1016/j.jeurceramsoc.2018.02.032.

(105) Huang, J.; Huang, Y.; Zhang, Z.; Gao, H.; Li, C. Li6.7La3Zr1.7Ta0.3O12 Reinforced PEO/PVDF-HFP Based Composite Solid Electrolyte for All Solid-State Lithium Metal Battery. *Energy Fuels* **2020**, *34* (11), 15011–15018. https://doi.org/10.1021/acs.energyfuels.0c03124.

(106) Zhang, J.; Zheng, C.; Lou, J.; Xia, Y.; Liang, C.; Huang, H.; Gan, Y.; Tao, X.; Zhang, W. Poly(Ethylene Oxide) Reinforced Li6PS5Cl Composite Solid Electrolyte for All-Solid-State Lithium Battery: Enhanced Electrochemical Performance, Mechanical Property and Interfacial Stability. *Journal of Power Sources* **2019**, *412*, 78–85. https://doi.org/10.1016/j.jpowsour.2018.11.036.

(107) Simon, F. J.; Hanauer, M.; Henss, A.; Richter, F. H.; Janek, J. Properties of the Interphase Formed between Argyrodite-Type Li6PS5Cl and Polymer-Based PEO10:LiTFSI. *ACS Appl. Mater. Interfaces* **2019**, *11* (45), 42186–42196. https://doi.org/10.1021/acsami.9b14506.

(108) Zou, C.; Yang, L.; Luo, K.; Liu, L.; Tao, X.; Yi, L.; Liu, X.; Luo, Z.; Wang, X. Preparation and Performances of Poly (Ethylene Oxide)-Li6PS5Cl Composite Polymer Electrolyte for All-Solid-State Lithium Batteries. *Journal of Electroanalytical Chemistry* **2021**, *900*, 115739. https://doi.org/10.1016/j.jelechem.2021.115739.

(109) Xu, R.; Zhang, X.-Q.; Cheng, X.-B.; Peng, H.-J.; Zhao, C.-Z.; Yan, C.; Huang, J.-Q. Artificial Soft–Rigid Protective Layer for Dendrite-Free Lithium Metal Anode. *Advanced Functional Materials* **2018**, *28* (8), 1705838. https://doi.org/10.1002/adfm.201705838.

(110) Patla, S. K.; Ray, R.; Asokan, K.; Karmakar, S. Investigation of Ionic Conduction in PEO–PVDF Based Blend Polymer Electrolytes. *Journal of Applied Physics* **2018**, *123* (12), 125102. https://doi.org/10.1063/1.5022050.

(111) Li, X.; Zhang, Z.; Yin, K.; Yang, L.; Tachibana, K.; Hirano, S. Mesoporous Silica/Ionic Liquid Quasi-Solid-State Electrolytes and Their Application in Lithium Metal Batteries. *Journal of Power Sources* **2015**, *278*, 128–132. https://doi.org/10.1016/j.jpowsour.2014.12.053.

(112) Fergus, J. W. Ceramic and Polymeric Solid Electrolytes for Lithium-Ion Batteries. *Journal of Power Sources* **2010**, *195* (15), 4554–4569. https://doi.org/10.1016/j.jpowsour.2010.01.076.

(113) Li, Y.; Arnold, W.; Thapa, A.; Jasinski, J. B.; Sumanasekera, G.; Sunkara, M.; Druffel, T.; Wang, H. Stable and Flexible Sulfide Composite Electrolyte for High-Performance Solid-State Lithium Batteries. *ACS Appl. Mater. Interfaces* **2020**, *12* (38), 42653–42659. https://doi.org/10.1021/acsami.0c08261.

(114) Wang, S.; Zhang, X.; Liu, S.; Xin, C.; Xue, C.; Richter, F.; Li, L.; Fan, L.; Lin, Y.; Shen, Y.; Janek, J.; Nan, C.-W. High-Conductivity Free-Standing Li6PS5Cl/Poly(Vinylidene Difluoride) Composite Solid Electrolyte Membranes for Lithium-Ion Batteries. *Journal of Materiomics* **2020**, *6* (1), 70–76. https://doi.org/10.1016/j.jmat.2019.12.010.

(115) Zheng, J.; Tang, M.; Hu, Y.-Y. Lithium Ion Pathway within Li7La3Zr2O12-Polyethylene Oxide Composite Electrolytes. *Angewandte Chemie* **2016**, *128* (40), 12726–12730. https://doi.org/10.1002/ange.201607539.

(116) Lu, J.; Liu, Y.; Yao, P.; Ding, Z.; Tang, Q.; Wu, J.; Ye, Z.; Huang, K.; Liu, X. Hybridizing Poly(Vinylidene Fluoride-Co-Hexafluoropropylene) with Li6.5La3Zr1.5Ta0.5O12 as a Lithium-Ion Electrolyte for Solid State Lithium Metal Batteries. *Chemical Engineering Journal* **2019**, *367*, 230–238. https://doi.org/10.1016/j.cej.2019.02.148.

(117) Daniel, C.; Mohanty, D.; Li, J.; Wood, D. L. Cathode Materials Review; Freiberg, Germany, 2014; pp 26–43. https://doi.org/10.1063/1.4878478.

(118) Xia, Y.; Zheng, J.; Wang, C.; Gu, M. Designing Principle for Ni-Rich Cathode Materials with High Energy Density for Practical Applications. *Nano Energy* **2018**, *49*, 434–452. https://doi.org/10.1016/j.nanoen.2018.04.062.

(119) Arnold, W.; Buchberger, D. A.; Li, Y.; Sunkara, M.; Druffel, T.; Wang, H. Halide Doping Effect on Solvent-Synthesized Lithium Argyrodites Li6PS5X (X= Cl, Br, I) Superionic Conductors. *Journal of Power Sources* **2020**, *464*, 228158. https://doi.org/10.1016/j.jpowsour.2020.228158.

(120) Wang, Y.; Richards, W. D.; Ong, S. P.; Miara, L. J.; Kim, J. C.; Mo, Y.; Ceder, G. Design Principles for Solid-State Lithium Superionic Conductors. *Nature Materials* **2015**, *14* (10), 1026–1031. https://doi.org/10.1038/nmat4369.

(121) Goodenough, J. B.; Park, K.-S. The Li-Ion Rechargeable Battery: A Perspective. *J. Am. Chem. Soc.* **2013**, *135* (4), 1167–1176. https://doi.org/10.1021/ja3091438.

(122) Yu, C.; Ganapathy, S.; Eck, E. R. H. van; Wang, H.; Basak, S.; Li, Z.; Wagemaker, M. Accessing the Bottleneck in All-Solid State Batteries, Lithium-Ion Transport over the Solid-Electrolyte-Electrode Interface. *Nat Commun* **2017**, *8*. https://doi.org/10.1038/s41467-017-01187-y.

(123) Kerman, K.; Luntz, A.; Viswanathan, V.; Chiang, Y.-M.; Chen, Z. Review—Practical Challenges Hindering the Development of Solid State Li Ion Batteries. *J. Electrochem. Soc.* **2017**, *164* (7), A1731–A1744. https://doi.org/10.1149/2.1571707jes.

(124) Boulineau, S.; Courty, M.; Tarascon, J.-M.; Viallet, V. Mechanochemical Synthesis of Li-Argyrodite Li6PS5X (X=Cl, Br, I) as Sulfur-Based Solid Electrolytes for All Solid State Batteries Application. *Solid State Ionics* **2012**, *221*, 1–5. https://doi.org/10.1016/j.ssi.2012.06.008.

(125) Yubuchi, S.; Uematsu, M.; Deguchi, M.; Hayashi, A.; Tatsumisago, M. Lithium-Ion-Conducting Argyrodite-Type Li_6PS_5X (X = Cl, Br, I) Solid Electrolytes Prepared by a Liquid-Phase Technique Using Ethanol as a Solvent. *ACS Appl. Energy Mater.* **2018**, *1* (8), 3622–3629. https://doi.org/10.1021/acsaem.8b00280.

(126) Bletskan, D. I.; Studenyak, I. P.; Vakulchak, V. V.; Lukach, A. V. Electronic Structure of Ag8GeS6. *Semiconductor Physics, Quantum Electronics & Optoelectronics* **2017**, *20* (1), 19–25. https://doi.org/10.15407/spqeo20.01.019.

(127) Minafra, N.; Culver, S. P.; Krauskopf, T.; Senyshyn, A.; Zeier, W. G. Effect of Si Substitution on the Structural and Transport Properties of Superionic Li-Argyrodites. *J. Mater. Chem. A* **2018**, *6* (2), 645–651. https://doi.org/10.1039/C7TA08581H.

(128) Zhang, Z.; Sun, Y.; Duan, X.; Peng, L.; Jia, H.; Zhang, Y.; Shan, B.; Xie, J. Design and Synthesis of Room Temperature Stable Li-Argyrodite Superionic Conductors *via* Cation Doping. *J. Mater. Chem. A* **2019**, *7* (6), 2717–2722. https://doi.org/10.1039/C8TA10790D.

(129) Schneider, H.; Du, H.; Kelley, T.; Leitner, K.; ter Maat, J.; Scordilis-Kelley, C.; Sanchez-Carrera, R.; Kovalev, I.; Mudalige, A.; Kulisch, J.; Safont-Sempere, M. M.; Hartmann, P.; Weiβ, T.; Schneider, L.; Hinrichsen, B. A Novel Class of Halogen-Free, Super-Conductive Lithium Argyrodites: Synthesis and Characterization. *Journal of Power Sources* **2017**, *366*, 151–160. https://doi.org/10.1016/j.jpowsour.2017.09.012.

(130) Yubuchi, S.; Teragawa, S.; Aso, K.; Tadanaga, K.; Hayashi, A.; Tatsumisago, M. Preparation of High Lithium-Ion Conducting Li6PS5Cl Solid Electrolyte from Ethanol Solution for All-Solid-State Lithium Batteries. *Journal of Power Sources* **2015**, *293*, 941–945. https://doi.org/10.1016/j.jpowsour.2015.05.093.

(131) Kong, S.-T.; Deiseroth, H.-J.; Reiner, C.; Gün, Ö.; Neumann, E.; Ritter, C.; Zahn, D. Lithium Argyrodites with Phosphorus and Arsenic: Order and Disorder of Lithium Atoms, Crystal

Chemistry, and Phase Transitions. *Chemistry – A European Journal* **2010**, *16* (7), 2198–2206. https://doi.org/10.1002/chem.200902470.

(132) Deiseroth, H.-J.; Maier, J.; Weichert, K.; Nickel, V.; Kong, S.-T.; Reiner, C. Li7PS6 and Li6PS5X (X: Cl, Br, I): Possible Three-Dimensional Diffusion Pathways for Lithium Ions and Temperature Dependence of the Ionic Conductivity by Impedance Measurements. *Zeitschrift für anorganische und allgemeine Chemie* **2011**, *637* (10), 1287–1294. https://doi.org/10.1002/zaac.201100158.

(133) Kong, S. T.; Gün, Ö.; Koch, B.; Deiseroth, H. J.; Eckert, H.; Reiner, C. Structural Characterisation of the Li Argyrodites Li7PS6 and Li7PSe6 and Their Solid Solutions: Quantification of Site Preferences by MAS-NMR Spectroscopy. *Chemistry – A European Journal* **2010**, *16* (17), 5138–5147. https://doi.org/10.1002/chem.200903023.

(134) Rao, R. P.; Adams, S. Studies of Lithium Argyrodite Solid Electrolytes for All-Solid-State Batteries. *physica status solidi (a)* **2011**, *208* (8), 1804–1807. https://doi.org/10.1002/pssa.201001117.

(135) Wang, H.; Hood, Z. D.; Xia, Y.; Liang, C. Fabrication of Ultrathin Solid Electrolyte Membranes of β-Li3PS4 Nanoflakes by Evaporation-Induced Self-Assembly for All-Solid-State Batteries. *J. Mater. Chem. A* **2016**, *4* (21), 8091–8096. https://doi.org/10.1039/C6TA02294D.

(136) Hood, Z. D.; Wang, H.; Pandian, A. S.; Peng, R.; Gilroy, K. D.; Chi, M.; Liang, C.; Xia, Y. Fabrication of Sub-Micrometer-Thick Solid Electrolyte Membranes of β-Li3PS4 via Tiled Assembly of Nanoscale, Plate-Like Building Blocks. *Advanced Energy Materials* **2018**, *8* (21), 1800014. https://doi.org/10.1002/aenm.201800014.

(137) Phuc, N. H. H.; Morikawa, K.; Mitsuhiro, T.; Muto, H.; Matsuda, A. Synthesis of Plate-like Li3PS4 Solid Electrolyte via Liquid-Phase Shaking for All-Solid-State Lithium Batteries. *Ionics* **2017**, *23* (8), 2061–2067. https://doi.org/10.1007/s11581-017-2035-8.

(138) Phuc, N. H. H.; Totani, M.; Morikawa, K.; Muto, H.; Matsuda, A. Preparation of Li3PS4 Solid Electrolyte Using Ethyl Acetate as Synthetic Medium. *Solid State Ionics* **2016**, *288*, 240–243. https://doi.org/10.1016/j.ssi.2015.11.032.

(139) Xu, R. C.; Xia, X. H.; Yao, Z. J.; Wang, X. L.; Gu, C. D.; Tu, J. P. Preparation of Li7P3S11 Glass-Ceramic Electrolyte by Dissolution-Evaporation Method for All-Solid-State Lithium Ion Batteries. *Electrochimica Acta* **2016**, *219*, 235–240. https://doi.org/10.1016/j.electacta.2016.09.155.

(140) Wang, Y.; Lu, D.; Bowden, M.; El Khoury, P. Z.; Han, K. S.; Deng, Z. D.; Xiao, J.; Zhang, J.-G.; Liu, J. Mechanism of Formation of Li7P3S11 Solid Electrolytes through Liquid Phase Synthesis. *Chem. Mater.* **2018**, *30* (3), 990–997. https://doi.org/10.1021/acs.chemmater.7b04842.

(141) Ito, S.; Nakakita, M.; Aihara, Y.; Uehara, T.; Machida, N. A Synthesis of Crystalline Li7P3S11 Solid Electrolyte from 1,2-Dimethoxyethane Solvent. *Journal of Power Sources* **2014**, *271*, 342–345. https://doi.org/10.1016/j.jpowsour.2014.08.024.

(142) Phuc, N. H. H.; Yamamoto, T.; Muto, H.; Matsuda, A. Fast Synthesis of Li2S–P2S5–LiI Solid Electrolyte Precursors. *Inorg. Chem. Front.* **2017**, *4* (10), 1660–1664. https://doi.org/10.1039/C7QI00353F.

(143) Kraft, M. A.; Culver, S. P.; Calderon, M.; Böcher, F.; Krauskopf, T.; Senyshyn, A.; Dietrich, C.; Zevalkink, A.; Janek, J.; Zeier, W. G. Influence of Lattice Polarizability on the Ionic Conductivity in the Lithium Superionic Argyrodites Li6PS5X (X = Cl, Br, I). *J. Am. Chem. Soc.* **2017**, *139* (31), 10909–10918. https://doi.org/10.1021/jacs.7b06327.

(144) Wang, S.; Zhang, Y.; Zhang, X.; Liu, T.; Lin, Y.-H.; Shen, Y.; Li, L.; Nan, C.-W. High-Conductivity Argyrodite Li6PS5Cl Solid Electrolytes Prepared via Optimized Sintering Processes for All-Solid-State Lithium–Sulfur Batteries. *ACS Appl. Mater. Interfaces* **2018**, *10* (49), 42279–42285. https://doi.org/10.1021/acsami.8b15121.

(145) Prasada Rao, R.; Adams, S. Performance Enhancement of Lithium-Polysulphide Batteries by Atomic Layer Deposition of Lithium Tantalate on Sulphide Solid Electrolytes. *Solid State Ionics* **2018**, *323*, 97–104. https://doi.org/10.1016/j.ssi.2018.05.014.

(146) Zhang, J.; Zhong, H.; Zheng, C.; Xia, Y.; Liang, C.; Huang, H.; Gan, Y.; Tao, X.; Zhang, W. All-Solid-State Batteries with Slurry Coated LiNi0.8Co0.1Mn0.1O2 Composite Cathode and Li6PS5Cl Electrolyte: Effect of Binder Content. *Journal of Power Sources* **2018**, *391*, 73–79. https://doi.org/10.1016/j.jpowsour.2018.04.069.

(147) Rao, R. P.; Sharma, N.; Peterson, V. K.; Adams, S. Formation and Conductivity Studies of Lithium Argyrodite Solid Electrolytes Using In-Situ Neutron Diffraction. *Solid State Ionics* **2013**, *230*, 72–76. https://doi.org/10.1016/j.ssi.2012.09.014.

(148) Boulineau, S.; Tarascon, J.-M.; Leriche, J.-B.; Viallet, V. Electrochemical Properties of All-Solid-State Lithium Secondary Batteries Using Li-Argyrodite Li6PS5Cl as Solid Electrolyte. *Solid State Ionics* **2013**, *242*, 45–48. https://doi.org/10.1016/j.ssi.2013.04.012.

(149) Zhang, Z.; Zhang, L.; Liu, Y.; Yu, C.; Yan, X.; Xu, B.; Wang, L. Synthesis and Characterization of Argyrodite Solid Electrolytes for All-Solid-State Li-Ion Batteries. *Journal of Alloys and Compounds* **2018**, *747*, 227–235. https://doi.org/10.1016/j.jallcom.2018.03.027.

(150) Ozturk, T.; Ertas, E.; Mert, O. A Berzelius Reagent, Phosphorus Decasulfide (P4S10), in Organic Syntheses. *Chem. Rev.* **2010**, *110* (6), 3419–3478. https://doi.org/10.1021/cr900243d.

(151) Inoue, Y.; Suzuki, K.; Matsui, N.; Hirayama, M.; Kanno, R. Synthesis and Structure of Novel Lithium-Ion Conductor Li7Ge3PS12. *Journal of Solid State Chemistry* **2017**, *246*, 334–340. https://doi.org/10.1016/j.jssc.2016.12.001.

(152) Bachman, J. C.; Muy, S.; Grimaud, A.; Chang, H.-H.; Pour, N.; Lux, S. F.; Paschos, O.; Maglia, F.; Lupart, S.; Lamp, P.; Giordano, L.; Shao-Horn, Y. Inorganic Solid-State Electrolytes for Lithium Batteries: Mechanisms and Properties Governing Ion Conduction. *Chem. Rev.* **2016**, *116* (1), 140–162. https://doi.org/10.1021/acs.chemrev.5b00563.

(153) Dietrich, C.; Weber, D. A.; Sedlmaier, S. J.; Indris, S.; Culver, S. P.; Walter, D.; Janek, J.; Zeier, W. G. Lithium Ion Conductivity in Li2S–P2S5 Glasses – Building Units and Local Structure Evolution during the Crystallization of Superionic Conductors Li3PS4, Li7P3S11 and Li4P2S7. *J. Mater. Chem. A* **2017**, *5* (34), 18111–18119. https://doi.org/10.1039/C7TA06067J.

(154) Takada, K.; Osada, M.; Ohta, N.; Inada, T.; Kajiyama, A.; Sasaki, H.; Kondo, S.; Watanabe, M.; Sasaki, T. Lithium Ion Conductive Oxysulfide, Li3PO4–Li3PS4. *Solid State Ionics* **2005**, *176* (31), 2355–2359. https://doi.org/10.1016/j.ssi.2005.03.023.

(155) Yu, C.; Ganapathy, S.; de Klerk, N. J. J.; Roslon, I.; van Eck, E. R. H.; Kentgens, A. P. M.; Wagemaker, M. Unravelling Li-Ion Transport from Picoseconds to Seconds: Bulk versus Interfaces in an Argyrodite Li6PS5Cl–Li2S All-Solid-State Li-Ion Battery. *J. Am. Chem. Soc.* **2016**, *138* (35), 11192–11201. https://doi.org/10.1021/jacs.6b05066.

(156) Dietrich, C.; Weber, D. A.; Culver, S.; Senyshyn, A.; Sedlmaier, S. J.; Indris, S.; Janek, J.; Zeier, W. G. Synthesis, Structural Characterization, and Lithium Ion Conductivity of the Lithium Thiophosphate Li2P2S6. *Inorg. Chem.* **2017**, *56* (11), 6681–6687. https://doi.org/10.1021/acs.inorgchem.7b00751.

(157) Kim, D. H.; Oh, D. Y.; Park, K. H.; Choi, Y. E.; Nam, Y. J.; Lee, H. A.; Lee, S.-M.; Jung, Y. S. Infiltration of Solution-Processable Solid Electrolytes into Conventional Li-Ion-Battery Electrodes for All-Solid-State Li-Ion Batteries. *Nano Lett.* **2017**, *17* (5), 3013–3020. https://doi.org/10.1021/acs.nanolett.7b00330.

(158) Tatsumisago, M.; Hayashi, A. Sulfide Glass-Ceramic Electrolytes for All-Solid-State Lithium and Sodium Batteries. *International Journal of Applied Glass Science* **2014**, *5* (3), 226–235. https://doi.org/10.1111/ijag.12084.

(159) Rayavarapu, P. R.; Sharma, N.; Peterson, V. K.; Adams, S. Variation in Structure and Li+-Ion Migration in Argyrodite-Type Li6PS5X (X = Cl, Br, I) Solid Electrolytes. *J Solid State Electrochem* **2012**, *16* (5), 1807–1813. https://doi.org/10.1007/s10008-011-1572-8.

(160) Wenzel, S.; Sedlmaier, S. J.; Dietrich, C.; Zeier, W. G.; Janek, J. Interfacial Reactivity and Interphase Growth of Argyrodite Solid Electrolytes at Lithium Metal Electrodes. *Solid State Ionics* **2018**, *318*, 102–112. https://doi.org/10.1016/j.ssi.2017.07.005.

(161) Li, Y.; Arnold, W.; Jasinski, J. B.; Thapa, A.; Sumanasekera, G.; Sunkara, M.; Narayanan, B.; Druffel, T.; Wang, H. Interface Stability of LiCl-Rich Argyrodite Li6PS5Cl with Propylene Carbonate Boosts High-Performance Lithium Batteries. *Electrochimica Acta* **2020**, *363*, 137128. https://doi.org/10.1016/j.electacta.2020.137128.

(162) Zhao, Y.; Wu, C.; Peng, G.; Chen, X.; Yao, X.; Bai, Y.; Wu, F.; Chen, S.; Xu, X. A New Solid Polymer Electrolyte Incorporating Li10GeP2S12 into a Polyethylene Oxide Matrix for All-Solid-State Lithium Batteries. *Journal of Power Sources* **2016**, *301*, 47–53. https://doi.org/10.1016/j.jpowsour.2015.09.111.

(163) Xu, B.; Duan, H.; Liu, H.; Wang, C.; Zhong, S. Stabilization of Garnet/Liquid Electrolyte Interface Using Superbase Additives for Hybrid Li Batteries. *ACS Appl. Mater. Interfaces* **2017**, *9* (25), 21077–21082. https://doi.org/10.1021/acsami.7b05599.

(164) Wang, C.; Sun, Q.; Liu, Y.; Zhao, Y.; Li, X.; Lin, X.; Banis, M. N.; Li, M.; Li, W.; Adair, K. R.; Wang, D.; Liang, J.; Li, R.; Zhang, L.; Yang, R.; Lu, S.; Sun, X. Boosting the Performance of Lithium Batteries with Solid-Liquid Hybrid Electrolytes: Interfacial Properties and Effects of Liquid Electrolytes. *Nano Energy* **2018**, *48*, 35–43. https://doi.org/10.1016/j.nanoen.2018.03.020.

(165) Xu, R.; Han, F.; Ji, X.; Fan, X.; Tu, J.; Wang, C. Interface Engineering of Sulfide Electrolytes for All-Solid-State Lithium Batteries. *Nano Energy* **2018**, *53*, 958–966. https://doi.org/10.1016/j.nanoen.2018.09.061.

(166) Fan, X.; Ji, X.; Han, F.; Yue, J.; Chen, J.; Chen, L.; Deng, T.; Jiang, J.; Wang, C. Fluorinated Solid Electrolyte Interphase Enables Highly Reversible Solid-State Li Metal Battery. *Science Advances* **2018**, *4* (12), eaau9245. https://doi.org/10.1126/sciadv.aau9245.

(167) Yu, T.; Liang, J.; Luo, L.; Wang, L.; Zhao, F.; Xu, G.; Bai, X.; Yang, R.; Zhao, S.; Wang, J.; Yu, J.; Sun, X. Superionic Fluorinated Halide Solid Electrolytes for Highly Stable Li-Metal in All-Solid-State Li Batteries. *Advanced Energy Materials* **2021**, *11* (36), 2101915. https://doi.org/10.1002/aenm.202101915.

(168) Lu, Y.; Tu, Z.; Archer, L. A. Stable Lithium Electrodeposition in Liquid and Nanoporous Solid Electrolytes. *Nature Mater* **2014**, *13* (10), 961–969. https://doi.org/10.1038/nmat4041.

(169) Lin, L.; Liang, F.; Zhang, K.; Mao, H.; Yang, J.; Qian, Y. Lithium Phosphide/Lithium Chloride Coating on Lithium for Advanced Lithium Metal Anode. *Journal of Materials Chemistry A* **2018**, *6* (32), 15859–15867. https://doi.org/10.1039/C8TA05102J.

(170) Han, F.; Yue, J.; Zhu, X.; Wang, C. Suppressing Li Dendrite Formation in Li2S-P2S5 Solid Electrolyte by LiI Incorporation. *Advanced Energy Materials* **2018**, *8* (18), 1703644. https://doi.org/10.1002/aenm.201703644.
(171) Yu, C.; Li, Y.; Willans, M.; Zhao, Y.; Adair, K. R.; Zhao, F.; Li, W.; Deng, S.; Liang, J.; Banis, M. N.; Li, R.; Huang, H.; Zhang, L.; Yang, R.; Lu, S.; Huang, Y.; Sun, X. Superionic Conductivity in Lithium Argyrodite Solid-State Electrolyte by Controlled Cl-Doping. *Nano Energy* **2020**, *69*, 104396. https://doi.org/10.1016/j.nanoen.2019.104396.
(172) Hood, Z. D.; Wang, H.; Li, Y.; Pandian, A. S.; Parans Paranthaman, M.; Liang, C. The "Filler Effect": A Study of Solid Oxide Fillers with β-Li3PS4 for Lithium Conducting Electrolytes. *Solid State Ionics* **2015**, *283*, 75–80. https://doi.org/10.1016/j.ssi.2015.10.014.
(173) Rangasamy, E.; Sahu, G.; Keum, J. K.; Rondinone, A. J.; Dudney, N. J.; Liang, C. A High Conductivity Oxide–Sulfide Composite Lithium Superionic Conductor. *J. Mater. Chem. A* **2014**, *2* (12), 4111–4116. https://doi.org/10.1039/C3TA15223E.
(174) Maier, J. Nanoionics: Ion Transport and Electrochemical Storage in Confined Systems. *Nature Mater* **2005**, *4* (11), 805–815. https://doi.org/10.1038/nmat1513.
(175) Kumar, B.; Nellutla, S.; Thokchom, J. S.; Chen, C. Ionic Conduction through Heterogeneous Solids: Delineation of the Blocking and Space Charge Effects. *Journal of Power Sources* **2006**, *160* (2), 1329–1335. https://doi.org/10.1016/j.jpowsour.2006.02.062.
(176) Dawson, J. A.; Canepa, P.; Clarke, M. J.; Famprikis, T.; Ghosh, D.; Islam, M. S. Toward Understanding the Different Influences of Grain Boundaries on Ion Transport in Sulfide and Oxide Solid Electrolytes. *Chem. Mater.* **2019**, *31* (14), 5296–5304. https://doi.org/10.1021/acs.chemmater.9b01794.
(177) Auvergniot, J.; Cassel, A.; Ledeuil, J.-B.; Viallet, V.; Seznec, V.; Dedryvère, R. Interface Stability of Argyrodite Li6PS5Cl toward LiCoO2, LiNi1/3Co1/3Mn1/3O2, and LiMn2O4 in Bulk All-Solid-State Batteries. *Chem. Mater.* **2017**, *29* (9), 3883–3890. https://doi.org/10.1021/acs.chemmater.6b04990.
(178) Yang, Q.; Li, C. Li Metal Batteries and Solid State Batteries Benefiting from Halogen-Based Strategies. *Energy Storage Materials* **2018**, *14*, 100–117. https://doi.org/10.1016/j.ensm.2018.02.017.
(179) Tarascon, J.-M. Key Challenges in Future Li-Battery Research. *Philosophical Transactions of the Royal Society A: Mathematical, Physical and Engineering Sciences* **2010**, *368* (1923), 3227–3241. https://doi.org/10.1098/rsta.2010.0112.
(180) Tan, D. H. S.; Wu, E. A.; Nguyen, H.; Chen, Z.; Marple, M. A. T.; Doux, J.-M.; Wang, X.; Yang, H.; Banerjee, A.; Meng, Y. S. Elucidating Reversible Electrochemical Redox of Li6PS5Cl Solid Electrolyte. *ACS Energy Lett.* **2019**, *4* (10), 2418–2427. https://doi.org/10.1021/acsenergylett.9b01693.
(181) Chen, M.; Yin, X.; V. Reddy, M.; Adams, S. All-Solid-State MoS 2 /Li 6 PS 5 Br/In–Li Batteries as a Novel Type of Li/S Battery. *Journal of Materials Chemistry A* **2015**, *3* (20), 10698–10702. https://doi.org/10.1039/C5TA02372F.
(182) Wu, X.; Song, K.; Zhang, X.; Hu, N.; Li, L.; Li, W.; Zhang, L.; Zhang, H. Safety Issues in Lithium Ion Batteries: Materials and Cell Design. *Front. Energy Res.* **2019**, *7*. https://doi.org/10.3389/fenrg.2019.00065.
(183) Liu, D.-H.; Bai, Z.; Li, M.; Yu, A.; Luo, D.; Liu, W.; Yang, L.; Lu, J.; Amine, K.; Chen, Z. Developing High Safety Li-Metal Anodes for Future High-Energy Li-Metal Batteries: Strategies and Perspectives. *Chem. Soc. Rev.* **2020**, *49* (15), 5407–5445. https://doi.org/10.1039/C9CS00636B.

(184) Zhang, Z.; Shao, Y.; Lotsch, B.; Hu, Y.-S.; Li, H.; Janek, J.; F. Nazar, L.; Nan, C.-W.; Maier, J.; Armand, M.; Chen, L. New Horizons for Inorganic Solid State Ion Conductors. *Energy & Environmental Science* **2018**, *11* (8), 1945–1976. https://doi.org/10.1039/C8EE01053F.

(185) Zhang, D.; Xu, X.; Qin, Y.; Ji, S.; Huo, Y.; Wang, Z.; Liu, Z.; Shen, J.; Liu, J. Recent Progress in Organic–Inorganic Composite Solid Electrolytes for All-Solid-State Lithium Batteries. *Chemistry – A European Journal* **2020**, *26* (8), 1720–1736. https://doi.org/10.1002/chem.201904461.

(186) Yu, C.; Ganapathy, S.; Eck, E. R. H. van; Eijck, L. van; Basak, S.; Liu, Y.; Zhang, L.; W. Zandbergen, H.; Wagemaker, M. Revealing the Relation between the Structure, Li-Ion Conductivity and Solid-State Battery Performance of the Argyrodite Li 6 PS 5 Br Solid Electrolyte. *Journal of Materials Chemistry A* **2017**, *5* (40), 21178–21188. https://doi.org/10.1039/C7TA05031C.

(187) Zhang, J.; Zheng, C.; Li, L.; Xia, Y.; Huang, H.; Gan, Y.; Liang, C.; He, X.; Tao, X.; Zhang, W. Unraveling the Intra and Intercycle Interfacial Evolution of Li6PS5Cl-Based All-Solid-State Lithium Batteries. *Advanced Energy Materials* **2020**, *10* (4), 1903311. https://doi.org/10.1002/aenm.201903311.

(188) Xu, H.; Yu, Y.; Wang, Z.; Shao, G. A Theoretical Approach to Address Interfacial Problems in All-Solid-State Lithium Ion Batteries: Tuning Materials Chemistry for Electrolyte and Buffer Coatings Based on Li 6 PA 5 Cl Hali-Chalcogenides. *Journal of Materials Chemistry A* **2019**, *7* (10), 5239–5247. https://doi.org/10.1039/C8TA11151K.

(189) Binti Faisol, I. Study on the Effects of Doping Argyrodite with LiCl and LiF: In a Solid State Lithium Ion Battery. **2018**.

(190) Han, X.; Sun, J. Design of a LiF-Rich Solid Electrolyte Interface Layer through Salt-Additive Chemistry for Boosting Fast-Charging Phosphorus-Based Lithium Ion Battery Performance. *Chemical Communications* **2020**, *56* (45), 6047–6049. https://doi.org/10.1039/D0CC01853H.

(191) Kim, H.; Kim, Y. S.; Yoo, J. In Situ Formed LiF Protective Layer on Li Metal Anode with Solventless Cross-Linking. **2020**.

(192) Cui, C.; Yang, C.; Eidson, N.; Chen, J.; Han, F.; Chen, L.; Luo, C.; Wang, P.-F.; Fan, X.; Wang, C. A Highly Reversible, Dendrite-Free Lithium Metal Anode Enabled by a Lithium-Fluoride-Enriched Interphase. *Advanced Materials* **2020**, *32* (12), 1906427. https://doi.org/10.1002/adma.201906427.

(193) Zhang, S.; Zhao, F.; Wang, S.; Liang, J.; Wang, J.; Wang, C.; Zhang, H.; Adair, K.; Li, W.; Li, M.; Duan, H.; Zhao, Y.; Yu, R.; Li, R.; Huang, H.; Zhang, L.; Zhao, S.; Lu, S.; Sham, T.-K.; Mo, Y.; Sun, X. Advanced High-Voltage All-Solid-State Li-Ion Batteries Enabled by a Dual-Halogen Solid Electrolyte. *Advanced Energy Materials* **2021**, *11* (32), 2100836. https://doi.org/10.1002/aenm.202100836.

(194) Zhu, Y.; He, X.; Mo, Y. Origin of Outstanding Stability in the Lithium Solid Electrolyte Materials: Insights from Thermodynamic Analyses Based on First-Principles Calculations. *ACS Appl. Mater. Interfaces* **2015**, *7* (42), 23685–23693. https://doi.org/10.1021/acsami.5b07517.

(195) Zhang, Z.; Zhang, L.; Yan, X.; Wang, H.; Liu, Y.; Yu, C.; Cao, X.; van Eijck, L.; Wen, B. All-in-One Improvement toward Li6PS5Br-Based Solid Electrolytes Triggered by Compositional Tune. *Journal of Power Sources* **2019**, *410–411*, 162–170. https://doi.org/10.1016/j.jpowsour.2018.11.016.

(196) He, M.; Guo, R.; Hobold, G. M.; Gao, H.; Gallant, B. M. The Intrinsic Behavior of Lithium Fluoride in Solid Electrolyte Interphases on Lithium. *PNAS* **2020**, *117* (1), 73–79. https://doi.org/10.1073/pnas.1911017116.
(197) Auvergniot, J.; Cassel, A.; Foix, D.; Viallet, V.; Seznec, V.; Dedryvère, R. Redox Activity of Argyrodite Li6PS5Cl Electrolyte in All-Solid-State Li-Ion Battery: An XPS Study. *Solid State Ionics* **2017**, *300*, 78–85. https://doi.org/10.1016/j.ssi.2016.11.029.
(198) Zhang, Q.; Cao, D.; Ma, Y.; Natan, A.; Aurora, P.; Zhu, H. Sulfide-Based Solid-State Electrolytes: Synthesis, Stability, and Potential for All-Solid-State Batteries. *Advanced Materials* **2019**, *31* (44), 1901131. https://doi.org/10.1002/adma.201901131.
(199) Park, K.-H.; Kaup, K.; Assoud, A.; Zhang, Q.; Wu, X.; Nazar, L. F. High-Voltage Superionic Halide Solid Electrolytes for All-Solid-State Li-Ion Batteries. *ACS Energy Lett.* **2020**, *5* (2), 533–539. https://doi.org/10.1021/acsenergylett.9b02599.
(200) Stamminger, A. R.; Ziebarth, B.; Mrovec, M.; Hammerschmidt, T.; Drautz, R. Ionic Conductivity and Its Dependence on Structural Disorder in Halogenated Argyrodites Li6PS5X (X = Br, Cl, I). *Chem. Mater.* **2019**, *31* (21), 8673–8678. https://doi.org/10.1021/acs.chemmater.9b02047.
(201) Brinek, M.; Hiebl, C.; Wilkening, H. M. R. Understanding the Origin of Enhanced Li-Ion Transport in Nanocrystalline Argyrodite-Type Li6PS5I. *Chem. Mater.* **2020**, *32* (11), 4754–4766. https://doi.org/10.1021/acs.chemmater.0c01367.
(202) Ruhl, J.; Riegger, L. M.; Ghidiu, M.; Zeier, W. G. Impact of Solvent Treatment of the Superionic Argyrodite Li6PS5Cl on Solid-State Battery Performance. *Advanced Energy and Sustainability Research* **2021**, *2* (2), 2000077. https://doi.org/10.1002/aesr.202000077.
(203) Morgan, B. *Mechanistic Origin of Superionic Lithium Diffusion in Anion-Disordered Li6PS5X Argyrodites*; preprint; 2020. https://doi.org/10.26434/chemrxiv.12349703.v1.
(204) Liao, C.; Yu, C.; Peng, L.; Miao, X.; Chen, S.; Zhang, Z.; Cheng, S.; Xie, J. Achieving Superior Ionic Conductivity of Li6PS5I via Introducing LiCl. *Solid State Ionics* **2022**, *377*, 115871. https://doi.org/10.1016/j.ssi.2022.115871.
(205) Wang, L.; Fu, S.; Zhao, T.; Qian, J.; Chen, N.; Li, L.; Wu, F.; Chen, R. In Situ Formation of a LiF and Li–Al Alloy Anode Protected Layer on a Li Metal Anode with Enhanced Cycle Life. *Journal of Materials Chemistry A* **2020**, *8* (3), 1247–1253. https://doi.org/10.1039/C9TA10965J.
(206) Jiang, Z.; Li, Z.; Wang, X.; Gu, C.; Xia, X.; Tu, J. Robust Li6PS5I Interlayer to Stabilize the Tailored Electrolyte Li9.95SnP2S11.95F0.05/Li Metal Interface. *ACS Appl. Mater. Interfaces* **2021**, *13* (26), 30739–30745. https://doi.org/10.1021/acsami.1c07947.
(207) Lee, Y.; Jeong, J.; Lim, H.-D.; Kim, S.-O.; Jung, H.-G.; Chung, K. Y.; Yu, S. Superionic Si-Substituted Lithium Argyrodite Sulfide Electrolyte Li6+xSb1–XSixS5I for All-Solid-State Batteries. *ACS Sustainable Chem. Eng.* **2021**, *9* (1), 120–128. https://doi.org/10.1021/acssuschemeng.0c05549.
(208) Zhang, Z.; Zhang, J.; Jia, H.; Peng, L.; An, T.; Xie, J. Enhancing Ionic Conductivity of Solid Electrolyte by Lithium Substitution in Halogenated Li-Argyrodite. *Journal of Power Sources* **2020**, *450*, 227601. https://doi.org/10.1016/j.jpowsour.2019.227601.
(209) Zhang, J.; Li, L.; Zheng, C.; Xia, Y.; Gan, Y.; Huang, H.; Liang, C.; He, X.; Tao, X.; Zhang, W. Silicon-Doped Argyrodite Solid Electrolyte Li6PS5I with Improved Ionic Conductivity and Interfacial Compatibility for High-Performance All-Solid-State Lithium Batteries. *ACS Appl. Mater. Interfaces* **2020**, *12* (37), 41538–41545. https://doi.org/10.1021/acsami.0c11683.
(210) Song, Y. B.; Kim, D. H.; Kwak, H.; Han, D.; Kang, S.; Lee, J. H.; Bak, S.-M.; Nam, K.-W.; Lee, H.-W.; Jung, Y. S. Tailoring Solution-Processable Li Argyrodites Li6+xP1–XMxS5I (M = Ge,

Sn) and Their Microstructural Evolution Revealed by Cryo-TEM for All-Solid-State Batteries. *Nano Lett.* **2020**, *20* (6), 4337–4345. https://doi.org/10.1021/acs.nanolett.0c01028.

(211) Sun, S.; Myung, S.; Kim, G.; Lee, D.; Son, H.; Jang, M.; Park, E.; Son, B.; Jung, Y.-G.; Paik, U.; Song, T. Facile Ex Situ Formation of a LiF–Polymer Composite Layer as an Artificial SEI Layer on Li Metal by Simple Roll-Press Processing for Carbonate Electrolyte-Based Li Metal Batteries. *Journal of Materials Chemistry A* **2020**, *8* (33), 17229–17237. https://doi.org/10.1039/D0TA05372D.

(212) Wang, S.; Xu, X.; Zhang, X.; Xin, C.; Xu, B.; Li, L.; Lin, Y.-H.; Shen, Y.; Li, B.; Nan, C.-W. High-Performance Li 6 PS 5 Cl-Based All-Solid-State Lithium-Ion Batteries. *Journal of Materials Chemistry A* **2019**, *7* (31), 18612–18618. https://doi.org/10.1039/C9TA04289J.

(213) Kim, J. H.; Xiao, C.-F.; Han, J.; Kim, Y. J.; Yagi, S.; Kim, H.-S. Interface Control for High-Performance All-Solid-State Li Thin-Film Batteries. *Ceramics International* **2020**, *46* (12), 19960–19965. https://doi.org/10.1016/j.ceramint.2020.05.063.

(214) Li, Y.; Cao, D.; Arnold, W.; Ren, Y.; Liu, C.; Jasinski, J. B.; Druffel, T.; Cao, Y.; Zhu, H.; Wang, H. Regulated Lithium Ionic Flux through Well-Aligned Channels for Lithium Dendrite Inhibition in Solid-State Batteries. *Energy Storage Materials* **2020**, *31*, 344–351. https://doi.org/10.1016/j.ensm.2020.06.029.

(215) Ren, Y.; Cui, Z.; Bhargav, A.; He, J.; Manthiram, A. A Self-Healable Sulfide/Polymer Composite Electrolyte for Long-Life, Low-Lithium-Excess Lithium-Metal Batteries. *Advanced Functional Materials* **2022**, *32* (2), 2106680. https://doi.org/10.1002/adfm.202106680.

(216) Yi, J.; Zhou, D.; Liang, Y.; Liu, H.; Ni, H.; Fan, L.-Z. Enabling High-Performance All-Solid-State Lithium Batteries with High Ionic Conductive Sulfide-Based Composite Solid Electrolyte and Ex-Situ Artificial SEI Film. *Journal of Energy Chemistry* **2021**, *58*, 17–24. https://doi.org/10.1016/j.jechem.2020.09.038.

(217) Wenzel, S.; Randau, S.; Leichtweiß, T.; Weber, D. A.; Sann, J.; Zeier, W. G.; Janek, J. Direct Observation of the Interfacial Instability of the Fast Ionic Conductor Li10GeP2S12 at the Lithium Metal Anode. *Chem. Mater.* **2016**, *28* (7), 2400–2407. https://doi.org/10.1021/acs.chemmater.6b00610.

(218) Yamamoto, K.; Takahashi, M.; Ohara, K.; Phuc, N. H. H.; Yang, S.; Watanabe, T.; Uchiyama, T.; Sakuda, A.; Hayashi, A.; Tatsumisago, M.; Muto, H.; Matsuda, A.; Uchimoto, Y. Synthesis of Sulfide Solid Electrolytes through the Liquid Phase: Optimization of the Preparation Conditions. *ACS Omega* **2020**, *5* (40), 26287–26294. https://doi.org/10.1021/acsomega.0c04307.

(219) Glynos, E.; Pantazidis, C.; Sakellariou, G. Designing All-Polymer Nanostructured Solid Electrolytes: Advances and Prospects. *ACS Omega* **2020**, *5* (6), 2531–2540. https://doi.org/10.1021/acsomega.9b04098.

(220) Zhang, Y.; Chen, R.; Wang, S.; Liu, T.; Xu, B.; Zhang, X.; Wang, X.; Shen, Y.; Lin, Y.-H.; Li, M.; Fan, L.-Z.; Li, L.; Nan, C.-W. Free-Standing Sulfide/Polymer Composite Solid Electrolyte Membranes with High Conductance for All-Solid-State Lithium Batteries. *Energy Storage Materials* **2020**, *25*, 145–153. https://doi.org/10.1016/j.ensm.2019.10.020.

(221) Dirican, M.; Yan, C.; Zhu, P.; Zhang, X. Composite Solid Electrolytes for All-Solid-State Lithium Batteries. *Materials Science and Engineering: R: Reports* **2019**, *136*, 27–46. https://doi.org/10.1016/j.mser.2018.10.004.

(222) Lou, S.; Zhang, F.; Fu, C.; Chen, M.; Ma, Y.; Yin, G.; Wang, J. Interface Issues and Challenges in All-Solid-State Batteries: Lithium, Sodium, and Beyond. *Advanced Materials* **2021**, *33* (6), 2000721. https://doi.org/10.1002/adma.202000721.

(223) Zheng, C.; Li, L.; Wang, K.; Wang, C.; Zhang, J.; Xia, Y.; Huang, H.; Liang, C.; Gan, Y.; He, X.; Tao, X.; Zhang, W. Interfacial Reactions in Inorganic All-Solid-State Lithium Batteries. *Batteries & Supercaps* **2021**, *4* (1), 8–38. https://doi.org/10.1002/batt.202000147.

(224) Ye, L.; Li, X. A Dynamic Stability Design Strategy for Lithium Metal Solid State Batteries. *Nature* **2021**, *593* (7858), 218–222. https://doi.org/10.1038/s41586-021-03486-3.

(225) Tan, J.; Matz, J.; Dong, P.; Shen, J.; Ye, M. A Growing Appreciation for the Role of LiF in the Solid Electrolyte Interphase. *Advanced Energy Materials* **2021**, *11* (16), 2100046. https://doi.org/10.1002/aenm.202100046.

(226) Cheng, X.-B.; Zhang, R.; Zhao, C.-Z.; Wei, F.; Zhang, J.-G.; Zhang, Q. A Review of Solid Electrolyte Interphases on Lithium Metal Anode. *Adv. Sci.* **2016**, *3* (3), 1500213. https://doi.org/10.1002/advs.201500213.

(227) Wu, F.; Feng, T.; Bai, Y.; Wu, C.; Ye, L.; Feng, Z. Preparation and Characterization of Solid Polymer Electrolytes Based on PHEMO and PVDF-HFP. *Solid State Ionics* **2009**, *180* (9), 677–680. https://doi.org/10.1016/j.ssi.2009.03.003.

(228) Liang, Y. F.; Deng, S. J.; Xia, Y.; Wang, X. L.; Xia, X. H.; Wu, J. B.; Gu, C. D.; Tu, J. P. A Superior Composite Gel Polymer Electrolyte of Li7La3Zr2O12- Poly(Vinylidene Fluoride-Hexafluoropropylene) (PVDF-HFP) for Rechargeable Solid-State Lithium Ion Batteries. *Materials Research Bulletin* **2018**, *102*, 412–417. https://doi.org/10.1016/j.materresbull.2018.02.051.

(229) Cong, L.; Li, Y.; Lu, W.; Jie, J.; Liu, Y.; Sun, L.; Xie, H. Unlocking the Poly(Vinylidene Fluoride-Co-Hexafluoropropylene)/Li10GeP2S12 Composite Solid-State Electrolytes for Dendrite-Free Li Metal Batteries Assisting with Perfluoropolyethers as Bifunctional Adjuvant. *Journal of Power Sources* **2020**, *446*, 227365. https://doi.org/10.1016/j.jpowsour.2019.227365.

(230) Meisner, Q. J.; Rojas, T.; Glossmann, T.; Hintennach, A.; Liu, Q.; Cao, J.; Redfern, P. C.; Ngo, A. T.; Curtiss, L. A.; Zhang, Z. Impact of Co-Solvent and LiTFSI Concentration on Ionic Liquid-Based Electrolytes for Li-S Battery. *J. Electrochem. Soc.* **2020**, *167* (7), 070528. https://doi.org/10.1149/1945-7111/ab76a3.

(231) Joraleechanchai, N.; Duangdangchote, S.; Sawangphruk, M. Insight into the Effect of Ionic Liquid-Based Additives at the Solid Electrolyte Interphase for Lithium Metal Batteries. *J. Electrochem. Soc.* **2021**, *168* (4), 040534. https://doi.org/10.1149/1945-7111/abf7e3.

APPENDIX

Adapted with permission from {W. Arnold, D.A. Buchberger, Y. Li, M. Sunkara, T. Druffel, H. Wang, Halide doping effect on solvent-synthesized lithium argyrodites Li_6PS_5X (X= Cl, Br, I) superionic conductors, Journal of Power Sources. 464 (2020) 228158.} Copyright {2020} Elsevier.

Adapted with permission from {W. Arnold, V. Shreyas, Y. Li, M.K. Koralalage, J.B. Jasinski, A. Thapa, G. Sumanasekera, A.T. Ngo, B. Narayanan, H. Wang, Synthesis of Fluorine-Doped Lithium Argyrodite Solid Electrolytes for Solid-State Lithium Metal Batteries, ACS Appl. Mater. Interfaces. 14 (2022) 11483–11492.} Copyright {2022} American Chemical Society.

Adapted with permission from {D.A. Ziolkowska, W. Arnold, T. Druffel, M. Sunkara, H. Wang, Rapid and Economic Synthesis of a Li_7PS_6 Solid Electrolyte from a Liquid Approach, ACS Appl. Mater. Interfaces. 11 (2019) 6015–6021.} Copyright {2019} American Chemical Society.

Adapted with permission from {Y. Li, W. Arnold, J.B. Jasinski, A. Thapa, G. Sumanasekera, M. Sunkara, B. Narayanan, T. Druffel, H. Wang, Interface stability of LiCl-rich argyrodite Li_6PS_5Cl with propylene carbonate boosts high-performance lithium batteries, Electrochimica Acta. 363 (2020) 137128.} Copyright {2020} Elsevier.

CURRICULUM VITA

NAME: William Richard Arnold

ADDRESS: J.B. Speed School of Engineering
220 Eastern Pkwy
University of Louisville
Louisville, KY 40292

DOB: Louisville, Kentucky – September 27, 1993

EDUATION
& TRAINING: B.S., Biosystems and Agricultural Engineering
University of Kentucky
2012-16

M.S., Mechanical Engineering
University of Louisville
2017-18

Ph.D, Mechanical Engineering
University of Louisville
2019-22

AWARDS: Hsing Chuang Award for Excellence in Graduate Study
2022

PROFESSIONAL SOCIETIES: ACS

PUBLICATIONS: [1] W. Arnold, D.A. Buchberger, Y. Li, M. Sunkara, T. Druffel, H. Wang, Halide doping effect on solvent-synthesized lithium argyrodites Li6PS5X (X= Cl, Br, I) superionic conductors, Journal of Power Sources. 464 (2020) 228158. https://doi.org/10.1016/j.jpowsour.2020.228158.

[2] W. Arnold, V. Shreyas, Y. Li, M.K. Koralalage, J.B. Jasinski, A. Thapa, G. Sumanasekera, A.T. Ngo, B. Narayanan, H. Wang, Synthesis of Fluorine-Doped Lithium Argyrodite Solid Electrolytes for Solid-State Lithium Metal Batteries, ACS Appl. Mater. Interfaces. 14 (2022) 11483–11492. https://doi.org/10.1021/acsami.1c24468.

[3] D.A. Ziolkowska, W. Arnold, T. Druffel, M. Sunkara, H. Wang, Rapid and Economic Synthesis of a Li7PS6 Solid Electrolyte from a Liquid Approach, ACS Appl. Mater. Interfaces. 11 (2019) 6015–6021. https://doi.org/10.1021/acsami.8b19181.

[4] Y. Li, W. Arnold, S. Halacoglu, J.B. Jasinski, T. Druffel, H. Wang, Phase-Transition Interlayer Enables High-Performance Solid-State Sodium Batteries with Sulfide Solid Electrolyte, Advanced Functional Materials. 31 (2021) 2101636. https://doi.org/10.1002/adfm.202101636.

[5] Y. Li, W. Arnold, J.B. Jasinski, A. Thapa, G. Sumanasekera, M. Sunkara, B. Narayanan, T. Druffel, H. Wang, Interface stability of LiCl-rich argyrodite Li6PS5Cl with propylene carbonate boosts high-performance lithium batteries, Electrochimica Acta. 363 (2020) 137128. https://doi.org/10.1016/j.electacta.2020.137128.

[6] Y. Li, W. Arnold, A. Thapa, J.B. Jasinski, G. Sumanasekera, M. Sunkara, T. Druffel, H. Wang, Stable and Flexible Sulfide Composite Electrolyte for High-Performance Solid-State Lithium Batteries, ACS Appl. Mater. Interfaces. 12 (2020) 42653–42659. https://doi.org/10.1021/acsami.0c08261.

[7] Q. Zhang, W. Arnold, Z.D. Hood, Y. Li, R. DeWees, M. Chi, Z. Chen, Y. Chen, H. Wang, Li0.625Al0.125H0.25Cl0.75O0.25 Superionic Conductor with Disordered Rock-Salt Structure, ACS Appl. Energy Mater. 4 (2021) 7674–7680. https://doi.org/10.1021/acsaem.1c01011.

[8] Y. Li, D. Cao, W. Arnold, Y. Ren, C. Liu, J.B. Jasinski, T. Druffel, Y. Cao, H. Zhu, H. Wang, Regulated lithium ionic flux through well-aligned channels for lithium dendrite inhibition in solid-state batteries, Energy Storage Materials. 31 (2020) 344–351. https://doi.org/10.1016/j.ensm.2020.06.029.

[9] Y. Li, S. Halacoglu, V. Shreyas, W. Arnold, X. Guo, Q. Dou, J.B. Jasinski, B. Narayanan, H. Wang, Highly efficient interface stabilization for ambient-temperature quasi-solid-state sodium metal batteries, Chemical Engineering Journal. 434 (2022) 134679. https://doi.org/10.1016/j.cej.2022.134679.

[10] M.K. Gupta, J. Ding, N.C. Osti, D.L. Abernathy, W. Arnold, H. Wang, Z. Hood, O. Delaire, Fast Na diffusion and anharmonic phonon dynamics in superionic Na3PS4, Energy Environ. Sci. 14 (2021) 6554–6563. https://doi.org/10.1039/D1EE01509E.